

Expanding the Scope of Impedance Analysis of Epithelial Barrier Function: Novel Assays and Devices

DISSERTATION

zur Erlangung des Doktorgrades der
Naturwissenschaften (Dr. rer. nat.)
der Fakultät für Chemie und Pharmazie
der Universität Regensburg



vorgelegt von **Florian Urban** aus Waldmünchen, 2019

Diese Doktorarbeit entstand in der Zeit von März 2016 bis September 2019 am Institut für Analytische Chemie, Chemo- und Biosensorik der Fakultät Chemie und Pharmazie der Universität Regensburg.

Die Arbeit wurde angeleitet von Prof. Dr. Joachim Wegener.

Promotionsgesuch eingereicht am: 12.09.2019

Kolloquiumstermin: _____

Prüfungsausschuss:

Vorsitzender:

Erstgutachter: Prof. Dr. Joachim Wegener

Zweitgutachterin: PD Dr. Miriam Breunig

Drittprüferin: Prof. Dr. Antje Bäumner

FÜR MEINE FAMILIE UND CARINA

1	Introduction	1
1.1	Epithelial barriers	1
1.1.1	Classification of cell-cell and cell-matrix contacts.....	2
1.1.2	Pathways of transepithelial transport	5
1.1.3	Quantification of epithelial barrier function	6
1.1.3.1	Ionic permeability.....	7
1.1.3.2	Molecular permeability.....	11
1.1.3.3	Water permeability.....	14
1.1.4	Diseases associated with dysfunctional epithelial barrier function	17
1.2	Aquaporins (AQPs).....	18
1.2.1	Physiological relevance of water-selective channels.....	20
1.2.2	Molecular architecture of aquaporins	20
1.2.3	Inhibitors of aquaporins	22
1.2.4	Diseases associated with dysfunction of aquaporins	23
2	Objectives	24
3	Theoretical background	26
3.1	Electrochemical impedance spectroscopy (EIS)	26
3.1.1	Data presentation and analysis	29
3.1.2	TER-measurements	31
3.1.3	Impedance spectroscopy in presence of a redox-active species	37
3.1.4	Electric cell-substrate impedance sensing (ECIS).....	39
3.2	Transepithelial permeability assays	43
3.2.1	Molecular permeability coefficient P_E	44
3.2.2	Osmotic water permeability coefficient P_{OS}	47
3.3	Poly-3,4-ethylenedioxythiophene (PEDOT) as electrode material for impedance-based analysis of epithelial barrier function	51
3.3.1	General and electrical properties of PEDOT	52

3.3.2	Conductivity enhancement by post-treatments.....	54
4	Material and methods	56
4.1	Cell culture techniques	56
4.1.1	Cell lines.....	56
4.1.2	General cell culture conditions	56
4.1.3	Subcultivation.....	57
4.1.4	Inoculation protocols.....	58
4.1.5	Buffers and solutions.....	60
4.2	Electrode fabrication	63
4.2.1	Gold electrodes	63
4.2.2	Stainless steel electrodes.....	67
4.2.3	PEDOT-film electrodes.....	68
4.3	Multi-mode impedance analysis	69
4.3.1	Experimental setup.....	69
4.3.2	Assay conditions	70
4.3.2.1	Combined electrochemical detection of P_E and TER (P_E TER-assay)	70
4.3.2.2	Determination of osmotically induced transepithelial water flux	73
4.3.2.3	Combined electrochemical detection of P_{OS} and TER (P_{OS} TER-assay)	75
4.3.2.4	TER-studies with stainless steel electrodes.....	76
4.3.2.5	TER-studies with PEDOT electrodes	76
4.3.2.6	ECIS-cytotoxicity studies	77
4.3.3	Equivalent circuit modeling.....	77
4.4	Fluorophore dilution method.....	78
4.5	PrestoBlue[®]-assay	79
5	Combined electrochemical determination of molecular and ionic permeability (P_ETER-assay).....	81
5.1	P_ETER-assay with integral readout	82

5.1.1	Characterization and calibration of the P _E TER-device	82
5.1.2	Investigation of epithelial monolayers expressing a broad range of barrier tightness.....	89
5.1.3	Calculation of P _E values	97
5.2	P_ETER-assay with spatially resolved readout	101
5.2.1	Characterization of the spatially resolved P _E TER-device	102
5.2.2	Investigation of epithelial monolayers expressing a broad range of barrier tightness.....	107
5.2.3	Investigation of mixed but segregated epithelial layers	113
5.3	Cytotoxicity studies of the redox tracers [Fe(CN)₆]^{3-/4-} and FcMeOH	116
5.4	Advantages and limitations of the P_ETER-assay in comparison to conventional permeability assays	121
5.4.1	Automated and time-resolved monitoring of tracer permeation.....	121
5.4.2	Determination of P _E values with internal TER control.....	122
5.4.3	Laterally resolved recording of tracer permeation	123
5.5	Summary and outlook	123
6	Impedance-based monitoring of osmotically induced water flux across epithelial cell layers	125
6.1	Central water flux measurements	126
6.1.1	Characterization of the electrode	126
6.1.2	Hypertonic stimulations of different epithelial cell layers	129
6.1.3	Hypotonic stimulations of MDCK-II monolayers	132
6.1.4	Analysis of transepithelial water flux kinetics.....	134
6.1.5	Hypertonic stimulations of MDCK-I-AQP1 monolayers	138
6.1.6	AQP-inhibition study with the AQP1-inhibitor H ₂ AuCl ₄ ·3H ₂ O	141
6.2	Spatially resolved monitoring of transepithelial water flux	143
6.2.1	Hypertonic stimulations of MDCK-I and MDCK-I-AQP1 monolayers.....	143
6.2.2	Hypertonic stimulation of mixed but segregated cell layers.....	145

6.3 Combined impedance-based monitoring of osmotically induced transepithelial water flux and TER (P_{OS}TER-assay)	147
6.3.1 Characterization of the electrode.....	148
6.3.2 Hypertonic stimulations of different epithelial monolayers.....	151
6.3.3 Hypotonic stimulations of MDCK-II monolayers	155
6.3.4 Calculation of P_{OS} values	157
6.3.5 AQP-inhibition study with the AQP1-inhibitor $H AuCl_4 \cdot 3H_2O$	162
6.4 Water flux measurements using the established fluorophore dilution method as an independent reference	164
6.5 Evaluation of the cytotoxic potential of the AQP1-inhibitor $H AuCl_4 \cdot 3H_2O$	166
6.6 Advantages and limitations of the impedance-based water flux assay in comparison to established methods	170
6.6.1 Automated monitoring of water flux with excellent time-resolution	170
6.6.2 Determination of P_{OS} values with internal TER-control.....	173
6.6.3 Laterally resolved recording of transepithelial water permeation.....	173
6.7 Summary and outlook	173
7 Transepithelial impedance analysis using PEDOT-electrodes	175
7.1 Comparative TER-studies of MDCK cells using PEDOT and stainless steel electrodes.....	175
7.2 Simulated impedance spectra of Caco-2 monolayers for PEDOT and stainless steel as electrode material	185
7.3 Long-term stability measurements	189
7.3.1 Stability study of the PEDOT-electrodes in absence of epithelial cells.....	189
7.3.2 Manipulation of barrier function of MDCK cells.....	191
7.4 Summary and outlook	195

8 Summary	197
9 Zusammenfassung	200
10 References	203
11 Appendix	216
11.1 Supplementary information	216
11.2 Abbreviations and symbols	232
11.3 Eidesstaatliche Erklärung	236
11.4 Curriculum vitae	237
11.5 Danksagung	238

1 Introduction

1.1 Epithelial barriers

There are four major groups of tissues in mammalian bodies: (I) the connective, (II) the muscle, (III) the nervous and (IV) the epithelial tissue (Patton 2015). Epithelial cells are barrier-forming cells acting as an interface tissue and exhibiting several physiological functions. They cover and protect all inner and outer surfaces of the body. Epithelial layers play an important role in the highly regulated transport of solutes and ions between the underlying tissues and a body cavity (Torrás *et al.* 2018). Besides, they are involved in glandular activity and control the secretion of hormones, sweat, mucus and enzymes (Patton 2015). Epithelia appear at numerous locations in the body, e.g. the outermost layer of the skin is formed by them. The lining of blood and lymphatic vessels represents a special case. This kind of cells is known as endothelial cells (Wegener and Seebach 2014).

Epithelial tissues are classified by the number of their layers and by the morphology of their cells. Basically, the different cell shapes lead to a discrimination between the (I) squamous, (II) cuboidal and (III) columnar epithelium (Eurell *et al.* 2006). The number of cell layers can vary in different epithelium types. The simple epithelium is composed of a monolayer. In that case, every cell has direct contact to the basement membrane separating it from the underlying tissue. Simple epithelial monolayers are especially found at places where absorption and filtration takes place. Supposedly, the one-layer structure of the simple epithelium facilitates these processes. Another class of epithelia is constituted by the stratified epithelium which is made up of multilayers. Such multilayered structures are found where body linings have to face enhanced mechanical and chemical pressure (Platzer and Spitzer 2009).

In the following chapters a brief overview of cell-cell and cell-matrix contacts which are the structural basis for epithelial barrier function as well as possible routes for transepithelial transport is given. Since epithelial barrier function is in the focus of this thesis established assays for its quantification are addressed separately. Additionally, a correlation between a defective barrier function and the development of diseases is highlighted emphasizing the fundamental importance of developing new devices and assays for the analysis of epithelial barrier properties.

1.1.1 Classification of cell-cell and cell-matrix contacts

Epithelial cells form a variety of junctions between two neighboring cells (cell-cell contacts) and to the basement membrane (cell-matrix contacts). These junctions are subdivided into three major classes: (I) *tight junctions*, (II) *anchoring junctions* and (III) *gap junctions* (Alberts 2017). The unique barrier properties of epithelial tissues are mainly due to the tight junctions which are sealing the paracellular gap. Anchoring junctions are also involved in establishing the epithelial barrier by mechanically stabilizing the connection between adjacent cells (adherens junctions, desmosomes) and their connection to the basement membrane (focal contacts, hemidesmosomes). The third subgroup of cell junctions is crucial in terms of cell communication and allows an exchange of nutrients and solutes within the epithelium.

There are two main tasks of tight junctions. First, uncontrolled diffusion between compartments with different chemical composition that are separated by an epithelial cell layer is prevented by sealing the intercellular space between adjacent cells (barrier function). Second, tight junctions also ensure the cell polarity of epithelial layers by building up a barrier to the intramembrane diffusion of proteins and lipids (fence function). Cell polarity is a basic requirement for an active and regulated transepithelial solute and water transport. Even more complex biological processes like gene transcription, tumor suppression and cell proliferation are indirectly associated with the tight junctional complex (Schneeberger and Lynch 2004). Tight junctions are localized in the apical region of epithelial cells (Shin *et al.* 2006). They are composed of a network of sealing strands which are formed from a row of opposing transmembrane proteins embedded in the plasma membranes of the adjacent cells. The extracellular domains of these proteins are interacting with each other resulting in the occlusion of the paracellular cleft. A multitude of different proteins – transmembrane and intracellular - are involved in the formation of the tight junctional complex. So far, three major types of transmembrane proteins are known: (I) occludin, (II) claudins and (III) junction adhesion molecule (JAM) proteins (Anderson and van Itallie 2009). Occludin was the first transmembrane protein which was identified. It is a 65 kDa protein with a tetraspan membrane topology consisting of two extracellular loops and a large C-terminal cytoplasmic domain (Wolburg *et al.* 2006). The participation of occludin in the tightness of epithelial barriers was clearly demonstrated by overexpression that led to an increase of the transepithelial electrical resistance in mammalian cells (Balda *et al.* 1996; McCarthy *et al.* 1996). A special case is formed by tricellulin which seals contact points of three neighboring cells (Ikenouchi *et al.* 2005). Such triple contacting points are supposed to constitute weak

points within the epithelium. The biggest fraction of tight junctional transmembrane proteins is constituted by the family of claudins. In mammals 27 different claudins have been identified (Krug *et al.* 2012; Tsukita *et al.* 2019). They show a similar membrane topology as occludin with two extracellular loops even though they are significantly smaller (20-27 kDa). Claudins possess several physiological functions, but they are primarily involved in forming transcellular contacts required to seal the intercellular gap (Mitic *et al.* 2000). The *in vivo* expression of claudins is diverse, e.g. claudin-3 and claudin-5 are predominantly expressed in brain endothelial cells contributing to the integrity of the BBB. JAMs are the third class of tight junctional transmembrane proteins. They differ from occludin and claudins in their topological structure possessing only a single transmembrane domain with a protein mass in the range of 40 kDa. So far, four different isoforms of JAMs have been observed. Their physiological relevance lies in facilitating the assembly of the tight junctional complex and in maintaining the cell polarity. In addition to transmembrane proteins a second class of proteins is crucial for the forming of tight junctions. These so-called tight junctional adapter proteins are localized within the cytoplasm (Luissint *et al.* 2012). Among them, membrane-associated guanylate kinase (MAGUK) family members have been largely documented: *zonula occludens*-1 (ZO-1, 225 kDa) (Stevenson *et al.* 1986), ZO-2 (160 kDa) (Gumbiner *et al.* 1991) and ZO-3 (130 kDa) (Haskins *et al.* 1998). It is well known that the ZO proteins connect the transmembrane tight junctional proteins with the actin cytoskeleton. All adapter proteins have in common that they exhibit at least one PDZ domain. PDZ is an initialism combining the first letters of the first three proteins discovered to possess the domain – post synaptic density protein (PSD95), *drosophila* disc large tumor suppressor (Dig1), and ZO-1 (Kennedy 1995). ZO proteins interact with the C-terminal domain of claudins via their first PDZ domain (Itoh *et al.* 1999), to JAMs by their third PDZ domain (Bazzoni *et al.* 2000) and to occludin via their GUK (guanylate kinase) domains (Fanning *et al.* 1998; Furuse *et al.* 1994). PDZ domains are a sequence of 80-90 amino acids folding to form a hydrophobic groove to which the C-terminal T/SXV (Ser/Thr-X-Val-COOH with X as an arbitrary amino acid) motif of the transmembrane protein bind (González-Mariscal *et al.* 2005). At present, it is known that many other types of tight junctional adapter proteins exist like for example membrane-associated guanylyl kinase inverted proteins MAGI-1, MAGI-2 and MAGI-3 (Schneeberger and Lynch 2004).

Anchoring junctions are important in the structural cohesion of tissues connecting the cytoskeleton of neighboring cells or establishing a linkage between the cytoskeleton and

basement membrane proteins (Johnson and Harley 2011). The best known type of anchoring junctions is represented by the *adherens junctions*. They are mainly involved in initiating cell-cell contacts and in promoting their maturation and maintenance. Adherens junctions are localized in a more basolateral region of the lateral plasma membrane relative to tight junctions. Although the molecular components of tight junctions and adherens junctions are different, they exhibit common features. In both junction types cell adhesion is moderated by transmembrane proteins which promote hydrophobic interactions between their extracellular domains and form a pericellular zipper-like structure. In case of adherens junctions, the family of cadherins takes this role. Cadherins are single-span, Ca^{2+} dependent transmembrane proteins. The cytoplasmic part of cadherins is connected to the actin cytoskeleton via different mediator proteins like catenins. Desmosomes appear underneath adherens junctions and belong also to the family of cadherin-based junctions. In contrast to adherens junctions desmosomes link the intermediate filaments of adjacent cells via adapter proteins and desmoplakin (Gallicano *et al.* 1998). Additionally, anchoring junctions can be found in the connection between the cytoskeleton and the basement membrane. In that context the superfamily of integrins are of particular interest. Integrins are composed of heterodimers with non-covalently associated α - and β -subunits (Harburger and Calderwood 2009). The extracellular face of integrins binds directly to specific amino acid motifs of diverse extracellular matrix (ECM) proteins like fibronectin or laminin (Hynes 2002). The linkage between the cytoskeleton and the integrins is accomplished by several mediator proteins like talin (Zaidel-Bar *et al.* 2007). The participating cytoskeletal structure defines the name of the cell-matrix junction: (I) focal contacts (actin cytoskeleton), (II) hemidesmosomes (intermediate filaments) (Borradori and Sonnenberg 1996; Litjens *et al.* 2006).

Gap junctions do not contribute to the establishment of a barrier or to the mechanical stability, but regulate a rapid exchange of nutrients, water, ions or other important solutes within the epithelium (Beyer *et al.* 1990). Besides, the coupling between epithelial cells via electrical signals is mediated by gap junctions (Pereda *et al.* 2013). They build an adjustable channel-like structure between two neighboring cells which is formed by channel-forming transmembrane *connexin* proteins. Six connexins associate to build a *connexon* which resembles a hemichannel. Two opposing connexons interact to create an intercellular, water-filled channel linking the cytoplasm of adjacent cells. The permeability of these connexons is mainly controlled by intracellular Ca^{2+} concentration and pH value. The inner

diameter of these pores is 1.4 nm. Moreover, they can be opened and closed instantly to react on external stimuli (Maeda *et al.* 2009; Nakagawa *et al.* 2010).

1.1.2 Pathways of transepithelial transport

Epithelial barriers play an important role in the context of drug development and drug targeting. There are numerous epithelial and endothelial barriers in the human body mediating and also limiting the uptake of certain compounds. A certain drug is able to cross such barriers on different paracellular and transcellular pathways which are summarized in Fig. 1.1. The preferred route of a molecule relies on its physicochemical properties (size / charge / lipophilicity / hydrogen binding potential / solution conformation) (Anderson 2001; Balimane *et al.* 2006; Hillgren *et al.* 1995).

Passive paracellular diffusion (Fig. 1.1 (1)) is minimal in moderately tight and tight epithelia due to the presence of tight junctions. Only small hydrophilic molecules are able to overcome the paracellular seal, unless particular modulators of tight junctions are administered at the same time. For example, it is possible to reduce the tightness of an epithelium by the presence of the tight junction modulator ephrin-A2 which directly phosphorylates claudin-4 (Matsuhisa *et al.* 2009). In case of transcellular pathways several mechanisms have to be considered. Passive transcellular diffusion (Fig. 1.1 (2)) across the phospholipid bilayer can take place for sufficiently hydrophobic or very small molecules. Transcellular diffusion can also be facilitated by particular membrane channels or transport proteins (Fig. 1.1 (3)). It is also possible that a substance is actively transported transcellularly against a concentration gradient by the help of specialized transporter systems (Fig. 1.1 (4)). In this case, the process requires energy which is obtained from a coupled reaction. In humans, there are two possibilities for the gain of energy which are denoted as (I) primary active transport and (II) secondary active transport. Primary active transport is based on an ATP-consuming step, whereas secondary active transport takes the energy from an electrochemical gradient of a different species. For large, hydrophilic compounds active transport is realized by receptor-mediated transcytosis (Fig. 1.1 (7)). A huge challenge in drug absorption appears in presence of apically or basolaterally localized efflux transporters (Fig. 1.1 (5)) like P-glycoprotein transporting compounds from inside the cell back into the intestinal lumen. Thus, the presence of efflux proteins results in a serious reduction of drug uptake. Reduced

drug absorption can also be caused when the absorbed molecule serves as a metabolic substrate (Fig. 1.1 (6)).

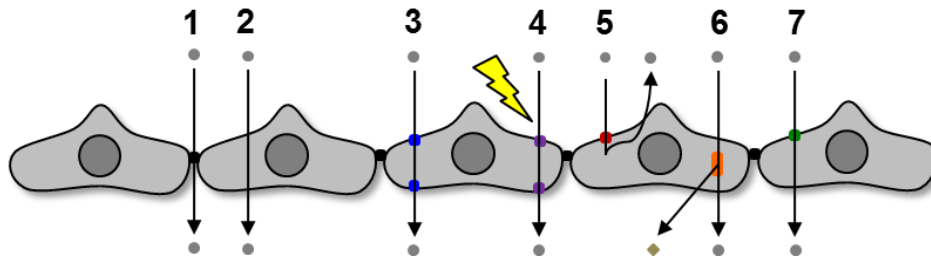


Fig. 1.1: Pathways of transepithelial transport: (1) passive paracellular diffusion, (2) passive transcellular diffusion, (3) facilitated diffusion, (4) primary active or secondary active transport, (5) efflux transporter, (6) metabolic conversion, (7) receptor-mediated transcytosis.

1.1.3 Quantification of epithelial barrier function

In general, three parameters are established for a comprehensive description of epithelial barrier properties: (I) the permeability of small inorganic ions is described by the transepithelial or -endothelial electrical resistance (TER); (II) the permeability of (macro-)molecular tracers across an epithelial barrier gives rise to the molecular permeability coefficient (P_E); (III) the permeability of water through epithelial cells is quantified by the hydraulic conductivity L_p and the osmotic water permeability coefficient (P_{OS}) (Wegener and Seebach 2014).

These three barrier-describing parameters are preferably measured via *in vitro* methods. In that context epithelial assays are of particular interest. Here, epithelial monolayers are cultivated on highly permeable filter supports. These so-called Transwell[®] filters consist of a plastic scaffold which is needed for the mounting of the support into specialized measurement chambers and of a porous membrane acting as a mechanical support and growth substrate for cells. The commercially available filter membranes differ in membrane material (polycarbonate / polyester) as well as in porosity (pore size and pore density). Tab. 1.1 shows an overview about different commercially available Transwell[®] filter inserts. Small pore sizes are recommended for drug transport studies whereas large pore sizes are basically used for cell migration assays. In this thesis polycarbonate membranes with small pores (0.4 μm pore diameter) and high pore density (10^8 pores/ cm^2) are used providing a percental pore area of 12 % related to the overall membrane area of 1.12 cm^2 . In epithelial assays, a cell-covered Transwell[®] filter is placed into a two chamber setup and thereby the cell layer is serving as a diffusion barrier between two fluid-filled compartments. Thus, two

independent compartments are created mimicking the physiological situation of an epithelium with an apical and basolateral area.

The following chapters give a description of the three parameters and summarize the most important corresponding *in vitro* assays. Special attention is directed to the problems and limitations of the established techniques.

Tab. 1.1: Commercially available Transwell® filter inserts consisting of different membrane materials, pore sizes and pore densities. The information is obtained from www.corning.com/lifesciences.

pore size / μm	nominal pore density / pores/ cm^2	
	polycarbonate membrane	polyester membrane
0.4	$1 \cdot 10^8$	$4 \cdot 10^6$
1.0	-	$1.6 \cdot 10^6$
3.0	$2 \cdot 10^6$	$2 \cdot 10^6$
5.0	$4 \cdot 10^5$	-
8.0	$1 \cdot 10^5$	$1 \cdot 10^5$

1.1.3.1 Ionic permeability

The permeability of small inorganic ions like Na^+ , Cl^- , K^+ and HCO_3^- across an epithelial barrier is quantified by the *transepithelial electrical resistance* (TER) (Günzel *et al.* 2010). The TER can be determined via both, direct current (DC) and alternating current (AC) methods. For both approaches, barrier-forming monolayers are cultivated on permeable filter membranes as described above. In DC-TER-readings a four electrode arrangement has to be applied with two electrodes on each side. One electrode pair injects a direct current through the cell layer, whereas the second electrode pair is responsible for measuring the associated voltage drop across the cell layer. Application of Ohm's Law ($R = U/I$) reveals a resistance value (in Ω) that has to be multiplied with the area of the filter surface (in cm^2) and the result is then referred to as the TER (in Ωcm^2). The resistance value of a cell-free filter insert has to be measured separately and subtracted to avoid an overestimation of the TER. Two different DC-based methods to determine the transepithelial electrical resistance are established and illustrated in Fig. 1.2:

- (I) In the first approach each compartment is equipped with a pair of point-like Ag/AgCl electrodes (Fig. 1.2A). The electrodes are referred to as "chopsticks" because they look like a two-armed fork with one current injecting electrode and one voltage sensing electrode on either arm. The two arms are dipped into the apical and basolateral compartment measuring the resistance of the monolayer. However, due to the random placement of the electrodes at the periphery of the

cell layer and due to the electrode geometry, the electric field is inhomogeneous leading to systemically overestimated TER values (Günzel *et al.* 2010; Jovov *et al.* 1991; Sheller *et al.* 2017).

- (II) The second DC method provides more reliable TER-readings (Fig. 1.2B). So-called Endohm™ chambers consist of planar current-injecting electrodes and point-like voltage sensing electrodes resulting in a more uniform current density across the cell layer (Sheller *et al.* 2017; Wegener and Seebach 2014). Thereby, the complete cell layer is taken into account. Additionally the position of the electrodes is fixed leading to more reproducible measurements.

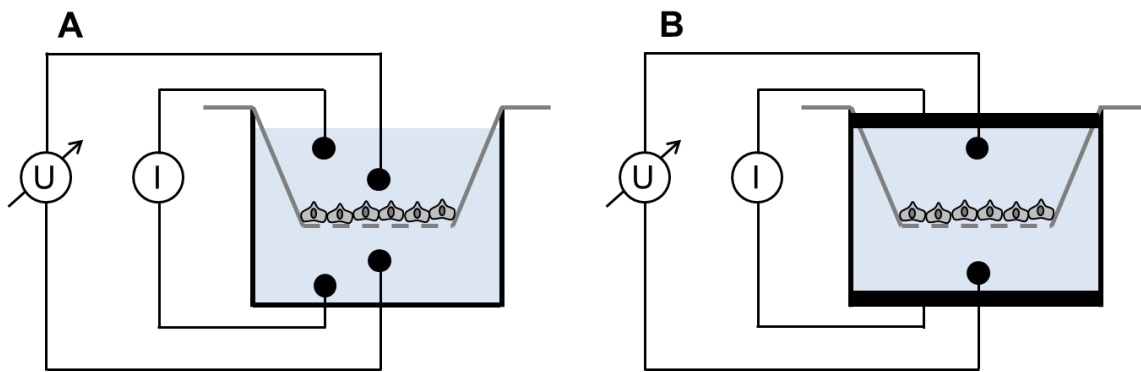


Fig. 1.2: Schematic of the DC-based methods to determine the transepithelial electrical resistance: **(A)** “Chopstick” electrode setup, **(B)** Endohm™ chamber.

Modern devices no longer rely on DC measurements due to a constant concern about membrane polarization and net charge displacement. Instead, electrochemical impedance spectroscopy (EIS, chapter 3.1) has gained increasing impact in terms of analyzing the transepithelial electrical resistance. EIS applies AC currents and AC voltages which are significantly less invasive and provide more information (Wegener *et al.* 2004). Fig. 1.3 displays a schematic of the experimental setup for AC-based TER measurements. A cell-covered filter is sandwiched between two fixed, planar electrodes in order to guarantee a homogenous electric field. Impedance measurements are carried out over a broad frequency range (usually $1 - 10^6$ Hz). The amplitude and the phase shift of an AC current are determined for a given set of discrete frequencies. One of the benefits of this technique is that the total AC impedance contains a higher level of information and returns next to the TER three further parameters:

- (I) The capacitance of the cell layer (C_{cl}) reflects predominantly the surface area of the plasma membrane and provides a measure for the degree of membrane foldings. Knowledge of the true membrane area is important, for example, when active transepithelial transport processes are examined (Kottra *et al.* 1993).
- (II) An additional parameter which can be retrieved from such experiments is the bulk resistance (R_{bulk}). The online monitoring of R_{bulk} shows even small changes in the medium conductivity which may be linked to temperature effects.
- (III) The stationarity of the electrodes is monitored by the measurement as well since in a two-electrode setup the impedance of the electrodes is always an integral part of the system and reported in the data. The parameter that describes the electrode stationarity is denoted as constant phase element (CPE) and is explained in a more detailed way in chapter 3.1.1.

All four parameters (TER, C_{cl} , R_{bulk} , CPE) can be extracted at any time point from the raw data by equivalent circuit modeling. Using two electrodes is justified as long as there is no significant faradaic current across the electrode/electrolyte interface. With the typical applied voltage amplitudes (10 – 50 mV) the two electrode arrangement is valid (Wegener *et al.* 2004).

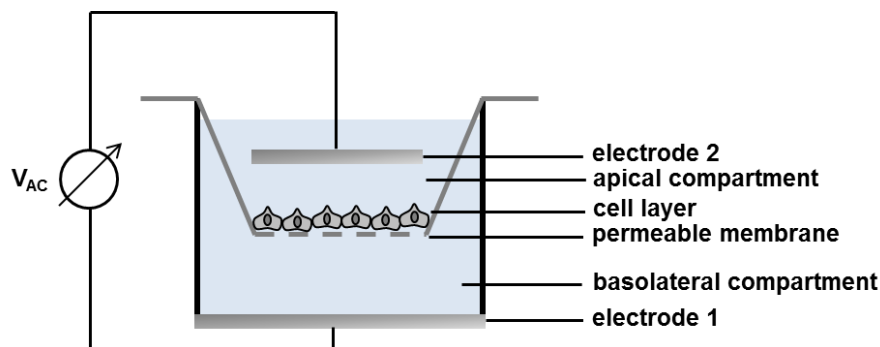


Fig. 1.3: Schematic of the experimental setup for AC-based TER measurements.

Although the impedance-based detection of the ionic permeability across epithelial layers possesses numerous advantages over other means to quantify TER, some pitfalls have to be considered that are common to all these devices and are not improved by using AC. All TER recording techniques represent integral readouts and are therefore prone to artefacts

(Klusmeier *et al.* 2019; Wegener and Seebach 2014). Small defect areas within the monolayer lead to a drastic underestimation of the measured TER. Even single missing cells are suspected to cause misinterpretations (Fromm *et al.* 2009; Wegener and Seebach 2014). Due to the non-transparent character of most Transwell[®] filters, a concomitant microscopic tracing of such defect spots is not possible. Such heterogeneities within cell layers can only be visualized by an increased experimental effort:

- (I) Defect areas have been located by conductance scanning using microelectrodes (Gitter *et al.* 1997; Gitter *et al.* 2001). The microelectrodes are placed directly above the cell surface. A heterogeneous clamp current is then induced across the barrier while the microelectrodes are scanning the local and confined potential. Unfortunately, this experimental handling is elaborate and consequently not relevant for high-throughput studies.

- (II) Another limitation is that the impedimetric determination of TER alone is not sufficient to discriminate between the paracellular resistance (R_{para}) and the transcellular resistance (R_{trans}) (Wegener and Seebach 2014). In most types of epithelia, changes in TER reflect primarily changes in R_{para} due to the extremely high values of R_{trans} . But in case of very tight cell layers, R_{para} can reach the same order of magnitude than R_{trans} . Hence, the contributions of the transcellular currents have to be taken into account for tight cell layers. In this regard, a novel impedance-based technique has been developed which allows the determination of R_{para} and R_{trans} individually (Günzel *et al.* 2012; Krug *et al.* 2009b). Briefly, EIS and permeability measurements of paracellular probes are combined. Provided that the probe is exclusively transported via paracellular diffusion, the contribution of R_{para} can be extracted from the total TER. This method is referred to as *two-path impedance spectroscopy* and is explained in a more detailed way in chapter 3.1.2.

- (III) An additional phenomenon comes into play when very leaky cell layers are investigated. Here, the paracellular resistance is not just determined by the strength of the tight junctions, but also from the lateral intercellular resistance and the resistive contribution arising in the cell-substrate adhesion zone (R_{adh}) (Lo *et al.* 1999). Up to now, there is no possibility to measure R_{adh} for cells grown on filter supports. When cells are grown on impermeable, but conductive surfaces such as

gold-film electrodes, the additional impedance contribution from the cell-substrate adhesion zone is assessable from impedance spectroscopy (Giaever 1993; Giaever and Keese 1984; Giaever and Keese 1991). This well-established technique is referred to as *electric cell-substrate impedance sensing* (ECIS, chapter 3.1.4).

1.1.3.2 Molecular permeability

Solute flux across epithelial cell layers is among others studied via *in vitro* permeability assays. Epithelial cell sheets cultivated on porous filter membranes are acting as a diffusion barrier between two different compartments, as it was described above. A schematic of the experimental setup for typical permeability measurements is given in Fig. 1.4. To analyze molecular barrier function, a permeability probe is added to one of the two compartments (donor compartment). If the permeability probe is able to cross the barrier, a time-dependent increase of the tracer concentration is observed in the other compartment (receiver compartment). The rate of tracer accumulation in the receiver compartment gives rise to the molecular permeability coefficient (P_E , denoted in cm/s). High permeability coefficients indicate leaky cell layers. To determine correct permeability coefficients, the impact of a cell-free filter insert on the measurement has to be investigated separately and subtracted, as it is necessary for TER-measurements. The physical background of P_E and a detailed calculation protocol are given elsewhere (chapter 3.2.1). Mild agitation is recommended for such permeability measurements to avoid additional diffusive contributions due to an unstirred water layer next to the cell sheet. Furthermore, a strict control of temperature and pH value is necessary (Youdim *et al.* 2003). The choice of the permeability probe depends on the transepithelial transport pathway which is to be examined. Highly water-soluble tracers are taken for the analysis of paracellular permeation, whereas transcellular mechanisms are studied by lipophilic molecules or by tracers for which particular carrier-systems are present in the plasma membrane. Typical paracellular permeability tracers for these standard *in vitro* assays are sucrose, mannitol, inulin or high molecular weight probes like dextrans or polyethylene glycols (PEG) (Ghandehari *et al.* 1997; Sanders *et al.* 1995). The paracellular permeation of larger compounds has initiated a great debate about the composition of tight junctions (Cohen *et al.* 1999; Neuhaus *et al.* 2006; Spring 1998; van Itallie *et al.* 2008; Watson *et al.* 2001). Originally, only small hydrophilic molecules have been regarded to be able to cross the tight junctional complex. Most of the TJs exhibit very small pores (diameter

~ 8 Å) located at the bicellular contact points. There are also larger pores (diameter ~ 100 Å) at the contact zone of three adjacent cells. These tricellular junctions are supposed to facilitate paracellular diffusion of even high molecular weight probes to a small extent. The contribution of these larger pores to the overall tight junctions is estimated to be in the range of 1 % (Krug *et al.* 2009a). The readout of tracer accumulation depends on the type of label. In general, two kinds of labels are used for permeability measurements: (I) Most often the tracers are linked to small fluorescent dyes (Sanders *et al.* 1995), e.g. fluorescein isothiocyanate (FITC). (II) The second approach operates with radiolabels which are introduced to the molecule at specific positions (Ghandehari *et al.* 1997). For the detection of unlabeled tracers usually liquid chromatography techniques are applied.

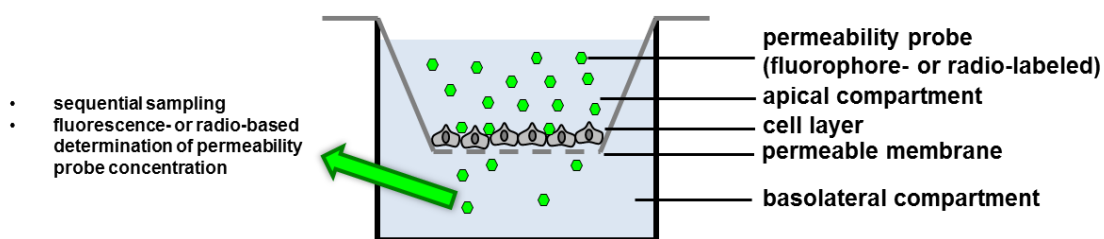


Fig. 1.4: Schematic of the experimental setup for *in vitro* permeability measurements to determine P_E values. In this example the basolateral compartment serves as the receiver compartment.

Several problems of the established permeability assays impede the determination of permeability coefficients and render the calculated values prone to errors:

- (I) An especially critical issue is related to the sampling. A sample has to be taken from the receiver compartment for every single time-point causing a continuous disturbance of the cellular system. The experimental procedure of such assays is both, time-consuming and expensive. This sequential sampling results also in a rather poor time-resolution and provides no online information about the tracer accumulation.
- (II) Furthermore, the coupling of a fluorescent label may alter the physicochemical properties of a tracer compound drastically.
- (III) Standard permeability assays should additionally be combined with separate TER-measurements prior to the actual permeability experiment to ensure barrier integrity. This creates again work load and cost.

- (IV) Similar to TER-readings, the established permeability assays offer an integral readout and hence, permeability coefficients are affected by defects within the epithelial layer. Such leaks in epithelial barriers may cause severe misinterpretations. Therefore, a spatially resolved determination of permeability coefficients creates a considerable advantage and progress.

Several strategies to enable laterally resolved permeability monitoring have already been reported and are summarized in the next paragraphs:

- (I) The first approach was described by Phelps and DePaola who exchanged a liquid receiver compartment against an agarose gel in order to visualize the local distribution of a 70 kDa FITC-dextran after permeation across endothelial barriers (Phelps and DePaola 2000). The fluorescent-labeled dextran diffuses across the cell layer directly into the agarose gel underneath the filter membrane, where its diffusional spread is retarded. Thereby, a spatial mapping of tracer permeability at a given time-point is accessible. However, the lateral resolution of this method was low and far beyond the size of a single cell.
- (II) A better spatial resolution was achieved by the use of high-affinity interactions (Dubrovskiy *et al.* 2013). In that case, the permeability probe is conjugated with avidin and the cells are cultured on a biotinylated gelatin network instead of a filter membrane.
- (III) Another approach of spatial mapping was published by Michaelis *et al.* in 2012. The assay uses mesoporous silicon as a growth substrate for epithelial cells. The pores in the substrate are densely packed and only open to the side facing the barrier-forming cells. Consequently, the pores serve as the receiver compartment and a lateral diffusion of the fluorescence-labeled permeability probe is impossible due to the walls of the pores. Imaging the filling of the pores with a confocal microscope uncovers the spatial permeability of the cell layer at subcellular level. Thus, the approach not only discovers defect areas, but also enables discrimination between para- and transcellular pathways (Michaelis *et al.* 2012).

- (IV) Besides the permeation of fluorescently labeled compounds, also the permeability of redox-active tracers has been studied locally resolved. For example, the diffusion of ferrocenemethanol (FcMeOH) or ruthenium hexamine chloride ($[\text{Ru}(\text{NH}_3)_6]\text{Cl}_3$) across MDCK-II layers was detected with spatial resolution by means of *scanning electrochemical microscopy* (SECM). Passive transport of these redox mediators was recorded with subcellular resolution by scanning the epithelial surface with ultramicroelectrodes (Bergner *et al.* 2012).

The bottom line is that a pool of different approaches for the detection of molecular permeability with spatial resolution exists. However, all of the methods have one common drawback. They are challenging from the experimental point of view and hence, they are not suitable for high-throughput studies. Furthermore, most of the described methods do not offer time-resolved data, but have to be classified as typical end-point assays.

1.1.3.3 Water permeability

For a comprehensive characterization of epithelial water permeability, several parameters are commonly used:

- (I) The hydraulic conductivity (L_P , in $\text{cm}\cdot\text{s}^{-1}\cdot\text{atm}^{-1}$) reflects the permeability of an epithelial barrier for water and relates volume flux to hydrostatic pressure as well as to osmotic pressure.
- (II) Often the impact of hydrostatic pressure is negligible and in those cases, the hydraulic conductivity is converted into the osmotic water permeability coefficient (P_{OS} , in $\mu\text{m}/\text{s}$).
- (III) In absence of any pressure gradients and under steady-state conditions, still a mere diffusional water flux occurs which is quantified by the diffusional water permeability coefficient (P_D , in $\mu\text{m}/\text{s}$). The diffusional water permeability coefficient is usually measured by radiolabeled water flux experiments (^3HHO , $^2\text{H}_2\text{O}$, H_2^{18}O) or by NMR-based techniques (Solomon 1989; Verkman 1995; Ye and Verkman 2002).

A detailed derivation of these three parameters (L_P , P_{OS} , P_D) and the exact calculation protocol for P_{OS} are shown elsewhere (chapter 3.2.2). Furthermore, discrimination between water flux across the entire cell layer (transepithelial) or through only one plasma membrane (transmembrane) is important. For quantification of transepithelial water permeability, standard *in vitro* assays using Transwell® filters (as described above) are performed. Fig. 1.5 shows a schematic of the experimental setup of typical epithelial water flux measurements. In the standardized procedure, an osmotic gradient across the cell layer is induced. One of two compartments is either filled with a hyper- or hypotonic solution leading to a water flux between the two fluid-filled sides. So far, two different readout techniques exist:

- (I) A fluorescent, membrane-impermeable dye with low permeation rate across the cell layer is added into one of the compartments (Levin *et al.* 2006). Due to the water flux between the apical and basolateral region and the associated concentration change, the fluorescence intensity is either decreasing or increasing time-dependently. This approach is also referred to as *fluorophore dilution method*. This technique has similar disadvantages as the standard permeability assays for P_E -determination. Samples have to be taken for every single time-point which means a high level of disturbance for the cells. Additionally, this method is also time-consuming and provides only a low time-resolution. The readout principle is highly prone to errors as there is a serious mixing problem in the fluorophore carrying compartment.

- (II) The second approach makes use of special capillary tubes connected to one of the compartments (Dorr *et al.* 1997). By monitoring the fluid height in the capillary tube, transepithelial water flux can be quantified time-resolved and with good precision. However, the preparation of the experimental setup is difficult and time-consuming. Thus, this technique is not appropriate for high-throughput studies. Another drawback for both approaches is that additional TER control measurements have to be performed to guarantee barrier integrity.

Up to now, no technique has been published that allows for transepithelial water flux detection in a spatially resolved manner. Due to possible heterogeneities of water permeability properties within a cell layer, water flux monitoring with a lateral resolution is worthwhile. Besides, diverse assays are established for detecting transmembrane water transport. Many of them utilize the correlation between cell volume changes (cell

shrinking, cell swelling) and optical properties, such as light transmission (Farinas *et al.* 1997; Farinas and Verkman 1996), absorbance (Levin *et al.* 2007) or scattering (Soveral *et al.* 1997; Soveral *et al.* 2008), and fluorescence (Hamann *et al.* 2002; Solenov *et al.* 2004; Soveral *et al.* 2007). In addition, water flux through the plasma membrane has been measured via impedance spectroscopy (Hua and Pennell 2009; Kimelberg *et al.* 1992) or surface plasmon resonance spectroscopy (Baumgarten and Robelek 2011; Robelek and Wegener 2010; Vala *et al.* 2013).

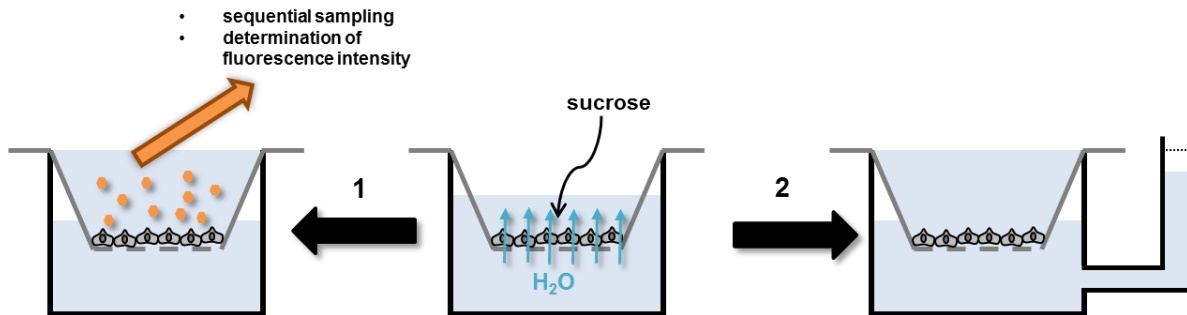


Fig. 1.5: Schematic of the experimental setup for osmotically induced transepithelial water flux measurements to determine P_{OS} values. The illustration refers to the addition of a hyperosmotic solution such as sucrose into the apical compartment. Two different readout principles are established: **(1)** fluorophore dilution method, **(2)** the use of a capillary tube that is connected to one of the two compartments.

The question how water molecules are transported across an epithelium has been discussed for a long time. The literature to that issue reveals a high diversity of answers that are obviously dependent on the cell types (Fischbarg *et al.* 2006; Fischbarg 2010; Tripathi and Boulpaep 1989). In principle, three different routes are relevant:

- (I) Water molecules may migrate across the phospholipid bilayer by simple passive diffusion. Due to the polar character of H₂O and the rather lipophilic properties of the plasma membrane, this kind of transcellular route requires a high level of activation energy and the plasma membrane to be in physiological, fluid-like phase.
- (II) In certain epithelial tissues, e.g. barrier-forming cells in the kidney, particularly high rates of water transport are needed to meet the physiological requirements. In that kind of tissues, a second transcellular pathway plays the prevailing role (Verkman 2003; Verkman 2006). Special water-selective channels integrated into the plasma membrane facilitate the diffusion of water across the epithelial barrier by significantly reducing the activation energy of the process. These channels are also

referred to as aquaporins (AQPs). A detailed description of aquaporins is provided elsewhere (chapter 1.2).

- (III) The third pathway is still highly controversial. For a long time a paracellular route was basically excluded due to the watertight character of tight junctions. Recently it was shown that claudin-2, a component of the tight junctional complex, forms a paracellular water channel (Günzel and Yu 2013; Krug *et al.* 2012; Rosenthal *et al.* 2010). The study demonstrated that an overexpression of claudin-2 in MDCK C7 cells significantly enhanced the paracellular water permeability. Otherwise, no other compound of the tight junctions has been identified to form water channels up to now which indicates a very small paracellular contribution to the overall transepithelial water transport.

So far, a differentiation between a diffusive pathway across the plasma membrane, a transcellular AQP-mediated transport or a paracellular route through the tight junctions is not possible by single measurements and is only indirectly accessible (Carpi-Medina and Whittembury 1988; Rosenthal *et al.* 2010).

1.1.4 Diseases associated with dysfunctional epithelial barrier function

A crucial function of epithelial and endothelial cell layers is the separation of two physiologically adjacent chemical environments from each other. As mentioned above, epithelial barrier function is mainly due to the formation of tight junctions. These intercellular seals regulate the diffusion of solutes or ions and allow the development of chemical and electrochemical gradients. Thus, epithelial barrier integrity is essential to maintain a constant and steady chemical milieu (homeostasis) within a compartment surrounded by epithelial tissues (e.g. lung, kidney, liver, brain, intestine). Alterations in molecular composition of cell-cell and cell-matrix contacts and the following impacts on barrier properties may provoke serious pathological conditions and subvert homeostasis. This chapter provides a brief overview about diseases caused by dysfunctional barrier properties without focusing on the very complex and still not totally resolved molecular mechanisms. Nevertheless, the importance and the number of pathological conditions associated with impaired epithelial barrier function emphasize the relevance of epithelial and endothelial physiology and the strong need to study it on all levels.

A big family of barrier-interfering ailments is constituted by allergic diseases (Schleimer and Berdnikovs 2017). When the mucus or other biological barriers are predisposed to disruption, microorganisms and antigens may invade the body by getting into the underlying connective tissue. Penetration of microbes may trigger strong immune responses. In *atopic dermatitis*, a loss of dermal barrier function is observed leading to the formation of skin lesions (Thyssen and Kezic 2014). An intact mucosal barrier is crucial for the preservation of airway homeostasis (Heijink *et al.* 2007; Ordoñez *et al.* 2001; Sweerus *et al.* 2017). The latter is disturbed in most forms of asthma due to an impaired barrier function of the airway epithelium. Disruption of tight and adherens junctions with a significant loss of E-cadherin and claudin-18 is typical for asthmatic epithelium. Dysfunctional mucosal epithelial barrier causes *allergic rhinitis* (Lee *et al.* 2016; Runswick *et al.* 2007; Wan *et al.* 1999). Allergens may contain proteases and have been proven to destroy epithelial tight junctions. Reduced levels of the barrier proteins E-cadherin and ZO-1 were determined in nasal mucosal tissue from allergic rhinitis patients. The esophagus consists of a stratified squamous epithelium similar to the structure of skin (Ravelli *et al.* 2006). In *eosinophilic esophagitis*, the intercellular gaps are dilated resulting in a disturbed barrier function. Endothelial dysfunction is also supposed to be an early marker for *atherosclerosis* (Davignon and Ganz 2004).

1.2 Aquaporins (AQPs)

Water is the major component of cells throughout all forms of life. Bidirectional transport of water and solutes across cell membranes is essential for osmoregulation and energy homeostasis which are a prerequisite for survival and adaption of living cells and tissues (Madeira *et al.* 2016). For many years it was assumed that biological membranes are freely permeable to water. However, particular membranes are more water permeable and have certain biophysical features, such as weakly temperature-dependent water transport and an enhanced osmotic compared to diffusional water permeability, which suggested a pore-like transepithelial water flux. In that context, specific water channels, also known as aquaporins (AQPs), located within the plasma membrane have been identified. Cells expressing AQPs exhibit a 5- to 50-fold higher osmotic water permeability than cells that do not (Verkman 2011). Compared to lipid bilayer diffusion, lower activation energy for water transport is a typical property of AQP-mediated diffusion. Hence, in epithelial tissues which rely on fast and efficient water movements, the route across aquaporins is the prevailing pathway, whereas

simple diffusion across lipid bilayers and paracellular flux under participation of claudin-2 only play a minor role. The most remarkable feature of AQPs is their high selectivity and efficiency on water and glycerol permeation, excluding ions and protons (Murata *et al.* 2000). Nevertheless, a number of other permeants such as urea, ammonia, hydrogen peroxide, carbon dioxide, metalloids and nitric oxide have been reported to be transported via aquaporins (Wu and Beitz 2007).

AQPs belong to a highly conserved family of membrane proteins (major intrinsic proteins) comprising more than 1700 integral membrane proteins (Madeira *et al.* 2016). In mammals, 13 different isoforms of AQPs are known (AQP0 – AQP12). These isoforms are found differentially expressed in body regions which are involved in fluid absorption and excretion, but also in other tissues like brain, fat, skin and liver. Generally, aquaporins are divided into three subgroups:

- (I) The classical or orthodox AQPs are primarily permeable to water, such as AQP1, AQP2, AQP4, AQP5 and AQP8.
- (II) A second class of AQPs is also selective for glycerol and is referred to aquaglyceroporins. AQP3, AQP7, AQP9 and AQP10 belong to this group.
- (III) The physiological relevance of S-aquaporins, also unorthodox AQPs, still remains obscure (Verkman 2005). This subfamily is only present in animals but not in plants, fungi and bacteria. AQP0, AQP11 and AQP12 form the family of S-aquaporins appearing in the eye lens, kidney, liver and pancreas (Ishibashi *et al.* 2009; Ishibashi *et al.* 2014).

In most cell types, AQPs remain constitutively in the plasma membrane. A striking exception is AQP2 of kidney tissue which undergoes vasopressin-regulated exo- and endocytosis (Verkman 2011). To assess AQP-function, typical *in vitro* water flux assays are performed (chapter 1.1.3.3).

In the following chapters, the physiological function of aquaporins as well as their molecular architecture are briefly described. Moreover, an overview about potential AQP-inhibitors is given. The last chapter deals with several pathophysiological conditions that are due to defective function or expression of aquaporins.

1.2.1 Physiological relevance of water-selective channels

AQPs are involved in the regulation of transepithelial fluid permeation and mediate processes like urine concentration or the secretion of gland fluids (Verkman 2011). However, their physiological impact goes far beyond this obvious task. For instance, AQPs are expressed in electrically excitable tissues in supportive cells adjacent to excitable cells, e.g. in astrocytes but not neurons of the brain. Impaired vision (Li *et al.* 2002), hearing (Li and Verkman 2001) and olfaction (Lu *et al.* 2008) were observed in AQP4-null mice via electrophysiological measurements. Besides the contribution of aquaporins to neural signaling, they have also a share in cell migration. Various cell types which were transfected with AQPs featured an increased cell migration (Verkman 2011). Regardless of the exact biological mechanism, AQP-facilitated cell migration is a general phenomenon involved not only in angiogenesis but also in tumor spread, wound healing and immune cell chemotaxis. Many types of tumor cells suffer from AQP-overexpression. It is supposed that the raised level of aquaporins enhance the ability of tumor cells to spread across blood vessels and to invade locally (Hu and Verkman 2006). Furthermore, aquaglyceroporins participate in important physiological processes. AQP3 plays a crucial role in skin hydration (Hara *et al.* 2002; Ma *et al.* 2002). Reduced epidermal glycerol permeability in AQP3-lacking mice led to reduced skin hydration and elasticity. AQP7, also an aquaglyceroporin, is directly involved in fat metabolism (Hara-Chikuma *et al.* 2005; Hibuse *et al.* 2005). It was shown that AQP7-null mice reveal a notably progressive increase in fat mass and adipocyte hypertrophy, accumulating glycerol in their adipocytes. Consequently, the correlation between AQPs and numerous biological activities makes them very attractive as potential drug targets which could be exploited for future clinical benefits. For example, treatments modulating AQP-expression or -function could act as diuretics, and in therapies for brain swelling, glaucoma, epilepsy, obesity and even cancer. This enormous potential of AQP-based drug development highlights the great importance of engineering new assays for the analysis of transepithelial water flux in order to assess AQP-function and thus, to find novel and better AQP-modulators.

1.2.2 Molecular architecture of aquaporins

AQPs are a family of small (~ 30kDa/monomer), integral membrane proteins consisting of four monomers which assemble to form tetramers. Each monomer is made up of six membrane-spanning helical domains and two short segments surrounding cytoplasmic and extracellular vestibules, respectively. These vestibules are decorated by a narrow aqueous

pore of 25 Å in length. Fig. 1.6 shows the structure of the well-studied AQP1. Several molecular dynamics simulations suggest that a single-file transport of water occurs through a narrow pore in each monomer. Thus, there is biophysical limitation on the efficiency with which AQPs can transport water, so that aquaporins have to be present in the plasma membrane at a high density to improve membrane water permeability in a significant way. Therefore, AQP-expressing cells contain at least several thousands of water channels per μm^2 of membrane, whereas ion channels only appear with a density not exceeding ten channels per μm^2 of membrane (Verkman 2005; Verkman 2011; Verkman and Mitra 2000).

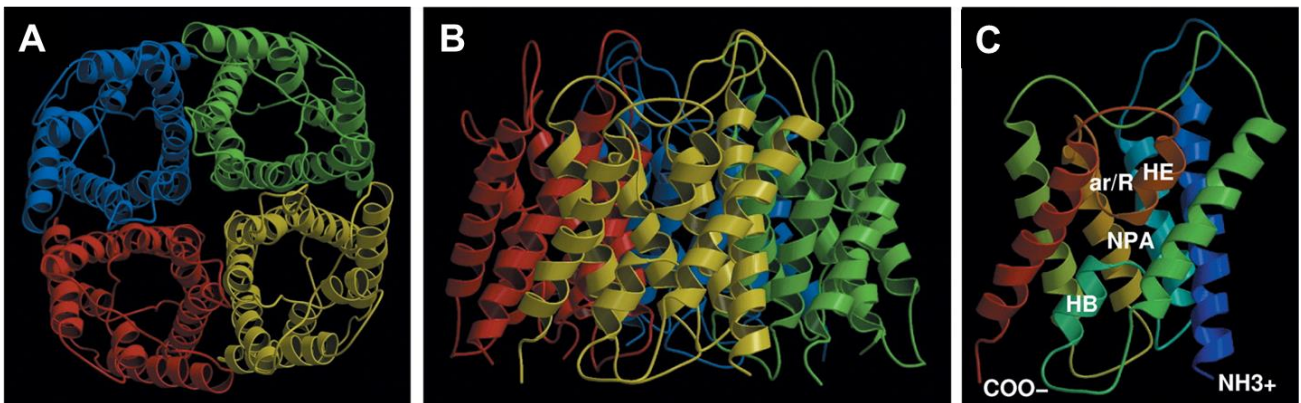


Fig. 1.6: The structure of AQP1. All AQPs are homotetramers made up of four monomeric channels, as shown in **(A)** top view and **(B)** side view. **(C)** The monomeric channels consist of six transmembrane helices connected by five loops which are referred to as A to E in AQP1. Loops B and E contain the highly conserved NPA motifs, which fold back into the channel and meet at the center. The ar/R constriction region which is the narrowest part of the channel is located approximately 7 Å extracellular to the NPA region. The image is taken from literature (Groot and Grubmüller 2005).

In virtually all organisms, proton gradients across epithelial barriers act as the primary energy source for the synthesis of ATP. For this reason, electrochemical gradients have to be strictly preserved. It is crucial that transepithelial water flux through AQPs is not coupled to proton transport. The stringent selectivity of aquaporins is due to two important regions within the channel:

- (I) The first stage of selectivity filter is located in the central part of the channel and is referred to as the NPA region. Two conserved Asn-Pro-Ala (NPA) motifs reside on opposite sides of the AQP-monomer spanning a strong electrostatic field along this region. Electrostatic interactions are the prevailing mechanism of proton exclusion in AQPs (Groot and Grubmüller 2005).

- (II) The second stage is formed by the aromatic/arginine (ar/R) constriction region and is located on the extracellular face of the channel. The ar/R constriction site serves both, as a steric and electrostatic filter. This region is the narrowest part of AQPs with a pore size of 2.8 Å. Aquaglyceroporins have a less-constricted ar/R region with a size of 3.4 Å (Verkman 2005; Verkman 2011). Due to its narrow character, the ar/R selectivity filter hinders larger molecules from passing through the channel. Additionally, it serves as a barrier for small hydrophobic solutes (Hub and Groot 2008).

AQPs achieve their water permeability through a fine-tuned choreography of hydrogen bonds. By that, the activation barrier is lowered to a large extent and hence, high permeability rates for water molecules are generated, despite the hydrophobic character of the pore (Groot and Grubmüller 2005).

1.2.3 Inhibitors of aquaporins

The identification of AQP-modulators has turned out to be unexpectedly challenging. Although a pool of AQP influencing compounds is known, their clinical applicability is low due to several side effects and a lack of selectivity. So far, no relevant inhibitors for aquaglyceroporins have been discovered, whereas most compounds target classical aquaporins (Almeida *et al.* 2014). The first potent AQP-inhibitor was found to be HgCl₂ (Preston *et al.* 1992; Preston *et al.* 1993; Yukutake *et al.* 2008). The inhibition of mercury has been attributed to the formation of a mercaptide bond with cysteine residue 189 located in the pore-forming region. Some inorganic salts (ZnCl₂, NiCl₂, CuSO₄) have been reported to affect the efficiency of certain aquaporins (Yukutake *et al.* 2009; Zelenina *et al.* 2004). Furthermore, quaternary ammonium salts like tetraethylammonium (TEA) are supposed to interact with AQP1 (Brooks *et al.* 2000; Detmers *et al.* 2006). Silver (AgNO₃) and gold (HAuCl₄) compounds are powerful AQP-blockers. Their inhibitory effect is comparable to that of HgCl₂ (Niemietz and Tyerman 2002). As for mercury, the mechanisms of silver and gold inhibition are most likely due to their ability to interact with sulfhydryl groups within the channel. In recent years a new class of potential AQP-modulators has been described. Coordination gold complexes are predicted to exhibit improved selectivity combined with less cytotoxicity. The exploration of such gold complexes as possible AQP-modulators may open the gate to novel approaches for targeting AQP-function and to new drug families (Almeida *et al.* 2014).

1.2.4 Diseases associated with dysfunction of aquaporins

A direct correlation between dysfunctional aquaporins and human diseases is only known for a few pathological conditions. In *congenital cataracts*, a mutation of AQP0 in the lens fiber leads to impaired vision or even to blindness (Berry *et al.* 2000; Chepelinsky 2009). A second human disease, which is directly coupled to AQP-dysfunction, is referred to as *neuromyelitis optica* (NMO). NMO is a variant of *multiple sclerosis* affecting the optic nerve and the spinal cord (Lennon *et al.* 2005). This disease has a poor prognosis as it quickly results in blindness, paralysis and death. A typical feature of NMO is the presence of serum antibodies directed against extracellular epitopes of AQP4. *Nephrogenic diabetes insipidus* is a further AQP-related human disease (Verkman 2012). Patients suffer from an excessive thirst and an enormous excretion of urine due to defects of AQP2. Dysfunctional AQP2 is linked to impaired vasopressin-regulated water permeability in the collecting duct. It is known that aquaporins are involved in a variety of biological processes (chapter 1.2.1). Therefore, AQP-based therapy for human diseases might be a useful tool and could become relevant in numerous fields like tumor chemotherapies, diuretics or treatments against obesity.

2 Objectives

Diverse pathological conditions are due to disrupted epithelial and endothelial barriers. Therefore, the development of novel and improved techniques for the analysis of epithelial barrier function is of utmost importance in basic as well as in applied research. *In vitro* assays are commonly used to mimic *in vivo* like conditions. Many studies on barrier-forming cells deal with monitoring the ionic permeability, which is expressed by the transepithelial and -endothelial electrical resistance (TER). While TER is assessable by impedance-based techniques, permeability coefficients (P_E) reflecting the permeability of a barrier-forming cell layer for molecules of interest have so far been determined by non-impedimetric methods. The first project of this thesis addresses the development of an optimized, impedance-based assay to determine permeability coefficients for redox-active probes like ferri-/ferrocyanide ($[\text{Fe}(\text{CN})_6]^{3-/4-}$) or ferrocenemethanol (FcMeOH). Their time- and barrier-dependent accumulation in the receiver compartment of a regular dual chamber should be monitored by specific electrode layouts integrated into the bottom of the receiver well. As a particular advantage of this approach, P_E and TER should become assessable simultaneously for the very same cell layer within one common experimental setup. Hence, every impedance-based permeability measurement should be accompanied by an automated recording of TER. By increasing the number of electrodes across the bottom of the receiver well, the impedance-based permeability assay should be extended for spatially resolved barrier analysis to account for barrier heterogeneities within a given cell layer. Possible harmful effects of the redox tracers are to be excluded by running cytotoxicity studies (PrestoBlue[®]-assays, ECIS).

Besides dysfunctional epithelial barriers, altered aquaporin (AQP) function is known to be associated with several diseases. AQP-targeted therapies are predicted to have a great future in different fields as water-selective channels are involved in numerous biological processes. So far, established assays for studying transepithelial water flux and AQP-function rely on simple and time-consuming readout principles that are prone to different experimental interferences. It is the aim of the second project to develop a novel, impedance-based assay for detecting osmotically induced water permeability coefficients (P_{Os}). Transepithelial water flux should be monitored by the help of gold-film electrodes deposited on the bottom of the device. The ionic concentration close to the electrodes changes time-dependently when water but not solutes permeate across the cell layer. A corresponding change in conductance should be assessable by tailored, time-resolved

impedance measurements and report on water flux. Laterally resolved detection of water flow should be enabled by increasing the number of electrodes at different locations underneath the cell layer. In addition, P_{OS} and TER should be recorded simultaneously within one common setup. Several AQP-studies should be performed with the novel technique in order to validate the new measurement principle. The impedance-based osmotic water permeability coefficients should be compared to those obtained from established assays like the fluorophore dilution method as a reference.

TER is the prevailing parameter recorded in studies addressing biological barriers. AC-based TER-determination has evolved to the most trusted and accepted method over the years. However, there are some limitations even with impedance-based TER-setups. Usually stainless steel or gold are chosen as the electrode material. Such electrodes show a limited capacitance at the electrode-electrolyte interface which translates into a rather high interface impedance of the electrodes at low AC frequencies. Under certain conditions, for example when cell layers with high membrane capacitances are being studied, the impedance contribution of the cell layer may get masked by the impedance of the electrode-electrolyte interface as the former is in series to the latter. Thus, the third project of this thesis should explore the use of poly-3,4-ethylenedioxythiophene (PEDOT) as electrodes or electrode coatings in regular impedance-based devices to measure TER. This well-known conductive polymer is known for its particular electrochemical properties reducing the influence of the electrode-electrolyte double layer capacitance. Using PEDOT-electrodes with their very high interface capacitance should improve the sensitivity of the approach for cell layers with high membrane capacitance. TER-studies using differently tight epithelial cell lines should be performed and theoretically analyzed to compare the performance of PEDOT-electrodes relative to those made from stainless steel. Additionally, cell-free and cell-based long-term measurements should be conducted to guarantee electrode stability and to prevent possible cytotoxic effects of the new setup.

3 Theoretical background

The theoretical section provides fundamental information about the routinely performed techniques and assays in this thesis. The first chapter deals with the basic physical background of impedance spectroscopy. This method is a powerful tool to study electric features of solid or liquid samples in general and biological systems in particular. In general, impedance spectroscopy captivates by its versatility and by offering outstanding time-resolution (K'Owino and Sadik 2005; Macdonald 1992). Application of impedance spectroscopy to cell-based assays and transfilter measurements of epithelial cell layers providing the TER is addressed in detail in this chapter. The effects of redox-active compounds at the electrode interface are highlighted due to their significance for impedimetric detection of permeability coefficients.

Besides ionic permeability, epithelial barrier function is additionally reflected in molecular and water permeability of the cell layers. The second chapter illustrates the fundamental equations and calculation protocols relevant for the impedance-based *in vitro* permeability assays (P_E and P_{OS}).

The last part of the theoretical section addresses the properties of electrically conducting polymers with a special interest in PEDOT. Several published strategies are described to enhance the conductivity of PEDOT with post-treatments.

3.1 Electrochemical impedance spectroscopy (EIS)

Impedance spectroscopy in general is based on measuring the impedance of a system while it is excited with alternating current (AC) or voltage (Muñoz-Berbel *et al.* 2008; Wegener 2010). The impedance spectrum is obtained by varying the excitation signal over a broad frequency range, usually covering several decades. The complex impedance Z provides detailed information about resistive, capacitive and inductive elements of the system under study. One of the most interesting benefits of impedance spectroscopy is its noninvasiveness, as the technique applies exclusively low amplitude AC currents and AC voltages ensuring damage-free observation with a minimum of disturbance. It is therefore ideally suited to study cells or tissues (Wegener 2010). The noninvasive character of the

method combined with its outstanding time-resolution has made it a versatile tool for biomedical research *in vitro*.

According to Ohm's law, the resistance R of an electric system in a direct current (DC) circuit is defined as the ratio of applied voltage U to corresponding current I . EIS uses a sinusoidal AC voltage as excitation signal. Consequently, the impedance Z becomes time-dependent, as described by equation 3.1:

$$Z = \frac{U(t)}{I(t)} \quad (3.1)$$

The AC voltage $U(t)$ is a function of time t and frequency ω :

$$U(t) = U_0 \sin(\omega t) \quad (3.2)$$

where $\omega = 2\pi f$ is the angular frequency, f is the AC frequency and U_0 is the applied voltage amplitude. The resulting AC current $I(t)$ is also sinusoidal in nature, of the same frequency as the excitation voltage characterized by amplitude I_0 . There is a phase shift between current and voltage, provided that the studied system is not ideally resistive:

$$I(t) = I_0 \sin(\omega t - \varphi) \quad (3.3)$$

Current and voltage can be transformed into complex quantities by means of Euler's formula with $i^2 = -1$:

$$I(t) = I_0 e^{i(\omega t - \varphi)} \quad (3.4)$$

$$U(t) = U_0 e^{i(\omega t)} \quad (3.5)$$

Combining equations 1, 4 and 5 provides the complex impedance in polar coordinates:

$$Z = \frac{U_0 e^{i(\omega t)}}{I_0 e^{i(\omega t - \varphi)}} = \frac{U_0}{I_0} e^{i\varphi} = |Z| e^{i\varphi} \quad (3.6)$$

Thus, at each frequency of the excitation signal the complex impedance is described by two quantities: (I) the magnitude of the impedance $|Z|$, which is the ratio of the amplitudes U_0 and I_0 , and (II) the phase angle φ between voltage and current.

In the complex Gaussian plane (imaginary part plotted against real part) the complex impedance is displayed as a vector (Fig. 3.1). The length of this vector equals the impedance

magnitude $|Z|$, whereas the phase shift φ is represented by the angle between the vector and the abscissa. The real part of the complex impedance, also known as resistance R , arises from current which is in-phase with the applied voltage. The imaginary part of the complex impedance describes the impedance contributions from current which is 90° out-of-phase with the voltage and is referred to as reactance X . The reactance emerges from the storage elements of electrical charges, such as capacitors or inductors. In some cases, it is more convenient to analyze the inverse quantities of Z , R and X , which are named admittance ($Y=1/Z$), conductance ($G=1/R$) or susceptance ($B=1/X$), respectively.

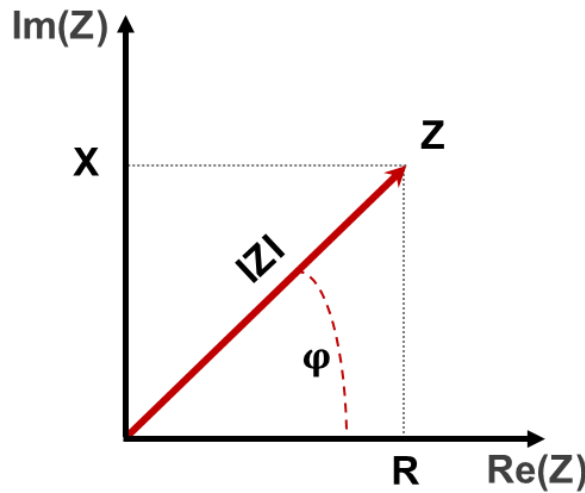


Fig. 3.1: Vector presentation of the complex impedance Z in a complex Gaussian plane. The abscissa shows the real part of the impedance, whereas the ordinate displays the imaginary part. The impedance magnitude $|Z|$ is represented by the vector length. The phase shift φ between voltage and current is indicated by the angle between the vector and the abscissa.

The complex impedance Z may be expressed in Cartesian coordinates:

$$Z = \text{Re}(Z) + i \text{Im}(Z) = R + i X = |Z| \cos\varphi + i |Z| \sin\varphi \quad (3.7)$$

The relation between Cartesian and polar coordinates of the complex impedance Z is given by equations 3.8 and 3.9:

$$|Z| = \sqrt{R^2 + X^2} \quad (3.8)$$

$$\varphi = \arctan\left(\frac{X}{R}\right) \quad (3.9)$$

3.1.1 Data presentation and analysis

There are two established ways of data presentation in impedance spectroscopy (Muñoz-Berbel *et al.* 2008; Wegener 2010). The first technique of visualizing impedance data is referred to as *Nyquist* plots. In these plots the imaginary part is plotted against the real part of the complex impedance. For biological systems the imaginary part is commonly negative due to the absence of inductive elements, so that $-\text{Im}(Z)$ is displayed on the ordinate. However, this presentation does not provide direct information on the frequency domain. Commonly, an arrow is used to indicate the direction in which the frequency increases. The second data presentation method plots the logarithm of the impedance magnitude ($\log |Z|$) and the phase shift (φ) against the logarithm of the applied AC frequency ($\log f$). This approach is denoted as *Bode plot*.

The established method for analyzing impedance data is by means of equivalent circuit modeling. Here, the system under study is described by an electrical network that represents the electrical features of the system. Such electric equivalent circuits are made up of serial or parallel connections of circuit elements like resistors R, capacitors C or inductors L. Complex equivalent circuits must be simplified in order to prevent over-parameterized (redundant) systems. Once an appropriate equivalent circuit is found, the transfer function of this circuit, which is its frequency-dependent complex impedance, is derived by applying Ohm's law and Kirchoff's laws. To quantify the impedance contribution of the individual elements of the system under study, the parameters of the equivalent circuit's transfer function are iteratively adjusted to match the experimental data. Parameter adjustment relies on least-squares optimization (Levenberg-Marquardt – or numerical algorithms). In many cases, it is necessary to add non-ideal elements to the electrical network to account for ionic phenomena such as adsorption and diffusion (Barsoukov and Macdonald 2005; Conway *et al.* 2002; Pajkossy 1994). One of these additional elements is the constant phase element (CPE), which represents a non-ideal capacitor. The CPE was introduced to describe the interface between noble metals and electrolytes. It is assumed to result from surface roughness and ion adsorption. The CPE is described by two parameters: n_{CPE} and A_{CPE} . Its complex impedance is given by:

$$Z(\omega) = \frac{1}{(i\omega)^n A} \quad (3.10)$$

In principle, there are two limiting cases: (I) with $n_{\text{CPE}} = 1$, the element behaves like an ideal capacitor, and (II) with $n_{\text{CPE}} = 0$, the CPE equals a pure resistor. For real measurements, n_{CPE} ranges between 0 and 1 accounting for both, the resistive and the capacitive properties of the electrode-electrolyte interface. The elements R (resistor), C (capacitor), L (inductor) and CPE are sufficient to fully describe electrochemical systems. The situation becomes more complex in presence of a redox-active species in solution. In this case, electron transfer between the compound and the electrode may occur resulting in additional faradaic circuit elements. A detailed description for an equivalent circuit containing faradaic elements is given in chapter 3.1.3. Tab. 3.1 summarizes the most important circuit elements with their corresponding impedance contribution and phase shift.

Tab. 3.1: Impedance contributions Z and phase shift φ of equivalent circuit elements relevant for data analysis in impedance spectroscopy.

circuit element	parameter	impedance Z	phase shift φ
resistor	R	R	0
capacitor	C	$1/(i\omega C)$	$-\pi/2$
inductor	L	$i\omega L$	$+\pi/2$
constant phase element CPE	A, n ($0 \leq n \leq 1$)	$1/[(i\omega)^n A]$	$-\pi n/2$

Fig. 3.2 shows a simulated Bode plot and the corresponding equivalent circuit for a noble metal electrode, which is in direct contact with an electrolyte. The equivalent circuit is composed of a serial connection of a resistance (R_{bulk}) and a constant phase element (CPE). R_{bulk} is determined by the electrolyte resistance and by possible resistive contributions appearing from the experimental setup itself. According to Ohm's law and Kirchoff's laws, the impedance of the electrode/electrolyte system is represented by the transfer function:

$$Z(\omega) = R_{\text{bulk}} + \frac{1}{(i\omega)^n A} \quad (3.11)$$

The Bode plot in Fig. 3.2 shows two frequency regimes. In the higher frequency range, the impact of R_{bulk} is dominating the overall impedance of the system under study. This is indicated by a horizontal line due to the frequency-independence of an Ohmic resistor. Additionally, no phase shift between current and voltage is visible at frequencies dominated by R_{bulk} . With lower frequencies, the capacitive character of the electrode-electrolyte interface gets more pronounced leading to a frequency-dependent increase of the impedance magnitude with decreasing frequency. Besides, a phase shift between voltage and current of almost -90° is induced by the capacitive properties of the electrode/electrolyte interface.

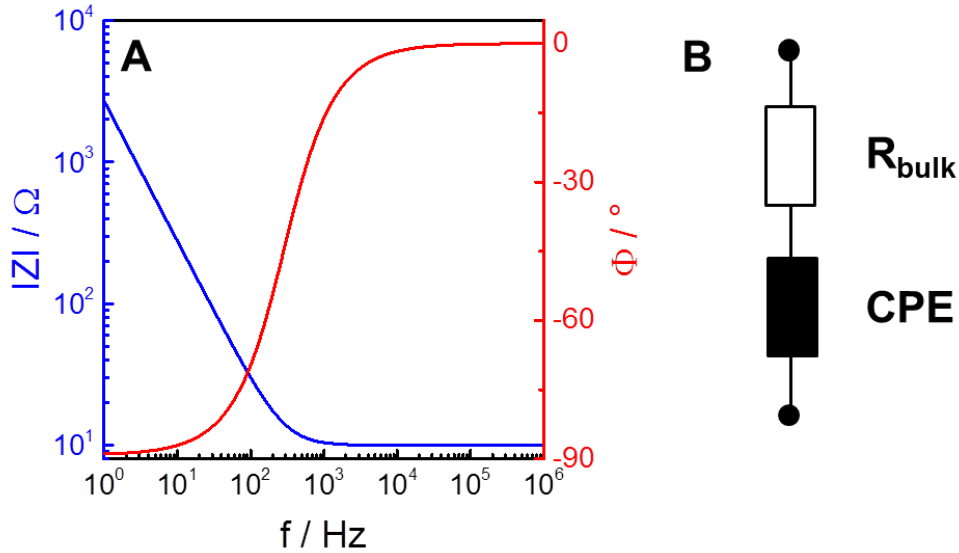


Fig. 3.2: (A) Simulated Bode plot and (B) corresponding electric equivalent circuit for a noble metal electrode which is in contact with an electrolyte. The Bode plot contains information about the impedance magnitude $|Z|$ and the phase shift φ . Parameters: $R_{\text{bulk}} = 10 \Omega$, $A_{\text{CPE}} = 60 \mu\text{Fs}^{n-1}/\text{cm}^2$, $n_{\text{CPE}} = 0.99$. Electrode area: $A_{\text{El}} = 1.12 \text{ cm}^2$.

3.1.2 TER-measurements

Impedance spectroscopy is an often used tool in the field of bioanalytical research. It has evolved to play a fundamental role for the analysis of epithelial and endothelial barriers. As mentioned earlier, confluent cell layers are cultivated on permeable filter membranes mimicking the physiological situation of interfacial tissues between two fluid-filled compartments (apical/basolateral). For the impedance-based quantification of the epithelial permeability for small inorganic ions like Na^+ , Cl^- , K^+ and HCO_3^- , one electrode is placed on each side of the cell sheet. One planar electrode is integrated into the bottom of the measurement chamber serving as a basolateral electrode, whereas the other stamp-like electrode is dipped into the apical solution. Usually, stainless steel or gold are used as the electrode material in such setups. The cell-covered filter is sandwiched between the two electrodes in a fixed position. An AC voltage with low-amplitude is applied to the two electrodes inducing an ionic current between the electrodes. The moving ions probe the tightness of the epithelial barrier. The transepithelial or -endothelial electrical resistance, i.e. the integral resistance of the cell layer, is extracted from the raw data by means of equivalent circuit modeling (Wegener *et al.* 2004).

To express the electric properties of a cellular system, the equivalent circuit of Fig. 3.2 has to be expanded by two additional elements representing the cell layer: (I) The cell layer resistance R_{cl} and (II) the cell layer capacitance C_{cl} which are combined in parallel. R_{cl} is

equivalent to the TER, C_{cl} represents the dielectric features of the plasma membrane and represents the serial combination of the apical and basolateral membrane capacitance. The transfer function for the given R_{bulk} - R_{cl}/C_{cl} -CPE circuit is derived (as described above):

$$Z(\omega) = R_{bulk} + \frac{1}{\frac{1}{R_{cl}} + i\omega C_{cl}} + \frac{1}{(i\omega)^n A} \quad (3.12)$$

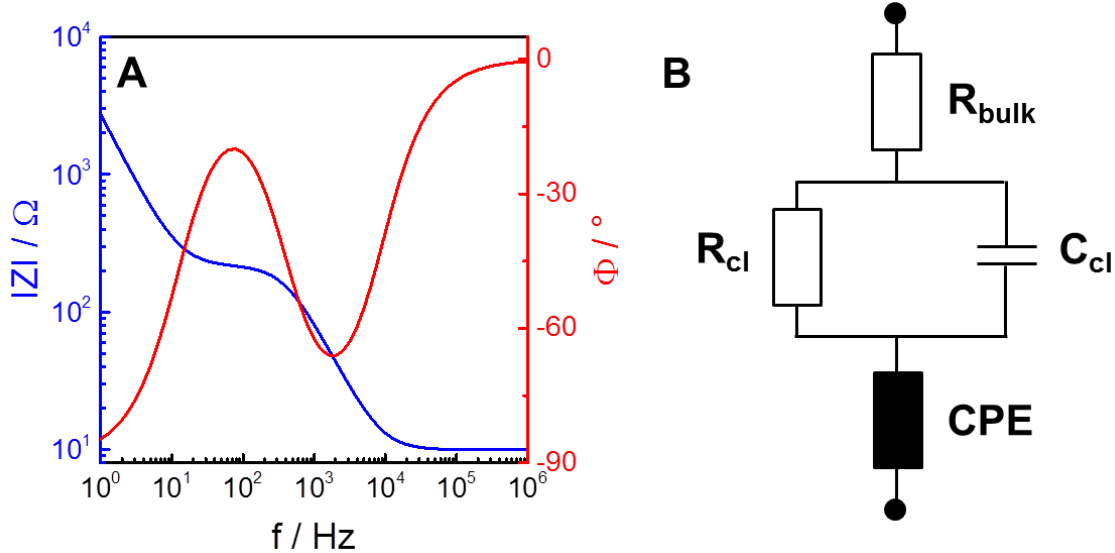


Fig. 3.3: (A) Simulated Bode plot and (B) corresponding electric equivalent circuits for an R_{bulk} - R_{cl}/C_{cl} -CPE system. Parameters: $R_{bulk} = 10 \Omega$, $A_{CPE} = 60 \mu Fs^{-1}/cm^2$, $n_{CPE} = 0.99$, $R_{cl} = 200 \Omega cm^2$, $C_{cl} = 2 \mu F/cm^2$. Electrode area: $A_{EI} = 1.12 cm^2$.

Fig. 3.3 represents a simulated Bode plot and the corresponding equivalent circuit for an arbitrary cell layer. The higher frequency regime is again dominated by the ohmic R_{bulk} ($\varphi = 0^\circ$), whereas the electrode-electrolyte interface for both electrodes is visible at lower frequencies ($\varphi \approx -90^\circ$) and represented by a constant phase element (CPE). The cell impact, which is described by R_{cl} and C_{cl} , is observed in the mid frequency area resulting in a plateau. With increasing TER, the plateau is shifted to higher impedance values. Higher cell layer capacitances lead to reduced width of the plateau. A detailed overview about the effects of alterations in TER and C_{cl} on the frequency-dependent impedance magnitude is illustrated by simulated impedance spectra (Fig. 3.4).

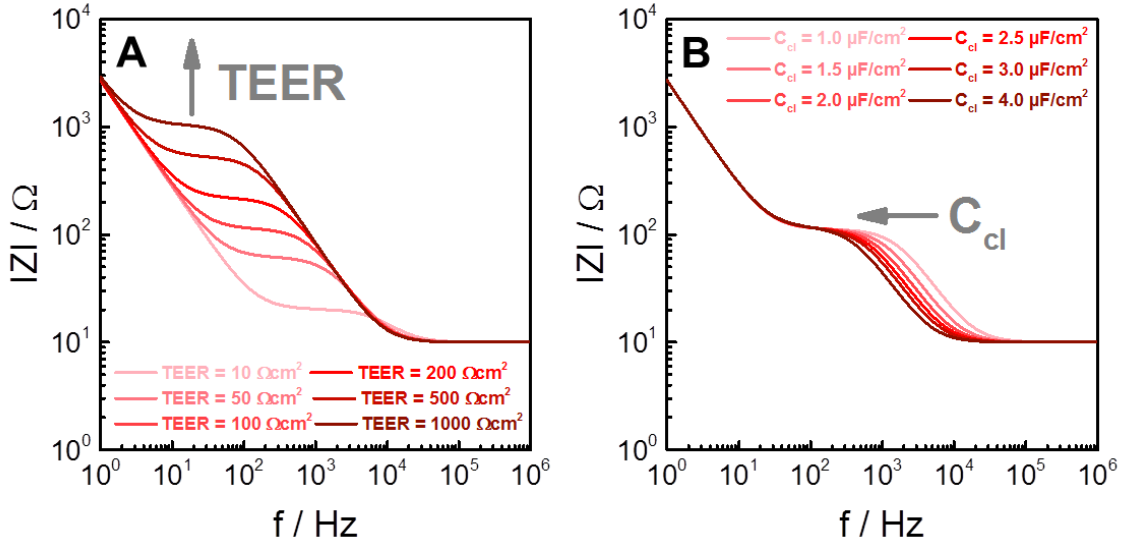


Fig. 3.4: Simulated impedance spectra for a $R_{bulk}-R_{cl}/C_{cl}$ -CPE system when the parameters of the cell layer are systematically varied. **(A)** TER (R_{cl}) and **(B)** C_{cl} . Parameters: $R_{bulk} = 10 \Omega$, $A_{CPE} = 60 \mu F s^{n-1}/cm^2$, $n_{CPE} = 0.99$, $TER = 100 \Omega cm^2$ (for (B)), $C_{cl} = 2 \mu F/cm^2$. (for (A)). Electrode area: $A_{EI} = 1.12 cm^2$.

Due to the resistive character of the filter insert itself, the apparent values of R_{cl} and C_{cl} have to be corrected by the contribution of a cell-free filter support. Commonly, this is realized by including a second R-C element which is connected in series to the R_{cl} - C_{cl} element (Fig. 3.5B). This additional impedance contribution accounts for the filter insert resistance R_{ins} and capacitance C_{ins} . The impact of the filter insert is also observable in the mid frequency range imitating a barrier (Fig. 3.5A). In terms of leaky and moderately tight cell layers, filter correction is a crucial step to avoid overestimation of the transepithelial electrical resistance. The mathematical expression of the corresponding transfer function is shown in equation 3.13:

$$Z(\omega) = R_{bulk} + \frac{1}{\frac{1}{R_{cl}} + i\omega C_{cl}} + \frac{1}{\frac{1}{R_{ins}} + i\omega C_{ins}} + \frac{1}{(i\omega)^n A} \quad (3.13)$$

Fitting the parameters of the equivalent circuit of Fig. 3.5B to the raw data provides two cell-specific parameters: (I) The parameter R_{cl} (TER) is a measure of the barrier tightness and is normalized to the total filter surface (denoted in Ωcm^2). (II) C_{cl} describes the capacitance of the plasma membrane and quantifies the degree of membrane foldings. The cell layer capacitance is also normalized to the filter area (denoted in $\mu F/cm^2$).

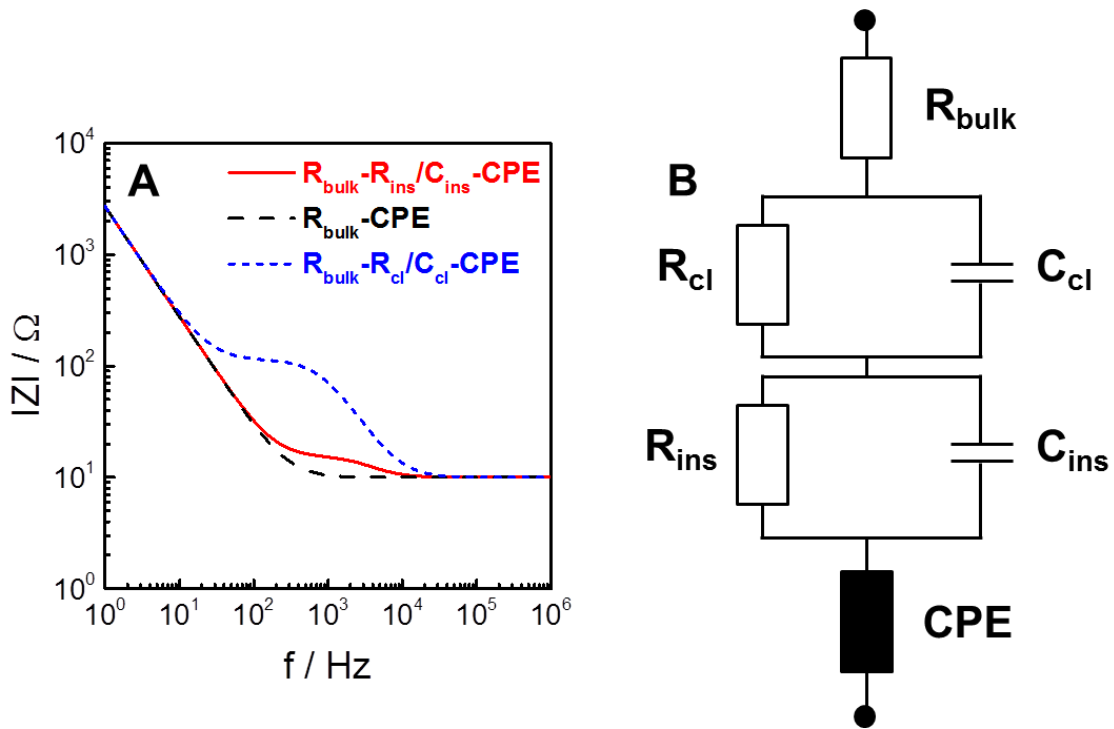


Fig. 3.5: (A) Simulated impedance spectra for a $R_{\text{bulk}}-R_{\text{ins}}/C_{\text{ins}}-\text{CPE}$, a $R_{\text{bulk}}-\text{CPE}$ and a $R_{\text{bulk}}-R_{\text{cl}}/C_{\text{cl}}-\text{CPE}$ system. (B) Electric equivalent circuit which is typically applied for the determination of filter-corrected TER and C_{cl} . R_{ins} represents the resistance arising from the filter support and C_{ins} displays the capacitance of the filter insert. Parameters: $R_{\text{bulk}} = 10 \Omega$, $A_{\text{CPE}} = 60 \mu\text{Fs}^{n-1}/\text{cm}^2$, $n_{\text{CPE}} = 0.99$, $R_{\text{ins}} = 5 \Omega\text{cm}^2$, $C_{\text{ins}} = 10 \mu\text{F}/\text{cm}^2$, $R_{\text{cl}} = 100 \Omega\text{cm}^2$, $C_{\text{cl}} = 2 \mu\text{F}/\text{cm}^2$. Electrode area: $A_{\text{El}} = 1.12\text{cm}^2$. The selected values for R_{ins} , C_{ins} , R_{cl} and C_{cl} are arbitrary examples.

In many bioanalytical studies, changes in R_{cl} are categorically assigned to the paracellular resistance (R_{para}). However, this assumption may lead to misinterpretations, as the transcellular resistance (R_{trans}) may have a share in the overall resistance. This is the case when the paracellular contribution becomes very high due to very tight cell-cell contacts (i.e. in very tight epithelia). Thus, in more detailed (but redundant) equivalent circuits, R_{cl} needs to be replaced by a parallel combination of R_{para} and R_{trans} . An exact assignment of R_{para} and R_{trans} to the total cell layer resistance is not possible with conventional impedance-based transfilter measurements. Concomitant permeability studies have to be performed to distinguish between paracellular and transcellular resistances. This approach is also known as *two-path impedance spectroscopy* (Krug *et al.* 2009b). Here, transcellular and paracellular contributions can be quantified, when three assumptions are met:

- (I) The permeability tracer has to penetrate the cellular barrier exclusively through the paracellular gap with permeability properties similar to that of ions mainly responsible for transepithelial current flow.

- (II) An experimental procedure has to be found to solely modify R_{para} without influencing R_{trans} .
- (III) The resistance of subepithelial components R_{sub} has to be known.

The rationale behind this method is briefly introduced in the following paragraph. Integral TER (R_{cl}) is composed of a parallel connection of R_{para} and R_{trans} :

$$\frac{1}{TER} = \frac{1}{R_{trans}} + \frac{1}{R_{para}} \quad (3.14)$$

To create a more convenient notation, the conductance G , which is the inverse of the resistance, is used instead of the resistance:

$$G_{TER} = G_{trans} + G_{para} \quad (3.15)$$

If the permeability tracer meets the assumptions detailed above, the paracellular conductance is directly proportional to the permeability tracer flux J with a proportionality factor s :

$$G_{TER} = G_{trans} + sJ \quad (3.16)$$

Equation 3.16 indicates a linear relationship between G_{TER} and J with G_{trans} as the y-intercept and s as the slope. By selective opening of the paracellular pathway (e.g. by addition of EGTA which interferes with the calcium-dependent cadherin-mediated cell-cell contacts), the cell layer is experimentally brought to different states of barrier tightness. It has to be characterized for its tightness by TER and flux measurements. When G_{TER} is plotted as a function of J , a linear function is achieved providing the values for R_{para} and R_{trans} , respectively. Tab 3.2 provides an overview about the values for TER, R_{para} and R_{trans} in the very tight MDCK C7 and moderately tight MDCK C11 monolayers that have been recently determined by two-path impedance spectroscopy (Krug *et al.* 2009b). Nevertheless, the essential experimental requirements have to be reevaluated for every single cell line under study.

Theoretical background

Tab. 3.2: Overview about the values for the integral cell layer resistance (TER), the paracellular resistance (R_{para}), the transcellular resistance (R_{trans}) and the cell layer capacitance (C_{cl}) in MDCK cells. The values have been determined by two-path impedance spectroscopy (Krug *et al.* 2009b). MDCK C7 cells form very tight monolayers similar to MDCK-I cells. MDCK C11 cells exhibit moderately tight barriers similar to MDCK-II cells. R_{sub} was similar for both cell lines ($10 \Omega\text{cm}^2$) and is assumed to primarily reflect the resistance of the filter insert.

cell line	TER / Ωcm^2	R_{para} / Ωcm^2	R_{trans} / Ωcm^2	C_{cl} / $\mu\text{F}/\text{cm}^2$
MDCK C7	1540 ± 154	4466 ± 1155	2849 ± 385	1.3 ± 0.2
MDCK C11	40 ± 18	105 ± 40	98 ± 35	1.9 ± 0.4

Besides very tight cell layers, leaky barriers have to be considered with caution in the context of transfilter studies. In this case, an additional resistive contribution might have an influence on the recorded resistance value. In TER-readings the current has to flow from the filter membrane pores underneath the cells through the narrow cleft between filter and basolateral plasma membrane before it reaches the paracellular gap. As this cleft is only 50-200 nm wide, the paracellular current flow is affected by the length and width of this cleft, in addition to the resistance resulting from the cell junctions. In this case, a serial combination of the junctional resistance R_j and the resistance arising from the cell-substrate adhesion zone R_{adh} accounts for the overall paracellular resistance R_{para} in more detailed (but also redundant) equivalent circuits. Both resistances contribute to R_{para} , but cannot be measured separately via impedance spectroscopy. The use of filter supports with high porosity is strongly recommended as the impact of R_{adh} is significantly increasing with decreasing porosity. Lo *et al.* modeled the situation in order to estimate values of this extra resistance (Lo *et al.* 1999). They applied two different models to get a maximum and a minimum estimation of R_{adh} :

- (I) Model 1 assumes that all pores under the cell coalesce to one large pore that is located beneath the center of the basolateral membrane of a single cell. The resistance share emerging from the cell-substrate adhesion zone is assessable as a function of cell-substrate distance h , cell-radius r_c as well as pore radius and solution resistivity ρ (equation 3.17). However, this approach overestimates the contribution of the cell-substrate adhesion zone to the overall resistance and provides a value of R_{adh} of $152 \Omega\text{cm}^2$ for MDCK-II cells. Thus, the estimated value for R_{adh} exceeds the measured TER of $(136 \pm 17) \Omega\text{cm}^2$.

$$R_{adh} = (\pi r_c^2) \cdot \left(\frac{\rho}{2\pi h}\right) \cdot \ln\left(\frac{\text{cell radius}}{\text{big pore radius}}\right) \quad (3.17)$$

- (II) The second model makes the assumption that the pores are smeared uniformly under the cells. Briefly, R_{adh} is calculated by equation 3.18 which contains the filter resistance per unit area R_f , the modified Bessel functions of first kind I_0 and I_1 as well as the impedance contribution arising from the cell-substrate adhesion zone α (equation 3.23). This approach leads to an underestimated contribution of R_{adh} to the overall TER and provides a value of R_{adh} of $28 \Omega\text{cm}^2$ for MDCK-II cells which is significantly smaller than the measured TER.

$$R_{adh} = 0.5\alpha \sqrt{R_f} \cdot I_0\left(\frac{\alpha}{\sqrt{R_f}}\right) \cdot I_1\left(\frac{\alpha}{\sqrt{R_f}}\right) \quad (3.18)$$

The bottom line is that the influence of R_{adh} is negligible for tight and moderately tight barriers, but has to be kept in mind for leaky cell layers with low junctional resistances. Furthermore, there is no experimental approach to quantify R_{adh} for cells grown on filter supports. Only rough estimates based on theoretical considerations of Lo et al. are possible. But the resistance arising from the cell-substrate adhesion zone α is measurable for cells grown on impermeable substrates using electric cell-substrate impedance sensing (chapter 3.1.4).

3.1.3 Impedance spectroscopy in presence of a redox-active species

All equivalent circuits presented in the previous chapters are composed of non-faradaic circuit elements. As already suggested earlier, the presence of an electroactive compound in the bulk solution may cause a new set of phenomena, which are commonly summarized as *faradaic effects*. At an appropriate potential, an electron transfer from the electroactive species to the electrode may occur. Such a faradaic charge transfer process is described by an empirical faradaic impedance element (Z_f) and is integrated into the equivalent circuit of Fig. 3.3 by placing it in to the constant phase element (Bard and Faulkner 2001). The faradaic impedance element is made up of a serial combination of two different elements:

- (I) The first component of Z_f is referred to as *charge-transfer resistance* (R_{CT}). R_{CT} is a kinetically controlled parameter and accounts for the rate at which oxidation and reduction processes take place at the electrode. The reaction rate depends on the

kind of reaction, the temperature, the concentration of the reactive species and the potential. All parameters that influence R_{CT} are summarized in Tab.3.3. The rate of a faradaic electron transfer is generally expressed by the Butler-Volmer equation (Muñoz-Berbel *et al.* 2008):

$$i = i_0 \left[\frac{c_O}{c_O^*} \exp\left(\frac{\alpha n F \mu}{RT}\right) - \left(\frac{c_R}{c_R^*} \exp\left(\frac{-(1 - \alpha) n F \mu}{RT}\right) \right) \right] \quad (3.19)$$

Under certain conditions, i.e. when the concentration of the redox-active compound in the bulk phase is equal to the concentration at the electrode and when the overpotential μ is very small, equation 3.19 is simplified and transformed into equation 3.20:

$$R_{CT} = \frac{RT}{n F i_0} \quad (3.20)$$

Tab. 3.3: Parameters of the charge-transfer resistance R_{CT} .

symbol	parameter
i_0	exchange current density
c_O / c_{R_s}	bulk concentration of the oxidized (O) and reduced (R) species
c_O / c_R	concentration of the oxidized (O) and reduced (R) species at the electrode interface
α	reaction order
n	stoichiometric number of transferred electrons
F	Faraday constant
μ	overpotential ($\mu = E - E_0$)
R	ideal gas constant
T	absolute temperature

- (II) The second component of Z_f is called *Warburg impedance* (Z_W). It accounts for the diffusional limitation of the electron transfer process. The Warburg impedance is a complex quantity consisting of a real and an imaginary part and is expressed as follows (Barsoukov and Macdonald 2005):

$$Z(\omega) = \frac{(1 - i)\sigma}{\sqrt{\omega}} \quad (3.21)$$

with the angular frequency $\omega = 2\pi f$, the AC frequency f and the Warburg coefficient σ which is mathematically described by equation 3.22:

$$\sigma = \frac{RT}{n^2 F^2 A \sqrt{2}} \left(\frac{1}{\sqrt{D_O} c_O^*} + \frac{1}{\sqrt{D_R} c_R^*} \right) \quad (3.22)$$

The different parameters determining the Warburg coefficient are listed in Tab. 3.4. The impact of the faradaic impedance element is strongly influenced by the concentration of the electroactive compound.

Tab. 3.4: Parameters influencing the Warburg coefficient σ .

symbol	parameter
R	ideal gas constant
T	absolute temperature
n	stoichiometric number of transferred electrons
F	Faraday constant
A	electrode area
D_O / D_R	diffusion coefficient of the oxidized (O) and reduced (R) species
C_O / C_R	bulk concentration of the oxidized (O) and reduced (R) species

The bottom line is that the presence of an electroactive compound has an impact to the impedance at lower frequencies ($\sim 1-100$ Hz). The higher the concentration of the redox-active species in the bulk solution, the lower is the impedance at low frequencies. An increasing bulk concentration leads to a decreased Warburg coefficient and thus to a decreased contribution of the Warburg impedance to the overall signal. If the concentration of the electroactive species in the electrolyte is high enough, the influence of the Warburg impedance is negligible. This is due to the fact that Z_W is a diffusion controlled parameter. In this case, the frequency-independent contribution of the charge-transfer resistance is dominating the overall impedance magnitude at low frequencies.

3.1.4 Electric cell-substrate impedance sensing (ECIS)

The experimental architecture of transfilter measurements mimics the *in vivo* situation and allows investigating solute and ion transport between two separated compartments. However, epithelial and endothelial barrier function is also assessable by another impedance-based approach which is referred to as *electric cell-substrate impedance sensing* (ECIS) (Giaever 1993; Giaever and Keese 1984; Giaever and Keese 1991). Instead of using porous filter membranes, cell monolayers are directly cultivated on the surface of the sensing electrodes, such as planar gold-film electrodes, so that the metal films are growth substrate and electrode at the same time. As for transfilter studies, the impedance is monitored as a

function of the applied frequency of the excitation signal. ECIS uses two gold electrodes which are deposited on a standard cell culture dish in a co-planar arrangement. The thickness of the gold-film is typically 50-100 nm, allowing for routine documentation via light microscopy. The electrical connection between the two electrodes is provided by the cell culture medium. The AC current flows between the two gold electrodes and crosses the cell layer at two different positions. Commonly, the two electrodes differ strongly in their electrode area. By making the counter electrode at least 100 times larger than the working electrode, the overall impedance is dominated by the working electrode impedance, as impedance scales with the inverse of the electrode area. This enables a highly sensitive investigation of a small cell population residing on the working electrode. Among other advantages, ECIS is suitable for high-throughput applications as the experimental requirements are easily automated and miniaturized into 8-well, 96-well and even 384-well formats. Since the cells are grown on gold-film electrodes, ECIS has been combined with other techniques, such as quartz crystal microbalance (QCM) (Janshoff *et al.* 1996; Steinem *et al.* 1997), surface plasmon resonance (SPR) (Michaelis *et al.* 2013), electroporation (Stolwijk *et al.* 2011) or wounding with the help of elevated electric fields (Keese *et al.* 2004). On the downside, ECIS provides a less *in-vivo* like environment as the cells are supplied with nutrients only from one side.

ECIS-measurements contain a higher level of information than transfilter experiments as they provide an additional parameter next to the cell layer resistance and capacitance. The impedance contributions resulting from the cell-substrate adhesion zone Z_{adh} is accessible from ECIS-readings, so that the remaining resistance of the paracellular route is now exclusively composed of the resistance of the cell-cell contacts. In contrast, transfilter recordings allow no discrimination between the junctional resistance and the resistance arising from the adhesion zone. Giaever and Keese introduced a physical model, which provides three parameters that describe the impedance contribution of the cell layer: R_b , C_m and α . The ohmic resistance due to the cell-cell junctions is characterized by R_b . C_m reflects the membrane capacitance and the frequency-dependent impedance contribution resulting from the cell-substrate adhesion zone is described by the parameter α :

$$\alpha = r_c \sqrt{\frac{\rho}{d}} \quad (3.23)$$

with ρ as the specific electrolyte resistance and d as the distance between the electrode and the basolateral membrane. In the original ECIS-model, the cells are considered as cylindrical objects with a radius r_c . Due to the fact that current flow between the basolateral membrane and the electrode area is position-dependent, a simple analysis via equivalent circuit modeling is not possible. Instead, the transfer function is derived from a set of differential equations. The final transfer function is represented by equation 3.24:

$$Z = R_{bulk} + \left[\frac{1}{Z_{CPE}} + \left(\frac{Z_{CPE}}{Z_{CPE} + Z_M} + \frac{\frac{Z_M}{Z_{CPE} + Z_M}}{\frac{1}{2}\gamma r_c \frac{I_0(\gamma r_c)}{I_1(\gamma r_c)} + R_b \left(\frac{1}{Z_{CPE}} + \frac{1}{Z_M} \right)} \right) \right]^{-1} \quad (3.24)$$

where Z_{CPE} represents the impedance of a constant phase element as a model for the electrode/electrolyte interface, Z_M is the membrane impedance and R_{bulk} reflects the electrolyte resistance. I_0 and I_1 are modified Bessel functions of the kind of order 0 and 1. The parameter α is included in the term γr_c which is expressed by equation 3.25:

$$\gamma r_c = r_c \sqrt{\frac{\rho}{d} \left(\frac{1}{Z_{CPE}} + \frac{1}{Z_M} \right)} = \alpha \sqrt{\left(\frac{1}{Z_{CPE}} + \frac{1}{Z_M} \right)} \quad (3.25)$$

By fitting the transfer function to the experimental ECIS-data, the cell-specific parameters R_b , C_m and α become accessible (Tab. 3.5).

Tab. 3.5: Cell-specific parameters which are accessible by ECIS-measurements.

symbol	unit	information
R_b	Ωcm^2	junctional resistance
C_m	$\mu\text{F}/\text{cm}^2$	capacitance of the cell membrane
α	$\Omega^{0.5}\text{cm}$	impedance of the cell-substrate adhesion zone

Fig. 3.6 displays simulated impedance spectra when R_b , C_m or α are systematically varied, respectively. Except the parameter under study, all other elements are kept constant. Similar to the impedimetric transfilter readings, the impedance contribution of the cell layer is obvious in the mid frequency range. The plateau height is increased with increasing barrier function (Fig. 3.6A). Higher cell membrane capacitances reduce the plateau width (Fig. 3.6B). The

additional parameter α which is only accessible from ECIS-readings but not from transfilter measurements changes the slope of the spectrum in the plateau region between 10 Hz and 10^3 Hz (Fig. 3.6C). Care has to be taken with respect to the different notations of the cell layer-related capacitances in ECIS- and transfilter measurements and the corresponding literature. Usually, the membrane capacitance C_m is used as parameter in ECIS-studies, whereas classical transfilter measurements provide the cell layer capacitance C_{cl} . C_{cl} includes both, the apical and the basolateral membrane which are connected in series. Assuming that both membranes are identical, C_{cl} is easily transformed into C_m ($C_{cl} = C_m/2$).

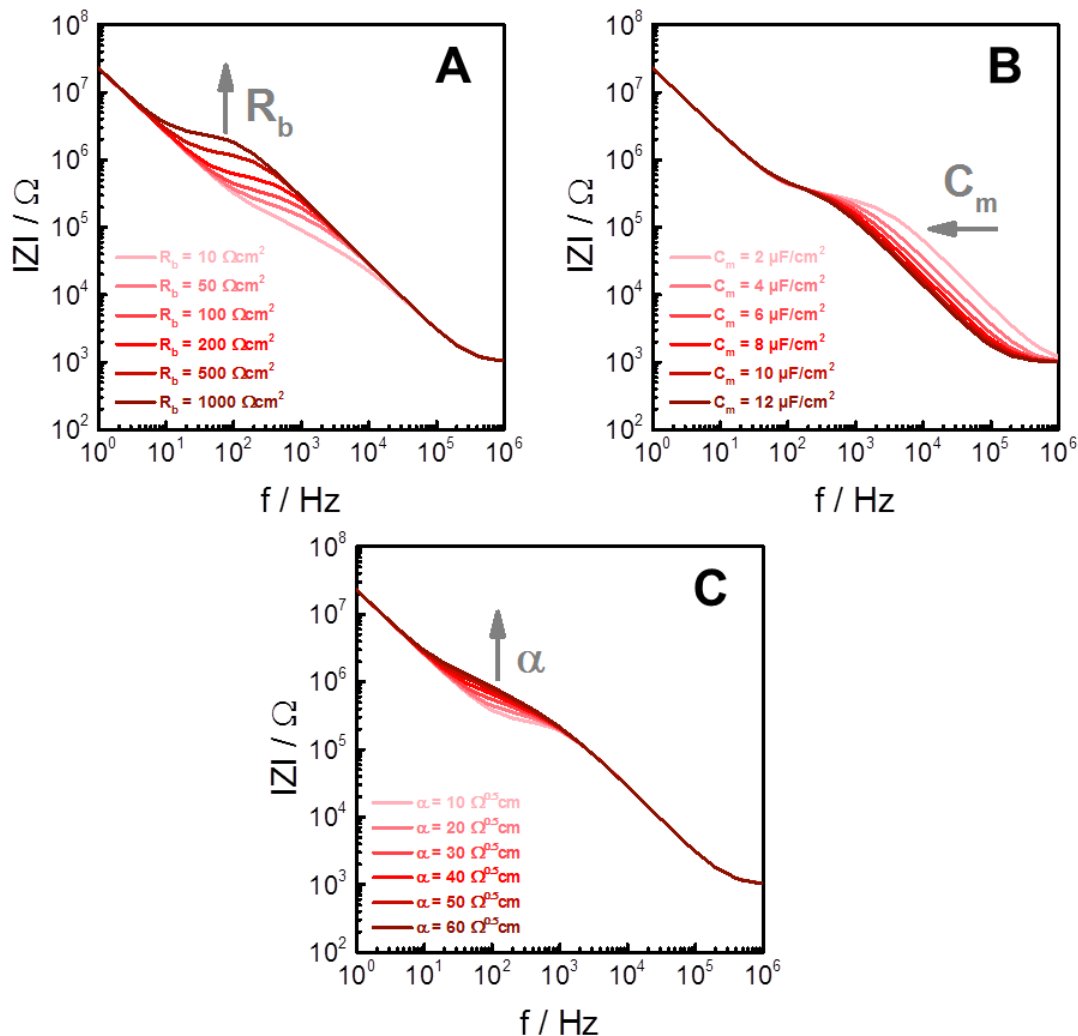


Fig. 3.6: Simulated impedance spectra for cell-covered gold-film electrodes when the cell-related parameters are systematically varied. **(A)** R_b representing barrier function, **(B)** cell membrane capacitance C_m representing the topography of the membrane or **(C)** the parameter α representing the impedance of the cleft beneath the cells. All calculations have been made for an electrode area of $5 \cdot 10^{-4} \text{ cm}^2$. Parameters: $R_{\text{bulk}} = 1000 \Omega$, $A_{\text{CPE}} = 15 \mu\text{Fs}^{-1}/\text{cm}^2$, $n_{\text{CPE}} = 0.96$, $R_b = 100 \Omega\text{cm}^2$, $C_m = 5 \mu\text{F}/\text{cm}^2$, $\alpha = 20 \Omega^{0.5}\text{cm}$. Except for the parameter under study, all other elements are kept constant.

3.2 Transepithelial permeability assays

In addition to the analysis of ionic permeability, the permeation of molecules and water has to be considered for a comprehensive evaluation of cellular barrier function (chapter 1.1.3). Therefore, barrier-forming cell layers are cultivated on porous filter membranes and mounted in special dual chambers. Here, two fluid-filled reservoirs (apical / basolateral) are separated by the cell sheet acting as a diffusion barrier.

To determine molecular permeability coefficients (P_E), a tracer compound is added to one of the two compartments (donor compartment) and the accumulation of the permeability probe on the other side (receiver compartment) is followed over time. The rate of marker accumulation in the receiver compartment allows calculating barrier- and tracer-specific P_E values (chapter 3.2.1). For a correlation between P_E and the strength of cell-cell contacts, the permeability tracer has to be selected with caution. Transepithelial transport routes, such as passive diffusion across the plasma membrane or transporter-mediated flux (chapter 1.1.2), have to be excluded. Furthermore, measurements have to be corrected for permeability of the filter membrane itself. Thus, control measurements with cell-free filter inserts should be always included in P_E -studies. However, this correction does not account for the additional diffusion layer which is located between the filter surface and the basolateral membrane. As for TER-readings filter supports with high porosity are strictly recommended to minimize the effect of these parasitic contributions to P_E values. Similar to TER measurements, permeability coefficients are integral parameters averaging the permeability properties of the entire barrier. As a consequence, small defect areas may evoke severe artefacts resulting in overestimated permeability coefficients.

To determine the water permeability of cellular monolayers, transepithelial osmotic gradients are induced. Commonly, substances like sucrose or mannitol are applied to one of both compartments. Hence, a water flux across the cell layer occurs balancing the osmotic gradient. The kinetics of this transport process enables calculating the osmotic water permeability coefficient P_{OS} (chapter 3.2.2). P_{OS} values cannot be corrected for the impact of cell-free filter supports, as a transepithelial osmotic gradient cannot be induced without the presence of a barrier-forming cell sheet. However, filter membranes with high porosity are also recommended to guarantee water transport that is only affected by the cell layer. In analogy to TER and P_E , the osmotic water permeability coefficient contains also integral

information. Thus, the parameter is prone to errors in presence of potential defect spots within the cell layer.

The following chapters provide a derivation of the relevant equations needed to calculate P_E (Wise 2002; Youdim *et al.* 2003) and P_{OS} values (Baylis 1988; Boyer 1985; Levin *et al.* 2006; Schafer *et al.* 1978; van Winkle 1999; Verkman *et al.* 1996) as well as detailed calculation protocols.

3.2.1 Molecular permeability coefficient P_E

Diffusive transport of a permeability probe across an epithelial barrier depends on the transepithelial concentration gradient and the diffusion coefficient of the tracer. The epithelial barrier is regarded as a chemically homogenous isotropic diffusion layer. By the help of Fick's first law, the tracer flow J between the two compartments is expressed as:

$$J = D \frac{dc(x)}{dx} \quad (3.26)$$

with the diffusion coefficient D , the distance from donor to receiver compartment x and the tracer concentration at position x in the barrier layer $c(x)$. The term for the concentration gradient is substituted by a term that contains the distribution coefficient K . K quantifies the tracer distribution between the barrier layer and the aqueous donor and receiver solutions. Consequently, the concentration in the borders of the barrier layer equals $K \times c_D$ at the donor and $K \times c_R$ at the receiver side:

$$\frac{dc(x)}{dx} = K \frac{c_R - c_D}{h} \quad (3.27)$$

with the thickness h of the barrier layer. The tracer flux must equal the accumulation rate of the permeability probe in the receiver compartment, normalized by the cross-sectional area of the barrier layer A :

$$J = \frac{dn_R(t)}{dt} \frac{1}{A} = -D \frac{dc(x)}{dx} = -D K \frac{c_R - c_D}{h} \quad (3.28)$$

with n_R as the amount of permeability probe in the receiver compartment. Equation 3.28 is mathematically transformed into equation 3.29:

$$\frac{dn_R(t)}{dt} = \frac{D K}{h} A (c_D - c_R) \quad (3.29)$$

The quantity $(D \times K)/h$ is also referred to as the *apparent permeability coefficient* P_{app} reflecting the rate by which a permeability compound penetrates the cellular barrier. The apparent permeability coefficient depends on the chemical properties of the tracer and the tightness of the barrier represented by the diffusion coefficient D and the distribution coefficient K . Emphasizing the time-dependence of n_R , c_D and c_R and introducing P_{app} , equation 3.29 can be rewritten as:

$$\frac{dn_R(t)}{dt} = P_{app} A (c_D(t) - c_R(t)) \quad (3.30)$$

Equation 3.30 represents a differential equation with the variables $c_D(t)$, $c_R(t)$ and $n_R(t)$. To calculate permeability coefficients, some simplifying assumptions have to be made. If the transport rate is very low, the concentration in both compartments will not alter significantly over time. In this case, the tracer concentration in the receiver compartment is considered as zero, whereas the concentration level in the donor compartment is set to the initial concentration $c_{D,0}$. These simplifications are summarized with the term *sink conditions*. Conventionally, a maximum receiver concentration of less than 10 % of c_D is accepted in order to guarantee sink conditions. Additionally, no diffusion back to the donor side is presumed. Under sink conditions, the differential equation 3.30 simplifies into equation 3.31:

$$\frac{dn_R(t)}{dt} = P_{app} A c_{D,0} \quad (3.31)$$

Equation 3.31 is further transformed into equation 3.32 to provide the mathematical expression to calculate P_{app} from experimental data (denoted in cm/s):

$$P_{app} = \frac{1}{A c_{D,0}} \frac{dn_R(t)}{dt} = \frac{V_{D,0}}{A n_{D,0}} \frac{dn_R(t)}{dt} \quad (3.32)$$

The permeability of a tracer across a filter-grown cell layer is additionally restricted to a small extent by the filter membrane itself. Therefore, permeability measurements always have to be corrected for the permeability of the cell-free filter inserts. This procedure is especially relevant in case of leaky barriers. A filter correction in epithelial permeability assays is provided by equation 3.33:

$$\frac{1}{P_E} = \frac{1}{P_{app}} - \frac{1}{P_{ins}} \quad (3.33)$$

with the (filter-corrected) molecular permeability coefficient P_E , the apparent permeability coefficient P_{app} and the permeability coefficient of a cell-free filter insert P_{ins} .

In some studies, the tracer flux J (denoted in $\text{nmol}/(\text{h}\times\text{cm}^2)$) between the two compartments is investigated instead of considering permeability coefficients. The relationship between P_E and J is provided by equation 3.34:

$$P_E = \frac{J}{c_{D,0}} \quad (3.34)$$

Since transepithelial solute transport is dependent on the initially applied tracer concentration in the donor compartment, P_E is a more accurate indicator for the tracer permeability than J . For the calculation of P_{app} , the parameters $V_{D,0}$, A and $n_{D,0}$ are preset by the experimental conditions. The information that is extracted from the permeability experiment is the time-dependent increase of tracer in the receiver compartment ($dn_R(t)/dt$). In case of passive transepithelial transport, n_R should increase linearly with time when the experiment is performed under sink conditions. However, deviations from this ideal behavior may appear due to a poor temperature control, cytotoxic effects or the participation of transport systems. Fig. 3.7 depicts a schematic time course of tracer accumulation in the receiver compartment which is often obtained in *in vitro* permeability studies. The time-dependent change of n_R is divided into three phases:

- (I) The *lag phase* might be observed in the beginning of the experiment, before the steady state transport rate is achieved. The lag phase is caused by temperature effects due to the experimental installation and by initial accumulation of the permeability probe in the plasma membrane or in the filter pores until saturation is established.
- (II) After a certain period of time the lag phase merges into the second phase which is called the *linear phase*. Only in this period sink conditions are valid which is a prerequisite to apply equation 3.32. In order to calculate P_{app} , the experimental data within this phase is analyzed by linear regression to extract the slope $dn_R(t)/dt$.

- (III) The last period is referred to as the *stationary phase* which is characterized by an abating tracer accumulation. This is due to a reduced transepithelial gradient over time leading to a stationary concentration in both compartments. All permeability coefficients determined in this thesis have been extracted by linear regression within the linear phase which is indicated by high coefficients of regression (R^2) above at least 0.9. To transform the apparent permeability coefficient P_{app} into the molecular permeability coefficient P_E , a filter correction according to equation 3.33 is conducted throughout all P_E -studies.

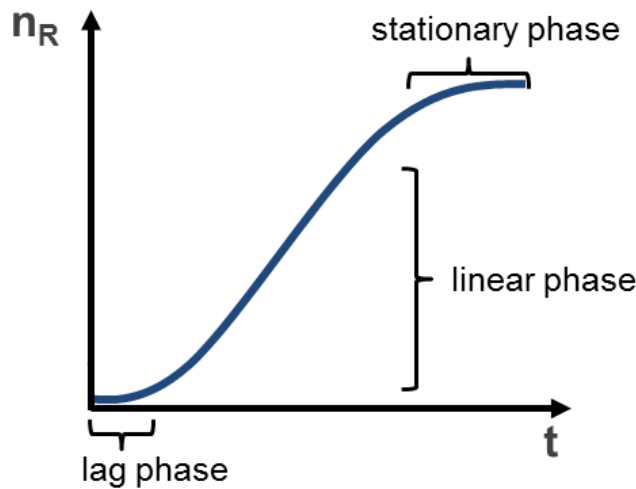


Fig. 3.7: Schematic time course of the tracer increase in the receiver compartment. Usually, three different periods are observable: (I) The beginning of the experiment is dominated by the *lag phase*. (II) The second period is referred to as the *linear phase* which is used for the calculation of P_{app} . (III) After the transepithelial concentration gradient is reduced significantly, a stationary concentration in both compartments is established resulting in the *stationary phase*.

3.2.2 Osmotic water permeability coefficient P_{Os}

Transepithelial water fluxes are mainly driven by hydrostatic (ΔP) or osmotic pressure gradients ($\Delta \Pi$), respectively. The volume flux J_V across a biological membrane is derived from the theory of irreversible thermodynamics (for further information: (Dainty 1976; Kedem and Katchalsky 1958; Steudle 1989)) and is described by the so-called Starling equation:

$$J_V = L_P S (\Delta P - \sigma_s \Delta \Pi) \quad (3.35)$$

with the hydraulic conductivity L_P (denoted in $\text{cm}/(\text{s}\cdot\text{atm})$), the membrane surface S and the solute reflection coefficient for the membrane σ_s . σ_s quantifies the membrane selectivity for the solute and determines its osmotic effectiveness. When σ_s equals zero, the membrane shows exactly the same permeability for a solute as for water. No solute permeability at all is

indicated by $\sigma_s = 1$. In most cases, the solute that induces the osmotic pressure cannot permeate the barrier significantly which justifies the simplification $\sigma_s \approx 1$. The hydraulic conductivity L_P is an important parameter for epithelial water transport describing the intrinsic permeability of a membrane to water and relating volume flux to hydrostatic and osmotic pressure gradients. Most often, water flux studies are performed without hydrostatic pressure gradients ($\Delta P = 0$). Thus, only the remaining osmotic pressure gradient is the driving force for water flow. The osmotic driving force (Ψ_{osm}) is calculated by equation 3.36:

$$\Delta\Psi_{osm} = \sigma_s \Delta\Pi = \sigma_s R T \Delta C \quad (3.36)$$

with R as the ideal gas constant, T as the absolute temperature and ΔC as the solute concentration gradient. A second parameter established in the field of transepithelial water flux is represented by the osmotic water permeability coefficient P_{OS} (denoted in $\mu\text{m/s}$). By means of equation 3.37, L_P is converted into P_{OS} , and vice versa:

$$P_{OS} = L_p \left(\frac{R T}{V_W} \right) \quad (3.37)$$

where V_W is the partial molar volume of H_2O . By simple transformation of equation 3.36, a term for the hydraulic conductivity is achieved:

$$L_P = \frac{J_V}{S (\Delta P - \sigma_s \Delta\Pi)} \quad (3.38)$$

Under specific experimental conditions, i.e. using an impermeable solute to induce an osmotic pressure gradient ($\sigma_s = 1$) and preventing hydrostatic pressure gradients ($\Delta P = 0$), P_{OS} is determined by equation 3.39 which follows from equations 3.36, 3.37 and 3.38:

$$P_{OS} = \frac{J_V}{S \Delta C V_W} \quad (3.39)$$

Water can also pass a biological barrier in absence of a hydrostatic or osmotic pressure gradient via simple diffusion across the phospholipid bilayer. Under steady-state conditions, Fick's first and second law give rise to the diffusive water flow J_W across a membrane which is quantified by the diffusional water permeability coefficient P_D (denoted in $\mu\text{m/s}$):

$$J_W = -D_W \left(\frac{\Delta c_W}{\delta} \right) = -P_D \Delta c_W \quad (3.40)$$

including the diffusion constant of water D_W , the membrane thickness δ and the water concentration difference Δc_W . P_D is usually determined by radiolabeled water flux ($^3\text{H}_2\text{O}$, $^2\text{H}_2\text{O}$, H_2^{18}O) or via NMR-techniques (Solomon 1989; Verkman 1995; Ye and Verkman 2002). The ratio P_{OS}/P_D may provide useful information about the presence of water channels like aquaporins (chapter 1.2). If the ratio equals 1, water permeation across the membrane is based on simple diffusion. When the ratio exceeds 1, the presence of water-selective membrane channels is supposed. Nevertheless, the P_{OS}/P_D -ratio does not contain unequivocal information, because unstirred water layers might cause an underestimation of P_D .

Determination of the osmotic water permeability coefficient is in the focus of this thesis. Equation 3.39 is commonly applied for the calculation of P_{OS} . The parameters S (filter surface), ΔC (solute concentration gradient) and V_W (partial molar volume) are controlled by the experimental settings. The information which has to be extracted from the experimental data is the net volume flux J_V . A variety of readout principles is available for osmotic water flux across plasma membranes, such as light scattering (Soveral *et al.* 1997; Soveral *et al.* 2008) or surface plasmon resonance (Baumgarten and Robelek 2011; Robelek and Wegener 2010; Vala *et al.* 2013). However, for the analysis of transepithelial water permeation in transfilter systems only two different techniques are established. The first technique operates with specialized glass capillaries connected to one of both compartments (Dorr *et al.* 1997). The exact fluid height in the capillary is determined via an electro-optical device. After an osmotic stimulation, the shift of the meniscus height is monitored over time. Thus, the capillary readout system offers a straightforward method, by which the volume flux J_V is quantified directly. Although this approach can measure the net water flow with an outstanding accuracy of ± 50 nL, the elaborate and expensive experimental setup prohibits an upscaling to a high-throughput method. The second technique is referred to as *fluorophore dilution method*. Here, a non-cytotoxic impermeable fluorophore is added to one of the two compartments. As a consequence of the osmotic pressure gradient, a transepithelial water flux changes the fluorophore concentration, which is the basis of the assay. Levin *et al.* introduced an approach for extracting J_V from the kinetics of the fluorescence response (Levin *et al.* 2006).

J_V is measured via monitoring the fluorescence intensity of the impermeable fluorophore. By fitting the time course of the normalized fluorescence change with a 1st order exponential

decay function (equation 3.41), the parameters τ (time-constant of the fit-function) and A (amplitude of the fit-function) are obtained:

$$\frac{F(t)}{F_0} = B + A \exp\left(\frac{-t}{\tau}\right) \quad (3.41)$$

with the initial fluorescence intensity F_0 and the constant of the fit-function B . Moreover, the time course of fluorescence is linked to the time course of volume change in the compartment containing the dye which is mathematically described by equation 3.42:

$$\frac{F(t)}{F_0} = \frac{V_0}{V_0 + V(t)} \quad (3.42)$$

with V_0 as the initial volume of the fluorophore containing chamber. Solving equation 3.42 for $V(t)$ and building the first derivative of this function yields equation 3.43:

$$V'(t) = \frac{-V_0 F_0 F'(t)}{(F(t))^2} \quad (3.43)$$

$F'(t)$ is provided by equation 3.41 after transformation and building the first derivative:

$$F'(t) = F_0 A \exp\left(\frac{-t}{\tau}\right) \left(\frac{-1}{\tau}\right) \quad (3.44)$$

Combining equations 3.43 and 3.44, a simple expression for the initial volume change $V'(0)$ is obtained which is equivalent to the volume flow J_V :

$$J_V = V'(0) = \frac{V_0 A}{\tau} \quad (3.45)$$

Hence, the quantity J_V is computed via the fit-parameters A and τ as well as by the initial volume of the compartment containing the dye V_0 .

3.3 Poly-3,4-ethylenedioxythiophene (PEDOT) as electrode material for impedance-based analysis of epithelial barrier function

Since their discovery, electrically conducting polymers (CPs) have gained in importance and have been successfully applied as organic but conducting materials in photovoltaic cells, organic light emitting diodes (OLEDs), electrochromic devices, chemical sensors, microelectronic actuators and organic field effect transistors (OFETs) (Patra *et al.* 2014; Rasmussen 2010). In addition, they play a role in bioanalytical applications, such as coatings of conventional electrodes used in neural sensing, electrically controlled drug delivery systems, modulators of muscle cells and as scaffold in tissue engineering. Conducting polymers exhibit a lower conductivity compared to metals, but offer advantages of conventional polymers such as ease of synthesis. The presence of conjugated double bonds along the polymer backbone gives rise to the conducting properties of CPs. The π -electrons in the conjugated backbone are able to delocalize into the conduction band and in an ideal situation of a uniform chain, the resulting conduction band provides metallic behavior. However, conductive polymers have a non-ideal conjugated backbone and hence, an energy gap between valence band and conduction band exists that causes a significantly reduced conductivity. By means of introducing dopant ions into the polymer structure the energy gap is reduced or overcome and thus, the conductivity of CPs is improved (Kaur *et al.* 2015). Conducting polymers are synthesized either chemically or electrochemically. Chemical synthesis of CPs includes condensation polymerization or addition polymerization and permits materials' upscaling. The more common approach is electrochemical synthesis, which allows simultaneous doping and entrapment of molecules during the procedure. Although the electrochemical method provides a straightforward and easy-to-handle synthesis, the resulting films are difficult to remove from the electrodes and post-synthesis covalent modification of CPs is complicated. Another striking difference between chemical and electrochemical synthesis of CPs is that electrochemical methods produce very thin films (in the order of 20 nm), whereas the chemical approach leads to powders and thicker films. Moreover, electrochemical synthesis of conducting polymers is limited to those systems in which the monomer can be oxidized at an electrode surface of the appropriate potential to generate reactive radicals or ion intermediates for polymerization. The most promising electrically conducting polymers for biomedical applications include polypyrrole (PPy),

polyaniline (PAni), polythiophene (PTh) and their derivatives such as poly-3,4-ethylenedioxythiophene (PEDOT). They can all be synthesized via electrochemical methods (Diaz *et al.* 1979; Guimard *et al.* 2007; Huang *et al.* 2014; Kaneto *et al.* 1983). Due to its unique properties, PEDOT has become the most successful commercially available conducting polymer.

The following chapters give an overview on the general and electrical properties of PEDOT highlighting why it is attractive for impedance spectroscopy. Moreover, various strategies for the enhancement of the intrinsic conductivity of PEDOT by special post-treatments are described.

3.3.1 General and electrical properties of PEDOT

PEDOT is regarded as the most successful conducting polymer due to its relatively high conductivity (0.4 – 400 S/cm, depending on the dopant ions) as well as chemical and thermal stability. The material is also proven to be biocompatible. PEDOT enables cost-effective and flexible devices allowing roll-to-roll mass production. Nevertheless, pristine PEDOT exhibits poor water solubility and is therefore difficult to handle. To overcome this problem, PEDOT is commonly mixed with polystyrene sulfonic acid (PSS) making it water soluble. PSS serves as a counter ion acting as an excellent oxidizing agent, charge compensator and as a template for polymerization. PEDOT:PSS-films are processed through conventional thin film technologies (e.g. spin coating) and exhibit high transparency in the visible range, high mechanical flexibility, and excellent thermal stability. The chemical structure of PEDOT:PSS is illustrated in Fig. 3.8. However, PEDOT:PSS suffers from a significant loss in conductivity (< 10 S/cm) which precludes applications as electrodes (Kim *et al.* 2011; Xia and Ouyang 2011). Different strategies have been developed to significantly increase the conductivity of PEDOT:PSS (chapter 3.3.2). Tab. 3.6 shows a comparison between the conductivity of doped PEDOT and different metals and CPs. Although other conducting polymers exhibit a higher conductivity than PEDOT, they are persistently hard to process due to their rigid and brittle mechanical features. It is obvious that even the best conducting polymers show drastically reduced conductivity compared to metals. However, their conductivity is sufficient to apply them as electrodes in certain electrochemical applications.

In terms of impedance spectroscopy, PEDOT offers some interesting properties. It has been shown that relatively thin (~ 1 μm) films of PEDOT:PSS dramatically reduced the

electrode-electrolyte-interface impedance of device electrodes (Cui and Martin 2003; Martin and Malliaras 2016). PEDOT-films provide an enormously effective surface area for charge transport due to its porous, open structure. A higher interfacial surface between the PEDOT-film and the electrolyte offers more sites with which ions are able interact. Therefore, the electrode-electrolyte-interface capacitance is significantly enlarged. Since capacitance and impedance behave indirectly proportional, the increased interface capacitance is linked to decreased interface impedance (Bobacka *et al.* 2000; Cui *et al.* 2001; Koutsouras *et al.* 2017; Ludwig *et al.* 2006). Due to the reduced impedance contribution of the electrode to the overall signal, PEDOT might cause a serious improvement of the sensitivity in bioanalytical impedimetric techniques, such as TER-measurements or ECIS.

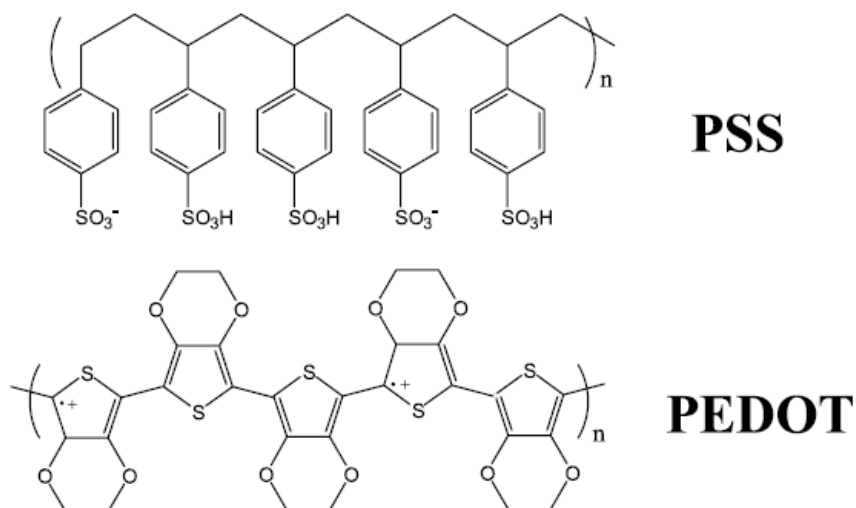


Fig. 3.8: Chemical structure of PEDOT:PSS. PEDOT provides the conducting properties, whereas PSS is responsible for the water solubility of the conducting polymer. The image is taken from literature (Ouyang 2013).

Tab. 3.6: Different metals and conducting polymers with their corresponding conductivities γ . The conductivities for the metals refer to 20°C.

material	γ / S/cm	reference
silver	$6.30 \cdot 10^5$	(Serway and Jewett 1998)
copper	$5.96 \cdot 10^5$	(Matula 1979)
gold	$4.10 \cdot 10^5$	(Serway and Jewett 1998)
stainless steel	$1.45 \cdot 10^4$	(Serway and Jewett 1998)
PEDOT	0.4 – 400	(Groenendaal <i>et al.</i> 2000; Gustafsson <i>et al.</i> 2008; Ouyang <i>et al.</i> 2005)
PTh	10 – 1000	(Balint <i>et al.</i> 2014; Dai 2004)
PAni	30 – 200	(Balint <i>et al.</i> 2014; Dai 2004)
PPy	10 – 7500	(Balint <i>et al.</i> 2014; Dai 2004)

3.3.2 Conductivity enhancement by post-treatments

As already mentioned above, PEDOT:PSS-films exhibit poor conductivity below 10 S/cm. For applications as electrodes considerably higher conductivities are needed. Therefore, several strategies have been developed for conductivity enhancement of PEDOT:PSS-films. The common rationale behind those methods is that PSS is removed from the films resulting in a conformational change of the PEDOT-chains.

One of the most important approaches is the addition of a polar organic compound with high boiling point (e.g. ethylene glycol (EG) or dimethyl sulfoxide (DMSO)) to the aqueous PEDOT:PSS-formulation. Significant conductivity improvement has been reported when PEDOT:PSS-films are treated with EG (Xia and Ouyang 2011). Kim et al. reported that the addition of ethylene glycol (6 % (v/v)) to a PEDOT:PSS-solution raised the conductivity of the PEDOT:PSS-films up to 735 S/cm. They enhanced the conductivity even further by a following post-treatment of the film with ethylene glycol (6 % (v/v)) for 30 minutes and achieved a value of 1418 S/cm (Kim *et al.* 2011). Besides the improved conducting properties, the doped films are thinner and become water insoluble. The reason for this is that ethylene glycol removes PSS from the films. The depletion of PSS results in the development of a compact thin film structure with increased chain interaction among the PEDOT-chains. This is due to a conformational change from a benzoid to a quinoid structure causing a change from a coil to a linear or expanded-coil formation of the chains. The driving force for this conformational alteration is formed by the interaction between the dipole of one polar group of EG and the charges on the PEDOT-chains (Ouyang *et al.* 2004).

Another method to enhance the conductivity is based on introducing anionic surfactants into the aqueous PEDOT:PSS-solution. For example, by application of sodium dodecyl sulfonate (SDS) a conductivity of 80 S/cm was observed. Again, the conductivity enhancement is associated with a conformational change of the conductive PEDOT-chains which is triggered by the anionic surfactant. In PEDOT:PSS-films the chains have to follow the structure of the PSS chains in water, causing distortions within the PEDOT-chains. The anionic surfactant replaces PSS as counter ions, so that there is less distortion in the conducting chains resulting in a significant higher conductivity (Fan *et al.* 2008).

The conductivity is also improved by treatment with various acids, including acetic acid, propionic acid, butyric acid, oxalic acid, sulfurous acid and hydrochloric acid. Best results ($\gamma = 197$ S/cm) were achieved with propionic acid. The advancement of the conductivity of

the PEDOT:PSS-substrates is attributed to acid-assisted loss of PSS and resulting conformational change of the PEDOT-chains (Xia and Ouyang 2010). Furthermore, the post-treatment of PEDOT:PSS-films with certain salts (CuCl_2 , InCl_3) or zwitterions may lead to improved conductivity (Xia *et al.* 2010; Xia and Ouyang 2009).

4 Material and methods

4.1 Cell culture techniques

4.1.1 Cell lines

In this thesis, the adherently growing epithelial cell lines MDCK-I and MDCKI-II (Madin Darby canine kidney, strain I and II) as well as the epithelial-like cell line NRK (normal rat kidney, clone 52E) were used for experiments. All of the three cell lines were obtained from *Deutsche Sammlung von Mikroorganismen und Zellkulturen* (DSMZ). For some measurements, a transfected MDCK-I cell line which overexpresses aquaporin 1 was used (MDCK-I-AQP1). This cell line was kindly provided by Prof. Peter Pohl (University of Linz, Austria). Details on the transfection protocol, on the expression construct as well as the immunological detection of AQP1 are reported elsewhere (Deen *et al.* 1997). An overview about the cell lines used in this thesis is provided by Tab. 4.1.

Tab. 4.1: Overview about the cell lines used in this thesis.

cell line	origin	morphology	literature	supplier
NRK-52E	normal rat kidney (clone 52E)	epithelial-like	(Larco and Todaro 1978)	DSMZ
MDCK-I	Madin-Darby canine kidney (strain I)	epithelial	(Fuller <i>et al.</i> 1984; Richardson <i>et al.</i> 1981)	DSMZ
MDCK-II	Madin-Darby canine kidney (strain II)	epithelial	(Richardson <i>et al.</i> 1981; Stevenson <i>et al.</i> 1988)	DSMZ
MDCK-I-AQP1	Madin-Darby canine kidney (strain I)	epithelial	(Deen <i>et al.</i> 1997)	Prof. Pohl

4.1.2 General cell culture conditions

All cell culture handling was performed under sterile conditions using a laminar flow hood (Thermo Fisher Scientific Inc, Waltham, USA). Buffers, media and other solutions were either autoclaved (20 min, 120 °C) or forced through a sterile filter with a pore diameter of 0.2 µm (TPP®, Sigma Aldrich, Munich, Germany and Sarstedt, Nürnberg, Germany). All cell lines were cultured on the bottom of sterile cell culture flasks with an area of 25 µm² (Greiner, Kremsmünster, Austria). The cells were stored in a cell culture incubator (Thermo Fisher Scientific Inc, Waltham, USA) at 37 °C and 5 % CO₂ in a humidified environment. Cell culture medium was exchanged 1 – 2 times per week. Tab. 4.2 shows the composition of the cell culture media as used for the individual cell lines. For cultivation of MDCK-I-AQP1 cells,

75 µg/mL hygromycin B were added to the medium to maintain selection pressure (Deen *et al.* 1997).

Tab. 4.2: Composition of the different cell culture media applied in this thesis. In case of MDCK-I-AQP1, 75 µg/mL hygromycin B were added to the standard MDCK medium to maintain selection pressure.

cell line	composition of cell culture medium
NRK-52E	Dulbecco's Modified Eagle's Medium (DMEM) incl. 4.5 g/L glucose 5 % (v/v) fetal calf serum (FCS) 100 µg/mL penicillin 100 µg/mL streptomycin 2 mM L-glutamine
MDCK-I / MDCK-II / MDCK-I-AQP1	Minimum Essential Medium Eagle (MEM-Eagle) incl. 1 g/L glucose 5 % (v/v) FCS 100 µg/mL penicillin 100 µg/mL streptomycin 4 mM L-glutamine

4.1.3 Subcultivation

All cell lines were subcultivated once a week by applying a standard protocol (Tab. 4.3). All solutions and cell culture media were prewarmed to 37 °C in a water bath (Julabo, type TW12, Seelbach, Germany). The composition and concentration of the individual solutions used for subcultivation are summarized in Tab. 4.4. At first, cells were washed twice with phosphate buffered saline without calcium and magnesium ions (PBS⁻, Sigma Aldrich, Munich, Germany) (4 mL, RT). In the next step, the cells were incubated 1 – 2 times with EDTA solution (ethylenediaminetetraacetic acid, Merck KGaA, Darmstadt, Germany) (4 mL, 37 °C, 10 min) followed by incubation in trypsin solution (Sigma Aldrich, Munich, Germany) (1 mL, 37 °C, 10 – 20 min). The enzymatic digestion reaction was stopped by adding 10 mL of the corresponding cell culture medium. In order to generate a cell pellet, the cell suspension was transferred into a centrifugation tube (Cellstar[®] centrifuge tubes, Greiner Bio-One, Kremsmünster, Austria) which was subsequently centrifuged (Heraeus 1-SR, Thermo Fisher Scientific Inc., Waltham, USA) (110xg, RT, 10 min). The supernatant was removed and the cell pellet was resuspended in 4 mL of fresh cell culture medium. Cells were diluted in a ratio of 1:20 and seeded into new cell culture flasks in a total volume of 4 mL.

Material and methods

Tab. 4.3: Summary of the subcultivation protocols for the different cell lines. For the passage of MDCK-I and MDCK-I-AQP1 a 10 fold higher concentrated trypsin solution was required (Tab. 4.4).

cell line	PBS ⁻	EDTA	trypsin
NRK-52E	2 x wash	1 x 10 min	10 min
MDCK-I	2 x wash	2 x 10 min	10 – 20 min
MDCK-II	2 x wash	1 x 10 min	10 min
MDCK-I-AQP1	2 x wash	1 x 10 min	10 – 15 min

Tab. 4.4: Composition and concentration of the solutions applied in the subcultivation procedure.

solution	composition
Dulbecco's Phosphate Buffered Saline (PBS ⁻)	0.2 g/L KCl
	0.2 g/L KH ₂ PO ₄
	8.0 g/L NaCl
	1.15 g/L Na ₂ HPO ₄
EDTA solution	1 mM EDTA in PBS ⁻
trypsin solution	0.025 % (w/v) trypsin in EDTA solution (for NRK-52E and MDCK-II)
	0.25 % (w/v) trypsin in EDTA solution (for MDCK-I and MDCK-I-AQP1)

4.1.4 Inoculation protocols

For the experiments, the cells were seeded in defined, cell-type specific cell densities upon the different cell culture substrates. These substrates comprise Transwell[®] filters (growth area: 1.12 cm², polycarbonate membrane, pore diameter: 400 nm, pore density: 10⁸ pores/cm², Corning, NY, USA), as well as 8-well and 96-well-ECIS-arrays (chapter 4.3.2.6, Applied BioPhysics, Troy, USA). The exact cell number was determined by using a Buerker-type hemocytometer (Marienfeld-Superior, Lauda Königshofen, Germany). Subsequently, the cell suspension was diluted to the desired cell density. The cell density was equal for all cell lines and was 495000 cells/cm² for Transwell[®] filters and 450000 cells/cm² for ECIS-electrode arrays. Before cell seeding the corresponding substrate was sterilized in an argon plasma (Harrick Plasma Inc., Ithaca, USA) for 30 seconds (ECIS-arrays) or 1 minute (Transwell[®] filters).

For ECIS-measurements the cells were cultivated directly on the electrodes. 400 µL or 200 µL cell suspension were used to inoculate 8-well or 96-well-ECIS electrode arrays, respectively. One day after seeding, the cell culture medium was refreshed. The substrates were ready for experiments after three days. When using Transwell[®] filter inserts, 500 µL of cell suspension were added to the apical compartment, whereas the basolateral side was filled with 1.5 mL cell culture medium (Fig. 4.1). The filter supports were stored in standard 12-well-plates (Costar Corning, Brigachtal, Germany). Again, the cell culture medium was

exchanged one day after seeding. On day three, the cell-covered Transwell[®] filters were used for experiments.

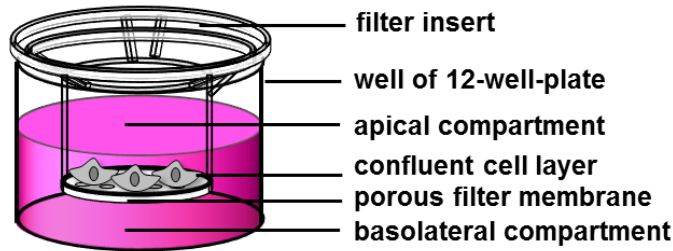


Fig. 4.1: Schematic of cell-covered Transwell[®] filter inserts.

For some experiments two different cell lines were cultivated on one common filter membrane (Fig. 4.2). Instead of placing them in 12-well-plates, Transwell[®] filter inserts were carefully positioned directly on the sterile bottom of a standard petri dish (Sarstedt, Nürnberg, Germany) which was adjusted in a skew position of approximately 45 °. To stabilize the petri dish in this position a polycarbonate lid (Carl Roth, Karlsruhe, Germany) was utilized. On day one, 200 µL of cell suspension (cell type A) were pipetted on the oblique filter membrane so that roughly one half of the membrane surface was covered with cell suspension. On day two, the overlaying cell culture medium was aspirated and the filter support was transferred into a standard 12-well-plate. 500 µL of cell suspension (cell type B) were added to the apical compartment, whereas the basolateral chamber was filled with 1.5 mL cell culture medium. The filter inserts with mixed but segregated cell populations were ready to use on day three.

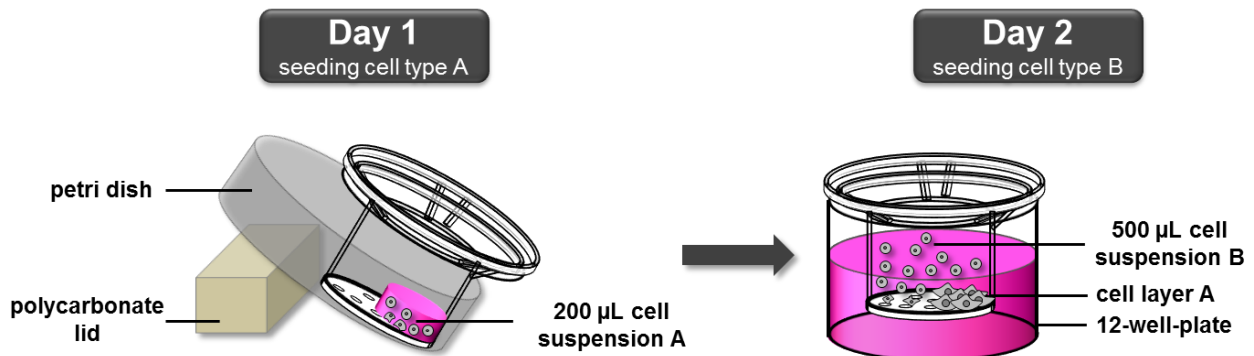


Fig. 4.2: Scheme illustrating the cell culture procedure to establish mixed but segregated cell populations on Transwell[®] filters.

4.1.5 Buffers and solutions

The experiments of chapter 5 and chapter 6 were mainly performed with phosphate buffered saline (Sigma Aldrich, Munich, Germany) which included 1 g/L D-glucose (Tab. 4.5). This buffer is denoted as PBS⁺⁺/glucose (1 g/L). D-Glucose was purchased from Sigma Aldrich (Munich, Germany). The measurements of chapter 7 were conducted with the corresponding cell culture medium.

Tab. 4.5: Composition of PBS⁺⁺. For cell-based experiments, D-glucose (1 g/L) was added to the buffer.

solution	composition
Dulbecco's Phosphate Buffered Saline (PBS ⁺⁺)	0.2 g/L KCl
	0.2 g/L KH ₂ PO ₄
	8.0 g/L NaCl
	1.15 g/L Na ₂ HPO ₄
	0.1 g/L CaCl ₂
	0.1 g/L MgCl ₂ ·6H ₂ O

Potassium ferrocyanide (K₄[Fe(CN)₆]·3H₂O) and potassium ferricyanide (K₃[Fe(CN)₆]) were purchased from Merck KGaA (Darmstadt, Germany) and dissolved in PBS⁺⁺/glucose (1 g/L). Mixtures including both types of cyanides in the same concentration were prepared. The mixtures are denoted as [Fe(CN)₆]^{3-/4-}. Ferrocenemethanol (FcMeOH, ABCR, Karlsruhe, Germany) was dissolved in PBS⁺⁺/glucose (1 g/L). The sterile solutions were stored at 4 °C.

Cytochalasin D was bought from Sigma Aldrich (Munich, Germany), diluted to a concentration of 9.85 mM (5 mg/mL) in DMSO (dimethyl sulfoxide, Carl Roth, Karlsruhe, Germany) and stored at -18 °C. For experiments, cytochalasin D was diluted in cell culture medium yielding an effective concentration of 5 μM.

KCl was acquired from Merck KGaA (Darmstadt, Germany) and dissolved in double distilled water. These solutions were not sterilized. The specific conductivity γ of the different KCl-solutions was determined using an inoLab[®] Cond 720 (cell constant: 0.478 cm⁻¹, WTW GmbH, Weilheim, Germany) and are listed in Tab. 4.6.

Tab. 4.6: Specific conductivity γ of different KCl-solutions (37 °C).

c (KCl) / mM	γ / mS/cm	c (KCl) / mM	γ / mS/cm
25	1.70	125	14.22
50	5.91	150	15.78
75	8.73	175	17.56
100	10.41	200	18.69

Different hypertonic, but iso-conductive buffers were prepared by the addition of sucrose (Sigma Aldrich, Munich, Germany) which was dissolved in PBS⁺⁺/glucose (1 g/L). Buffer conductivity γ was adjusted to the value of PBS⁺⁺/glucose (1 g/L) by using 1.5 M NaCl (VWR International GmbH, Ismaning, Germany) in double distilled water. Buffer osmolalities π were determined by using a cryoscopic osmometer Osmomat 030 (Gonotec, Berlin, Germany). Physiological osmolalities are in the range from 260 to 320 mOsmol/kg for most cell lines (Freshney 2010). Due to the specific liquid handling in the water flux measurements (chapter 6), γ and π were measured for the 1:1-mixtures of PBS⁺⁺/glucose (1 g/L) and a double-concentrated sucrose solution. The final sucrose concentrations are listed in Tab. 4.7. By including the mass density of water ($\rho_{H_2O} = 997 \text{ kg/m}^3$), $\Delta\pi$ can be converted into the solute concentration gradient ΔC , also referred to as *osmolarity difference*:

$$\Delta C = \Delta\pi \times \rho_{H_2O} \quad (4.1)$$

Tab. 4.7: Specific conductivity γ (at 37 °C) and osmolalities π of different sucrose solutions that were used as hypertonic buffers. Osmolality differences $\Delta\pi$ are converted into osmolarity differences ΔC by including the mass density of water ρ_{H_2O} . The resulting osmotic pressure gradients $\Delta\Pi$ are calculated from ΔC according equation 4.1.

c (sucrose) / mM	γ / mS/cm	π / mOsmol/kg	ΔC / mol/L	$\Delta\Pi$ / bar
0	16.03	278	0	0
10	16.10	305	0.027	0.70
50	16.20	361	0.083	2.14
100	16.07	428	0.150	3.87
150	16.02	496	0.218	5.62
200	16.02	565	0.287	7.40

The AQP1-inhibitor $\text{HAuCl}_4 \cdot 3\text{H}_2\text{O}$ was purchased from Sigma Aldrich (Munich, Germany) and dissolved in PBS⁺⁺/glucose (1 g/L). The concentration of the stock solution was 1 mM. It was stored at 4 °C. For inhibition experiments, $\text{HAuCl}_4 \cdot 3\text{H}_2\text{O}$ was diluted to a concentration of 100 μM in PBS⁺⁺/glucose (1 g/L). Due to the specific liquid handling in the inhibition experiments (chapter 6), γ and π were determined for the 1:1-mixture of PBS⁺⁺/glucose (1 g/L) that contained 100 μM $\text{HAuCl}_4 \cdot 3\text{H}_2\text{O}$ and a 400 mM sucrose solution that contained 100 μM $\text{HAuCl}_4 \cdot 3\text{H}_2\text{O}$. The final solutions are presented in Tab. 4.8.

Material and methods

Tab. 4.8: Specific conductivity γ (at 37 °C) and osmolalities π of 100 μM $\text{HAuCl}_4 \cdot 3\text{H}_2\text{O}$ containing sucrose solutions serving as hypertonic buffers. Osmolality differences $\Delta\pi$ are converted into osmolarity differences ΔC by including the mass density of water $\rho_{\text{H}_2\text{O}}$. The applied osmotic pressure gradients $\Delta\Pi$ is calculated from ΔC according equation 4.1.

c (sucrose) / mM	γ / mS/cm	π / mOsmol/kg	ΔC / mol/L	$\Delta\Pi$ / bar
0	16.05	318	0	0
200	16.08	545	0.227	5.85

Different hypertonic solutions that contain an impermeable fluorophore were prepared. The basic buffer (PBS⁺⁺/glucose (1 g/L)) was adjusted in terms of osmolality by adding sucrose (Tab. 4.9). Again, γ and π of the 1:1-mixtures of PBS⁺⁺/glucose (1 g/L) and a 400 mM sucrose solution that both had the same concentration of a membrane-impermeable fluorophore were determined. FITC-dextran (fluorescein isothiocyanate labeled dextran, 0.25 mg/mL, 500 kDa, Sigma Aldrich, Munich, Germany) was added to the hypertonic buffers and used as the fluorophore for the *fluorophore dilution method*. The sterile solutions were stored at 4 °C and protected from light.

Tab. 4.9: Osmolalities π for FITC-dextran containing (0.25 mg/mL) sucrose solutions serving as hypertonic buffers in the *fluorophore dilution method*. Osmolality differences $\Delta\pi$ are converted into osmolarity differences ΔC by including the mass density of water $\rho_{\text{H}_2\text{O}}$. The applied osmotic pressure gradient $\Delta\Pi$ is calculated from ΔC following equation 4.1.

c (sucrose) / mM	π / mOsmol/kg	ΔC / mol/L	$\Delta\Pi$ / bar
0	301	0	0
200	483	0.182	4.69

For preparation of hypotonic buffers, a basic buffer with low basic conductivity and osmolality (Tab. 4.10) was prepared according to the protocol of O'Connor and co-workers (O'Connor *et al.* 1993). The pH value of this buffer was adjusted to 7.4 by using NaOH (1 M, Merck KGaA, Darmstadt, Germany).

Tab. 4.10: Composition of a basic buffer needed for the preparation of hypotonic solutions. The pH value was adjusted to 7.4.

solution	composition	supplier
basic buffer	3.3 mM KCl	Merck KGaA, Darmstadt, Germany
	1.2 mM KH_2PO_4	Merck KGaA, Darmstadt, Germany
	1.3 mM CaCl_2	Sigma Aldrich, Munich, Germany
	0.4 mM MgSO_4	Sigma Aldrich, Munich, Germany
	10 mM D-(+)-glucose	Merck KGaA, Darmstadt, Germany
	25 mM HEPES	Carl Roth, Karlsruhe, Germany

To generate iso- and various hypotonic buffers, different amounts of sucrose (Sigma Aldrich, Munich, Germany) and NaCl (VWR International, Radnor, USA) were added to the basic

buffer (Tab. 4.11). γ and π were measured for the 1:1-mixtures of isotonic and hypotonic buffers. The sterile solutions were stored at 4 °C. All solutions were adjusted to a specific conductivity of around 4.3 mS/cm, which was achieved by adding a certain amount of NaCl (VWR International, Radnor, USA) as it is indicated by “x” in Tab. 4.11. Higher specific conductivity was not compatible with the iso- and hypotonic osmolalities and lower specific conductivity had severe impacts on impedance spectra.

Tab. 4.11: Recipes for the different iso- ($V_{\text{iso}} = 50$ mL) and hypotonic ($V_{\text{hypo}} = 10$ mL) buffers. The specific conductivity γ (at 37 °C) and osmolalities π of the solutions were measured and converted into the corresponding osmolarity difference ΔC and osmotic pressure gradient $\Delta\Pi$, respectively.

solution	recipe	γ / mS/cm	π / mOsmol/kg	ΔC / mol/L	$\Delta\Pi$ / bar
isotonic (ISO)	basic buffer + 2.9 g sucrose + x NaCl	4.29	289	0	0
hypotonic B (HYPO B)	basic buffer + x NaCl	4.31	194	0.095	2.45
hypotonic A (HYPO A)	basic buffer + 0.2 g sucrose + x NaCl	4.25	231	0.058	1.50

4.2 Electrode fabrication

4.2.1 Gold electrodes

The major fraction of gold electrodes applied in this thesis was self-fabricated by using standard photolithographic techniques (Fig. 4.3). LEXAN[®] plates which were coated with a 100 nm thick gold layer (GE, Munich, Germany) by means of a sputter coating device (Balzers sputter coater SCD 050, Bal-Tec, Pfäffikon, Switzerland) served as substrates.

At the beginning, the LEXAN[®] substrates were uniformly covered by a positive photoresist (AZ[®]-ECI3027, Microchemicals, Ulm, Germany) via spin coating (model WS-650-23B, Laurell Technologies Corporation, North Wales, USA) using 2000 rpm for 1 min (Fig. 4.3 (1)). The photopolymer is cured by a soft-bake (100 °C, 30 min, Heraeus, Thermo Scientific, T6, Hanau, Germany). Subsequently the photopolymer was irradiated by UV light (2 min, isel[®] UV illumination device nr. 2, Elterfeld, Germany, Fig. 4.3 (2)) at specific positions that delineate the gold pattern using a self-designed mask. The light exposed areas of the photoresist were developed for 20 seconds with a solution of sodium hydroxide (7 g/L, Fisher Chemical, Schwerte, Germany) in double distilled water (Fig. 4.3 (3)). By putting the substrate into an etching solution for 30 seconds under constant agitation, the gold surface was removed where no longer protected by the photoresist (Fig. 4.3 (4)). An aqueous

solution of KI (0.265 mM, Merck KGaA, Darmstadt, Germany) and I₂ (0.499 mM, Merck KGaA, Darmstadt, Germany) served as the etching reagent. The etching process was stopped by a simple washing step with double distilled water. In order to get rid of the remaining photoresist, the substrate was exposed to UV light without the use of a mask and subsequently the photoresist was developed following the protocol of step 3 (Fig. 4.3 (5)). For some electrode layouts, the photolithographic procedure was already finished at this point. In other cases, the gold leads had to be covered by insulating photoresist. For this purpose, a second spin coating process (2000 rpm, 1 min, Fig. 4.3 (6)) was performed to spread a uniform layer of positive photoresist upon the pre-established gold pattern. A further soft bake (100 °C, 30 min) was applied, before specific areas of the photoresist were irradiated by UV light (2 min, Fig. 4.3 (7)) using a second mask. The masks were printed in black (UV blocking black dye inkjet ink, Matte Slot, Harke Group, Mühlheim, Germany) on a transparent foil (Ink Jet Films, Folex, Seewen, Switzerland) with an ordinary printer (Sure Color P400, Epson, Suwa, Japan). The positions of the photoresist which were exposed to UV irradiation were developed and removed according step 3 (Fig. 4.3 (8)) uncovering the gold structures. To stabilize the remaining photoresist, a hard bake (118 °C, 2 h, Fig. 4.3 (9)) was performed at the end of the photolithographic procedure.

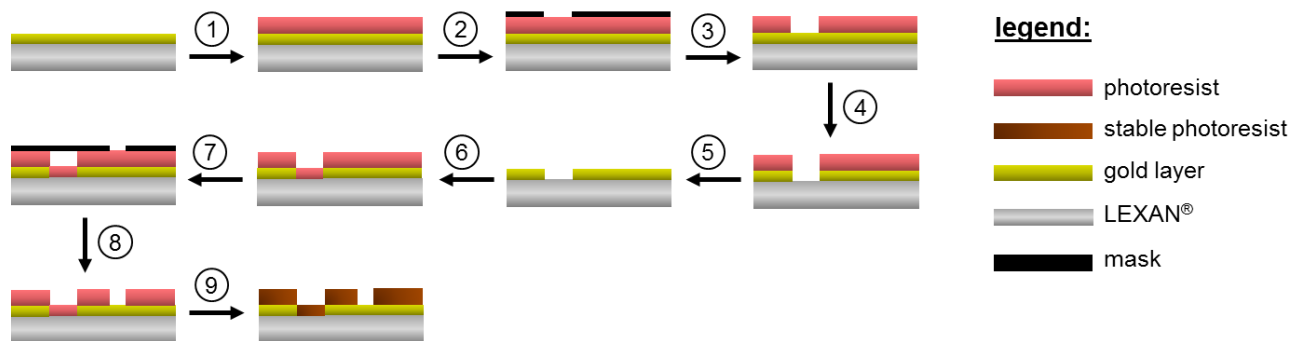


Fig. 4.3: Schematic of the photolithographic fabrication of the gold electrodes used in this thesis. Thickness of gold and photoresist layer are not drawn to scale.

Gold electrodes with an interdigitated layout were utilized in chapter 5 and chapter 6. Three different kinds of interdigitated electrodes (IDEs) were prepared which were denoted as IDE-200, IDE-400 and IDE-combi. Fig. 4.4 shows photographic images of the three electrodes and their corresponding masks which were used for the photolithographic fabrication. The protocol of Fig. 4.3 was performed up to and including step 5. The three IDEs differed with respect to the width of the conductive gold paths and the gap between those.

IDE-400 had gold structures with a width of 400 μm and a gap of 400 μm , whereas the width and gap were 200 μm in case of IDE-200. IDE-combi had a thick (1000 μm) and a thin (200 μm) gold area with a gap of 200 μm . The contacting pads enabled a connection between the electrodes and the impedance analyzer via a standard array holder. A glass ring (10 mm height / 24 mm diameter) glued to the base substrate with a non-cytotoxic silicone glue (Master fix Aquarium Silikon, Warenimport und Handels GmbH, Vienna, Austria) defined the measurement chamber. The extra gold lane outside the ring was included for optional experimental settings.

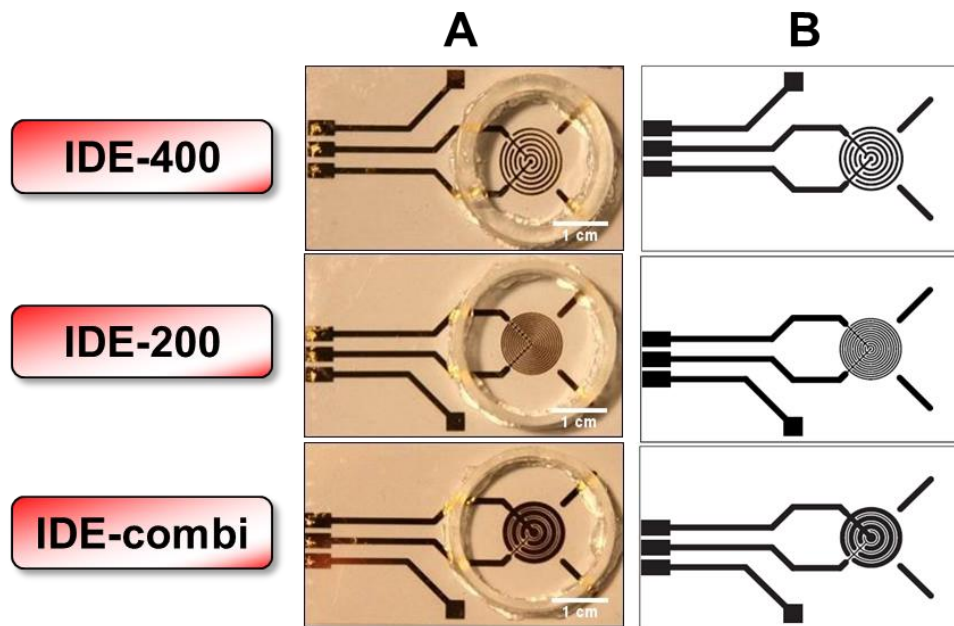


Fig. 4.4: (A) Photographic images of the IDEs upon the bottom of the measurement chamber. Three different interdigitated gold electrodes were fabricated: (top) IDE-400 (400 μm width / 400 μm gap), (middle) IDE-200 (200 μm width / 200 μm gap), (bottom) IDE-combi (1000 μm width #1 / 200 μm gap / 200 μm width #2). (B) Corresponding masks as they were used in the photolithographic process.

Another gold electrode which was used in chapter 6 consisted of two circular gold electrodes (500 μm diameter) in a co-planar arrangement (Fig. 4.5). The distance between the two electrodes was 800 μm . The leads were covered and passivated by an insulating photoresist. Two square contacting pads were used to connect to the impedance analyzer. The electrode chamber was constituted by a glass ring similar to the fabrication of the IDEs.

The electrode design of Fig. 4.5 was expanded for some experiments of chapter 6. For this purpose, three pairs of circular gold electrodes were prepared upon the bottom of the measurement chamber. The geometry of each individual electrode pair was identical to the

one above. However, one of the two electrodes of each pair was placed on a common gold pattern in order to reduce the number of contact pads. The leads as well as the contacting pads were scaled down to provide a connection to the impedance analyzer via a standard array holder. The measurement chamber was formed by a glass ring with similar geometry as described for Fig. 4.4.

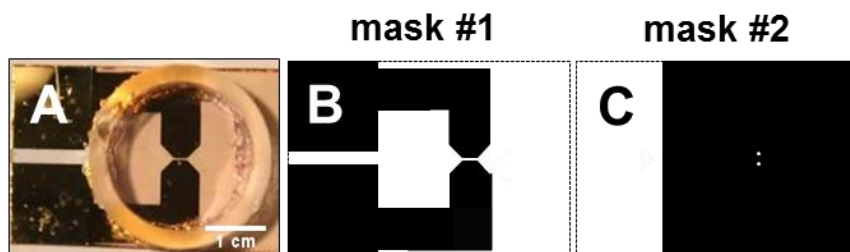


Fig. 4.5: (A) Photograph of an electrode layout consisting of two circular gold electrodes (diameter 500 μm) in a co-planar arrangement. The distance between the two electrodes was 800 μm . (B) The first photolithographic mask defined the basic electrode structure. (C) The second mask created the two circular electrodes as well as the contacting pads and allowed passivating the leads with an insulating photoresist.

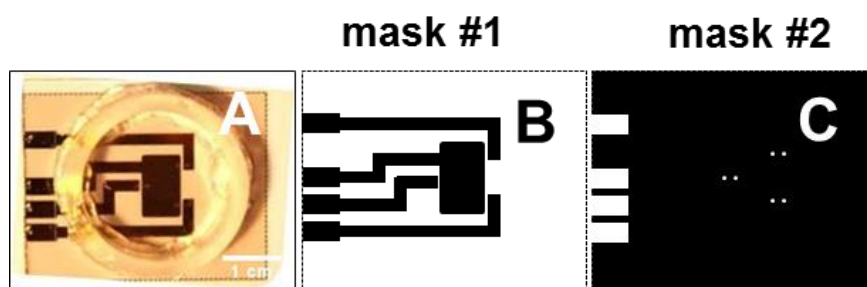


Fig. 4.6: (A) Photograph of an electrode design which was made up of three co-planar gold electrode pairs with a circular geometry (each diameter 500 μm). The distance between the opposing electrodes was 800 μm . (B) The first photolithographic mask defined the basic electrode layout. (C) The second mask defined the circular gold electrodes as well as the contacting pads and provided passivation of the leads with an insulating photoresist.

Another gold electrode was fabricated as custom array 2W6x1E (Fig. 4.7) by Applied BioPhysics (Troy, USA). Each base substrate (PET-foil) included six circular working electrodes (diameter 1 mm) and a common circular counter electrode with an area of 3.8 cm². The contact pads were arranged to fit into a standard array holder. The measurement chamber was formed by a glass ring with the same dimensions as for the electrodes described above.

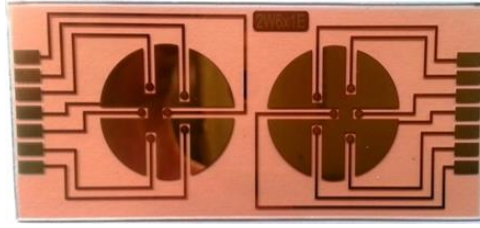


Fig. 4.7: Photograph of custom array 2W6x1E which was fabricated by Applied BioPhysics. The layout consisted of six individually addressable circular gold electrodes (diameter 1 mm) and a common circular counter electrode (area 3.8 cm²). The gold leads were covered by an insulating layer of photoresist.

For cytotoxicity studies, two different ECIS-PET-arrays (Fig. 4.8) were purchased from Applied BioPhysics (Troy, USA). The first array was denoted as 8W10E+ array. Each of the eight wells contained an area of 0.8 cm² and consisted of two sets of 20 circular gold electrodes (each diameter 250 μm) located on an interdigitated comb arrangement. The second array was referred to as 96W1E+. Each well included two circular gold electrodes with a diameter of 350 μm.

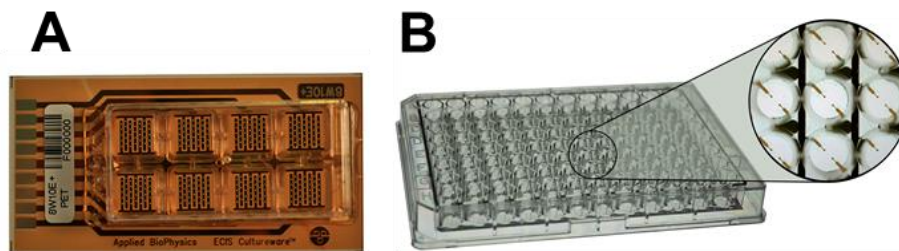


Fig. 4.8: Commercially available ECIS-PET-arrays from Applied BioPhysics which were used for cytotoxicity studies: **(A)** 8W10E+, **(B)** 96W1E+. The images were taken from www.biophysics.com.

4.2.2 Stainless steel electrodes

For standard TER-measurements stainless steel electrodes were used to record impedance data (Fig. 4.9). A stainless steel plate (thickness 2 mm, cut to size by the machine shop of the University of Regensburg) glued on a LEXAN[®] foil (GE, Munich, Germany) was applied as a basolateral electrode. The measurement well was built by a glass ring (height 20 mm / diameter 24 mm) which was fixed on the stainless steel plate. Cell-covered filter inserts were placed into the glass ring. A stamp-like electrode made up of stainless steel (fabricated by the University of Regensburg machine shop) was additionally dipped into the apical buffer. The stem-like part of the dipping electrode had a diameter of 4 mm and was flattened at one end to a circular disk with a height of 1 mm and a diameter of 10 mm. In

order to guarantee equal distances between the apical electrode and the filter membrane as well as to close the device, the dipping electrode was integrated into a standard petri dish lid ($\varnothing = 40$ mm, TPP[®], Sigma Aldrich, Munich, Germany). The electrode was fixed 2 mm above the porous membrane.

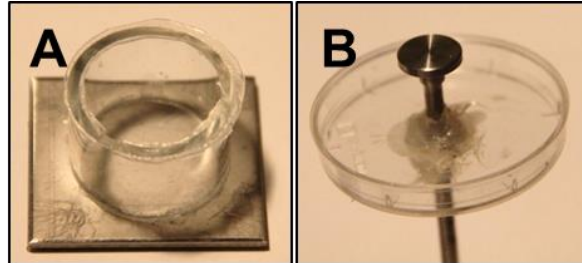


Fig. 4.9: Stainless steel electrodes as used in TER-studies. **(A)** A stainless steel plate with a thickness of 2 mm served as a basolateral electrode. A glass ring defined the measurement chamber and provided mechanical fixation of the filter supports. **(B)** Stamp-like stainless steel electrode acting as an apical electrode. This dipping electrode was flattened at one end to a circular disk with a height of 1 mm and a diameter of 10 mm. The electrode was fixed by the use of a standard petri dish lid leading to a constant distance of 2 mm between the stainless steel electrode and the porous filter membrane.

4.2.3 PEDOT-film electrodes

PEDOT-film electrodes (Fig. 4.10) were applied as electrode coating and planar basolateral electrode in modified TER-setups. A commercially available PEDOT-foil (Orgacon EL-350, Agfa, Mortsel, Belgium) was used as a basolateral electrode. The measurement chamber was formed by a glass ring (height 20 mm / diameter 24 mm) which was glued onto the substrate. The Transwell[®] filters were mechanically fixed by the glass ring. The inner area of the ring remained untreated, whereas the surroundings were covered with a 100 nm thick gold layer via sputter coating (Balzers sputter coater SCD 050, Bal-Tec, Pfäffikon, Switzerland). This modification step was crucial to provide a sufficiently high conductivity of the planar film that served as basolateral electrode. A second PEDOT-electrode was dipped into the apical solution. In case of this dipping electrode, a stainless steel stamp-like electrode similar to the one shown in Fig. 4.9B was covered by a thin PEDOT-layer with unknown thickness. The covering was achieved by dipping a cleaned stainless steel electrode for 30 seconds into a PEDOT:PSS-solution (Clevios, PH1000, Heraeus, Hanau, Germany) to which ethylene glycol (Sigma Aldrich, Munich, Germany) was added in a concentration of 8 % (v/v). After the dipping step, the PEDOT-covered electrode was dried at 100 °C for 15 minutes (Heraeus, Thermo Scientific, T6, Hanau, Germany). To achieve a complete coverage, this step was reproduced 3-5 times. However, more than five repeats of this step led to mechanically instable PEDOT-electrodes. Subsequently, the dipping

electrodes were bathed in ethylene glycol for 30 minutes at room temperature in order to remove PSS from the PEDOT-layer. At the end, the dipping electrodes were again dried at 100 °C for 1-2 hours. As already mentioned in chapter 4.2.2, a standard petri dish lid ($\varnothing = 40$ mm, TPP[®], Sigma Aldrich, Munich, Germany) was used to place the dipping electrode in a fixed distance of 2 mm from the permeable membrane.

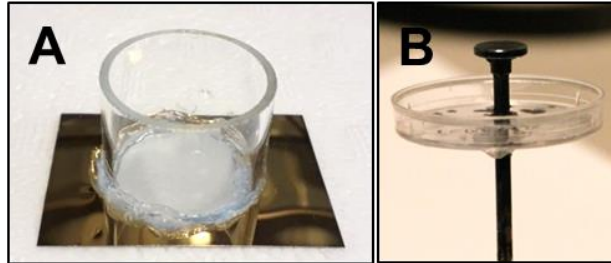


Fig. 4.10: PEDOT-electrodes as applied in a modified TER-setup. **(A)** A commercially available PEDOT-foil constituted the basolateral electrode. The inner part of the glass ring remained untreated, whereas the surroundings were covered with a 100 nm thick gold layer to enhance the conductivity of the device. **(B)** A PEDOT-coated stainless steel dipping electrode reached into the apical solution. The electrode was fixed by a petri dish lid providing a constant distance of 2 mm between the filter membrane and the dipping electrode.

4.3 Multi-mode impedance analysis

4.3.1 Experimental setup

All impedance measurements were performed under standard cell culture conditions. The electrodes were placed inside an incubator (Ultima[®] II, Revco[®], Thermo Fisher Scientific, Waltham, USA and Galaxy 48S, New Brunswick Scientific[™], Fisher Scientific, Schwerte, Germany and CO₂ cell, MMM Group, Munich, Germany and Modell C170, Binder, Tuttlingen, Germany) to provide a constant temperature of 37 °C and relative humidity of 95 %. The electrodes were connected to a relay via a standard ECIS-array holder (Applied BioPhysics, Troy, USA) or by a self-fabricated measurement table. The relay was necessary to switch between different electrode combinations and linked them to an impedance analyzer (type: SI-1260, Solartron Instruments, Farnborough, UK). Relay and impedance analyzer were connected to an ordinary PC (Fig. 4.11). The impedance analyzer applied a sinusoidal AC voltage of a preset frequency and amplitude to the electrodes and detected the resulting AC current. The impedance magnitude and the corresponding phase shift between voltage and current were recorded over a wide frequency range. In general, 61 individual frequencies were analyzed, equally spaced on a logarithmic scale. However, the applied frequency window was narrowed for some experiments to improve time-resolution (chapter 4.3.2). The

impedimetric measurements were controlled by a standard PC using a LabVIEW™ based software (National Instruments, Austin, USA) written by Prof. Wegener (University of Regensburg). Experimental details for the different impedance-based assays performed in this thesis are summarized in the following chapters.

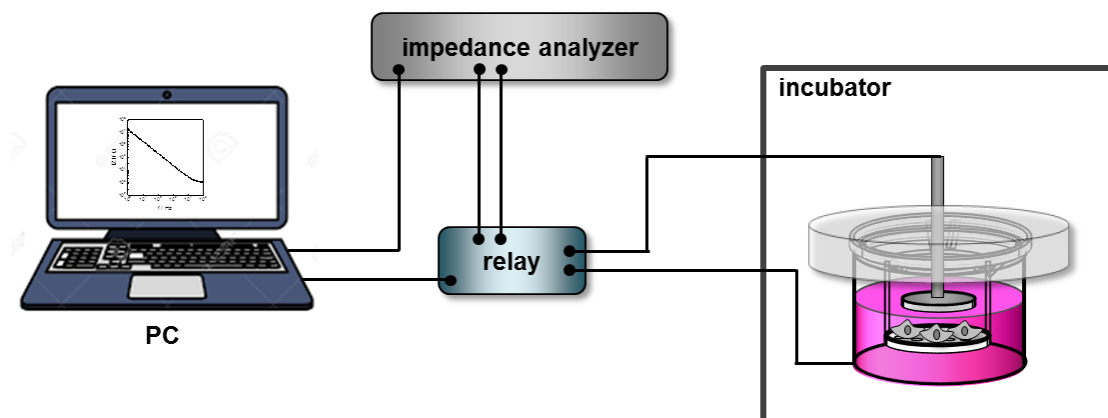


Fig. 4.11: Schematic of the experimental setup used for impedance studies performed in this thesis.

4.3.2 Assay conditions

All electrodes were sterilized prior to the experiment by using an argon plasma treatment (Harrick plasma, Ithaca, USA). Gold and PEDOT-electrodes were put into the cleaner for 30 seconds, whereas stainless steel electrodes were sterilized for 1 minute.

4.3.2.1 Combined electrochemical detection of P_E and TER (P_E TER-assay)

All impedimetric permeability measurements were carried out at 37 °C and 0 % CO_2 . PBS^{++} /glucose (1 g/L) served as the measurement buffer. The P_E TER-assay provides two different readout modes that are denoted as “integral readout” and “spatially resolved readout”.

P_E TER-assay with integral readout

To determine integral P_E values, a Teflon® disk (thickness 100 μm , inner diameter 1.12 cm, Fig. 4.12, fabricated by the University of Regensburg machine shop) was placed upon the bottom plate of the measurement chamber. Filter inserts were placed onto the Teflon® disk. Hence, a small cylindric buffer reservoir was created between the permeable membrane and the gold electrodes, which was denoted as *receiver volume* (V_R). V_R was defined by the thickness h and the disk radius r (equation 4.2). Exact knowledge of V_R was inevitable for the

calculation of P_E as it was included in the determination of $dn_R(t)/dt$ (chapter 3.2.1, equation 3.32).

$$V_R = \pi r^2 h = \pi \cdot (0.56 \text{ cm})^2 \cdot 100 \mu\text{m} = 9.85 \cdot 10^{-3} \text{ cm}^3 \quad (4.2)$$

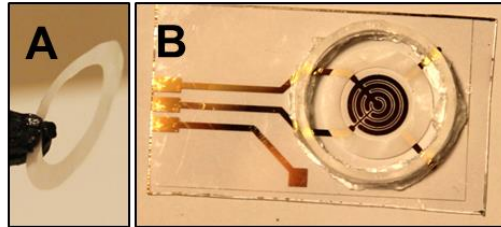


Fig. 4.12: (A) Teflon[®] disk with a thickness of 100 μm and an inner diameter of 1.12 cm. (B) The disk was placed directly on the substrate bottom. Filter inserts were positioned on the disk giving rise to a defined receiver volume. Hence, the Teflon[®] disk served as a spacer in the P_E TER-assay with integral readout.

A schematic illustration of the P_E TER-assay with integral readout is given in Fig. 4.13A. Interdigitated concentric gold-film electrodes (IDE-200, IDE-combi, chapter 4.2.1, Fig. 4.4) served as basolateral, co-planar electrodes. The two interdigitated gold combs were used to monitor tracer accumulation in the receiver compartment (P_E -mode: 1 vs. 2). An additional stainless steel electrode (chapter 4.2.2, Fig. 4.9B) which was dipped into the apical compartment was needed for simultaneous recording of TER (TER-mode: 1 vs. 3). The dipping electrode was connected to a standard ECIS-array holder via an ordinary electric cable. In order to provide sufficient time-resolution (~ 1.2 min), the impedance was only recorded at two distinct frequencies (1 Hz / 10 Hz) in P_E -mode, whereas the impedance was acquired along a frequency region of five decades (1 Hz – 10^5 Hz) to extract TER by equivalent circuit modeling in TER-mode. Besides different frequency settings, P_E - and TER-mode were performed at 50 mV or 10 mV (rms) amplitude, respectively.

P_E TER-assay with spatially resolved readout

In some experiments, the permeability of redox-active tracers was recorded laterally resolved (Fig. 4.13B). In this case, a gold electrode layout consisting of six individually addressable working electrodes with one common circular counter electrode was utilized (chapter 4.2.1, Fig. 4.7). By using one of the working electrodes and the counter electrode, tracer accumulation was monitored at different locations underneath the cell layer (P_E -mode: 1 – 6 vs. 7). Again, a stamp-like electrode composed of stainless steel (chapter 4.2.2, Fig. 4.9B) was dipped into the apical solution (TER-mode: 7 vs. 8). To guarantee a high time-resolution

(~ 1.9 min), only two distinct frequencies (1 Hz / 10 Hz) were recorded in P_E -mode. In contrast, frequencies from 1 Hz to 10^5 Hz were analyzed in TER-mode. A striking difference between the integral and spatially resolved P_E TER-assay addressed filter insertion. In the latter approach, filter supports were directly placed onto the substrate bottom without using a Teflon[®] spacer. Thereby, lateral diffusion of the permeability probe was reduced on the receiver side. Tab. 4.12 summarizes the different experimental conditions for both P_E TER-versions.

Tab. 4.12: Overview about the experimental conditions for P_E TER-assays. Substrate permeability can be monitored either integrally or spatially resolved.

readout	basolateral electrode	filter position	P_E -mode		TER-mode	
			f / Hz	U / mV	f / Hz	U / mV
integral	IDE-200 / IDE-combi	Teflon [®] disk	1 + 10	50	1 – 10^5	10
spatially resolved	2W6x1E	substrate bottom	1 + 10	50	1 – 10^5	10

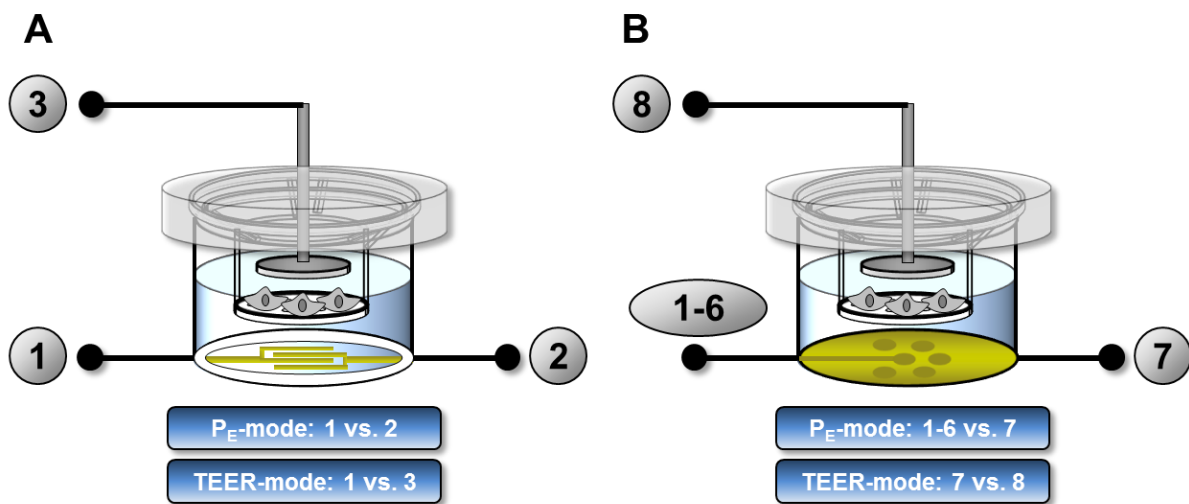


Fig. 4.13: Schematic of the experimental setup of the P_E TER-assay. **(A) Integral readout:** filter inserts were placed onto a Teflon[®] spacer defining the receiver volume. Two interdigitated concentric gold electrodes were integrated into the bottom of the measurement chamber to monitor tracer permeation across the cellular barrier (P_E -mode: 1 vs. 2). An apical, stainless steel electrode enabled TER-recordings (TER-mode: 1 vs. 3). **(B) Spatially resolved readout:** filter supports were placed directly onto the bottom of the chamber without any spacer. The permeation of a redox-active compound was followed at different positions via six, individually addressable gold electrodes deposited in the basolateral chamber (P_E -mode: 1/2/3/4/5/6 vs. 7). A stainless steel dipping electrode reached into the apical solution and provided the measurement of TER (TER-mode: 7 vs. 8).

Three different cell lines (MDCK-I / MDCK-II / NRK) with individually different barrier function were examined with the new device. The basolateral compartment was filled with 700 μ L and the apical side with 500 μ L PBS⁺⁺/glucose (1 g/L). The addition of a redox-active compound occurred apically by replacing 250 μ L of the initial buffer by 250 μ L of a double-concentrated

permeability probe solution. Two different redox tracers were investigated ($[\text{Fe}(\text{CN})_6]^{3-/4-}$ and FcMeOH). $[\text{Fe}(\text{CN})_6]^{3-/4-}$ was used in a final concentration of 1 mM. FcMeOH was only used for the P_{ETER} -assay with spatially resolved readout and was applied in a final concentration of 0.5 mM. For special assay types, a final cytochalasin-D concentration of 5 μM was added to the donor compartment by substituting 250 μL of the apical buffer by 250 μL of a double-concentrated cytochalasin-D solution. Additionally, the permeability of $[\text{Fe}(\text{CN})_6]^{3-/4-}$ (applied concentrations: 0.5 mM / 1 mM) across filter-grown cell layers containing mixed but segregated cell types was investigated with the laterally resolved P_{ETER} -readout. Mixtures of MDCK-I / MDCK-II, MDCK-I / NRK and MDCK-II / NRK were examined.

4.3.2.2 Determination of osmotically induced transepithelial water flux

All water flux experiments were performed at 37 °C and 0 % CO_2 . The impedance-based water flux assay provides two different readout modes that are referred to as “central readout” and “spatially resolved readout”.

Transepithelial water flux assay with central readout

Experimental studies comprised both, hypertonic and hypotonic stimulations of the cellular barriers. For hypertonic stimulations, 700 μL PBS^{++} /glucose (1 g/L) were filled into the basolateral side and 500 μL of the buffer were added to the apical chamber. Sucrose solutions with different concentrations (chapter 4.1.5, Tab. 4.7) were applied apically by replacing 250 μL of the initial buffer by 250 μL of a double-concentrated sucrose solution. The filter inserts were placed directly onto the bottom of the chamber. Two circular gold electrodes (chapter 4.2.1, Fig. 4.5) were used to measure transepithelial water flux (Fig. 4.14A, 1 vs. 2). Impedance-based water flow experiments were conducted with MDCK-I and MDCK-II cell layers. In addition, MDCK-I-AQP1 cells were investigated. In some experiments, a 100 μM $\text{HAuCl}_4 \cdot 3\text{H}_2\text{O}$ solution (chapter 4.1.5, Tab. 4.8) replaced the buffer in both compartments ($V_{\text{basolateral}} = 700 \mu\text{L}$ / $V_{\text{apical}} = 500 \mu\text{L}$) while the baseline was recorded. Subsequently, the cells were osmotically stimulated with sucrose in a final concentration of 200 mM which also contained the AQP1-inhibitor in a concentration of 100 μM . The experimental procedure of hypotonic stimulations was similar, but the basic buffer was different (chapter 4.1.5, Tab. 4.10). Different hypotonic solutions (chapter 4.1.5, Tab 4.11) replaced the isotonic buffer in the apical compartment by a 1:1-exchange. Impedance was recorded at 21 distinct AC frequencies in a range from 10^4 Hz to 10^6 Hz, that were equally

spaced on a logarithmic scale to guarantee high time-resolution (~ 0.6 min). The AC voltage amplitude was set to 10 mV (rms).

Spatially resolved water flux assay

Besides the central readout with one pair of electrodes, transepithelial water flow was also monitored laterally resolved (Fig. 4.14B, 1/2/3 vs. 4). Instead of using one electrode pair, the number of electrode pairs was increased to three (chapter 4.2.1, Fig. 4.6). Again, PBS⁺⁺/glucose (1 g/L) served as the measuring buffer ($V_{\text{basolateral}} = 700 \mu\text{L}$, $V_{\text{apical}} = 500 \mu\text{L}$). Filter-grown MDCK-I and MDCK-I-AQP1 cells were hypertonically stimulated by replacing 250 μL of the apical buffer by 250 μL of a double-concentrated sucrose solution. The final sucrose concentration was 200 mM. For some measurements, a mixed cell population consisting of MDCK-I and MDCK-I-AQP1 cells was investigated. Impedance was recorded at 21 discrete AC frequencies in a range from 10^4 Hz to 10^6 Hz, equally distributed on a logarithmic scale, to increase time-resolution (~ 1 min). The AC voltage amplitude was adjusted to 10 mV (rms). The experimental conditions for both versions of the impedimetric water flux assay are presented in Tab. 4.13.

Tab. 4.13: Overview about the experimental details of impedance-based water flux detection. Water flow was recorded either centrally or spatially resolved.

readout	electrode	filter position	f / Hz	U / mV
central	1 pair (Fig. 4.5)	substrate bottom	$10^4 - 10^6$	10
spatially resolved	3 pairs (Fig. 4.6)	substrate bottom	$10^4 - 10^6$	10

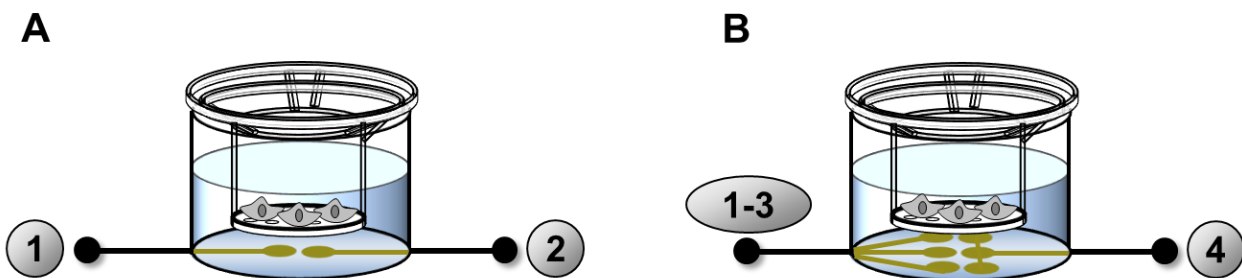


Fig. 4.14: Schematic of the experimental setup for an impedance-based water flux assay. **(A) Central readout:** filter inserts were directly placed above the electrode structure. One electrode pair consisting of two circular, co-planar gold electrodes was integrated underneath the center of the filter membrane providing local monitoring of transepithelial water transport. **(B) Spatially resolved readout:** filter supports were placed directly onto the bottom of the chamber. Three laterally distributed electrode pairs with same dimensions as described for (A) were used for spatially resolved monitoring of transepithelial water flow.

4.3.2.3 Combined electrochemical detection of P_{OS} and TER ($P_{OS}TER$ -assay)

All measurements aiming for a combined recording of P_{OS} and TER were carried out at 37 °C and 0 % CO_2 . A Teflon[®] disk (thickness 100 μm , inner diameter 1.12 cm, Fig. 4.12, fabricated by the University of Regensburg machine shop) was fixed upon the bottom of the measurement chamber. Filter inserts were then mounted onto the spacer and thereby, a very small and well-defined initial basolateral volume (V_0) was created. V_0 was determined by the thickness h and the disk radius r of the disk and amounted to a value of $9.85 \cdot 10^{-3} \text{ cm}^3$ (chapter 4.3.2.1, equation 3.45). Exact knowledge of V_0 was crucial for the calculation of the osmotic water permeability coefficient.

A schematic illustration of the experimental setup of the $P_{OS}TER$ -assay is given in Fig.4.15. The device differs from the P_E TER-setup only in the layout of the co-planar electrode structure (IDE-400, chapter 4.2.1, Fig. 4.4). By using the two interdigitated gold electrodes, transepithelial water permeation was monitored (P_{OS} -mode: 1 vs. 2) integrally underneath most of the cell layer. A stainless steel dipping electrode (chapter 4.2.2, Fig. 4.9B) was applied for simultaneous detection of TER (TER-mode: 1 vs. 3). The apical electrode was linked to the impedance analyzer via a conventional electric cable. In order to improve time-resolution ($\sim 1.3 \text{ min}$), different frequency ranges were analyzed in P_{OS} - ($10^4 \text{ Hz} - 10^6 \text{ Hz}$) and TER-mode ($1 \text{ Hz} - 10^5 \text{ Hz}$). The AC voltage amplitude was set to 10 mV (rms) for both modes. Diverse hyper- and hypotonic stimulations as well as AQP1-inhibition studies were performed using the $P_{OS}TER$ -assay. MDCK-I, MDCK-II and MDCK-I-AQP1 were used as epithelial barriers.

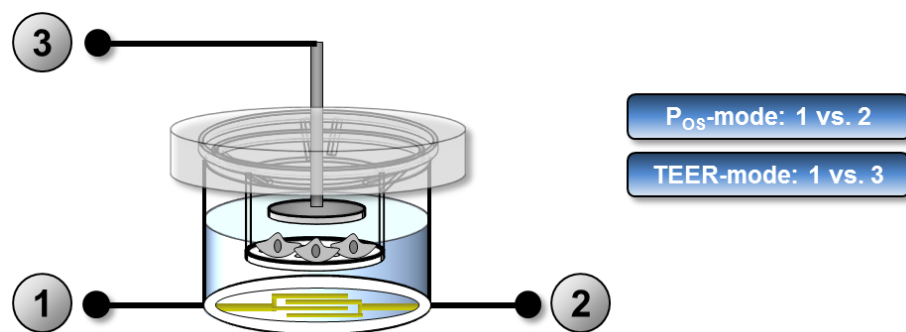


Fig. 4.15: Schematic illustration of the experimental setup of the $P_{OS}TER$ -assay. Filter inserts were placed on a Teflon[®] disk defining the basolateral volume. Two interdigitated gold electrodes were integrated into the bottom of the well and used for monitoring water flux across the cellular barrier (P_{OS} -mode: 1 vs. 2). An apical, stainless steel electrode provided simultaneous TER-recordings (TER-mode: 1 vs. 3).

4.3.2.4 TER-studies with stainless steel electrodes

For standard TER-assays (Fig. 4.16), 2 mL of the corresponding cell culture medium was filled into the basolateral compartment, whereas the apical side contained 0.5 mL. A stainless steel plate (chapter 4.2.2, Fig. 4.9A) served as a basolateral electrode and a stainless steel dipping electrode (chapter 4.2.2, Fig. 4.9B) was reached into the apical medium. Cell-covered filter inserts were fixed by a glass ring. The filter membrane was not placed directly onto the stainless steel plate, but with a distance of approximately 1 mm. TER-measurements were run at 37 °C and 5 % CO₂. In total, 61 frequencies in a range from 1 Hz to 10⁶ Hz, equally located on a logarithmic scale, were applied leading to a high time-resolution (~ 1.1 min). AC voltage amplitude of 10 mV (rms) was used for the measurements to guarantee non-invasiveness of the TER-measurement.

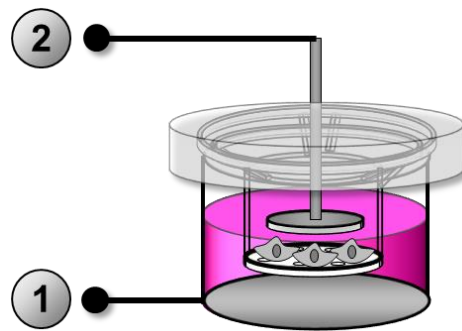


Fig. 4.16: Conventional setup for TER-studies composed of a basolateral stainless steel plate and an apical stainless steel dipping electrode.

4.3.2.5 TER-studies with PEDOT electrodes

TER-measurements were additionally conducted with a novel experimental setup made up of PEDOT-films as electrodes or electrode coatings (Fig. 4.17). The basolateral electrode of the regular TER-setup was exchanged by a commercially available PEDOT foil which was partially covered by a 100 nm thick gold layer (chapter 4.2.3, Fig. 4.10A) and a stainless steel dipping electrode encased by a thin PEDOT-layer (chapter 4.2.3, Fig. 4.10B). According to the standard TER-procedure, 2 mL of the corresponding cell culture medium were filled into the basolateral chamber and 0.5 mL into the apical compartment. The filter membrane was fixed in a distance of about 1 mm from the basolateral PEDOT-surface. The studies were performed at 37 °C and 5 % CO₂. A frequency range from 1 Hz to 10⁶ Hz was analyzed with a total number of 61 frequencies enabling an adequate time-resolution (~ 1.1 min). The preset AC voltage amplitude was 10 mV (rms). In some experiments, 5 µM cytochalasin-D were added to the apical compartment.

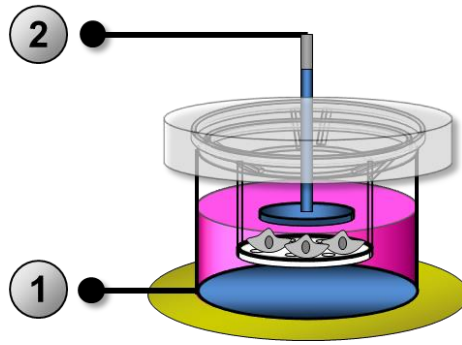


Fig. 4.17: PEDOT-based setup for TER-studies. A PEDOT foil sputter-coated with a thin gold layer outside the measurement chamber served as a basolateral electrode. The apical electrode was constituted by a stainless steel dipping electrode covered by a thin PEDOT-layer.

4.3.2.6 ECIS-cytotoxicity studies

A commercial 96W1E+ PET array (chapter 4.2.1, Fig. 4.8B) was used to investigate possible cytotoxic effects of the two permeability probes $[\text{Fe}(\text{CN})_6]^{3-/4-}$ and FcMeOH upon incubation with confluent monolayers of MDCK-I, MDCK-II and NRK. 200 μL PBS⁺⁺/glucose (1 g/L) were prepared in each well pre-loaded with confluent cell layers of either type. After establishing a stable baseline, 200 μL of different tracer concentrations were added to each well. The ECIS-measurements were performed at 37 °C and 0 % CO₂. The array was connected via a 96-well station to an ECIS Z instrument (both manufactured by Applied BioPhysics, Troy, USA). The impedance magnitude was monitored at a single frequency of 16 kHz over time to provide sufficient time-resolution (~ 1.2 min).

Potential harmful influences of the AQP1-inhibitor H₂AuCl₄·3H₂O on confluent monolayers of MDCK-I-AQP1 cells were examined via a 8W10E+ PET array (chapter 4.2.1, Fig. 4.8A). 200 μL PBS⁺⁺/glucose (1 g/L) were added to each well. After reaching constant impedance magnitudes, 200 μL of the inhibitor were added into each well resulting in an effective concentration of 100 μM H₂AuCl₄·3H₂O. The ECIS-cytotoxicity studies were again run at 37 °C and 0 % CO₂. The array was linked to an ECIS Z instrument by means of a 8-well station (both purchased from Applied BioPhysics, Troy, USA). The ECIS measurements were conducted at a single frequency of 16 kHz to provide proper time-resolution (~ 0.4 min).

4.3.3 Equivalent circuit modeling

Cell-related parameters were received by fitting the elements of a non-redundant equivalent circuit to the measured impedance data (chapter 3.1.1 and 3.1.2, Fig. 3.3). For this purpose,

LabVIEW™- and MATLAB-based programs were used. This software was written by Prof. Wegener (University of Regensburg). The weighted sum of squares (S) of the differences between the raw data (Z_i) and the calculated impedances of the transfer function ($Z_{i,calc}$) were minimized by searching for the best values of the adjustable circuit elements (Bevington and Robinson 2003; Lasia 2002) according to equation 4.3:

$$S = \sum_{i=1}^N \left\{ \omega_i [Z_i - Z_{i,calc}]^2 \right\} \quad (4.3)$$

The summation ran over all N frequencies of a given spectrum under analysis. The minimization was carried out by using a non-linear least-square method. A basic requirement for this procedure was a suitable estimate for the starting values. Automated analysis of a set of repeatedly recorded impedance spectra was achieved by using dynamic start values, i.e. the fit result for the parameters of the transfer function of spectrum i is used as start value for spectrum (i + 1). ω_i represented a data proportional weighting factor (equation 4.4) which was needed to avoid an overestimation of high impedance values at low frequencies. Every recorded impedance value (Z_i) was multiplied by a relative error (p):

$$\omega_i = \frac{1}{(p Z_i)^2} \quad (4.4)$$

This procedure provided all parameters of the equivalent circuit (A_{CPE} , n_{CPE} , TER, C_{cl} , R_{bulk}). The resistance of the cell layer (TER in Ωcm^2) and the cell layer capacitance (C_{cl} in $\mu\text{F}/\text{cm}^2$) were calculated and normalized to the filter membrane area as both elements are area-specific parameters. The parameters of an uncovered filter membrane (R_{ins} , C_{ins}) were integrated into the transfer function to provide automated data correction for the electrical properties of the porous support (chapter 3.1.2, Fig. 3.5).

4.4 Fluorophore dilution method

Osmotically induced water flux across confluent monolayers of MDCK-II was additionally measured via an established *fluorophore dilution assay* (chapter 1.1.3.3). For this purpose, an impermeable, non-cytotoxic fluorophore was added to the apical compartment (FITC-dextran, 500 kDa, 0.25 mg/mL in PBS⁺⁺/glucose (1 g/L), chapter 4.1.5, Tab. 4.9).

Slightly different volumes ($V_{\text{apical}} = 0.2 \text{ mL PBS}^{++}/\text{glucose (1 g/L)} + 0.25 \text{ mg/mL FITC-dextran}$, $V_{\text{basolateral}} = 1 \text{ mL PBS}^{++}/\text{glucose (1 g/L)}$) were applied compared to the standard impedimetric water flux measurements. Prior to the osmotic stimulation, the cell-covered filter inserts were stabilized for 20 minutes in the measurement incubator (37 °C, 0 % CO₂). By replacing 250 µL of the dye-containing apical solution by 250 µL of a dye-containing sucrose solution (final sucrose concentration 200 mM), a transepithelial osmotic pressure gradient was induced. Samples were taken from the apical side every 10 minutes (t = 0 / 10 / 20 / 30 / 40 min). Before sampling, the apical buffer was mixed with a pipette and 5 µL of the apical solution were diluted and mixed with 1 mL PBS⁺⁺/glucose (1 g/L). Subsequently, the fluorescence intensity was measured with an ordinary cuvette-fluorimeter ($\lambda_{\text{ex}} = 485 \text{ nm}$ / emission spectrum (480 -550) nm, step size 5 nm, SLM Aminco Bowman Series 2 (AB2), Thermo Fisher Scientific, Waltham, USA). By monitoring the fluorescence intensity at a wavelength of 515 nm, net volume flux J_V was determined yielding the osmotic water permeability coefficient (chapter 3.2.2, equations 3.39 and 3.45).

4.5 PrestoBlue[®]-assay

The PrestoBlue[®]-reagent is a resazurin-based and membrane permeable probe. Generally, this kind of assay provides information on the mitochondrial activity of cells as the PrestoBlue[®]-reagent is reduced to resorufin by NADH/H⁺. Resorufin is a red fluorescent compound. In cells with impaired mitochondrial activity, less NADH/H⁺ is present resulting in a smaller concentration of the fluorophore resorufin. Thus, more vital cells show higher fluorescence intensities compared to damaged cells (Lall *et al.* 2013).

Possible cytotoxic effects of the permeability probes $[\text{Fe}(\text{CN})_6]^{3-/4-}$ and FcMeOH on confluent monolayers of MDCK-I, MDCK-II and NRK cells were tested via PrestoBlue[®]-assays. The cells were incubated with 200 µL of different tracer concentrations (37 °C, 0 % CO₂, 3 h, chapter 4.1.5). Afterwards, the solutions were substituted by 200 µL of PrestoBlue[®] reagent (1:10 (v/v) in PBS⁺⁺/glucose (1 g/L), Invitrogen, Darmstadt, Germany) and the cells were incubated for a second time (37 °C, 0 % CO₂, 2 h). Fluorescence intensity of each well was measured with a 96-well plate fluorimeter ($\lambda_{\text{ex}} = 532 \text{ nm}$, $\lambda_{\text{em}} = 600 \text{ nm}$, Genios, Tecan, Maennedorf, Switzerland).

Furthermore, the cytotoxic potential of the AQP1-inhibitor $\text{HAuCl}_4 \cdot 3\text{H}_2\text{O}$ was addressed with PrestoBlue[®]-assays. The basic procedure was identical to the protocol described above except for the incubation time which was reduced to one hour (37 °C, 0 % CO_2 , 1 h).

5 Combined electrochemical determination of molecular and ionic permeability (P_ETER-assay)

Prior to *in vitro* permeability studies, non-invasive TER-measurements are usually performed to ensure epithelial barrier integrity. Both assays provide integral information and have been performed separately so far. Local heterogeneities or even small defect spots within the cell layer cannot be determined by the integral readout and thus might lead to severe overestimation of P_E values or significant underestimation of TER values, respectively.

The first project of this thesis addresses an improved, impedance-based permeability assay that is denoted as P_ETER-assay and that provides simultaneous monitoring of molecular and ionic permeability across epithelial barriers. The rationale of this approach has been introduced in 2017 by Dr. Kathrin Hajek and Prof. Wegener (Hajek Kathrin 2017). A cell-covered filter insert is sandwiched between one apical and one basolateral electrode to record the transepithelial electrical resistance (TER). The same cell layer is exposed apically to an electroactive compound ($[\text{Fe}(\text{CN})_6]^{3-/4-}$ or FcMeOH) that serves as the permeability probe. The time- and barrier-dependent permeation of the redox tracer (P_E) is recorded over time by different electrode layouts deposited on the bottom of the basolateral compartment. The impedance-based readout makes use of two faradaic phenomena - (I) *charge transfer resistance* R_{CT} and (II) *Warburg impedance* Z_W – both arising from the presence of redox-active substances and their reversible electrochemical redox reactions at the gold electrodes. Impedance measurements provide highly automated data collection and thus, no liquid handling has to be performed during the experiment. Basically, the P_ETER-assay has been performed in two different experimental settings:

- (I) Integral readout: The first kind of basolateral electrode design – interdigitated concentric gold electrodes (IDE-200, IDE-combi) – allows for an integral determination of permeability coefficients that represent the average barrier tightness of the cell layer under study.

- (II) Spatially resolved readout: By reducing the size and increasing the number of gold electrodes on the bottom of the measurement chamber, even laterally resolved monitoring of substrate permeability gets accessible.

All electrode layouts are validated by performing proof-of-principle permeability studies across filter-grown cell layers of different tightness (MDCK-I, MDCK-II, NRK). The laterally resolved readout is additionally performed for mixed but segregated cell layers to highlight the spatial resolution of the assay. Potential cytotoxicity of the redox tracers in contact to the cell lines under study are investigated by PrestoBlue[®]-assays as well as ECIS-cytotoxicity studies.

5.1 P_ETER-assay with integral readout

The device presented here intends to combine permeability (P_E) and resistance (TER) measurements across epithelial cell layers by using an impedance-based approach not only for the TER-assay but also for the determination of P_E values. Interdigitated gold electrodes (chapter 4.2.1, Fig. 4.4) that are located on the bottom of the lower compartment beneath most of the cell layer provide integral monitoring of substrate permeability with excellent time-resolution. By integrating a ring-shaped Teflon[®] spacer (thickness 100 μm, chapter 4.3.2.1, Fig. 4.12) into the measurement chamber on which the cell-covered filter inserts are placed, the receiver compartment is clearly defined by the thickness and inner diameter of the spacer ($V_R = 9.85 \cdot 10^{-3} \text{ cm}^3$) which is a prerequisite for calculating P_E values. An apical electrode composed of stainless steel (chapter 4.2.2, Fig. 4.9B) enables simultaneous recording of TER values for the very same cell layer.

5.1.1 Characterization and calibration of the P_ETER-device

Characterization of the P_ETER-device with integral readout

Cell-free filter inserts were placed onto the Teflon[®] spacer that was described above. Interdigitated concentric gold electrodes with a width of 200 μm and a gap of 200 μm (IDE-200) were used as co-planar, basolateral electrodes. A stainless steel dipping electrode was dipped into the apical buffer. The impedance was measured both, in **P_E-mode (1 vs. 2, Fig. 5.1A)** and **TER-mode (1 vs. 3, Fig. 5.1A)**. Fig. 5.1B-D displays spectra of the impedance magnitude |Z|, the resistance R and the capacitance C of both measurement modes. The spectra are similar in P_E- and TER-mode. In absence of an electroactive species, all spectra are dominated by the double layer capacitance of the electrode-electrolyte interface at lower frequencies (1 Hz – 10³ Hz) and by the bulk resistance at higher frequencies

(10⁴ Hz - 10⁵ Hz). By equivalent circuit modeling, the elements of the equivalent circuit presented in chapter 3.1.2 (Fig. 3.3) are assessable and listed in Tab. 5.1. The values for the bulk resistance are in the same order for both modes, with values of (46.3 ± 0.3) Ω for P_E- and (39.0 ± 0.6) Ω for TER-mode. The constant phase element (CPE) which is described by two parameters (A_{CPE}, n_{CPE}) is slightly different for both modes. Whereas n_{CPE} is almost equal, the A_{CPE} value is smaller for P_E-mode. The resistance R_{ins} and the capacitance C_{ins} of the cell-free filter insert are only determined for TER-mode providing values of R_{ins} = (13 ± 2) Ωcm² and C_{ins} = (8.6 ± 0.6) μF/cm². The transepithelial electrical resistance of cell-covered filter inserts needs to be corrected for the values of R_{ins} and C_{ins} by applying an expanded equivalent circuit which was described in chapter 3.1.2 (Fig. 3.5). The contribution of the filter insert is irrelevant for P_E-mode as the impact of the cell-free filter support is only slightly visible in the mid frequency range. However, tracer accumulation is followed at a discrete frequency of 1 Hz.

The second interdigitated gold electrode that was tested as the basolateral electrode in the P_ETER-assay consisted of two differently sized gold combs (IDE-combi, width #1 1000 μm, width #2: 200 μm, gap 200 μm). The major difference compared to IDE-200 is that the two co-planar interdigitated electrodes have different surface areas. The experimental setup for electrode characterization was identical to the one above. The impedance was recorded in both, **P_E-mode** (1 vs. 2, Fig. 5.2A) and **TER-mode** (1 vs. 3, Fig. 5.2A). Spectra of the impedance magnitude |Z|, the resistance R and the capacitance C are shown in Fig. 5.2B-D. The higher frequencies reflect again the resistance of the buffer, whereas lower frequencies are dominated by the electrode-electrolyte interface capacitance. The idea of this modified layout is to use the larger of the two interdigitated electrodes as the basolateral electrode in TER-mode and thereby increase the active electrode area. Bigger electrodes in TER-mode provide enhanced accuracy of the TER-measurements with the P_ETER-device. The parameters of the equivalent circuit described in chapter 3.1.2 (Fig. 3.3) are quantified by equivalent circuit modeling and summarized in Tab. 5.2. The bulk resistance has a value of (57.3 ± 0.7) Ω in P_E-mode and (42.3 ± 0.7) Ω in TER-mode. The values for A_{CPE} are higher compared to IDE-200 due to an increased active area of the basolateral electrode. The resistance R_{ins} and the capacitance C_{ins} of a cell-free filter insert are R_{ins} = (19 ± 1) Ωcm² and C_{ins} = (9.8 ± 0.2) μF/cm² for TER-mode.

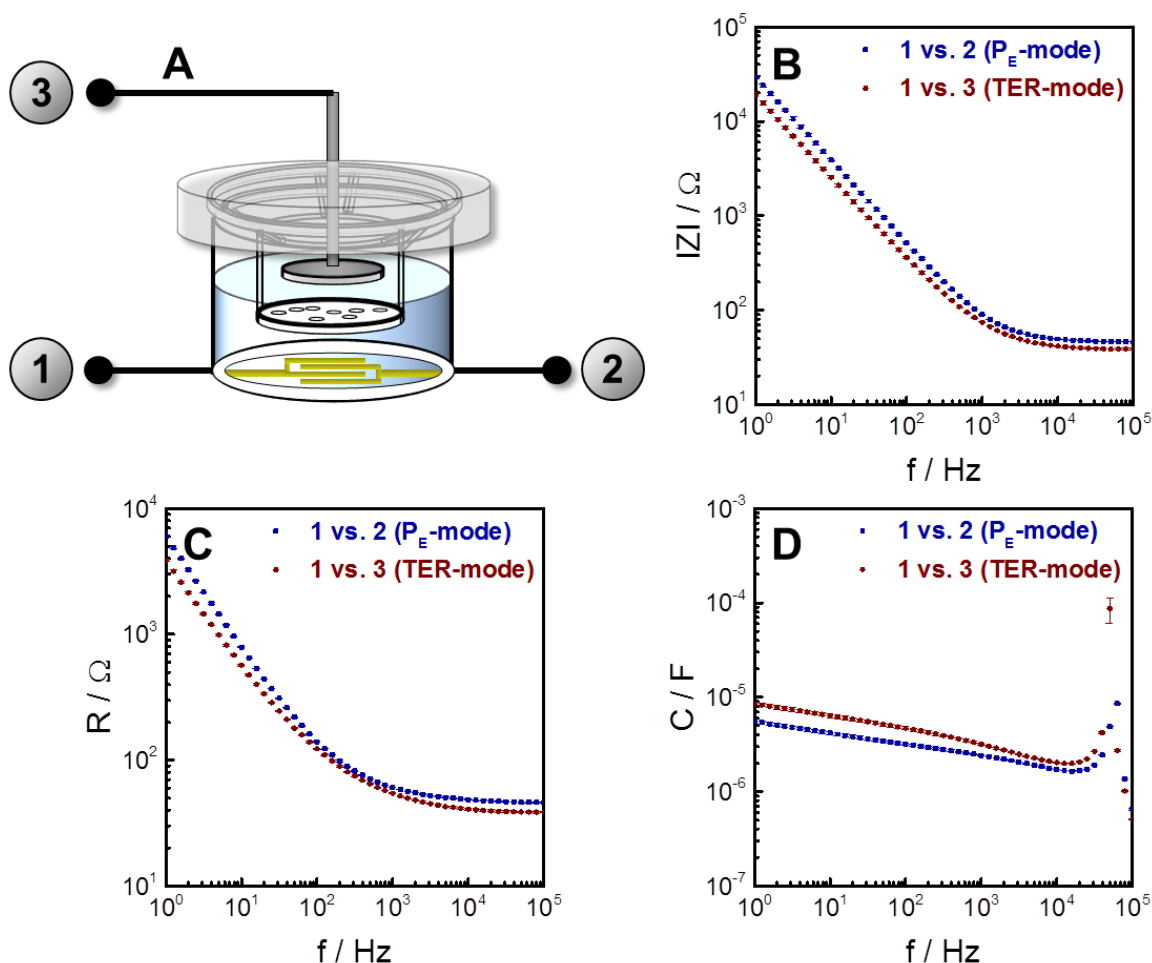


Fig. 5.1: (A) Schematic of the experimental setup for electrode characterization of the P_E TER-device using IDE-200 (width 200 μm / gap 200 μm). A cell-free filter insert is placed onto a Teflon[®] spacer. Spectra of the frequency-dependent (B) impedance magnitude $|Z|$, (C) resistance R and (D) capacitance C are compared when cell-free inserts are used in both measurement modes (mean \pm SE, $n = 3$).

Tab. 5.1: Values of the different circuit elements after equivalent circuit modeling of the data of Fig. 5.1 (mean \pm SE, $n = 3$) for IDE-200. The resistance of the filter insert R_{ins} and the filter membrane capacitance C_{ins} are only determined for TER-mode.

parameter	P_E -mode (1 vs. 2)	TER-mode (1 vs. 3)
R_{bulk} / Ω	46.3 ± 0.3	39.0 ± 0.6
$A_{\text{CPE}} / \mu\text{Fs}^{n-1}$	6.0 ± 0.2	9.4 ± 0.4
n_{CPE}	0.88 ± 0.00	0.87 ± 0.00
$R_{\text{ins}} / \Omega\text{cm}^2$		13 ± 2
$C_{\text{ins}} / \mu\text{F}/\text{cm}^2$		8.6 ± 0.6

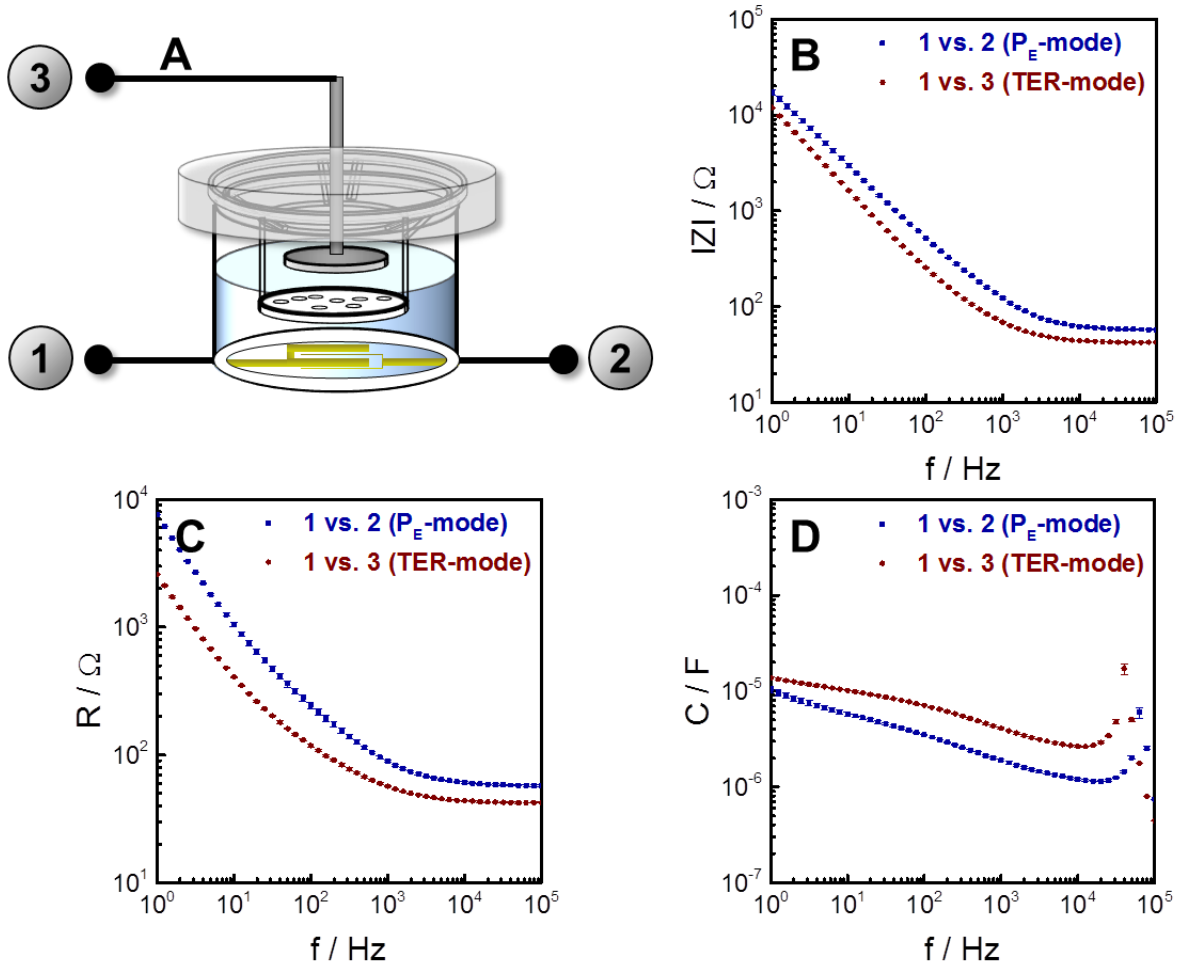


Fig. 5.2: (A) Schematic of the experimental setup for electrode characterization of the P_E TER-device using IDE-combi (width #1 1000 μm , width #2 200 μm , gap 200 μm). A cell-free filter insert is positioned onto a Teflon[®] disk. Spectra of the frequency-dependent (B) impedance magnitude $|Z|$, (C) resistance R and (D) capacitance C are compared when cell-free inserts are used in both measurement modes (mean \pm SE, $n = 3$).

Tab. 5.2: Values of the different circuit elements after equivalent circuit modeling of the data of Fig. 5.2 (mean \pm SE, $n = 3$) for IDE-combi. The resistance of the filter insert R_{ins} and the filter membrane capacitance C_{ins} are only determined for TER-mode.

parameter	P_E -mode (1 vs. 2)	TER-mode (1 vs. 3)
R_{bulk} / Ω	57.3 ± 0.7	42.3 ± 0.7
$A_{\text{CPE}} / \mu\text{Fs}^{n-1}$	13 ± 1	16.1 ± 0.3
n_{CPE}	0.77 ± 0.02	0.85 ± 0.00
$R_{\text{ins}} / \Omega\text{cm}^2$		19 ± 1
$C_{\text{ins}} / \mu\text{F}/\text{cm}^2$		9.8 ± 0.2

Calibration of the P_ETER-device with integral readout

Two prerequisites have to be met for the impedance-based calculation of P_E values:

- (I) The volume of the receiver compartment (V_R) has to be well-defined in order to calculate the amount of tracer that accumulates in the receiver compartment (n_R) from its concentration c_R . The use of a thin Teflon[®] spacer guarantees a constant and exactly defined V_R .

- (II) In addition, the experimental readings of the inverse impedance magnitude ($1/|Z|_{1\text{Hz}}$) have to be converted into the tracer concentration in the receiver volume (c_R). With the defined volume v_R and the time-dependent concentration $c_R(t)$, the term $dn_R(t)/dt$ is assessable and provides a final calculation of P_E values (chapter 3.2.1, equation 3.32).

For this purpose, $[\text{Fe}(\text{CN})_6]^{3-/4-}$ solutions with different concentrations (0 / 0.1 / 0.2 / 0.4 / 0.6 / 0.8 / 1.0 mM) were added to the measurement chamber in absence of a Transwell[®] filter insert. The impedance was measured in P_E-mode over five decades (1 Hz – 10⁵ Hz). The resulting spectra of the inverse impedance magnitude are displayed in Fig. 5.3A/C for IDE-200 or IDE-combi, respectively. Whereas $1/|Z|$ is not influenced by the presence of the redox pair at frequencies that are dominated by the bulk resistance (10³ Hz - 10⁵ Hz), $1/|Z|$ shows a dose-dependent response at lower frequencies (1 Hz – 100 Hz). The inverse impedance magnitude at a frequency of 1 Hz changes by almost two orders of magnitude when the concentration of $[\text{Fe}(\text{CN})_6]^{3-/4-}$ is increased from zero to 1 mM. The average readings of $1/|Z|_{1\text{Hz}}$ for each individual tracer concentration recorded with the two different interdigitated electrodes are listed in Tab. 5.3. Plotting $1/|Z|$ as a function of $[\text{Fe}(\text{CN})_6]^{3-/4-}$ concentration (Fig. 5.3B/D) provides a strictly linear correlation ($R^2 = 0.999$) with a slope of $(1142 \pm 15) \mu\text{S}/\text{mM}$ for IDE-200 or $(670 \pm 7) \mu\text{S}/\text{mM}$ for IDE-combi, respectively. The slope of this calibration quantifies the sensitivity of the measurement for a given redox probe in the P_ETER-assay. This is the reason for selecting $1/|Z|_{1\text{Hz}}$ instead of $|Z|_{1\text{Hz}}$ as the final readout parameter in P_E-mode. The correlation between $|Z|_{1\text{Hz}}$ and $[\text{Fe}(\text{CN})_6]^{3-/4-}$ concentration is mathematically expressed by an exponential decay function of 1st order and is therefore less convenient for data analysis (appendix: Fig. 11.1). The slopes of Fig. 5.4B/D indicate that IDE-200 is superior to IDE-combi in terms of the sensitivity in P_E-mode.

Tab. 5.3: Inverse impedance magnitudes at 1 Hz in response to different [Fe(CN)₆]^{3-/4-} concentrations for IDE-200 and IDE-combi (P_E-mode, mean ± SE, n = 3).

c([Fe(CN) ₆] ^{3-/4-} / mM)	1/ Z _{1Hz} / μS	
	IDE-200	IDE-combi
0.0	20.37 ± 0.05	21 ± 2
0.1	141 ± 2	99 ± 14
0.2	276 ± 4	173 ± 7
0.4	485 ± 7	296 ± 8
0.6	730 ± 11	428 ± 29
0.8	955 ± 17	570 ± 23
1.0	1158 ± 20	696 ± 21

The results of Fig. 5.3 are in perfect agreement with impedance theory and experimental reports on the impedance characteristics of [Fe(CN)₆]^{3-/4-} in physiological buffers (Magdić *et al.* 2016; Vogt *et al.* 2016; Yokoshima *et al.* 2015). The electrochemical detection of the redox tracer is based on the fact that gold-film electrodes are almost ideally polarizable electrodes when bathed in physiological buffers, i.e. no charge-transfer across the electrode-electrolyte interface occurs. However, when electroactive species with a matching electrochemical potential are added to the bathing fluid, there is a charge-transfer across the electrode-electrolyte interface. This phenomenon has been demonstrated repeatedly, for instance, when equimolar mixtures of ferri- and ferrocyanide [Fe(CN)₆]^{3-/4-} were used as well-behaved redox species. The associated impedance change is dependent on the concentration of the species and easily measured at low AC frequencies. Accordingly, it is the rationale of the P_ETER-assay to add an electrochemically active species to the apical compartment at time zero and measure its accumulation in the basolateral compartment by impedance measurements with the help of the interdigitated gold-film electrodes integrated in the bottom of the measurement chamber. In order to determine P_E values, it is indispensable to establish the concentration dependence of the impedance changes that are associated with the accumulation of the probe. From impedance theory, the presence of electrochemically active species gives rise to a charge-transfer resistance R_{ct} that represents the resistance associated with electron transfer from the metal electrode to the ionic species in solution and vice versa. In series to R_{ct} there is the so-called Warburg impedance Z_w that represents the impedance associated with the diffusion-limited mass transfer of the redox species to/from the electrode. These two impedance elements, which are sometimes bundled to a so-called *faradaic impedance* Z_f, are aligned in parallel to the constant phase element that represents the impedance of the electrode in absence of redox species. The parallel

arrangement of Z_f and Z_{CPE} is in series (insert in Fig. 5.3A/C) to the bulk resistance R_{bulk} (Bard and Faulkner 2001; Barsoukov and Macdonald 2005; Muñoz-Berbel *et al.* 2008).

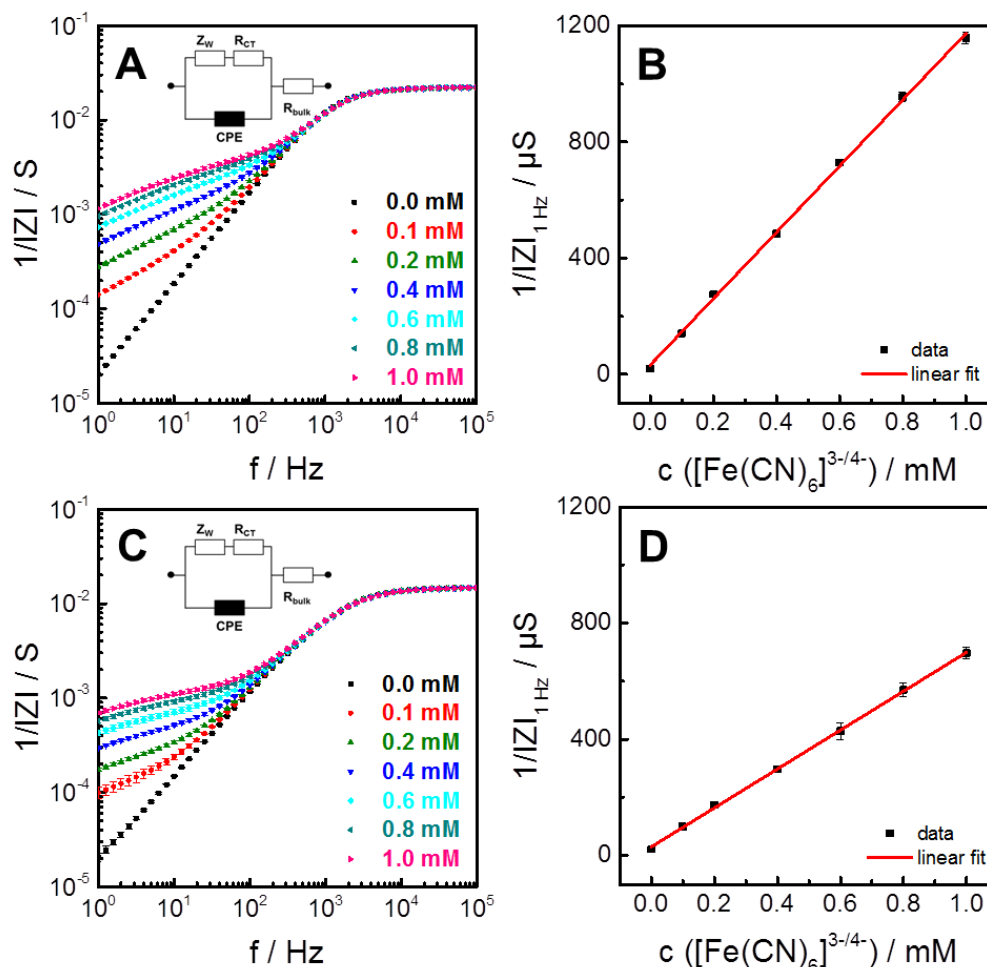


Fig. 5.3: Frequency spectra of the inverse impedance magnitude (P_E -mode, mean \pm SE, $n = 3$) in presence of variable $[Fe(CN)_6]^{3-/4-}$ concentrations recorded with **(A)** IDE-200 and **(C)** IDE-combi. There is a linear correlation between $1/|Z|_{1Hz}$ and $[Fe(CN)_6]^{3-/4-}$ concentration for **(B)** IDE-200 and **(D)** IDE-combi. The linearity between $1/|Z|_{1Hz}$ and the tracer concentration is analyzed by linear regression: IDE-200: slope = (1142 ± 15) $\mu S/mM$; y-intercept = (32 ± 8) μS ; $R^2 = 0.999$; IDE-combi: slope = (670 ± 7) $\mu S/mM$; y-intercept = (29 ± 4) μS ; $R^2 = 0.999$.

Stainless steel dipping electrode instead of gold dipping electrode

The use of a stainless steel dipping electrode instead of a gold electrode provides a significant advantage for the P_E TER-approach as it avoids the necessity of a more sophisticated equivalent circuit to extract TER values from the impedance spectra. This more complex fitting routine has been avoided in this thesis by using stainless steel instead of gold as the apical electrode material, as no charge-transfer occurs between $[Fe(CN)_6]^{3-/4-}$ and a stainless steel dipping electrode at the applied voltage amplitude of 50 mV (rms). Even

higher [Fe(CN)₆]^{3-/4-} concentrations of 5 mM do not induce charge-transfer across the electrode-electrolyte interface which gets obvious by the unaffected impedance values at low frequencies using stainless steel electrodes (appendix: Fig. 11.2). Therefore, simple equivalent circuit modeling is still applicable. The impact of the low tracer concentration that accumulates in the basolateral compartment during the measurement is negligible. When the P_ETER-approach was first described, a gold electrode reached into the apical solution (Hajek Kathrin 2017). The addition of the redox-active compound [Fe(CN)₆]^{3-/4-} in its starting concentration of 1 mM to the apical compartment induces an immediate and drastic change of the impedance spectra in TER-mode at low frequencies which complicates data analysis significantly. In this original description of the P_ETER-assay, the impedance raw data was analyzed by narrowing the frequency window for the fitting process. As a consequence, accuracy and reliability of the final TER values was affected.

5.1.2 Investigation of epithelial monolayers expressing a broad range of barrier tightness

The P_ETER-assay with integral readout was performed with confluent monolayers of differently tight cell lines (NRK << MDCK-II < MDCK-I). The impedance was followed at 1 Hz in **P_E-mode** and from 1 Hz to 10⁵ Hz in **TER-mode**. At time point zero, the permeability probe [Fe(CN)₆]^{3-/4-} was added to the apical buffer in a concentration of 1 mM. Adding a 1 mM [Fe(CN)₆]^{3-/4-} solution as the permeability probe is suitable, as no significant cytotoxic effects of the tracer were observed for the cell lines under study (chapter 5.3). Any significant signal changes due to liquid handling in the beginning of the experiment are negligible since control experiments with a mere buffer exchange did not alter the inverse impedance magnitude at 1 Hz significantly (appendix: Fig. 11.3). The following paragraphs show typical time course data of 1/|Z|_{1Hz} and TER for all three cell lines and cell-free filter inserts.

Impedance-based permeability measurements using cell-free filter inserts

Prior to the P_ETER-assays with cell-covered filter supports, cell-free filter inserts (Fig. 5.4) were examined for both, IDE-200 and IDE-combi, to allow for proper correction of apparent permeability coefficients. In this case, the experiment was only run in P_E-mode.

1/|Z|_{1Hz} increases drastically after the addition of 1 mM [Fe(CN)₆]^{3-/4-} to the apical solution. IDE-200 shows a signal increase of around 827 μS within 15 minutes (Fig. 5.4A). After one

hour, $1/|Z|_{1\text{Hz}}$ reaches a value of 935 μS . IDE-combi displays a similar time-course (Fig. 5.4B). Within 15 minutes, the inverse impedance magnitude alters from 20 μS to 725 μS . Finally, a saturation value of 787 μS is reached. The differences of the overall change of $1/|Z|_{1\text{Hz}}$ reflect the sensitivity differences between the two interdigitated concentric electrodes layouts.

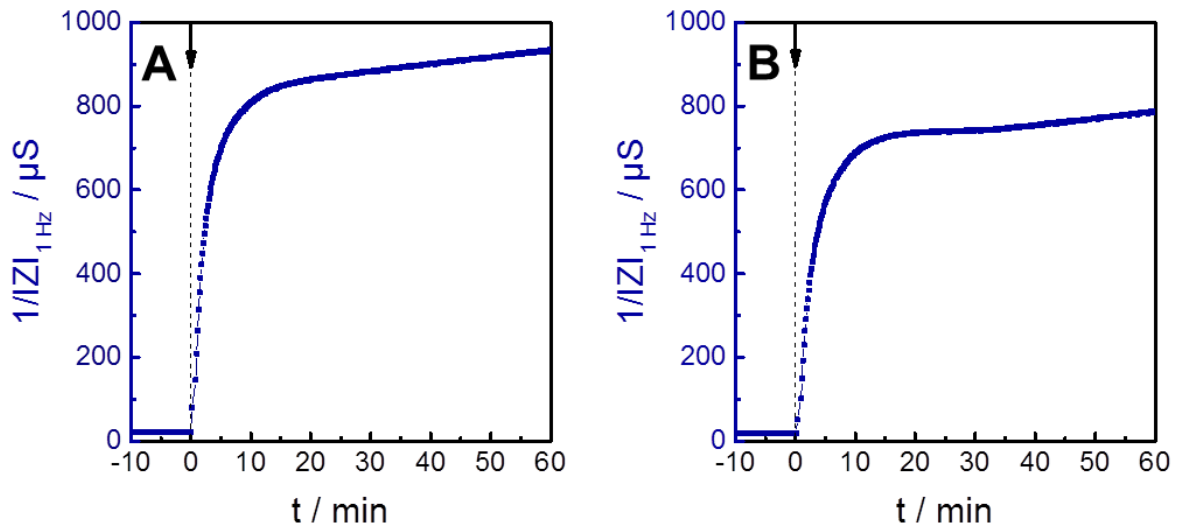


Fig. 5.4: Impedance-based permeability assay with a cell-free filter insert recorded with (A) IDE-200 and (B) IDE-combi. At $t = 0$ min, the permeability probe ($1 \text{ mM } [\text{Fe}(\text{CN})_6]^{3-/4-}$) is added to the apical compartment. The inverse impedance magnitude is followed over time at a frequency of 1 Hz (P_E -mode) to monitor tracer accumulation in the basolateral compartment. The associated permeability coefficients of the empty filter inserts (P_{ins}) are used to correct experiments with cells for the filter permeability (chapter 5.1.3) to provide P_E values.

$P_{E}TER$ -assays with integral readout using (leaky) NRK monolayers

Simultaneous recording of molecular and ionic permeability across intact NRK monolayers is displayed in Fig. 5.5. The transepithelial electrical resistance remains stable ($\sim 18 \Omega\text{cm}^2$) during the experiment when using IDE-200 (Fig. 5.5A). The accumulation of the redox probe in the basolateral compartment is detectable shortly after addition. $1/|Z|_{1\text{Hz}}$ increases from 20 μS to 402 μS within the first 15 minutes. At $t = 30$ min, the inverse impedance magnitude is saturated and levels off to a value of 619 μS . The time-course of $1/|Z|_{1\text{Hz}}$ monitored with IDE-combi shows similar shape (Fig. 5.5B). There is an increase of 332 μS within the first 15 minutes. Finally, a saturation value of 565 μS is observed. However, TER shows a slight decrease from $14 \Omega\text{cm}^2$ ($t = 0$ min) to $11 \Omega\text{cm}^2$ ($t = 60$ min).

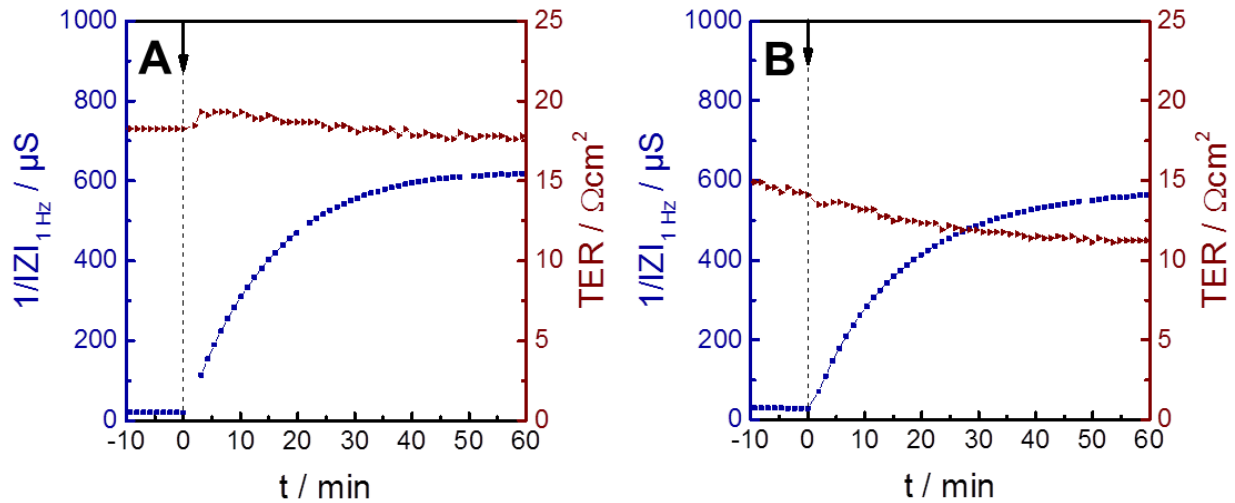


Fig. 5.5: P_ETER-assay for confluent NRK monolayers performed with (A) IDE-200 and (B) IDE-combi. The NRK monolayer is incubated with 1 mM [Fe(CN)₆]^{3-/4-} at t = 0 min. Tracer accumulation in the basolateral compartment is followed over time by monitoring 1/|Z|_{1Hz} (P_E-mode). The transfilter electrode combination (TER-mode) is used to record the TER of the same monolayer simultaneously.

The time-dependent changes of the inverse impedance magnitude fit to the expectations. The epithelial-like NRK monolayers form only weak tight junctions (Liu *et al.* 2012) and hence, the paracellular gap is not sealed effectively. The redox tracer permeates almost unhindered across the NRK layer due to its leakiness. However, a slight barrier function is observed for NRK cells compared to the cell-free filter insert. The P_ETER-measurements using a cell-free filter membrane (Fig. 5.4) and one that is covered by a confluent monolayer of NRK cells (Fig. 5.5) reveal two major differences:

- (I) The initial increase of 1/|Z|_{1Hz} is significantly reduced in presence of NRK cells compared to the cell-free device.
- (II) The overall change of 1/|Z|_{1Hz} within one hour of tracer incubation is also slightly decreased when NRK cells are present.

The time-course of TER allows two conclusions:

- (I) The permeability probe has no negative impact on the barrier integrity of NRK cells as TER remains almost constant during the entire incubation time.
- (II) The values determined by IDE-combi are in a reasonable range and fit to literature data (Tab. 5.4). However, IDE-200 indicates suspiciously high TER values. This inaccuracy is connected to the leakiness of NRK layers. Large amounts of

$[\text{Fe}(\text{CN})_6]^{3-/4-}$ accumulate in the basolateral compartment in which the interdigitated gold electrodes are deposited. Consequently, a charge-transfer between the electroactive species in the basolateral buffer and the interdigitated electrodes at the bottom of the measurement chamber occurs, inducing faradaic effects in the impedance spectra recorded in TER-mode (appendix: Fig. 11.4). For this purpose, the fitting routine was not performed over the entire frequency regime, but only from 160 Hz to 10^5 Hz. Thereby, undesired influences of the redox probe on the impedance spectra are reduced and the standard equivalent circuit modeling is still applicable. Nevertheless, the narrowed frequency window may lead to lower accuracy of the TER-determination compared to the established impedance-based TER-assay.

$P_{E}TER$ -assays with integral readout using (moderately tight) MDCK-II monolayers

Fig. 5.6 displays $P_{E}TER$ -studies for confluent MDCK-II cell layers grown on filter-supports. The TER values recorded with IDE-200 (Fig. 5.6A) show a slight decrease over time from $85 \Omega\text{cm}^2$ ($t = 0$ min) to $71 \Omega\text{cm}^2$ ($t = 60$ min). The inverse impedance magnitude is linearly increasing after tracer addition from $17.2 \mu\text{S}$ ($t = 0$ min) to $19.8 \mu\text{S}$ ($t = 60$ min). Experiments conducted with IDE-combi indicate a stationary time-course of TER (Fig. 5.6B). TER alters from $89 \Omega\text{cm}^2$ at the beginning of the experiment to $81 \Omega\text{cm}^2$ after one hour of tracer incubation. The time-course of $1/|Z|_{1\text{Hz}}$ indicates a higher $[\text{Fe}(\text{CN})_6]^{3-/4-}$ permeation into the basolateral compartment compared to the $P_{E}TER$ -study that was performed with IDE-200 with an increase of $19.3 \mu\text{S}$ within one hour of tracer incubation. In a third experiment, the MDCK-II monolayer was additionally challenged with $5 \mu\text{M}$ cytochalasin-D (cD) which inhibits actin polymerization and hence, affects barrier function (Fig. 5.6C). After the addition of the fungal toxin, there is a significant loss of barrier function, as indicated by the rapid TER decrease from $80 \Omega\text{cm}^2$ ($t = 76$ min) to $32 \Omega\text{cm}^2$ ($t = 110$ min) which corresponds to a reduction in barrier function of 60 %. The inverse impedance magnitude shows an increase from $17.5 \mu\text{S}$ ($t = 0$ min) to $19.8 \mu\text{S}$ ($t = 60$ min) in absence of the actin polymerization inhibitor. After cD-addition, there is an enormous permeation of $[\text{Fe}(\text{CN})_6]^{3-/4-}$ into the basolateral compartment from $20 \mu\text{S}$ ($t = 76$ min) to $99 \mu\text{S}$ ($t = 110$ min) which is consistent with the break down of TER. The barrier-opening effect of cytochalasin-D is based on the inhibitory effect of the fungal toxin on g-actin polymerization without affecting

f-actin-depolymerization resulting in an actin disassembly (Stevenson and Begg 1994). Please note the different scales for $1/|Z|_{1\text{Hz}}$ in Fig. 5.6A/B and Fig. 5.6C.

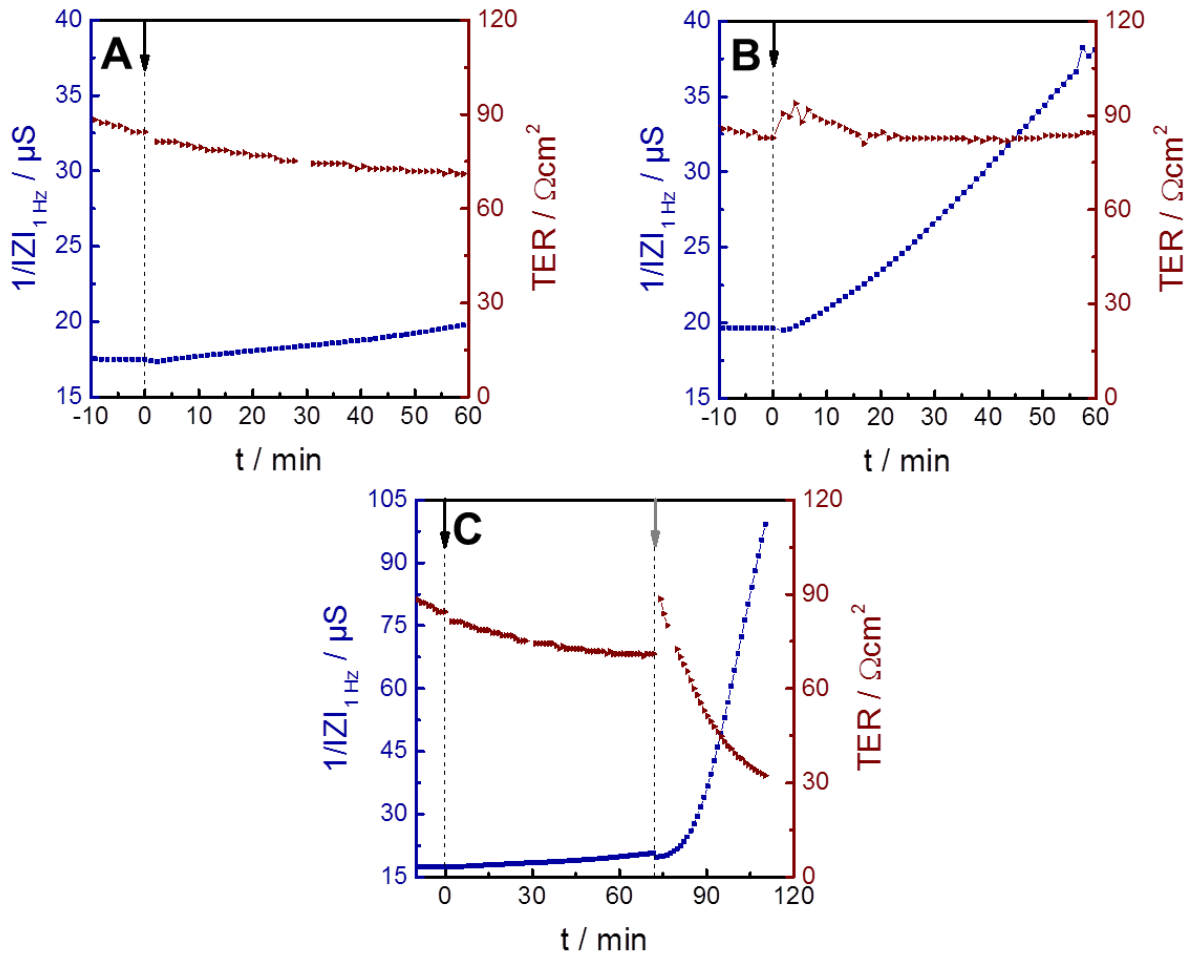


Fig. 5.6: P_ETER-assay for a confluent MDCK-II monolayer performed with **(A)** IDE-200 and **(B)** IDE-combi. The MDCK-II monolayer is exposed apically to **1 mM [Fe(CN)₆]^{3-/4-}** at $t = 0$ min. The accumulation of the redox probe in the basolateral compartment is followed by monitoring $1/|Z|_{1\text{Hz}}$ (**P_E-mode**). The transfilter measurement (**TER-mode**) is used to investigate time-dependent changes of TER of the same monolayer simultaneously. **(C)** P_ETER-assay recorded with IDE-200. Barrier function of a MDCK-II monolayer is manipulated using **5 μM cytochalasin-D** which inhibits actin polymerization.

$[\text{Fe}(\text{CN})_6]^{3-/4-}$ permeation across MDCK-II monolayers is less pronounced compared to the permeation across NRK barriers, as indicated by the significantly different time-courses of $1/|Z|_{1\text{Hz}}$. There is a constant increase of the inverse impedance magnitude after the addition of the redox probe, but the presence of tight junctions reduces basolateral tracer accumulation. The change of the inverse impedance magnitude recorded with IDE-combi suggests a higher $[\text{Fe}(\text{CN})_6]^{3-/4-}$ permeability as for IDE-200. However, the enhanced tracer permeability is rather due to differences in cell age and cell passage number and not due to

the electrode design in the basolateral compartment, since epithelial barrier function depends strongly on the exact age of the cell line under study (Srinivasan *et al.* 2015).

The time-courses of TER after $[Fe(CN)_6]^{3-/4-}$ addition indicate no significant influences of the redox probe on the barrier function of MDCK-II cell layers. Additionally, other impedance-based TER-measurements analyzing the impact of $[Fe(CN)_6]^{3-/4-}$ on the cell lines under study clearly indicate that 1 mM $[Fe(CN)_6]^{3-/4-}$ do not affect barrier function significantly (appendix: Fig. 11.5). The recorded TER values are in a reasonable range and fit well to literature data (Tab. 5.4). The incubation with cytochalasin-D shows a strong influence on the moderately tight MDCK-II layer with an increase of the $1/|Z|_{1Hz}$ of 79 μS within 34 minutes.

$P_{E}TER$ -assays with integral readout using (very tight) MDCK-I monolayers

$P_{E}TER$ -studies on filter-grown MDCK-I cells are displayed in Fig. 5.7. TER shows fluctuations during the entire experiment for both, IDE-200 and IDE-combi. In case of IDE-200 (Fig. 5.7A), TER starts with a value of 606 Ωcm^2 before a first maximum of 752 Ωcm^2 is reached after five minutes. Subsequently, the TER values are decreasing until a value of 473 Ωcm^2 is established at $t = 30$ min. In the following 30 minutes there is in turn an increase to 796 Ωcm^2 . The inverse impedance magnitude shows a slight increase of 1.7 μS in response to the addition of $[Fe(CN)_6]^{3-/4-}$. Afterwards, $1/|Z|_{1Hz}$ runs into a saturated value and shows even a small decrease at the end of the measurement. IDE-combi displays similar time-courses as IDE-200 (Fig. 5.7B). TER increases from 681 Ωcm^2 to 1058 Ωcm^2 within one hour of tracer incubation. The time-course of $1/|Z|_{1Hz}$ shows a short lag phase in which $1/|Z|_{1Hz}$ remains at around 20 μS , before a slight change to 22 μS is detected. A second $P_{E}TER$ -assay using IDE-200 shows a TER value of 542 Ωcm^2 at the beginning (Fig. 5.7C). Subsequently, TER drops to 442 Ωcm^2 at $t = 20$ min, before a constant increase to 880 Ωcm^2 gets obvious. At $t = 63$ min, 5 μM cytochalasin-D (cD) were added to the apical compartment in order to manipulate barrier function. The addition of cD provokes a breakdown in barrier function. After a maximum of 1738 Ωcm^2 the transepithelial electrical resistance is significantly decreasing. At $t = 120$ min, the TER value is only 68 Ωcm^2 which corresponds to a reduction of barrier function of 92 %. The time-course of the inverse impedance magnitude is consistent with the loss of tightness indicated by the strong increase of $1/|Z|_{1Hz}$. As already mentioned above, the breakdown in barrier function in presence of cytochalasin-D is due to the well-known inhibitory effect of the membrane-permeable fungal toxin on g-actin

polymerization without affecting f-actin depolymerization leading to actin disassembly (Stevenson and Begg 1994).

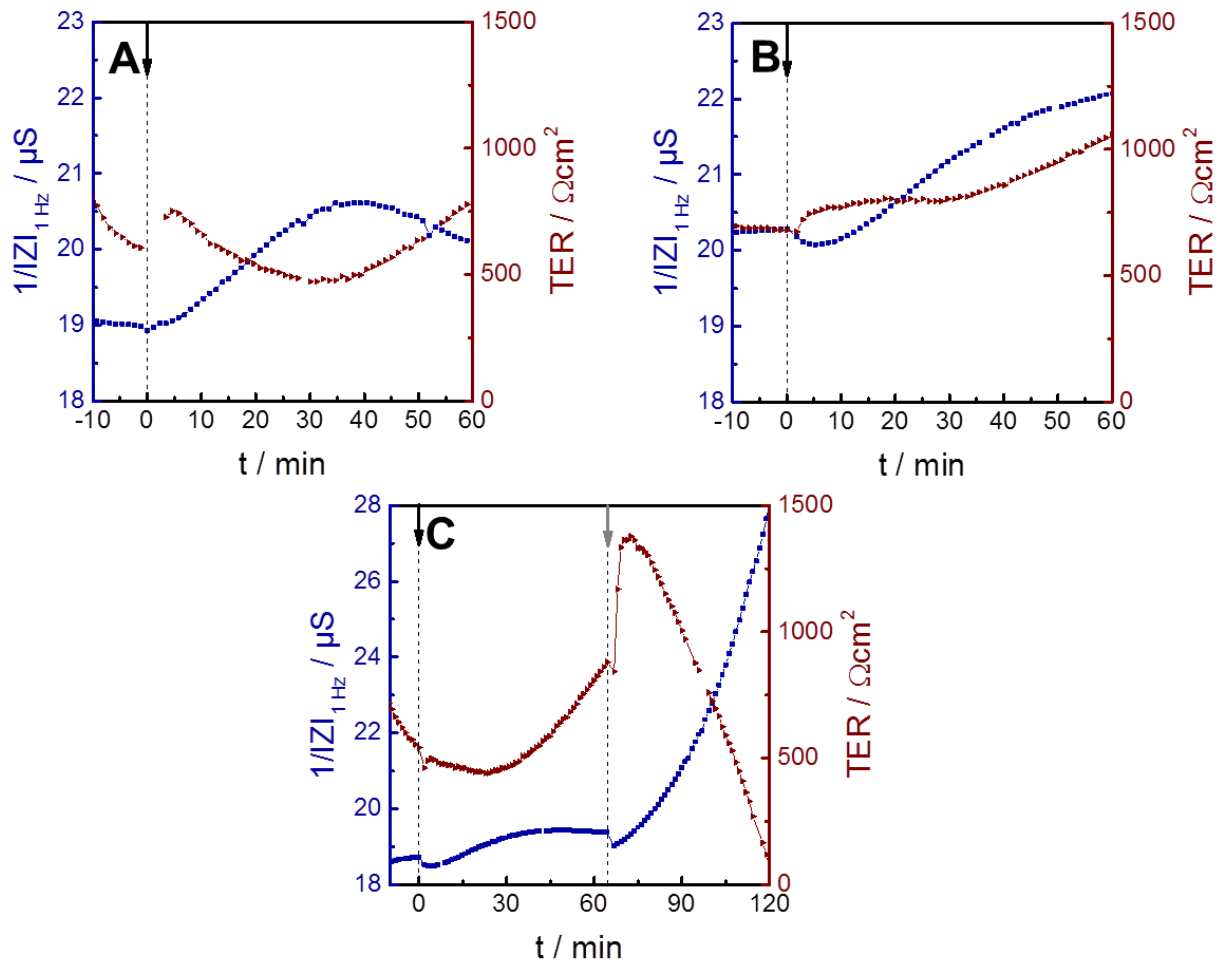


Fig. 5.7: P_ETER-assay for confluent MDCK-I monolayers recorded with **(A)** IDE-200 and **(B)** IDE-combi. The MDCK-I monolayer is incubated with 1 mM [Fe(CN)₆]^{3-/4-} at t = 0 min. Tracer accumulation in the basolateral compartment is followed by monitoring 1/|Z|_{1Hz} (P_E-mode). The transfilter measurement (TER-mode) is used to measure the TER of the same monolayer simultaneously. **(C)** P_ETER-assay performed with IDE-200. Epithelial barrier function is manipulated by the apical addition of 5 μM cytochalasin-D which inhibits actin polymerization.

The time-courses of $1/|Z|_{1\text{Hz}}$ differ strongly for MDCK-I, MDCK-II and NRK monolayers. MDCK-I cells build very strong tight junctions resulting in a very tight barrier (Inai *et al.* 1999). As [Fe(CN)₆]^{3-/4-} is supposed to permeate across epithelial barriers exclusively via passive paracellular diffusion, the immense tightness of MDCK-I layers effectively prevents the redox tracer to diffuse into the basolateral compartment to a significant degree. However, a small amount of [Fe(CN)₆]^{3-/4-} is able to permeate across the MDCK-I layer and is detectable by the co-planar, interdigitated electrodes that are integrated in the basolateral compartment. The

striking difference of the cell lines under study in barrier function gets obvious by analyzing the total change of $1/|Z|_{1\text{Hz}}$. NRK layers show a more than 450 times stronger increase of $1/|Z|_{1\text{Hz}}$ within the total observation time of the assay in comparison to MDCK-I layers. MDCK-II cells form significantly less tight barriers compared to MDCK-I cells due to a different composition of the tight junctional complex (Gonzalez-Mariscal *et al.* 1985). The incubation with cytochalasin-D shows a stronger influence on the moderately tight MDCK-II layer with an increase of the $1/|Z|_{1\text{Hz}}$ of 79 μS within 34 minutes, whereas $1/|Z|_{1\text{Hz}}$ changes only about 9 μS for MDCK-I cells within one hour of incubation with cytochalasin-D.

The TER values of the MDCK-I cells under study fit well to literature data (Tab. 5.4). It is striking that the barrier function of MDCK-I cells shows significant fluctuations during the permeability experiment indicated by strong changes of TER. Nevertheless, no negative impact of $[\text{Fe}(\text{CN})_6]^{3-/4-}$ on barrier integrity of MDCK-I cells is observed, as no significant breakdown of TER is detected. Accordingly, the order of barrier tightness NRK \ll MDCK-II $<$ MDCK-I is unequivocally reproduced by the individual TER values which compare favorably with data taken from literature (Tab .5.4). It is noteworthy when comparing TER values recorded in different labs for the same cell lines that they are readily affected by the external conditions and the medium composition (Hakvoort *et al.* 1998).

Tab. 5.4: TER and C_{cl} as recorded in this work for the epithelial cell lines MDCK-I, MDCK-II and NRK in comparison to literature studies. * indicates that results are given as mean \pm SE. # indicates that the reported values were recorded for cells grown directly on gold-film electrodes (ECIS).

cell line	TER / Ωcm^2	reference	C_{cl} / $\mu\text{F}/\text{cm}^2$	reference
NRK	13 \pm 1	(Prozialeck <i>et al.</i> 2006)	0.60 \pm 0.08	(Reiss and Wegener 2015) [#]
	12	(Limonciel <i>et al.</i> 2012)		
	12	(Pfannkuch <i>et al.</i> 2014)		
	13 \pm 2	this work* (IDE-200)		
	14 \pm 1	this work* (IDE-combi)		
MDCK-I	11 \pm 1	this work* (2Wx1E)	0.75 \pm 0.04	this work* (IDE-200)
	1500	(Cho <i>et al.</i> 1989)	0.88 \pm 0.04	this work* (IDE-combi)
	4000	(Kim Kit Lee 2014)	0.9 \pm 0.1	this work* (2Wx1E)
	876 \pm 53	(Kadam <i>et al.</i> 2012)	0.96 \pm 0.07	(Reiss and Wegener 2015) [#]
	1650 \pm 110	this work* (IDE-200)	1.3 \pm 0.2	(Krug <i>et al.</i> 2009b)
MDCK-II	3000 \pm 130	this work* (IDE-combi)	1.54 \pm 0.06	this work* (IDE-200)
	2800 \pm 400	this work* (2Wx1E)	1.91 \pm 0.06	this work* (IDE-combi)
	180 – 250	(Kim Kit Lee 2014)	2.11 \pm 0.01	this work* (2Wx1E)
	82 \pm 3	(Carr <i>et al.</i> 2010)	1.52 \pm 0.03	(Reiss and Wegener 2015) [#]
	136 \pm 17	(Lo <i>et al.</i> 1999)	1.9 \pm 0.4	(Krug <i>et al.</i> 2009b)
MDCK-I	98 \pm 4	this work* (IDE-200)	1.32 \pm 0.09	this work* (IDE-200)
	92 \pm 4	this work* (IDE-combi)	1.37 \pm 0.09	this work* (IDE-combi)
	85 \pm 3	this work* (2Wx1E)	1.80 \pm 0.04	this work* (2Wx1E)

Quantifying TER values by means of impedance analysis provides several striking advantages:

- (I) Using two planar, parallel electrodes ensures a homogenous electric field across the cell layer. Thus, the entire monolayer contributes to the recorded impedance preventing a systematic overestimation of the resistance of the cell layer, as it has been reported for chopstick electrodes (Jovov *et al.* 1991; Sheller *et al.* 2017). Moreover, planar electrodes make TER readings independent of the position of the electrodes providing significantly improved reliability and reproducibility.
- (II) The P_ETER-device or technically similar approaches provide time-resolved TER monitoring (~ 1.1 min per filter) without breaking the physiological temperature or humidity.
- (III) Besides TER, cell layer capacitance (C_{cl}), bulk resistance (R_{bulk}) and constant phase element (CPE) are recorded and documented simultaneously. Since R_{bulk} is strongly temperature-dependent, it provides an internal temperature control of the experiment. C_{cl} values are strongly related to the degree of plasma membrane foldings and hence, provide information about the topography of the membrane under study. The parameter CPE describes the electrode-electrolyte double layer capacitance and thus, provides information of electrode conditions.
- (IV) The TER-assays as performed here are highly automated and are conducted under sterile conditions. Thus, the approach ensures measurements under well-controlled external conditions.

5.1.3 Calculation of P_E values

Substrate and cell-type specific permeability coefficients have been extracted from *in vitro* permeability measurements (chapter 3.2.1). The accumulation of a particular permeability probe in the receiver compartment is followed over time by sequential sampling. The apparent permeability coefficient P_{app} is determined by the rate of this permeation (equation 3.32). In impedance-based permeability measurements, the (initial) donor volume V_{D,0} (0.5 cm³), the filter membrane area A (1.12 cm²) and the (initial) amount of tracer in the donor compartment n_{D,0} (5 · 10⁻⁴ mmol) are preset by the experimental conditions.

Time-dependent accumulation of the tracer in the receiver compartment $dn_R(t)/dt$ is quantified by the interdigitated gold electrodes at the bottom of the measurement chamber. Faradaic phenomena – the charge-transfer resistance R_{CT} and the Warburg impedance Z_W – which are induced by reversible redox reactions of $[\text{Fe}(\text{CN})_6]^{3-/4-}$ at the surface of the gold electrodes, are the physical background of the assay principle. By experimental calibration of the setup (chapter 5.1.1, Fig. 5.3) and by the exact definition of the receiver volume V_R ($9.85 \cdot 10^{-3} \text{ cm}^3$, chapter 4.3.2.1, equation 4.2), $1/|Z|_{1\text{Hz}}$ is transformed into n_R in the receiver compartment at any single time point. Only the linear phase of the time-dependent change of n_R , for which *sink-conditions* apply, is analyzed by linear regression providing the value of $dn_R(t)/dt$. A graphical illustration of this procedure is given in the supplementary information (appendix: Fig. 11.6). The apparent permeability coefficients P_{app} need to be corrected by the permeability coefficient of a cell-free filter insert P_{ins} (equation 3.33) to obtain the molecular permeability coefficients P_E (in cm/s).

The electrochemical P_E assay was conducted for the three differently tight cell lines NRK, MDCK-I and MDCK-II. Tab. 5.5 summarizes the individual P_E values that were corrected for P_{ins} . The order of decreasing P_E values $\text{NRK} \gg \text{MDCK-II} > \text{MDCK-I}$ mirrors the tightness of the cell layers for the permeation of $[\text{Fe}(\text{CN})_6]^{3-/4-}$ and corresponds to the order of increasing TER values. The lowest tracer permeability is observed for MDCK-I cells which form extremely tight monolayers as already indicated by their TER values. A slightly higher P_E value is obtained for MDCK-II cells that build moderate barriers. NRK monolayers grown on permeable supports are very leaky due to the lack of functional tight junctions. This low-barrier phenotype is reflected in a more than 500 times higher P_E value in comparison to MDCK-I layers.

The order of P_E values $\text{NRK} \gg \text{MDCK-II} > \text{MDCK-I}$ suggests that $[\text{Fe}(\text{CN})_6]^{3-/4-}$ behaves as a pure paracellular tracer. The differences in barrier function for the three cell lines under study are presumably due to a variable molecular composition of the tight junctional complex determining the paracellular resistance and causing differently tight barriers. The idea of $[\text{Fe}(\text{CN})_6]^{3-/4-}$ acting as a mere paracellular probe is supported by the intrinsic charge of the compound impeding the transcellular pathway across the epithelium. Additionally, no specific transporter systems located in the plasma membranes of the cell lines under study have been reported for $[\text{Fe}(\text{CN})_6]^{3-/4-}$. Taking all these aspects into account, $[\text{Fe}(\text{CN})_6]^{3-/4-}$ is considered to act exclusively as a paracellular permeability tracer.

Since [Fe(CN)₆]^{3-/4-} is slightly coloured, it is possible to quantify the time-dependent concentration of the probe in the basolateral compartment also by photometry at a wavelength of 405 nm as an independent control of the impedance-based approach. This optical permeability studies have been performed earlier in our lab (Hajek Kathrin 2017). Optical concentration analysis returned very similar permeability coefficients of MDCK-II and MDCK-I cells that were determined to be $(1 \pm 3) \cdot 10^{-6}$ cm/s. So the outcome of optical and impedance-based concentration analysis was essentially the same. P_E values recorded for NRK cells were significantly smaller following optical analysis compared to the impedance-based readout. But with either technique, the P_E value indicates that NRK cells form very leaky epithelial barriers compared to MDCK-II and MDCK-I cells. It is noteworthy that the impedance-based P_E values show significantly better reproducibility as indicated by the standard errors of the measurements. This is at least in part due to the fact that the impedance-based approach does not require any sampling from the basolateral compartment since the [Fe(CN)₆]^{3-/4-} concentration is determined *in situ*. Once the redox probe is added to the apical compartment, the assay runs completely automated without any interference by the operator or opening of the incubator door. This is very different from the optical readout as performed here and throughout the literature that requires repeated opening of the incubator and liquid handling in the lower compartment raising severe constraints to the time-resolution and to the reproducibility of the optical assay. Reducing the number of data points to a minimum is the only way to limit the invasiveness of these readout approaches but makes the readout prone to artefacts (Beasley *et al.* 2014; Kaiser *et al.* 2015; Sukma Dewi *et al.* 2017).

Tab. 5.5: Permeability coefficients P_E for the cell lines under study using [Fe(CN)₆]^{3-/4-} as a permeability probe (mean ± maximal error, n = 3). The results of the impedance-based P_E-assay are compared to P_E values obtained by measuring the [Fe(CN)₆]^{3-/4-} permeation rate by UV/VIS spectrophotometry as independent validation (Hajek Kathrin 2017).

cell line	P _E / ·10 ⁻⁶ cm/s		
	IDE-200	IDE-combi	optical
NRK	390 ± 93	710 ± 35	19 ± 8
MDCK-I	0.5 ± 0.2	0.6 ± 0.2	1 ± 3
MDCK-II	1.6 ± 0.5	3.4 ± 0.8	1 ± 3

To the best of our knowledge, no permeability studies using [Fe(CN)₆]^{3-/4-} as a permeability probe have been conducted and no P_E values for this probe have been reported so that a

direct comparison to other studies is impossible. However, we compared the $P_{E\text{TER}}$ -based permeability coefficients for $[\text{Fe}(\text{CN})_6]^{3-/4-}$ with data recorded for other commonly used probes for MDCK-II cells and found meaningful agreement that strongly supports the usefulness of the new assay (Tab. 5.6). Commonly used P_E probes differ with respect to their molecular mass and their charge. Whereas the dependence of P_E values on probe size has been systematically documented recently (Ghandehari *et al.* 1997; Hakvoort *et al.* 1998), we are not aware of any study that addresses the dependence of permeation rates on the net charge of the probe even though it is very likely to play a role. In terms of mass and charge fluorescein is the probe that is closest to $[\text{Fe}(\text{CN})_6]^{3-/4-}$ and the individual P_E values agree nicely within the limits of experimental errors. Fluorescein is supposed to pass cellular barriers predominantly across bicellular tight junctions (van Itallie *et al.* 2009). In contrast, the paracellular permeation of macromolecules across MDCK-II layers is mainly provided by large tricellular tight junctions (Krug *et al.* 2009a). The question whether $[\text{Fe}(\text{CN})_6]^{3-/4-}$ is transported primarily via bicellular or tricellular tight junctions cannot be addressed by the entirely integral $P_{E\text{TER}}$ -assay.

Taken together, the impedance-based permeability measurement provides reliable P_E estimates that agree favourably with measurements reported by others using conventional approaches. Moreover, the P_E values are supported by the parallel TER readings that provide consistent characterization of the individual epithelial barrier function. The novel technique provides online permeability monitoring and the extraction of time course data for the permeability coefficient that has not been reported before. The downside of the new assay at the current stage of development is the limited number of permeation probes. Fluorescence-based assays offer a pool of permeability probes with varying molecular mass from small molecules like fluorescein to macromolecules like FITC-dextran. This set of tracers enables systematic investigations of size-dependent molecular permeability across epithelial cell layers. Such a variety of probes is not yet available or identified for the impedance-based readout but a direction of future research. Another problem of *in vitro* permeability measurements in general is the potential impact of unstirred water layers on either side of the cell layer that build a second barrier to permeability probes and hence, may lead to an underestimation of P_E values (Youdim *et al.* 2003). Mild agitation of the incubation fluid on either side of the permeable support may solve this issue but the current setup is not yet compatible with that like most established P_E approaches.

Tab. 5.6: Permeability coefficients P_E for different permeability probes that are commonly used to characterize epithelial barrier function. All P_E values have been recorded for confluent MDCK-II cells grown on permeable supports from different manufacturers.

substrate	M / g/mol	charge	P _E / ·10 ⁻⁶ cm/s	reference
sucrose	342	0	0.11	(Amidon <i>et al.</i> 1999)
10kDa-FITC-dextran	10000	0	0.13 ± 0.03	(Krug <i>et al.</i> 2009a)
4kDa-FITC-dextran	4000	0	0.5 ± 0.1	(Krug <i>et al.</i> 2009a)
mannitol	182	0	2.5	(Amidon <i>et al.</i> 1999)
PEG-400	900	0	4.8 ± 0.5	(Krug <i>et al.</i> 2009a)
fluorescein	332	-2	5 ± 1	(Krug <i>et al.</i> 2009a)
[Fe(CN) ₆] ^{3-/4-}	212	-3/-4	1.6 ± 0.5	this work (IDE-200)
[Fe(CN) ₆] ^{3-/4-}	212	-3/-4	3.4 ± 0.8	this work (IDE-combi)

5.2 P_ETER-assay with spatially resolved readout

By increasing the number of gold electrodes deposited on the bottom of the basolateral compartment, the P_ETER-assay provides laterally resolved monitoring of the permeation of redox tracers across epithelial cell layers. Therefore, an electrode array that consists of six circular, co-planar gold electrodes (each Ø 1 mm) and a common counter electrode was used and denoted as 2W6x1E array (chapter 4.2.1, Fig. 4.7). In analogy to the P_ETER-setup with integral readout, a stainless steel dipping electrode reaching into the apical solution provides simultaneous monitoring of TER when used in combination with the common counter electrode in the basolateral compartment (chapter 4.2.2, Fig. 4.9B).

The P_ETER-device with spatially resolved readout has been originally introduced in 2017 (Hajek Kathrin 2017). However, some experimental details have been modified and enhanced in this thesis compared to the original version of the approach:

- (I) The material of the upper electrode was exchanged. A stainless steel dipping electrode was used instead of a gold dipping electrode to reduce the impact of faradaic currents on the total impedance data in TER-mode. This aspect has already been discussed in chapter 5.1.1.
- (II) The time-resolution of the impedance-based permeability assay was significantly improved. In the original approach, the entire frequency regime (1 Hz to 10⁵ Hz) was analyzed in both, P_E- and TER-mode, which means that seven complete impedance spectra were recorded for each time-point. Here, a complete impedance spectrum covering five frequency decades is only measured in TER-mode, whereas P_E-mode is run at one discrete frequency of 1 Hz. Thereby,

the time-resolution was enhanced from ~ 8 min to ~ 1 min. The improvement of time-resolution was achieved by a modification of the LabView™- and MATLAB-based data acquisition program which was written by Prof. Wegener.

- (III) Besides [Fe(CN)₆]^{3-/4-}, a second electroactive compound – ferrocenemethanol (FcMeOH) – was tested as a potential permeability probe in P_ETER-assays.

5.2.1 Characterization of the spatially resolved P_ETER-device

Analysis of P_E- and TER-mode in absence of electroactive compounds

Cell-free filter inserts were placed directly onto the planar electrode array to reduce lateral tracer diffusion within the basolateral compartment. The electrode layout consists of six individually addressable gold electrodes and a common counter electrode, all deposited on the bottom of the measurement chamber. A stainless steel electrode was dipped into the apical buffer (Fig. 5.8A). The impedance of the device was recorded in both, **P_E-mode: 1/2/3/4/5/6 vs. 7** and **TER-mode: 7 vs. 8**. Frequency spectra of the impedance magnitude |Z|, the resistance R and the capacitance C of both modes are presented in Fig. 5.8B-D. The impedance in both modes is dominated by the double layer capacitance of the electrode-electrolyte interface at low and middle frequencies (1 Hz - 10³ Hz), whereas the bulk resistance dominates the impedance at higher frequencies (10⁴ Hz - 10⁵ Hz). However, the impedance is significantly higher in P_E-mode, since the effective electrode area is lower compared to the electrode area that is involved in TER-mode. By equivalent circuit modeling, the elements of the equivalent circuit presented in chapter 3.1.2 (Fig. 3.3) are assessable and listed in Tab. 5.7. The bulk resistance is 6.5 times higher in P_E-mode than in TER-mode. The resistance R_{ins} and capacitance C_{ins} of the cell-free filter insert are only determined in TER-mode and have values of R_{ins} = (23 ± 16) Ωcm² and C_{ins} = (14.23 ± 0.00) μF/cm².

A striking difference between the integral and spatially resolved P_ETER-assays is the way of filter insertion into the measurement chamber. Whereas the receiver volume is well-defined by the Teflon® ring in the integral P_ETER-device, the cell-covered filter inserts are placed directly onto the electrode arrangement without using a Teflon® spacer in the spatially resolved approach. The removal of the spacer is crucial to ensure laterally resolved monitoring of tracer permeation across epithelial layers. As a consequence of the manufacturing process, each of the small electrodes provides its own receiver volume

defined by the back side of the filter membrane, the surface of the gold electrodes and the photopolymer that passivates the leads. These three entities define the receiver volume. However, the exact values for the individual receiver volumes are not assessable with our methods and hence, the spatially resolved P_E TER-assay provides relative rather than absolute permeability coefficients. Taken together, the P_E TER-approach offers relative information about local tracer permeation across epithelial cells and gives rise to time-resolved analysis of the kinetics of the epithelial permeability.

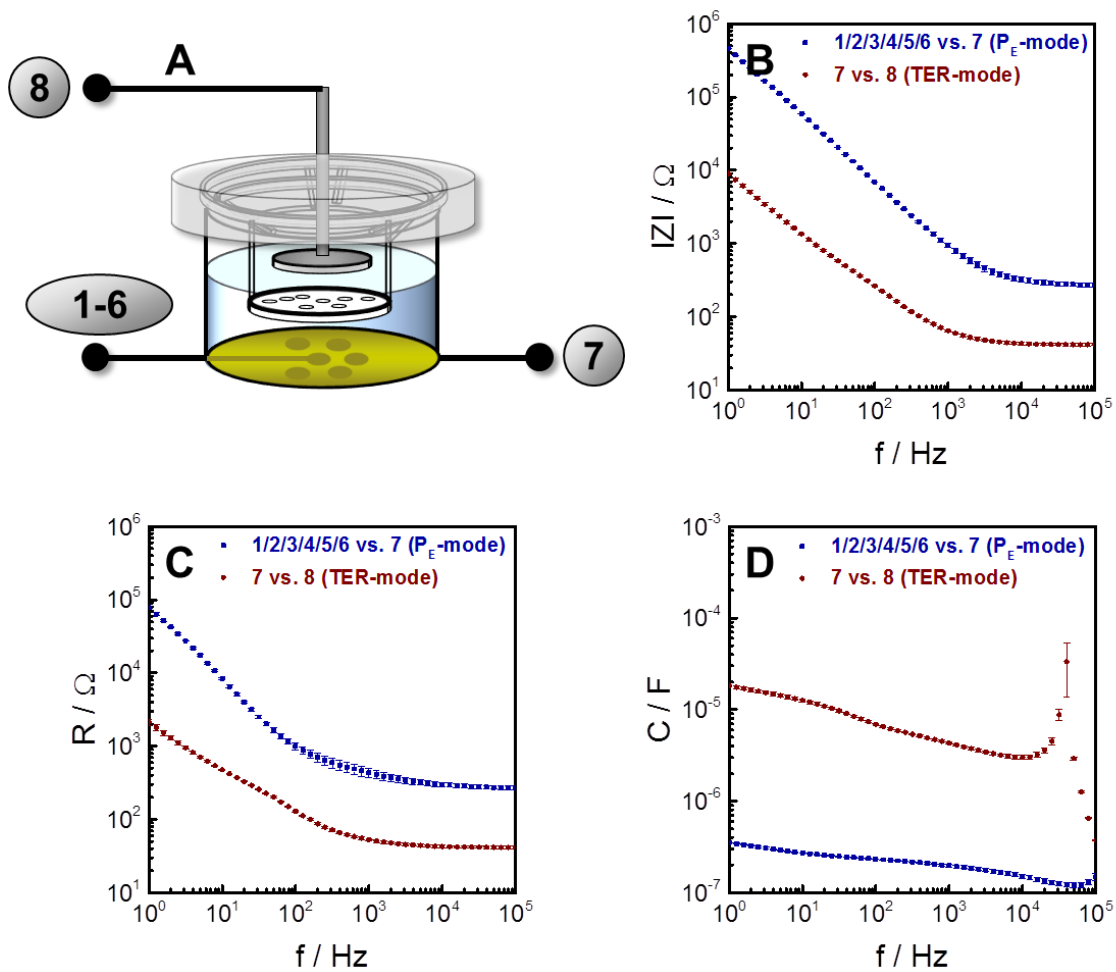


Fig. 5.8: (A) Schematic of the experimental setup for electrode characterization in the P_E TER-device using a 2W6x1E electrode array with small working electrodes of 1mm diameter. A cell-free filter insert is placed directly onto the bottom of the basolateral well. Spectra are shown as (B) impedance magnitude $|Z|$, (C) resistance R and (D) capacitance C for both measuring modes (mean \pm SE, $n = 6$).

Tab. 5.7: Values of the different circuit elements after equivalent circuit modeling of the data of Fig. 5.8 (mean ± SE, n = 6). The values have been recorded using a 2W6x1E electrode array. The resistance of the filter insert R_{ins} and the filter membrane capacitance C_{ins} are only determined for TER-mode.

parameter	P _E -mode (1/2/3/4/5/6 vs. 7)	TER-mode (7 vs. 8)
R _{bulk} / Ω	270 ± 15	42 ± 2
A _{CPE} / μFs ⁿ⁻¹	0.35 ± 0.01	16 ± 7
n _{CPE}	0.918 ± 0.007	0.81 ± 0.01
R _{ins} / Ωcm ²		23 ± 16
C _{ins} / μF/cm ²		14.23 ± 0.00

Analysis of P_E-mode in presence of electroactive compounds

As already mentioned above, the spatially resolved P_ETER-assay does not provide P_E values, since the receiver volume V_R is not known. Therefore, the accumulating tracer concentration c_R in the basolateral compartment cannot be transformed into the values of n_R. Nevertheless, the P_ETER-device with laterally resolved readout was calibrated by adding differently concentrated tracer solutions to the measurement chamber in absence of filter supports. For this purpose, the impedance was measured in P_E-mode over five decades (1 Hz – 10⁵ Hz) in presence of (0 – 1) mM [Fe(CN)₆]^{3-/4-} and (0 – 0.5) mM FcMeOH. Ferrocenemethanol was used in lower concentrations compared to the equimolar mixtures of ferri- and ferrocyanide due to a stronger cytotoxic impact on the cell lines that were used in this thesis (chapter 5.3). The frequency-dependent spectra of the inverse impedance magnitude are averaged for all six gold electrodes and presented in Fig. 5.9A/C for [Fe(CN)₆]^{3-/4-} or FcMeOH, respectively. The inverse impedance magnitude is not affected by the presence of the redox compounds at higher frequencies (10³ Hz – 10⁵ Hz), because the impedance is dominated by the resistance of the buffer at these frequencies. The impact of the electroactive species is visible at low frequencies from 1 Hz to 100 Hz. It is striking that [Fe(CN)₆]^{3-/4-} exerts a significant stronger influence to the impedance compared to FcMeOH. The corresponding values of 1/|Z|_{1Hz} for each individual concentration of both redox tracers are listed in Tab. 5.8. Plotting 1/|Z| as a function of [Fe(CN)₆]^{3-/4-} or FcMeOH concentration, respectively, yields a strictly linear correlation (R² = 0.999) with a slope of (56.6 ± 0.9) μS/mM for [Fe(CN)₆]^{3-/4-} and (13.2 ± 0.1) μS/mM for FcMeOH (Fig. 5.9B/D).

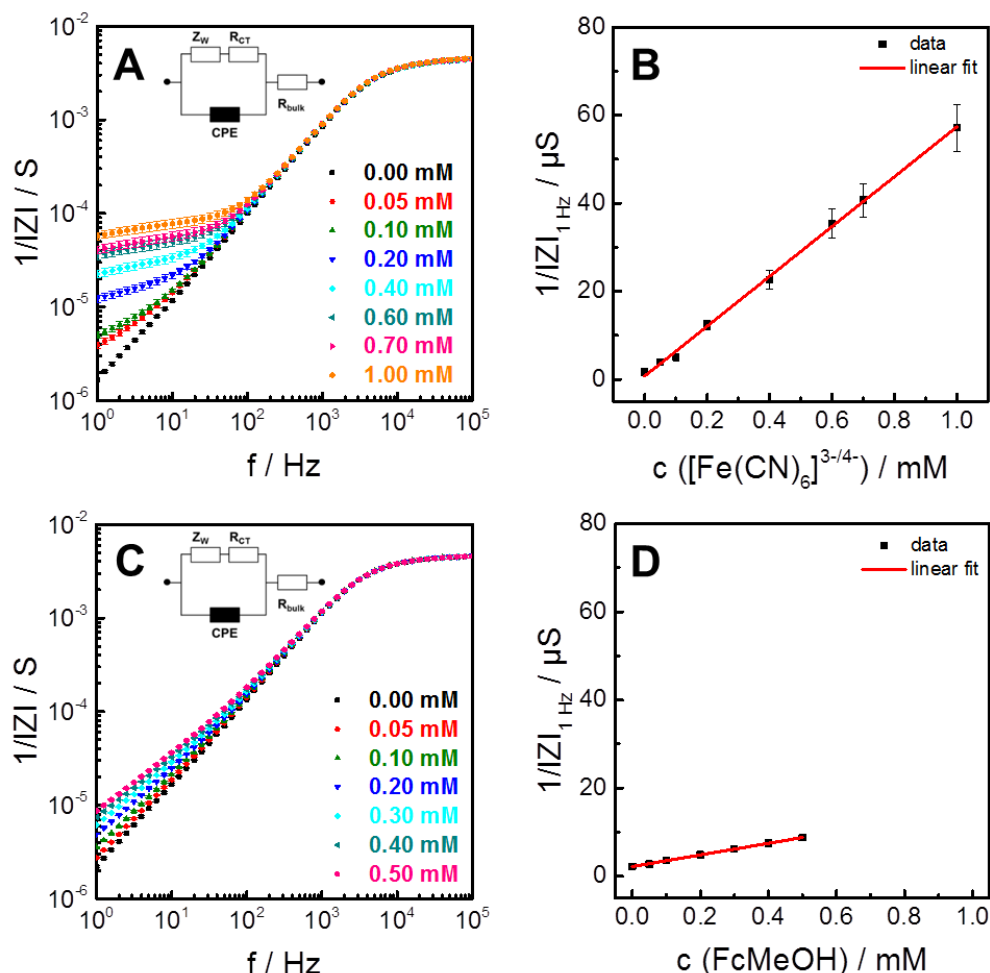


Fig. 5.9: Frequency spectra of the inverse impedance magnitude (P_E-mode, mean ± SE, n = 6) in presence of variable (A) [Fe(CN)₆]^{3-/4-} and (C) FcMeOH concentrations recorded with the 2W6x1E electrode array. There is a linear correlation between 1/|Z|_{1Hz} and (B) [Fe(CN)₆]^{3-/4-} as well as (D) FcMeOH concentration. The linearity between 1/|Z|_{1Hz} and tracer concentrations is analyzed by linear regression: [Fe(CN)₆]^{3-/4-}: slope = (56.6 ± 0.9) μS/mM; y-intercept = (0.7 ± 0.5) μS; R² = 0.999; FcMeOH: slope = (13.2 ± 0.1) μS/mM; y-intercept = (2.18 ± 0.04) μS; R² = 0.999.

Tab. 5.8: Inverse impedance magnitudes at 1 Hz in response to different [Fe(CN)₆]^{3-/4-} or FcMeOH concentrations, respectively, for the 2Wx61E electrode array (P_E-mode, mean ± SE, n = 6).

c([Fe(CN) ₆] ^{3-/4-} / mM	1/ Z _{1Hz} / μS	c(FcMeOH) / mM	1/ Z _{1Hz} / μS
0.00	1.66 ± 0.04	0.00	2.21 ± 0.04
0.05	3.9 ± 0.3	0.05	2.73 ± 0.04
0.10	5.0 ± 0.4	0.10	3.53 ± 0.04
0.20	12 ± 1	0.20	4.87 ± 0.04
0.40	23 ± 2	0.30	6.18 ± 0.05
0.60	35 ± 3	0.40	7.46 ± 0.05
0.70	41 ± 4	0.50	8.73 ± 0.06
1.00	57 ± 5		

The bottom line of the comparison between the two redox probes is that [Fe(CN)₆]^{3-/4-} is the redox tracer of choice for the P_ETER-assay as it has several important advantages:

- (I) As mentioned above, the slope of the calibration describes the sensitivity of the measurement for a given redox tracer in the P_ETER-assay. The slope, i.e. the sensitivity for the detection of the redox tracer in the basolateral compartment, is four times higher for the equimolar mixtures of ferri- and ferrocyanide compared to FcMeOH.
- (II) In addition, [Fe(CN)₆]^{3-/4-} has no cytotoxic impact which will be shown and discussed in chapter 5.3. In contrast, FcMeOH has some significant influences on the cell lines under study at higher concentrations.
- (III) Whereas [Fe(CN)₆]^{3-/4-} permeates across epithelial barriers exclusively via passive paracellular diffusion, FcMeOH is suspected to permeate through a cell layer on both, para- and transcellular pathways. The exact transepithelial transport route is connected, among others, to the lipophilicity of the permeability probe. FcMeOH is significantly more lipophilic than [Fe(CN)₆]^{3-/4-} (Bergner *et al.* 2012).

The presence of the redox tracers induces an electron exchange between the electrode and the electroactive species in solution. As already explained in chapter 5.1.1, faradaic effects - R_{CT} and Z_W (insert in Fig. 5.9A/C) – influence the recorded impedance at low frequencies. The influence of [Fe(CN)₆]^{3-/4-} on the inverse impedance magnitude at lower frequencies (1 Hz to 100 Hz) is much more pronounced than the impact of FcMeOH. For example, a 0.4 mM solution of the different redox species leads to values of (23 ± 2) μS for [Fe(CN)₆]^{3-/4-} and (7.46 ± 0.05) μS for FcMeOH. The different impact of [Fe(CN)₆]^{3-/4-} and FcMeOH to the impedance spectra may be due to a different rate of the electron transfer between the redox species in solution and the surface of the gold electrodes. The electron transfer is known to exhibit fast reversible kinetics in terms of FcMeOH with an apparent charge-transfer rate constant k_{app} of (19 ± 2) · 10⁻³ cm/s (Karimi Shervedani *et al.* 2011). The electron exchange is reported to be clearly slower for [Fe(CN)₆]^{3-/4-} with a value of (1.93 ± 0.02) · 10⁻³ cm/s (Nkosi *et al.* 2010). Besides R_{CT}, also the Warburg impedance Z_W

plays an important role. As equation 3.22 reveals (chapter 3.1.3), the Warburg coefficient σ is influenced by diverse parameters, but only the diffusion coefficients are different for $[Fe(CN)_6]^{3-/4-}$ ($6.4 \cdot 10^{-6} \text{ cm}^2/\text{s}$ in aqueous solution (Kasem 2006)) and FcMeOH ($7.9 \cdot 10^{-6} \text{ cm}^2/\text{s}$ in aqueous solution (Sun and Mirkin 2006)).

5.2.2 Investigation of epithelial monolayers expressing a broad range of barrier tightness

The $P_{E}TER$ -assay with spatially resolved readout was performed with confluent monolayers of different tightness (NRK \ll MDCK-II $<$ MDCK-I). The impedance was monitored at 1 Hz in P_E -mode and from 1 Hz to 10^5 Hz in TER-mode. At time zero, the redox probes, either 1 mM $[Fe(CN)_6]^{3-/4-}$ or 0.5 mM FcMeOH, were added to the apical solution. Using different concentrations of $[Fe(CN)_6]^{3-/4-}$ and FcMeOH is based on their different cytotoxic impact on the cell lines under study (chapter 5.3). Effects arising from liquid handling have been experimentally ruled out, since an apical buffer exchange does not alter the inverse impedance magnitude at 1 Hz significantly (appendix: Fig. 11.7). The following paragraphs show exemplary data with typical time courses of $1/|Z|_{1\text{Hz}}$ and TER for all three cell lines and both redox tracers.

Spatially resolved $P_{E}TER$ -assay using $[Fe(CN)_6]^{3-/4-}$ as permeability probe

Simultaneous monitoring of substrate and ionic permeability across differently tight cell layers is illustrated in Fig. 5.10. A rough estimate of the filter position is indicated by a white, dashed circle. The six gold electrodes deposited on the bottom of the measurement chamber are color-coded (Fig. 5.10A).

The TER value of NRK cells is $11.4 \text{ } \Omega\text{cm}^2$ at $t = 0 \text{ min}$ and remains stable throughout the entire measurement (Fig. 5.10B). The time-courses of $1/|Z|_{1\text{Hz}}$ of the six, laterally distributed electrodes that are used for permeation monitoring have all in common that the signal increases drastically after tracer addition to the apical compartment above NRK cell layers levelling off into saturation after 15 minutes. However, the saturated $1/|Z|_{1\text{Hz}}$ values that are recorded for the six working electrodes are not identical which is inconsistent with the expectations. After establishing equilibrium, the inverse impedance magnitudes are thought to be in the same range, but obviously the different electrodes show different equilibrated $1/|Z|_{1\text{Hz}}$ values. Electrodes **1 / 2 / 3 / 6** reveal $1/|Z|_{1\text{Hz}}$ values that are in the same range,

whereas electrodes **4** / **5** indicate significant lower or higher values, respectively. The inverse impedance magnitude recorded for **electrode 4** is only 4.9 μS at t = 60 min which is significantly less than expected. This reduced P_E signal increase may be due to a shifted position of the filter insert in the measurement chamber. The edge of the filter membrane that is linked to a plastic scaffold may be accidentally placed above **electrode 4** pretending a reduced [Fe(CN)₆]^{3-/4-} permeation of the corresponding region within the NRK layer. Nevertheless, the increased tracer permeation above **electrode 5**, indicated by an overall 1/|Z|_{1Hz} change of 19.0 μS, cannot be explained by a shifted position of the filter support. However, the different time-courses of 1/|Z|_{1Hz} recorded for a cell-free insert with the spatially resolved P_ETER-assay are also significantly different (appendix: Fig. 11.8). The equilibrated 1/|Z|_{1Hz} values measured with the six laterally distributed electrodes range from 25 μS to 60 μS. Thus, the differences of the overall changes of 1/|Z|_{1Hz} for NRK cell layers are rather due to different electrode conditions than to heterogeneous barrier function. However, a comparison between the time-dependent changes of 1/|Z|_{1Hz} for NRK barriers and a cell-free membrane reveals a slight, but distinct barrier function of NRK cells to [Fe(CN)₆]^{3-/4-}.

The transepithelial electrical resistance of the MDCK-II monolayer is 61.0 Ωcm² at t = 0 min (Fig. 5.10C). The addition of [Fe(CN)₆]^{3-/4-} does not have a significant impact on ionic permeability, since TER has still a magnitude of 57.9 Ωcm² after one hour of tracer incubation. The linear time-courses of the inverse impedance magnitude suggest heterogeneities of [Fe(CN)₆]^{3-/4-} permeation across the MDCK-II cell layer. For example, the area of the cell layer located above **electrode 6** appears to be leakier compared to the region above **electrode 4**, as the the slope of the initial change of the inverse impedance magnitude is (0.132 ± 0.001) μS/min at **electrode 6** and only (0.0312 ± 0.0003) μS/min at **electrode 4**. As already mentioned above, the differences of the time-courses of 1/|Z|_{1Hz} are due to both, heterogeneous barrier function within one monolayer and the different electrode conditions that read different 1/|Z|_{1Hz} values for the same [Fe(CN)₆]^{3-/4-} concentration.

The MDCK-I monolayer (Fig. 5.10D) constitutes an extremely tight barrier, as indicated by the TER value of 4029 Ωcm² prior to tracer addition. Subsequently, TER reaches a maximum of 5218 Ωcm² after 21 minutes, before it is in turn decreasing to 4654 Ωcm² at t = 60 min. The immense tightness of the cell layer is also reflected in the time-courses of 1/|Z|_{1Hz}. The signals remain constant in a range from 1.3 μS to 1.7 μS for all six electrodes indicating that the MDCK-I layer effectively impedes [Fe(CN)₆]^{3-/4-} permeation and that the sensitivity of the spatially resolved P_ETER-device is not high enough to detect the very small tracer

concentration in the basolateral compartment. This is in contrast to the P_ETER-device with integral readout.

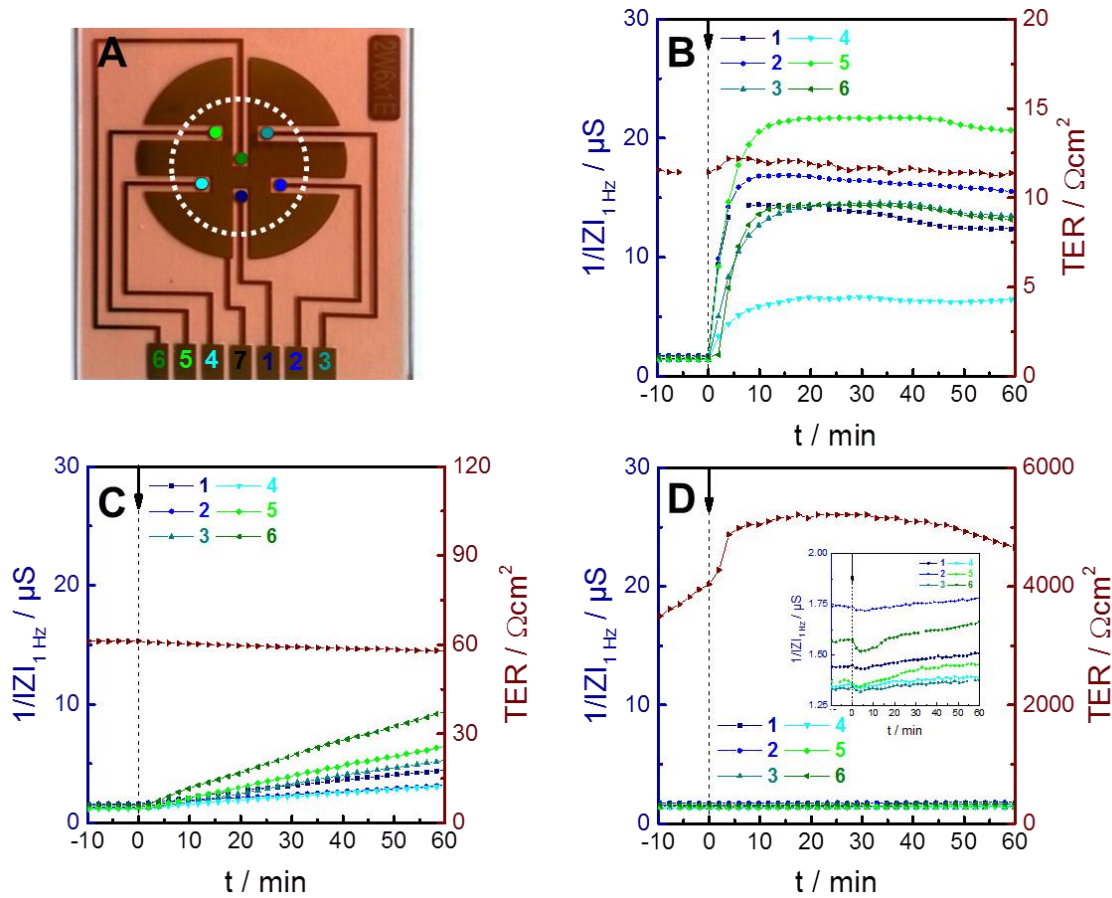


Fig. 5.10: P_ETER-assay with differently tight epithelial monolayers recorded with (A) a 2W6x1E electrode array providing laterally resolved monitoring of tracer permeation. The six gold electrodes that are located at the bottom of the basolateral compartment are color-coded and the approximate filter position is indicated by a white, dashed circle. (B) NRK, (C) MDCK-I and (D) MDCK-II cells are incubated with 1 mM [Fe(CN)₆]^{3-/4-} at time zero. Tracer accumulation in the basolateral compartment is followed at variable locations underneath the cell layer by monitoring 1/|Z|_{1Hz} of the individual gold electrodes (P_E-mode). The transfilter measurement (TER-mode) is used to record the TER of the same monolayer simultaneously using the apical dipping electrode and the common counter electrode in the basolateral compartment.

Tab. 5.9: Individual and averaged initial slopes of the increase of 1/|Z|_{1Hz} as an estimate of local permeability (mean ± SE, n = 6) recorded with the spatially resolved P_ETER-device using 1 mM [Fe(CN)₆]^{3-/4-} as the permeability probe.

cell line	$\Delta 1/ Z _{1\text{Hz}} / \mu\text{S}$						mean ± SE
	1	2	3	4	5	6	
NRK	3.0 ± 0.6	3.2 ± 0.6	1.78 ± 0.04	0.8 ± 0.1	3.4 ± 0.3	2.3 ± 0.3	2.4 ± 0.4
MDCK-II	0.049 ±	0.0247 ±	0.0712 ±	0.0312 ±	0.0888 ±	0.132 ±	0.07 ±
MDCK-I	0.00125 ±	0.00104 ±	0.00083 ±	0.00094 ±	0.0020 ±	0.0024 ±	0.0014 ±
	0.00005	0.00004	0.00003	0.00006	0.0001	0.0001	0.0003

The TER values that are extracted from the spatially resolved P_E TER-studies fit well to other reported TER values for the cell lines under study (Tab. 5.4). The order of the transepithelial electrical resistances NRK < MDCK-II < MDCK-I perfectly reflects the different tightness of the individual cell layers. The different initial slopes of the time-dependent $1/|Z|_{1\text{Hz}}$ increase (Tab. 5.9), which is a relative estimate of local permeability, are consistent with these findings, proving the rationale of the impedance-based permeability assay.

Cellular monolayers grown on permeable filter supports are known to form differently tight areas within one layer (Wegener and Seebach 2014). Therefore, barrier function is not homogeneous, but is characterized by certain heterogeneities or even defect spots, when cultured on filter supports. Most of the established permeability assays share a completely integral readout. However, heterogeneously tight cell layers may subvert permeability measurements and may lead to severe overestimation of P_E values or underestimation of TER values, respectively. The spatially resolved P_E TER-approach provides monitoring of tracer permeation across epithelial barriers with lateral resolution and hence, represents a powerful tool for the identification of such heterogeneities or even small defect spots. The results of Fig. 5.10C confirm this claim, as significant differences in the initial slopes of the time-dependent $1/|Z|_{1\text{Hz}}$ increase are observable for one and the same cell layer. The potential of the P_E TER-assay to localize even small defect spots within epithelial layers was shown recently by our lab (Hajek Kathrin 2017). Similar observations have been reported by another lab (Klusmeier *et al.* 2019). They examined the spatially dependent permeation of a FITC-dextran and albumin across endothelial barriers using a TIRF-based readout. Distinct heterogeneities in substrate permeability were uncovered throughout the entire cell layer as well as for the periphery of single cells alone. These findings are in perfect agreement with the results of the P_E TER-approach with lateral resolution.

Spatially resolved P_E TER-assay using FcMeOH as permeability probe

Besides $[\text{Fe}(\text{CN})_6]^{3-/4-}$, a second potential redox probe - ferrocenemethanol - was tested (Fig. 5.11). Therefore, P_E TER-assays with lateral resolution were performed using three cell lines with different barrier function. A rough estimate of the filter position is indicated by a white, dashed circle. The six gold electrodes deposited on the bottom of the measurement chamber are color-coded (Fig. 5.11A).

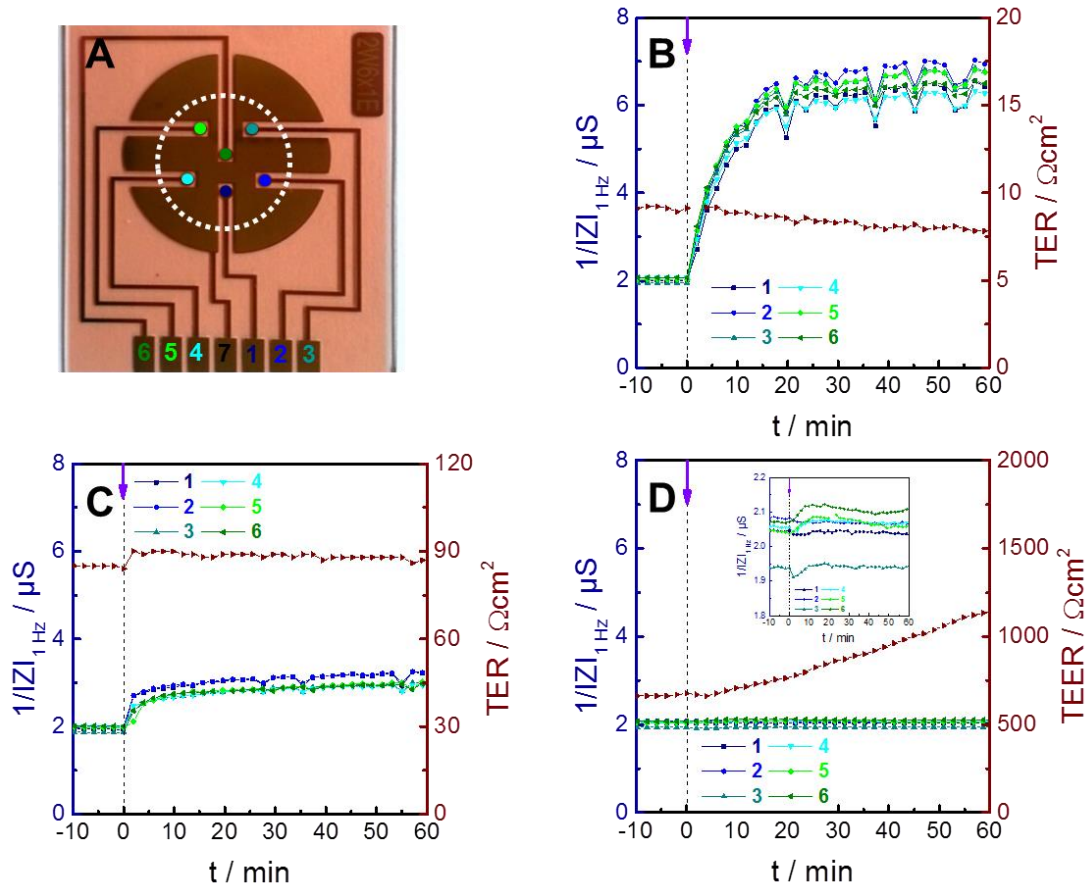


Fig. 5.11: P_ETER-assay with differently tight epithelial monolayers recorded with **(A)** a 2W6x1E electrode array providing laterally resolved monitoring of tracer permeation. The six gold electrodes that are located at the bottom of the basolateral compartment are color-coded and the approximate filter position is indicated by a grey, dashed circle. **(B)** NRK, **(C)** MDCK-I and **(D)** MDCK-II cells are incubated with **0.5 mM FcMeOH** at time zero. Tracer accumulation in the basolateral compartment is followed at variable locations underneath the cell layer by monitoring $1/|Z|_{1\text{Hz}}$ of the individual gold electrodes (P_E-mode). The transfilter measurement (TER-mode) using the apical dipping electrode and the common counter electrode in the basolateral compartment provides the TER of the same monolayer simultaneously.

Tab. 5.10: Individual and averaged initial slopes of the increase of $1/|Z|_{1\text{Hz}}$ as an estimate of local permeability (mean \pm SE, n = 6) recorded with the spatially resolved P_ETER-device using 0.5 mM FcMeOH as the permeability probe.

cell line	$\Delta 1/ Z _{1\text{Hz}} / \mu\text{S}$						mean \pm SE
	1	2	3	4	5	6	
NRK	0.41 ± 0.03	0.489 ± 0.001	0.501 ± 0.004	0.439 ± 0.004	0.52 ± 0.03	0.52 ± 0.04	0.52 ± 0.04
MDCK-II	0.2 ± 0.1	0.21 ± 0.09	0.17 ± 0.05	0.14 ± 0.04	0.14 ± 0.04	0.14 ± 0.03	0.14 ± 0.03
MDCK-I	0.0007 ± 0.0002	0.0003 ± 0.0003	0.0022 ± 0.0003	0.0046 ± 0.0004	0.0046 ± 0.004	0.0056 ± 0.0009	0.0026 ± 0.0009

NRK cells show an instant increase of the inverse impedance magnitude for all six working electrodes. For example, from **electrode 2** shows a signal increase from 2.0 μS (t = 0 min) to

6.3 μS ($t = 15 \text{ min}$) (Fig. 5.11B). TER shows a minor decrease from $9.1 \Omega\text{cm}^2$ ($t = 0 \text{ min}$) to $7.7 \Omega\text{cm}^2$ ($t = 60 \text{ min}$).

MDCK-II cells indicate an unexpected response to FcMeOH exposition (Fig. 5.11C). A slight increase of $1/|Z|_{1\text{Hz}}$ is observable for **electrode 2** from $2.0 \mu\text{S}$ ($t = 0 \text{ min}$) to $2.8 \mu\text{S}$ ($t = 5 \text{ min}$) instantaneously after FcMeOH addition. Afterwards, only slight changes of $1/|Z|_{1\text{Hz}}$ are visible resulting in a value of $3.2 \mu\text{S}$ after one hour of tracer incubation for **electrode 2**. The time-courses of the inverse impedance magnitude of the other working electrodes are similar indicating a homogeneous barrier function of the MDCK-II layer under study. The simultaneously measured TER is $84.7 \Omega\text{cm}^2$ at time point zero and remains constant during the entire measurement.

In case of an MDCK-I cell layer (Fig. 5.11D), no noteworthy change of $1/|Z|_{1\text{Hz}}$ is observable after FcMeOH addition. The signal stays constant at around $2 \mu\text{S}$. TER shows a continuous increase after tracer application from $676 \Omega\text{cm}^2$ ($t = 0 \text{ min}$) to $1148 \Omega\text{cm}^2$ ($t = 60 \text{ min}$).

The advantages of $[\text{Fe}(\text{CN})_6]^{3-/4-}$ over FcMeOH as the redox tracer in P_ETER-assays were already discussed in chapter 5.2.1. The results of Fig. 5.11C provide another argument for selecting $[\text{Fe}(\text{CN})_6]^{3-/4-}$ as the favored permeability probe. FcMeOH may permeate the MDCK-II barrier on a transcellular transport route directly after addition, as it is indicated by the rapid increase of $1/|Z|_{1\text{Hz}}$. However, the P_E signal does not change after a few minutes of incubation time which may be a hint that the lipophilic FcMeOH accumulates within the lipophilic plasma membrane leading to a reduced permeation rate (Bergner *et al.* 2012). The order of barrier tightness $\text{NRK} < \text{MDCK-II} < \text{MDCK-I}$ is also reflected in the initial slopes of the time-dependent increase of $1/|Z|_{1\text{Hz}}$ (Tab. 5.10) using FcMeOH as the redox probe.

A striking difference between the integral and the laterally resolved readout of the P_ETER-assay is the differently sensitive detection of $[\text{Fe}(\text{CN})_6]^{3-/4-}$ in the basolateral compartment. The integral approach using interdigitated gold electrodes provides a 20 times higher sensitivity for $[\text{Fe}(\text{CN})_6]^{3-/4-}$ detection when IDE-200 is compared to the 2W6x1E electrode array. This P_E sensitivity difference is reflected by the different slopes of the calibration plots (chapter 5.1.1 and 5.2.1, Fig. 5.3 and Fig. 5.9) with a slope of $(1142 \pm 15) \mu\text{S}/\text{mM}$ for IDE-200 or $(56.6 \pm 0.9) \mu\text{S}/\text{mM}$ for the 2W6x1E electrode array, respectively. The consequences of the impaired sensitivity for the assay with lateral resolution are reflected in the time-dependent changes of $1/|Z|_{1\text{Hz}}$ that were observed for MDCK-I monolayers. Whereas

$1/|Z|_{1\text{Hz}}$ shows a clear increase in the integral approach (Fig. 5.7), the signal does not alter significantly in the laterally resolved method (Fig. 5.10C).

5.2.3 Investigation of mixed but segregated epithelial layers

Besides the P_ETER-studies using uniform monolayers, also mixed but segregated cell layers were analyzed with the spatially resolved P_ETER-assay to highlight the lateral resolution of the device. Therefore, different combinations of NRK, MDCK-I and MDCK-II cells were examined. The impedance was measured at 1 Hz in P_E-mode and from 1 Hz to 10⁵ Hz in TER-mode. At time zero, the redox probe [Fe(CN)₆]^{3-/4-} was added to the apical compartment either in a concentration of 0.5 mM or 1 mM. Please note that tracer concentration was reduced, when leaky NRK cells were involved in the mixed cell layer to allow an improved discrimination between the differently tight cell lines.

Fig. 5.12A shows the spatially resolved tracer permeation across the mixed but segregated cell layers as well as the integral TER values that were recorded simultaneously. The individual impedance raw data recorded in TER-mode is displayed in Fig. 5.12B. In addition, the impedance raw data of the corresponding uniform monolayers is shown in the plots. Please note that the TER-measurements of the uniform cell layers were performed separately and are thought to provide a better evaluation of the impedance spectra of the mixed cell layer. To yield a better overview about the exact orientation of the cell layers, the individual electrodes are assigned to their overlying cell type by a color code in Fig. 5.12C.

MDCK-I / MDCK-II cell layer

The MDCK-I and MDCK-II covered membrane areas are clearly discriminable. The inverse impedance magnitude is increasing for electrode 5 from 1.9 μS (t = 0 min) to 5.4 μS (t = 30 min) and for electrode 6 from 2.0 μS (t = 0 min) to 5.3 μS (t = 30 min). Both electrodes are located beneath moderately tight MDCK-II cells. The MDCK-II dominated region above electrode 3 indicates a stronger barrier to the redox tracer with an overall signal change of only 0.8 μS. However, even this tighter area of MDCK-II cells is distinguished from the MDCK-I covered regions. All three electrodes that are located beneath MDCK-I domains reveal only a slight increase of $1/|Z|_{1\text{Hz}}$. For example, electrode 4 shows an increase of $1/|Z|_{1\text{Hz}}$ from 1.9 μS to 2.2 μS after 30 minutes. The TER of the MDCK-I / MDCK-II layer is a mixture of the corresponding individual TER values with a value of around 200 Ωcm². The

addition of the redox tracer has no negative impact on barrier integrity of the mixed cell layer as TER remains constant over time. Typical TER values for the uniform monolayers of the cell lines under study are summarized in Tab. 5.4.

NRK / MDCK-II cell layer

Areas covered with leaky NRK cells indicate completely different tracer permeability compared to MDCK-II covered regions. Electrodes 1/2/4 show an instant increase of $1/|Z|_{1\text{Hz}}$ after $[\text{Fe}(\text{CN})_6]^{3-/4-}$ addition with the highest signal change for electrode 2 from 2 μS ($t = 0$ min) to 20 μS ($t = 30$ min). The inverse impedance magnitudes for these electrodes run all into a saturation after around 10 minutes. In contrast, electrodes 3/5/6 which are located beneath MDCK-II dominated zones show only a moderate increase of the inverse impedance magnitude. The leakiest part of the MDCK-II domain resides above electrode 6 with a total increase of 10.1 μS at $t = 30$ min. The transepithelial electrical resistance of around 43 Ωcm^2 for the NRK / MDCK-II cell layer is a mixture of the values for uniform NRK and MDCK-II layers (Tab. 5.4).

NRK / MDCK-I cell layer

It is also possible to distinguish between NRK and MDCK-I covered membrane areas. The situation resembles the results for mixed NRK / MDCK-II cell layers. NRK-covered regions of the filter support show a rapid increase of the inverse impedance magnitude indicating high $[\text{Fe}(\text{CN})_6]^{3-/4-}$ permeability. The leakiest zone of the mixed epithelial barrier is located above electrode 2 with a signal gain from 3.1 μS ($t = 0$ min) to 28.8 μS ($t = 30$ min). The change of $1/|Z|_{1\text{Hz}}$ of electrode 3 and electrode 5 is muted fitting to the strong barrier function of MDCK-I cells. Nevertheless, higher substrate permeability is observed for electrode 6 with an overall increase of 14.8 μS . This zone is still tighter than pure NRK barriers, but has a strongly impaired barrier function compared to uniform MDCK-I monolayers. The TER of a NRK / MDCK-I cell layer is strongly dominated by the leaky NRK cells with a value of around 30 Ωcm^2 within the incubation time.

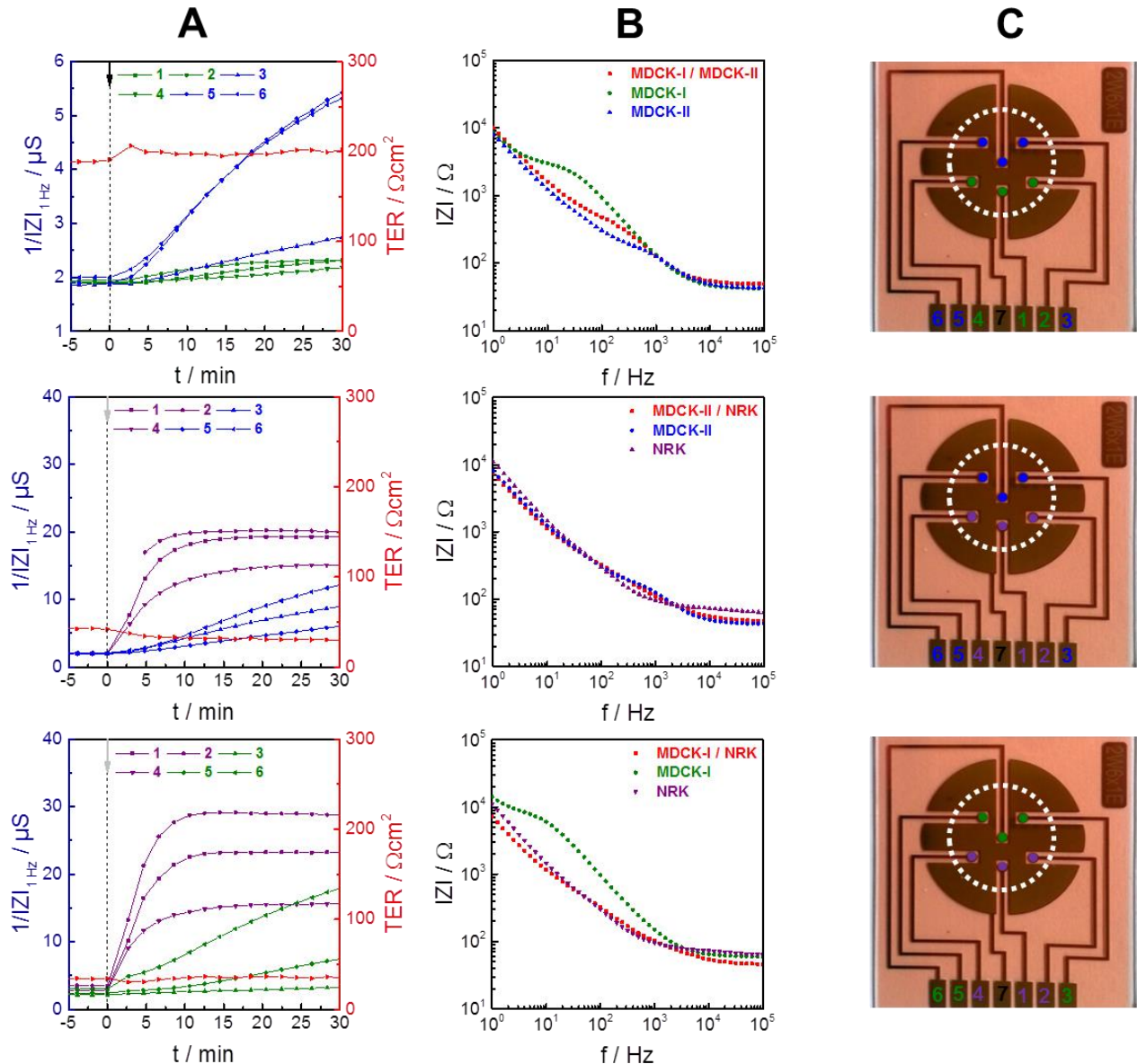


Fig. 5.12: (A) P_ETER-assay with mixed but segregated cell layers recorded with a 2W6x1E electrode array providing laterally resolved monitoring of tracer permeation. **0.5 mM** or **1 mM** $[\text{Fe}(\text{CN})_6]^{3-/4-}$, respectively, are added to the apical compartment at $t = 0$ min. Tracer accumulation in the basolateral compartment is followed over time with lateral resolution by monitoring time-dependent changes of $1/|Z|_{1\text{Hz}}$ of the six laterally distributed gold electrodes (P_E-mode). TER of the same cell layer is recorded simultaneously (TER-mode). (B) Impedance raw spectra of the mixed cell layers and of their corresponding uniform monolayers recorded in TER-mode. Please note that the impedance spectra of the uniform cell layers were recorded separately. (C) Images of a 2W6x1E array and the cell distribution above the electrode structure. The position of the filter insert is roughly indicated by a white, dashed circle. The location of the different cell types is color coded (NRK, MDCK-I, MDCK-II).

5.3 Cytotoxicity studies of the redox tracers [Fe(CN)₆]^{3-/4-} and FcMeOH

A prerequisite for the feasibility of impedance-based permeability measurements is an appropriate, non-cytotoxic permeability probe. Any cytotoxic influences of the redox tracer have to be excluded to ensure barrier integrity and reliable monitoring of tracer permeability. Therefore, the of the two applied redox tracers ([Fe(CN)₆]^{3-/4-}, FcMeOH) impact on the cells under study was analyzed by two different established techniques:

- (I) Possible negative effects on mitochondrial activity were examined by *PrestoBlue*[®]-assays that are classified as typical end-point assays.
- (II) ECIS-cytotoxicity studies provide online monitoring of cytotoxic effects and hence, allow a more detailed investigation.

The results of these two different cytotoxicity studies are described in the next paragraphs.

PrestoBlue[®]-assays using NRK, MDCK-I and MDCK-II cells

PrestoBlue[®]-assays were conducted with confluent layers of NRK, MDCK-I and MDCK-II cells. [Fe(CN)₆]^{3-/4-} was tested in a concentration range from (0 – 10) mM. In case of FcMeOH a concentration window from (0 – 5) mM was investigated. The cell layers were incubated with the different tracer solutions for three hours. Please note that the typical measurement time in P_ETER-assays is only one hour. Every assay included a negative control (PBS⁺⁺/glucose (1 g/L)) and a positive control (0.5 % (v/v) Triton-X-100 in PBS⁺⁺/glucose (1 g/L)). The final readout parameter is referred to as *cytotoxic index* CI [in %] which is calculated from the corrected fluorescence intensity of the negative control F_0 and the corrected fluorescence intensity of the corresponding sample F_x :

$$CI = \left(1 - \frac{F_x}{F_0}\right) \times 100\% \quad (5.1)$$

Consequently, a low CI value is an indicator for negligible influences on mitochondrial activity. The cytotoxic indices are plotted as a function of tracer concentration (Fig. 5.13).

1 mM $[\text{Fe}(\text{CN})_6]^{3-/4-}$ exerts no significant influences on NRK cells (Fig. 5.13A). The incubation with a 9 mM solution results in a CI value of $(16 \pm 4) \%$. A similar trend is observed MDCK-I cells (Fig. 5.13B). For the concentrations (0.05 - 5) mM, the cytotoxic indices are lower than 10 %. The exposure to a 9 mM solution yielded higher CI values of $(25 \% \pm 5 \%)$. The highest cytotoxic index $(30 \% \pm 10 \%)$ is determined for MDCK-II cells when applying a 10 mM solution (Fig. 5.13C). However, no significant CI values are observable for 1 mM $[\text{Fe}(\text{CN})_6]^{3-/4-}$ which is the relevant concentration in P_ETER-measurements.

The incubation with FcMeOH leads to even smaller CI values compared to the equimolar mixtures of ferri- and ferrocyanide. In case of NRK cells (Fig. 5.13D), the highest CI value is determined for a 5 mM solution $(11 \% \pm 2 \%)$. The CI values for MDCK-I cells are throughout slightly negative indicating no negative impact on the mitochondrial activity at all (Fig. 5.13E). The cytotoxic indices for MDCK-II cells are also continuously close to zero (Fig. 5.13F). No significant CI values are determined for 0.5 mM FcMeOH which is the applied tracer concentration in P_ETER-assays.

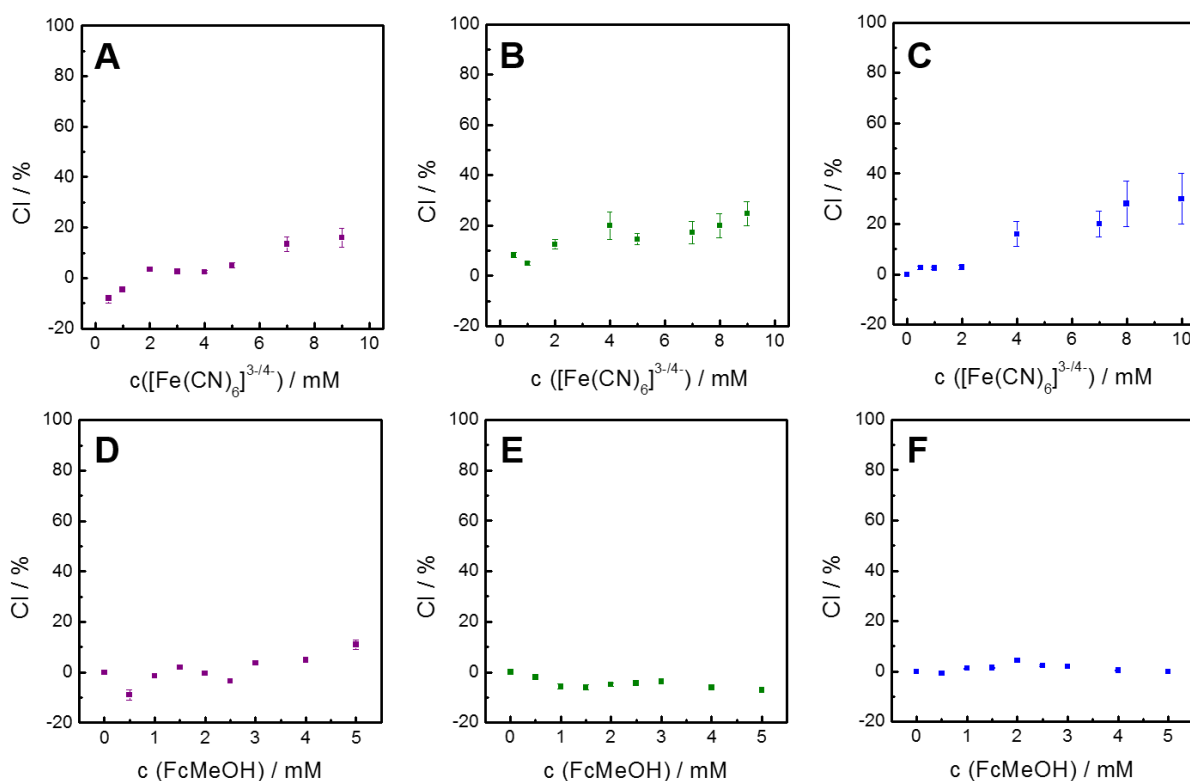


Fig. 5.13: Results of the PrestoBlue[®]-assays for the investigation of possible cytotoxic influences of **(A,B,C)** $[\text{Fe}(\text{CN})_6]^{3-/4-}$ (mean \pm SE, $n = 8$) and **(D,E,F)** FcMeOH (mean \pm SE, $n = 6$) on the cell lines under study (**NRK**, **MDCK-I**, **MDCK-II**). The individual cell monolayers are incubated for three hours with the different tracer solutions. The positive controls provide cytotoxic indices above 85 % in all cases (data not shown).

Tab. 5.11: Cytotoxic indices CI for the two redox tracers and the cell lines under study. The given CI refers to the tracer concentration as it is applied in P_ETER-assays: 1 mM [Fe(CN)₆]^{3-/4-} (mean ± maximal error, n = 8) and 0.5 mM FcMeOH (mean ± maximal error, n = 6). The incubation time was, however, three hours instead of one hour, as it is performed in P_ETER-assays.

redox tracer	cell line	CI _{relevant} / %
[Fe(CN) ₆] ^{3-/4-}	NRK	-5 ± 1
	MDCK-I	5 ± 1
	MDCK-II	3 ± 1
FcMeOH	NRK	-9 ± 2
	MDCK-I	-2 ± 1
	MDCK-II	-1 ± 1

The results of the PrestoBlue[®]-assay clearly prove that neither [Fe(CN)₆]^{3-/4-} nor FcMeOH has significantly negative impact on mitochondrial activity of NRK, MDCK-I and MDCK-II cells. Slightly higher CI values are exclusively observed for higher [Fe(CN)₆]^{3-/4-} concentrations. In the impedance-based permeability assay, the redox tracers are at most applied in a concentration of 1 mM ([Fe(CN)₆]^{3-/4-}) or 0.5 mM (FcMeOH), respectively. At these concentrations, all cytotoxic indices are close to zero (Tab. 5.11).

ECIS-cytotoxicity studies using NRK, MDCK-I and MDCK-II cells

To confirm this result and to provide a more detailed examination of the cytotoxic potential of the redox tracers, additional ECIS-cytotoxicity studies were performed. For this purpose, different tracer concentrations (0.5 / 1.0 / 2.0 mM) were added at time point zero to confluent monolayers of the cell lines under study. The addition of PBS⁺⁺/glucose (1 g/L) served as a control measurement. The impedance was monitored over time at a distinct frequency of 16 kHz. This frequency is appropriate to monitor NRK, MDCK-I and MDCK-II cells (appendix: Fig. 11.9). The results for the ECIS-cytotoxicity measurements are summarized in Fig. 5.14.

In case of NRK cells, [Fe(CN)₆]^{3-/4-} induces a significant decrease of IZ_{I16kHz} in all applied concentrations after around 90 minutes (Fig. 5.14A). Whereas the impedance magnitude stays constant (9.3 kΩ ± 0.1 kΩ) in the control measurement, the signal is decreasing for a 0.5 mM solution from (9.0 ± 0.1) kΩ (t = 0 h) to (4.1 ± 0.1) kΩ (t = 3 h). However, IZ_{I16kHz} remains unaffected within the first 90 minutes of tracer incubation. The analysis of a MDCK-I monolayer reveals no signal alterations (Fig. 5.14B). In contrast, the values for the three concentrations are even slightly higher compared to the control value (11.9 kΩ ± 0.7 kΩ) after

three hours of incubation. The addition of 2 mM [Fe(CN)₆]^{3-/4-} results in a magnitude of (14.3 ± 0.5) kΩ. The investigation of MDCK-II cells indicates no influences on the impedance magnitude at all, since the time-courses of all concentrations remain constant during the entire experiment (Fig. 5.14C). The control value is determined to be (11.7 ± 0.3) kΩ three hours after tracer addition.

The exposure to FcMeOH causes no significant impedance changes with respect to NRK cells (Fig. 5.14D). Except a slight addition peak at the beginning of the measurement, the signal is not altered over time. A 2 mM solution leads to a magnitude of (9.0 ± 0.1) kΩ at time point zero and (9.2 ± 0.1) kΩ after three hours. The situation is more complicated for MDCK-I cells (Fig. 5.14E). The control measurement shows a slight decrease from (13.8 ± 0.3) kΩ (t = 0 h) to (12.8 ± 0.2) kΩ (t = 3 h). The impedance magnitude observed for a 0.5 mM solution remains constant during the incubation time with a starting value of (12.0 ± 0.1) kΩ and (11.9 ± 0.1) kΩ at t = 3h. Nevertheless, the addition of a 1 mM FcMeOH solution induces significant signal response. Directly after FcMeOH addition, $I_{ZI_{16kHz}}$ is decreasing from (12.3 ± 0.7) kΩ to a first minimum value of (11.1 ± 0.6) kΩ after 0.2 h. Subsequently, the impedance magnitude is increasing to a transient maximum of (17.0 ± 1.5) kΩ at t = 1.5 h. In the second half of the experiment, the signal is again decreasing to a value of (11.3 ± 0.5) kΩ at t = 3 h. The addition of 2 mM FcMeOH results in a first signal drop from (12.8 ± 0.7) kΩ at the beginning to a magnitude of (10.3 ± 0.6) kΩ after 0.3 h. The impedance magnitude is recovering to a maximum of (15.0 ± 0.6) kΩ at t = 1 h. Subsequently, $I_{ZI_{16kHz}}$ decreases to (9.6 ± 0.3) kΩ at t = 2 h, before it is reaching an end of (11.0 ± 0.4) kΩ. Consequently, the addition of both, a 1 mM and a 2 mM FcMeOH solution, cause severe cell response which makes them disputable for the application as a permeability probe in the P_ETER-assay. However, 0.5 mM FcMeOH shows no negative influences and hence, is used as a redox tracer. Furthermore, a 0.5 mM FcMeOH solution does not change $I_{ZI_{16kHz}}$ using MDCK-II cells (Fig. 5.14F). Similar to the control measurement, the signal remains stable at around (11.1 ± 0.3) kΩ. The addition of 1 mM FcMeOH leads to a slight impedance minimum of (10.3 ± 0.1) kΩ after 0.5 h, before the signal is recovering to a final value of (11.4 ± 0.1) kΩ. A stronger influence is observed for the addition of a 2 mM FcMeOH solution. The impedance magnitude is decreasing instantly after tracer addition to (9.5 ± 0.1) kΩ at t = 0.3 h. Subsequently, the signal is increasing to a maximum of (14.3 ± 0.1) kΩ after 1.5 h and reaches an end value of (13.3 ± 0.7) kΩ. However, FcMeOH induces more pronounced changes of $I_{ZI_{16kHz}}$ for MDCK-I compared to MDCK-II cells.

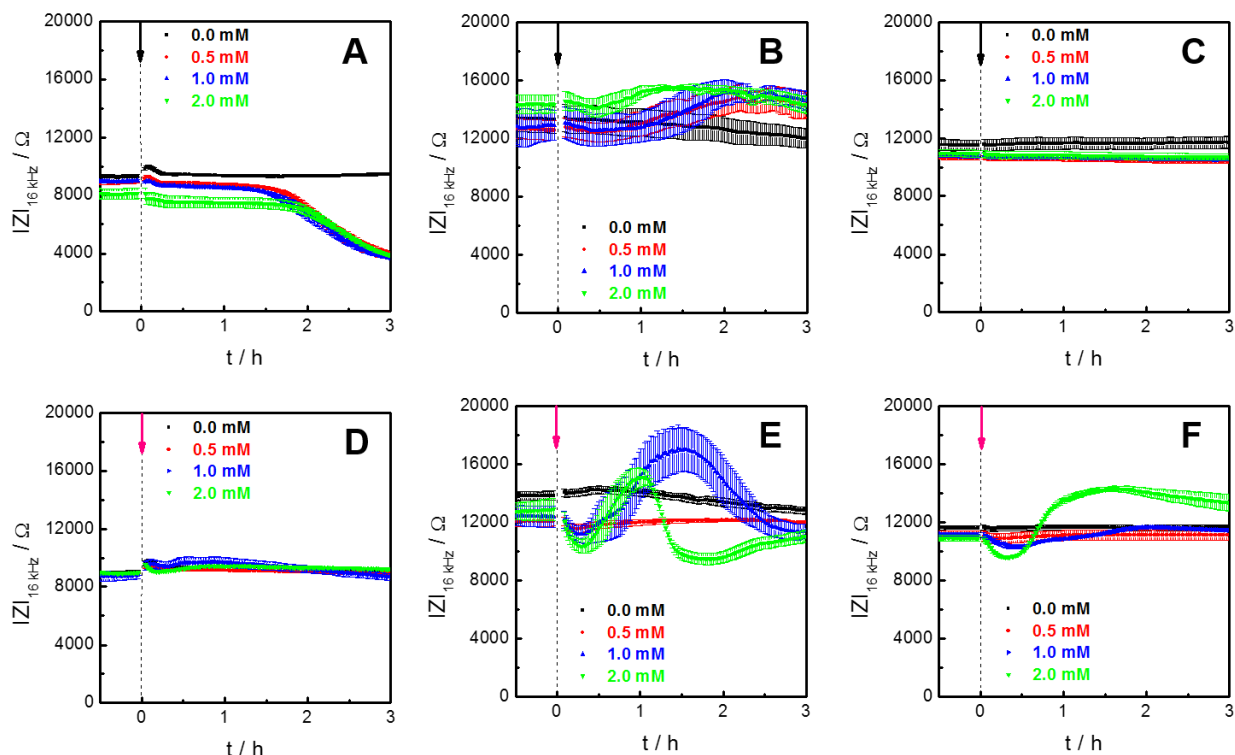


Fig. 5.14: Results of the ECIS-cytotoxicity studies of $[\text{Fe}(\text{CN})_6]^{3-/4-}$ and **FcMeOH** on (A, D) NRK (mean \pm SE, $n \geq 2$), (B, E) MDCK-I (mean \pm SE, $n \geq 2$) and (C, F) MDCK-II cells (mean \pm SE, $n \geq 3$) recorded with a 96W1E+1 array. The impedance magnitude $|Z|$ is followed over time at a common sensitive frequency of 16 kHz. The redox tracers are added at $t = 0$ h.

The results of both cytotoxicity studies clearly prove that 1 mM $[\text{Fe}(\text{CN})_6]^{3-/4-}$ is suitable to be applied as a non-cytotoxic permeability probe in the P_ETER-assay. Except for the ECIS-based analysis of NRK cells, no cytotoxic effects at all are observable for this concentration. This signal response of NRK cells does not play a big role due to the leakiness of NRK cells and the very short assay time in impedance-based permeability studies. Usually, tracer incubation time in P_ETER-studies does not exceed one hour and in case of NRK cells the incubation time could be easily reduced to only several minutes. For an improved analysis of very tight barriers, $[\text{Fe}(\text{CN})_6]^{3-/4-}$ concentration could be even increased to at least 2 mM, as shown by the two cytotoxicity tests. The situation is less convenient for ferrocenemethanol. Although the PrestoBlue[®]-assay does not indicate negative impact on the mitochondrial activity of the cell lines under study, the impedance measurements uncover significant perturbing influences of FcMeOH on MDCK-I and MDCK-II cells. However, this impact is only detectable for concentrations of at least 1 mM. The application of a 0.5 mM FcMeOH solution does not induce any significant changes of the impedance magnitude. As a consequence, the concentration of FcMeOH that is applied in P_ETER-measurements is

reduced to 0.5 mM. The non-cytotoxicity of 1 mM [Fe(CN)₆]^{3-/4-} and 0.5 mM FcMeOH is additionally supported by other impedance-based measurements that investigate influences of the two tracers on epithelial barrier function (appendix: Fig. 11.5 and Fig. 11.10) and by the time-courses of TER observed in the P_ETER-studies shown in this thesis.

The findings of the cytotoxicity studies confirm the general assessment of ferri- and ferrocyanide to behave as a compound with low cytotoxic potential. Another PrestoBlue[®]-assay which was carried out with human lymphocytes revealed only minor influences of K₄[Fe(CN)₆]^{3-/4-} on mitochondrial activity (Basu *et al.* 2013). A three hour long exposure of a 10 mM potassium ferrocyanide solution yielded a cytotoxicity index of 25 % which is comparable to the results of Fig. 5.13A-C. Furthermore, ferrocenemethanol is also not regarded as a cytotoxic compound in low concentrations. A cytotoxicity study relying on Trypan blue proved that a long-time exposure of a 1 mM FcMeOH solution had negligible effects on the cell viability of HeLa cells (Li and Bard 2009).

5.4 Advantages and limitations of the P_ETER-assay in comparison to conventional permeability assays

The novel P_ETER-device allows for simultaneous observation of two key parameters of epithelial barrier function – P_E and TER – with high quality. The exact benefits of the P_ETER-assay will be discussed in the following chapters.

5.4.1 Automated and time-resolved monitoring of tracer permeation

Tracer accumulation in the receiver compartment is typically followed via fluorescence-based (Sanders *et al.* 1995) or radio analytic readouts (Ghandehari *et al.* 1997). For this purpose, samples have to be taken from the receiver compartment at specific time-points. In a separated measurement, the tracer concentration in the receiver compartment is subsequently determined. A problematic issue which is implicated by this sequential sampling involves a possible disturbance of the epithelial barrier. Due to the liquid handling in the receiver compartment during the entire permeability measurement, the assays may become invasive to some extent and may bias inherent barrier properties. A common workaround is the massive cutback of data points. In this regard, very few time points are

analyzed to reduce negative influences on barrier integrity (Beasley *et al.* 2014; Kaiser *et al.* 2015; Sukma Dewi *et al.* 2017). As a consequence, the time-resolution of such permeability assays deteriorates which makes the determination of $dn_R(t)/dt$ very error-prone. The impedance-based P_ETER-method provides an enormous improvement concerning the liquid handling and the poor time-resolution. Once the permeability tracer is added to the donor side, the experiment runs totally automated and no sampling has to be carried out during the measurement. Thereby, the novel approach guarantees a non-invasive investigation of tracer permeability across epithelial layers. In addition, the experimental procedure of the novel P_ETER-assay is very convenient due to the totally automated data collection of the approach. Therefore, the performance of the P_ETER-assay is not restricted to experts with the long-term experience, but can be easily conducted by laymen. Furthermore, the P_ETER-assay excels the conventional methods by far in terms of time-resolution. The impedance-based and combined detection of substrate and ionic permeability across cell layers provides an excellent time-resolution of 0.6 minutes. In contrast, the original P_ETER-method had an inferior time-resolution of 8 minutes (Hajek Kathrin 2017) and other established permeability assays have even worse time-resolution due to the problematic sampling. Even increased time-resolution in the range of seconds is achieved when focusing on solely tracer permeability without the internal TER control. Thus, the new technique provides online permeability monitoring that offers not only the calculation of permeability coefficients (at least for the integral approach), but also insights about the kinetics of the permeation process. In contrast, most of the established assays are rather classified as endpoint assays.

5.4.2 Determination of P_E values with internal TER control

Prior to non-impedance-based permeability studies, the TER has to be determined to ensure barrier integrity (Groschwitz *et al.* 2009; Laukoetter *et al.* 2007; Mohamed *et al.* 2017). This leads to an inevitable additional effort of time and costs. No established permeability assay has the ability to measure P_E and TER of the same cell layer in one single experiment. The novel P_ETER-assay solves this problem by permitting a simultaneous detection of P_E and TER with one common setup. The combined determination is enabled by the impedance-based detection of both parameters. TER is monitored as an internal control at any single time-point of the permeability measurement. Defective barriers or cytotoxic influences of the permeability probe are easily tracked by the time-resolved TER control.

5.4.3 Laterally resolved recording of tracer permeation

Heterogeneous barrier function or even small defect areas of filter-grown monolayers pose a problem in permeability assays with integral readout (Klusmeier *et al.* 2019; Wegener and Seebach 2014). Significant overestimation of P_E values or underestimation of TER values, respectively, is the consequence of defective barriers that are not noticed due to a completely integral readout. For this purpose, several techniques were developed to provide laterally resolved information about substrate permeability across cell layers. However, these methods (chapter 1.1.3.2) have one common drawback. They all require high experimental efforts and are therefore not suitable for high-throughput research. The P_ETER-assay presented here offers next to integral readout also laterally resolved readout. Although the lateral resolution is limited to the number of electrodes that are integrated into the bottom of the measurement chamber and although the lateral resolution is inferior to other approaches that record transepithelial tracer permeation at subcellular level (Bergner *et al.* 2012; Klusmeier *et al.* 2019), the P_ETER-assay allows an automated and easy-to-handle approach that is easily scalable to multi-well formats like 12-well, 24-well or 96-well formats.

5.5 Summary and outlook

The first project of this thesis picked up the impedance-based permeability assay which was originally reported in 2017 (Hajek Kathrin 2017) and refined certain experimental details of the assay (P_E-calculation, time-resolution, redox probes). Simultaneous and automated monitoring of two key parameters of epithelial barrier function – the molecular permeability coefficient (P_E) and the transepithelial electrical resistance (TER) – was provided by the impedance-based P_ETER-assay. Two suitable redox tracers were investigated ([Fe(CN)₆]^{3-/4-}, FcMeOH). Different arguments (sensitivity, cytotoxic potential, transepithelial transport route) certified [Fe(CN)₆]^{3-/4-} to be the permeability probe of choice for P_ETER-assays. Impedance-based P_E measurements with integral readout yielded P_E values in a reasonable range that is similar to other well-known permeability probes like for example fluorescein. By increasing the number of working electrodes that are localized at the bottom of the measurement chamber, tracer permeability was followed with lateral resolution. In this context, heterogeneities in barrier function of uniform monolayers and of mixed but segregated cell layers were visualized.

So far, only three cell lines were investigated with the P_ETER-assay. It is desirable to screen less robust cell lines, as for example brain endothelial cells (P_ETER-studies / cytotoxicity evaluation). Furthermore, only two appropriate redox tracers have been discovered until now. A creation of a pool of redox-active permeability probes with different molar masses might be the next step to broaden the information content of the measurement. Thereby, systematic analysis of cell junctions might be accessible as it is the case for fluorescence-based permeability probes. However, redox pairs like NAD⁺/NADH or [Ru(NH₃)₆]^{2+/3+} are not suitable due to a non-matching potential and the associated missing charge-transfer across the electrode-electrolyte interface. Besides, the new device might be a useful tool to distinguish between trans- and paracellular resistance contributions according to the two-path impedance spectroscopy (Krug *et al.* 2009b), but without the necessity of performing two separated experiments. One of the limitations of the spatially resolved P_ETER-assay is that the approach provides only relative permeability monitoring due to an undefined receiver volume. Therefore, it is desirable to improve the experimental setup to create a well-defined receiver volume providing the calculation of permeability coefficients of different spots within one cell layer.

6 Impedance-based monitoring of osmotically induced water flux across epithelial cell layers

The analysis of water permeability across epithelial cell layers plays an important role in the field of drug development and -delivery. Among others, *in vitro* water permeability assays are crucial for the investigation of membrane water channels that are denoted as *aquaporins* (AQPs). Many pathological conditions are both, directly and indirectly, associated with defective function of aquaporins. Consequently, AQPs are predicted to constitute promising targets for future drugs and therapies. However, established methods for quantifying water flux across barrier-forming cell layers are prone to errors and elaborate making them uninteresting for high-throughput research.

The second project of this thesis introduces a novel, impedance-based assay for monitoring osmotically induced water flux across epithelial cell layers. Therefore, a cell-covered filter insert is mounted into a standard dual chamber to create two separated compartments with different chemical compositions. The crucial point of the experimental setup is the creation of a very small basolateral volume. By integrating suitable electrode layouts into the bottom of the basolateral compartment, changes of the conductance of the basolateral buffer are recorded with excellent time-resolution and high sensitivity. Water but no solute flux across epithelial barriers is induced by challenging the cell layer under study with non-isotonic but iso-conductive solutions on one side of the barrier. The recorded conductance of the basolateral buffer is directly connected to transepithelial water flux, because water flow between the two compartments alters the ionic concentration of the basolateral buffer. The impedance-based water flux assay has been performed in three different experimental settings:

- (I) Central readout: This variant of the assay provides the most sensitive readout and is based on using one electrode pair that is localized beneath the center of the overlaying cell layer. Thus, this assay version with central readout provides local monitoring of transepithelial water flow.

- (II) Spatially resolved readout: By increasing the number of electrode pairs at the bottom of the lower compartment, osmotically induced water flux is recorded with lateral resolution.

- (III) P_{OS}TER-assay: A combined and simultaneous detection of water flux and ionic permeability across one and the same cell layer is possible using an interdigitated electrode array (IDE-400) instead of an electrode pair. Both parameters, the *osmotic water permeability coefficient* (P_{OS}) and the *transepithelial electrical resistance* (TER), are determined integrally in the P_{OS}TER-assay.

The different versions of the impedance-based water flux assay were performed with different epithelial cell layers (MDCK-I, MDCK-II). In addition, studies on cell lines that ectopically express the water channel AQP1 were conducted with the new device highlighting the potential of the new assay for pharmaceutical interests. Furthermore, water flux measurements were performed using the established *fluorophore dilution method* to provide P_{OS} values as an independent reference.

6.1 Central water flux measurements

The new device aims to monitor water flow between two separated compartments by an impedance-based approach. An electrode array that consists of a co-planar arrangement of two circular gold electrodes (chapter 4.2.1, Fig. 4.5) is integrated at the bottom of the lower compartment beneath the center of a cell-covered filter insert. Thereby, transepithelial water flux is monitored locally in the center of the cell layer. This approach is a powerful tool for recording transepithelial water flow with outstanding time-resolution but does not permit the calculation of P_{OS} values due to an undefined volume of the basolateral compartment.

6.1.1 Characterization of the electrode

Frequency spectra of the impedance using PBS⁺⁺/glucose (1 g/L)

Cell-free filter supports were directly placed onto the electrode array. A co-planar arrangement of two circular gold electrodes (each Ø 500 µm, distance between electrodes

800 μm) was integrated into the bottom of the basolateral compartment (Fig. 6.1A). The impedance was recorded over five decades (1 Hz – 10^6 Hz). Fig. 6.1B-C displays frequency spectra of the impedance magnitude $|Z|$, the conductance G (which is the inverse of the resistance R) and the capacitance C .

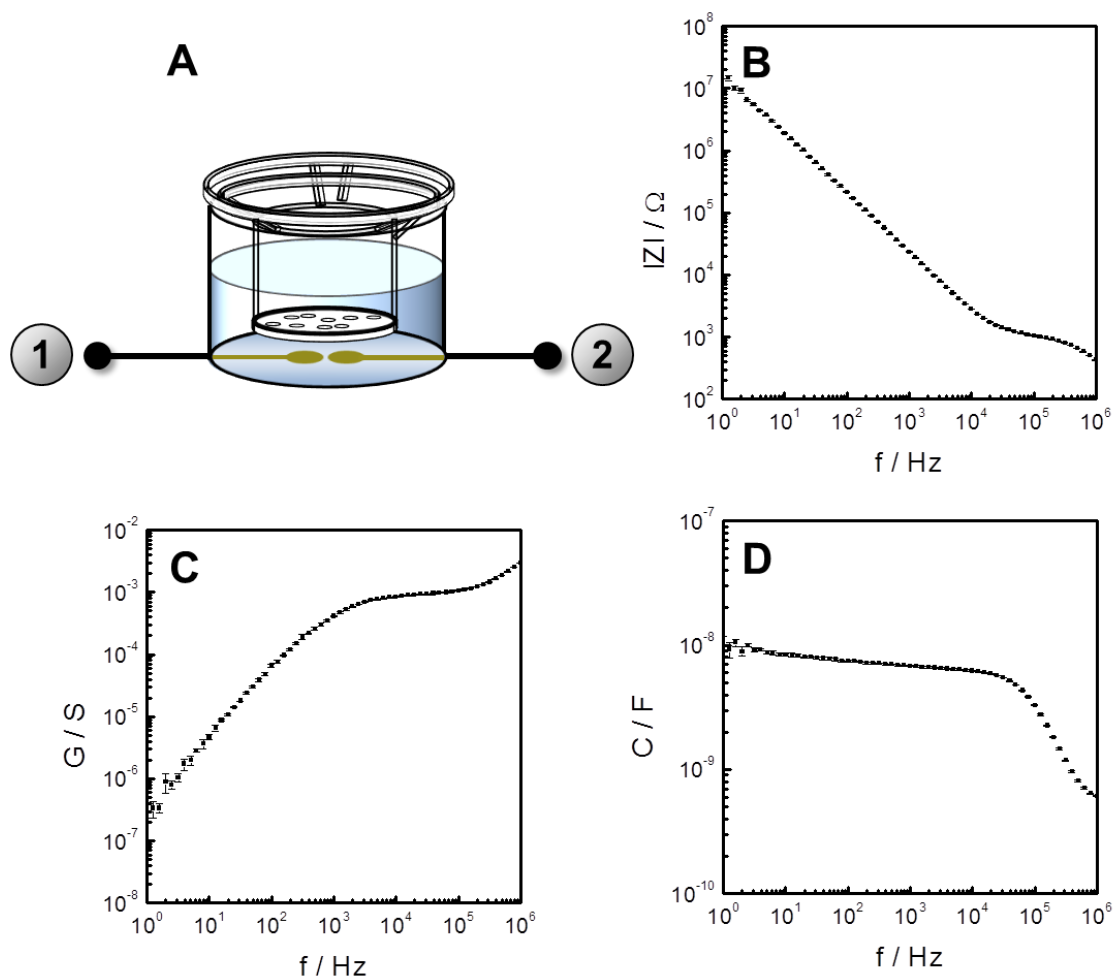


Fig. 6.1: (A) Schematic of the experimental setup for electrode characterization of the impedance-based water flux device using one central electrode pair (each \varnothing 500 μm , distance between electrode 800 μm). A cell-free filter insert is placed directly onto the electrode structure that is integrated into the bottom of the basolateral compartment. Frequency spectra are displayed as (B) impedance magnitude $|Z|$, (C) conductance G and (D) capacitance C (mean \pm SE, $n = 3$).

Tab. 6.1: Values of the different circuit elements after equivalent circuit modeling of the data of Fig. 6.1 (mean \pm SE, $n = 3$). The values are related to the electrode array that consists of one central electrode pair and that is applied in impedance-based water flux measurements.

parameter	central water flux mode (1 vs. 2)
R_{bulk} / Ω	1063 ± 16
$A_{\text{CPE}} / \mu\text{Fs}^{n-1}$	9.3 ± 0.5
n_{CPE}	0.950 ± 0.006

All frequency spectra show the same trend: (I) The impedance is dominated by the electrode-electrolyte interface over a broad range from 1 Hz to 10^4 Hz. The interface impedance of the device is relatively high with magnitudes of (20 ± 5) M Ω at $f = 1$ Hz due to the small active electrode area. (II) The frequency regime that is dominated by the bulk resistance is the decisive region for the readout of the impedance-based water flux assay and ranges from 10^4 Hz to 10^6 Hz. At a frequency of 100 kHz, the impedance magnitude and the conductance are (1074 ± 10) Ω or (1056 ± 17) μ S, respectively. However, the recorded impedance indicates a parasitic impact at very high frequencies ($> 10^5$ Hz). This phenomenon is due to a parasitic capacitance arising from the large area of the leads that are passivated by an insulating photopolymer and due to connecting cables. Therefore, frequencies above 100 kHz are not suitable for the readout of the assay. By equivalent circuit modeling, the elements of the equivalent circuit presented in chapter 3.1.1 (Fig. 3.2) are assessable and listed in Tab. 6.1.

Determination of the cell constant of the device

The impact of changing the ionic concentration of the buffer on the recorded conductance is demonstrated in Fig. 6.2A. The impedance was measured over six frequency decades in presence of different KCl concentrations (25 / 50 / 75 / 100 / 125 / 150 / 175 / 200 mM) to simulate different ionic concentrations. The specific conductivity γ of the individual KCl concentrations was determined separately by means of a conductivity sensor (chapter 4.1.5, Tab. 4.6). The conductance of the buffer at 100 kHz is increasing with increasing KCl concentrations. Tab. 6.2 provides an overview about the measured conductances of the individual KCl solutions at a frequency of 100 kHz.

Tab. 6.2: Conductances that are recorded by a central electrode pair at a frequency of 100 kHz for variable KCl concentrations simulating different ionic concentrations (mean \pm SE, $n = 3$).

c (KCl) / mM	G_{100kHz} / mS	c (KCl) / mM	G_{100kHz} / mS
25	0.37 ± 0.01	125	1.10 ± 0.01
50	0.57 ± 0.01	150	1.28 ± 0.01
75	0.794 ± 0.001	175	1.45 ± 0.01
100	0.964 ± 0.002	200	1.61 ± 0.01

As already observed in Fig. 6.1, also Fig. 6.2 reveals a serious signal perturbation at very high frequencies arising from the parasitic capacitance of the passivated leads. Obviously,

the impact of the parasitic capacitance on the impedance gets more emphasized in presence of low conductivity buffers. The conductance spectrum of a 25 mM KCl solution indicates already an impact at 30 kHz. Nevertheless, impedance-based water flux measurements are performed with hyper- and isotonic buffers having significantly higher specific conductivities in the range of 16 mS/cm. A 150 mM KCl solution has approximately the same specific conductivity as the hyper- and isotonic buffers that were used in this thesis. As Fig. 6.2A shows, no significant influence of the parasitic capacitance is observed for solutions with sufficient specific conductivity. The individual specific conductivities γ of the different KCl solutions are plotted as a function of the conductance ($f = 100$ kHz) determined by the impedance measurement (Fig. 6.2B). There is a linear relationship between γ and $G_{100\text{kHz}}$ which is analyzed by linear regression. The slope of this linear fit-function provides an electrode-specific parameter that is referred to as the *cell constant* $K (= \gamma/G)$. The cell constant resembles the slope of the linear fit-function and is $(13.5 \pm 0.9) \text{ cm}^{-1}$ for the central electrode pair that is applied for impedance-based water flux monitoring ($f = 100$ kHz).

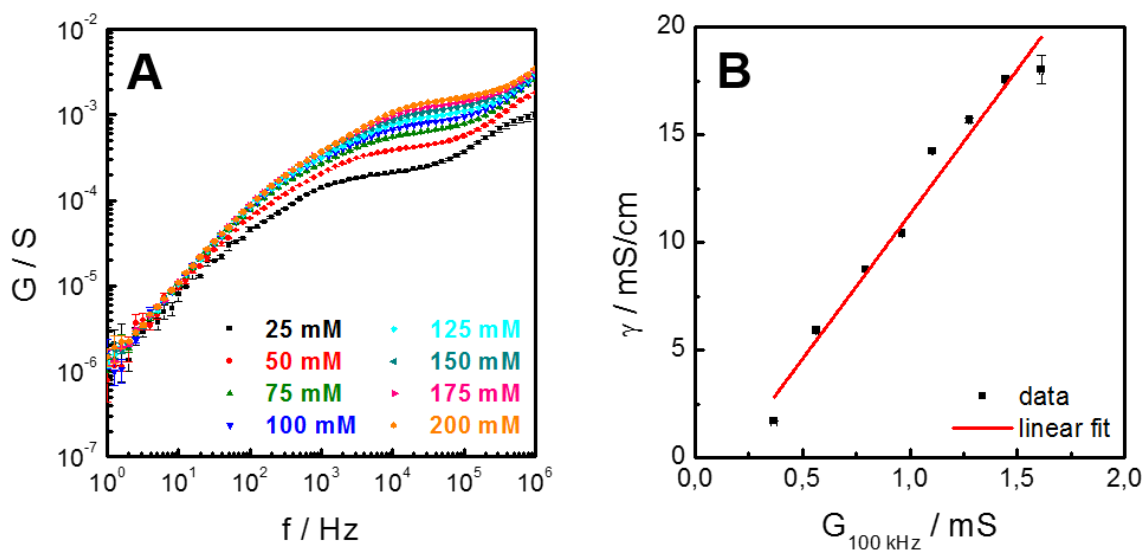


Fig. 6.2: (A) Conductance spectra recorded with the central electrode pair in presence of variable KCl concentrations (mean \pm SE, $n = 3$) mimicking different ionic concentrations of the buffer. (B) Determination of the cell constant of the device ($K = \gamma/G$). The individual specific conductivities γ of the different KCl solutions are plotted as a function of the recorded conductance at a frequency of 100 kHz (mean \pm SE, $n = 3$). The linear relationship between the two parameters is analyzed by linear regression revealing a cell constant of $(13.5 \pm 0.9) \text{ cm}^{-1}$. The error is provided by Origin2016 ($R^2 = 0.972$).

6.1.2 Hypertonic stimulations of different epithelial cell layers

Impedimetric water flux measurements with confluent monolayers of different epithelial cell lines (MDCK-I, MDCK-II) were performed with the new device. The impedance was measured in a frequency regime from 10^4 Hz to 10^6 Hz. At time point zero, differently

concentrated but iso-conductive sucrose solutions (0 / 10 / 50 / 100 / 150 / 200 mM) were added to the apical compartment. The sucrose solutions act as hypertonic buffers and induce different hyperosmotic pressure gradients across the cell layers. Additionally, several control experiments were conducted supporting the rationale of the impedance-based water flow assay (appendix: Fig. 11.11). The following paragraphs present the results of the impedance-based approach to locally monitor transepithelial water flow for hypertonic stimulations of MDCK-I and MDCK-II monolayers.

Fig. 6.3A displays the time-courses of the conductance at a frequency of 100 kHz for MDCK-I cells. All conductances are normalized to the conductance recorded at $t = 0$ min. No signal response is visible for a mere buffer exchange. The addition of a 10 mM sucrose solution does not cause a time-dependent change of the conductance that is discriminable from the control curve. In contrast, the concentrations from 50 mM to 200 mM lead to a dose-dependent increase of the conductance of the basolateral buffer. The addition of 50 mM sucrose results in a short lag phase of five minutes followed by a slight signal increase of (7.8 ± 0.7) % is received. A stronger response is observed for 100 mM sucrose with an increase of (15 ± 1) % after 40 minutes. The addition of a 150 mM or a 200 mM sucrose solution, respectively, causes an immediate signal gain and provides conductance changes of (21 ± 1) % and (25 ± 1) % at the end of the experiment.

Similar time-courses of the normalized conductance get obvious for MDCK-II cells (Fig. 6.3B). The addition of PBS⁺⁺/glucose (1 g/L) and 10 mM sucrose does not alter the basolateral conductance significantly. The sucrose concentrations from 50 mM to 200 mM reveal a strict dose-dependent conductance increase. Again, $\text{norm.G}_{100\text{kHz}}$ is characterized by a short lag phase after the osmotic stimulation with 50 mM sucrose and reaches a total increase of (8.5 ± 0.2) %. The conductance alteration after 40 minutes that is measured with 100 mM sucrose is (17 ± 1) %. The addition of a 150 mM sucrose solution generates a rapid signal response with an overall increase of (19 ± 1) % after 40 minutes. The strongest gain of the conductance is observed for 200 mM sucrose with a final increase of (27 ± 2) %. Although the absolute conductance changes are in the same order for MDCK-I and MDCK-II cells, the kinetics of water permeation differ for the two cell lines. Apparently, transepithelial water flux occurs faster for MDCK-II layers. A detailed analysis of water flux is provided by chapter 6.1.4. The overall increase of the (normalized) conductance for the individual sucrose concentrations for both, MDCK-I and MDCK-II cells, are summarized in Tab. 6.3.

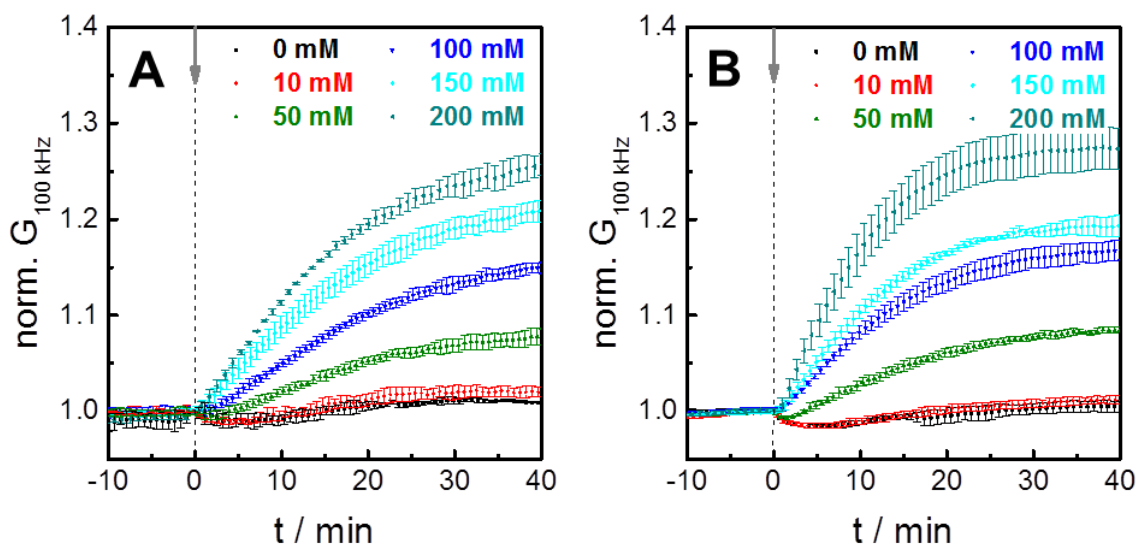


Fig. 6.3: Impedance-based monitoring of osmotically induced water flux between two separated compartments using (A) MDCK-I (mean \pm SE, $n = 2$) and (B) MDCK-II cells (mean \pm SE, $n = 3$). The assay was performed with one electrode pair located beneath the center of the overlying cell layer. The epithelial barriers are exposed to different concentrations of **sucrose** inducing an osmotic pressure gradient across the cell layers at $t = 0$ min. Transepithelial water flux is followed by monitoring time-dependent changes of the (normalized) conductance of the basolateral buffer at a frequency of 100 kHz. Absolute conductance at $t = 0$ min: $G_{100\text{kHz}}$ (0 mM, MDCK-I) = (1122 ± 127) μS , $G_{100\text{kHz}}$ (10 mM, MDCK-I) = (1159 ± 60) μS , $G_{100\text{kHz}}$ (50 mM, MDCK-I) = (1182 ± 54) μS , $G_{100\text{kHz}}$ (100 mM, MDCK-I) = (1188 ± 47) μS , $G_{100\text{kHz}}$ (150 mM, MDCK-I) = (1202 ± 36) μS , $G_{100\text{kHz}}$ (200 mM, MDCK-I) = (1191 ± 50) μS , $G_{100\text{kHz}}$ (0 mM, MDCK-II) = (1274 ± 19) μS , $G_{100\text{kHz}}$ (10 mM, MDCK-II) = (1281 ± 13) μS , $G_{100\text{kHz}}$ (50 mM, MDCK-II) = (1272 ± 25) μS , $G_{100\text{kHz}}$ (100 mM, MDCK-II) = (1249 ± 3) μS , $G_{100\text{kHz}}$ (150 mM, MDCK-II) = (1247 ± 11) μS , $G_{100\text{kHz}}$ (200 mM, MDCK-II) = (1248 ± 7) μS .

Tab. 6.3: Overall changes of the basolateral (normalized) conductance in response to hypertonic stimulations of MDCK-I and MDCK-II cell layers (mean \pm SE, $n \geq 2$). The signal changes refer to the time interval between $t = 0$ min and $t = 40$ min.

c (sucrose) / mM	$\Delta\pi$ / mOsmol/kg	$\Delta\text{norm. } G_{100\text{kHz}} / \%$	
		MDCK-I	MDCK-II
0	0	0.8 ± 0.1	0.4 ± 0.5
10	27	2.0 ± 0.5	1.3 ± 0.3
50	83	7.8 ± 0.7	8.5 ± 0.2
100	150	15 ± 1	17 ± 1
150	218	21 ± 1	19 ± 1
200	287	25 ± 1	27 ± 2

The results of Fig. 6.3 prove the rationale of the novel water flux assay. The addition of a hypertonic solution to the apical compartment induces a hyperosmotic pressure gradient across the epithelial cell layer. Subsequently, water flow but no solute flow occurs from the basolateral to the apical side to balance the osmotic pressure difference. As a result, the ionic concentration of the basolateral buffer is increasing time-dependently. The increase of the ionic concentration in the basolateral compartment is associated with an increase of the conductance of the basolateral buffer and therefore, the recorded conductance is increasing

over time. In addition, the impedance-based water flux assay provides strictly dose-dependent monitoring of transepithelial water flux, as the increase of the basolateral conductance is increasing with higher hyperosmotic pressure gradients that are induced by higher sucrose solutions.

6.1.3 Hypotonic stimulations of MDCK-II monolayers

The next step of assay development was to reverse the osmotic pressure gradient. For this purpose, two different hypotonic buffers were added to the apical compartment of filter-grown MDCK-II cells. The impedance was recorded from 10^4 Hz to 10^6 Hz. A different readout frequency was used for the hypotonic stimulations, since the specific conductivities of the hypotonic buffers (chapter 4.1.5, Tab. 4.11) were approximately four times lower compared to the hypertonic buffers. As mentioned above, the perturbances of parasitic effects get more pronounced in presence of low conductivity buffers. Therefore, water flux between the two compartments was analyzed at a frequency of only 10 kHz. Control measurements indicated that the impedance is not significantly affected at 10 kHz using buffers with low specific conductivity (appendix: Fig. 11.12).

Fig. 6.4 illustrates the time-dependent decrease of the conductance of the basolateral buffer after hypotonic stimulations of MDCK-II monolayers. All conductances are normalized to the conductance measured at $t = 0$ min. A mere buffer exchange (ISO) causes a slight peak directly after the addition. However, the signal is recovering within five minutes and reaches finally the initial values. A different time-course of $\text{norm.G}_{10\text{Hz}}$ is observed for a hypotonic solution that induces an osmotic pressure gradient of 58 mOsmol/kg (HYPO A). The decrease of the conductance is (4.7 ± 0.1) % after 15 minutes. At $t = 40$ min, an overall signal change of (5.2 ± 0.3) % is recorded. The apical addition of a hypotonic buffer that generates an osmotic pressure gradient of 95 mOsmol/kg (HYPO B) leads to a similar time-course of $\text{norm.G}_{10\text{kHz}}$. However, the decrease of the basolateral conductance is slightly stronger and reaches alterations of (6 ± 1) % at $t = 15$ min or (7 ± 1) at $t = 40$ min, respectively. Tab 6.4 summarizes the overall decrease of the basolateral conductance. A detailed examination of water permeation after hypotonic stimulations is presented in the following chapter.

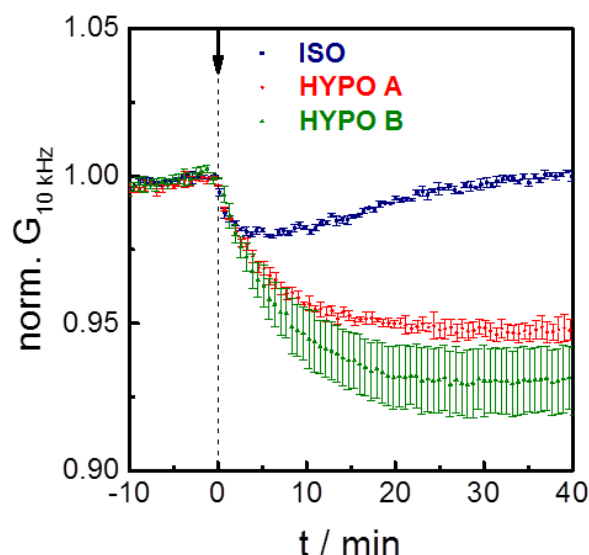


Fig. 6.4: Impedance-based monitoring of osmotically induced water flux between two separated compartments using MDCK-II cells (mean \pm SE, $n = 3$). The assay was performed with one electrode pair located beneath the center of the overlying cell layer. The cell layers are exposed to different hypotonic solutions inducing an osmotic pressure gradient across the filter-grown MDCK-II cells at $t = 0$ min. Transepithelial water flux is followed by monitoring time-dependent changes of the (normalized) conductance of the basolateral buffer at a frequency of 10 kHz. Absolute conductance at $t = 0$ min: $G_{10\text{kHz}}$ (ISO) = $(247.3 \pm 0.3) \mu\text{S}$, $G_{10\text{kHz}}$ (HYPO A) = $(259 \pm 10) \mu\text{S}$, $G_{10\text{kHz}}$ (HYPO B) = $(279 \pm 12) \mu\text{S}$.

Tab. 6.4: Overall changes of the basolateral (normalized) conductance in response to hypotonic stimulations of MDCK-II barriers (mean \pm SE, $n = 3$). The signal changes refer to time intervals from $t = 0$ min to $t = 40$ min.

buffer	$\Delta\pi$ / mOsmol/kg	$\Delta G_{10\text{kHz}}$ / %
ISO	0	0.1 ± 0.1
HYPO A	58	4.7 ± 0.1
HYPO B	95	7 ± 1

The results of Fig. 6.4 support the assay principle and prove that the impedance-based water flux assay is able to monitor transepithelial water permeation bidirectionally. Besides water flow from the basolateral to the apical side of an epithelial cell layer, water flux that occurs from the apical to the basolateral compartment is also detectable. The induced hypoosmotic pressure gradient leads to water but no solute flux into the basolateral compartment causing a decrease of the ionic concentration of the basolateral buffer. Since the ionic concentration is linearly proportional to the conductance, the conductance of the basolateral buffer is time-dependently decreasing, as indicated by the recorded time-courses of $\text{norm.}G_{10\text{kHz}}$ after hypotonic stimulations of MDCK-II cells.

6.1.4 Analysis of transepithelial water flux kinetics

Time-dependent conductance changes after osmotic stimulations of chapter 6.1.2 and chapter 6.1.3 are further analyzed in the following paragraphs. By fitting the parameters of an exponential growth function of 1st order ($y = A \times \exp\left(\frac{x}{\tau}\right) + y_0$) or exponential decay function of 1st order ($y = A \times \exp\left(\frac{-x}{\tau}\right) + y_0$), respectively, to the recorded time-courses of the basolateral conductance, two parameters are revealed:

- (I) The *time-constant* τ describes the period in which the signal is changing to 1/e of the overall signal change.
- (II) The *amplitude* A is a measure for the total signal change. All time-constants and amplitudes are expressed as absolute values for better comparison.

The fitting procedure was conducted with Origin2016 (appendix: Fig. 11.13). The raw data of the control experiments as well as of 10 mM sucrose are not analyzed. The resulting values of τ and A for MDCK-II and MDCK-I layers are summarized in Tab. 6.5 and Tab. 6.6 and compared in Fig. 6.5.

Tab. 6.5: Time-constants τ and amplitudes A of the fit-function for MDCK-II cell layers in hyper- and hypotonic stimulation experiments (mean \pm SE, $n = 3$). The quality of the fitting process is quantified by the regression coefficient R^2 .

solution	$\Delta\pi$ / mOsmol/kg	τ / min	A	R^2 -value
HYPO B	-95	6.61 \pm 0.06	0.0691 \pm 0.0004	0.998
HYPO A	-58	6.00 \pm 0.08	0.0468 \pm 0.0001	0.998
50 mM sucrose	83	35 \pm 4	0.115 \pm 0.009	0.983
100 mM sucrose	150	24 \pm 1	0.219 \pm 0.006	0.992
150 mM sucrose	218	15 \pm 0.3	0.227 \pm 0.002	0.997
200 mM sucrose	287	12.4 \pm 0.3	0.297 \pm 0.003	0.997

Tab. 6.6: Time-constants τ and amplitudes A of the fit-function for MDCK-I cell layers in hypertonic stimulation experiments (mean \pm SE, $n = 2$). The quality of the fitting process is quantified by the regression coefficient R^2 .

solution	$\Delta\pi$ / mOsmol/kg	τ / min	A	R^2 -value
50 mM sucrose	83	58 \pm 7	0.19 \pm 0.02	0.983
100 mM sucrose	150	35 \pm 1	0.243 \pm 0.006	0.993
150 mM sucrose	218	22.9 \pm 0.4	0.262 \pm 0.002	0.999
200 mM sucrose	287	17.3 \pm 0.6	0.324 \pm 0.005	0.997

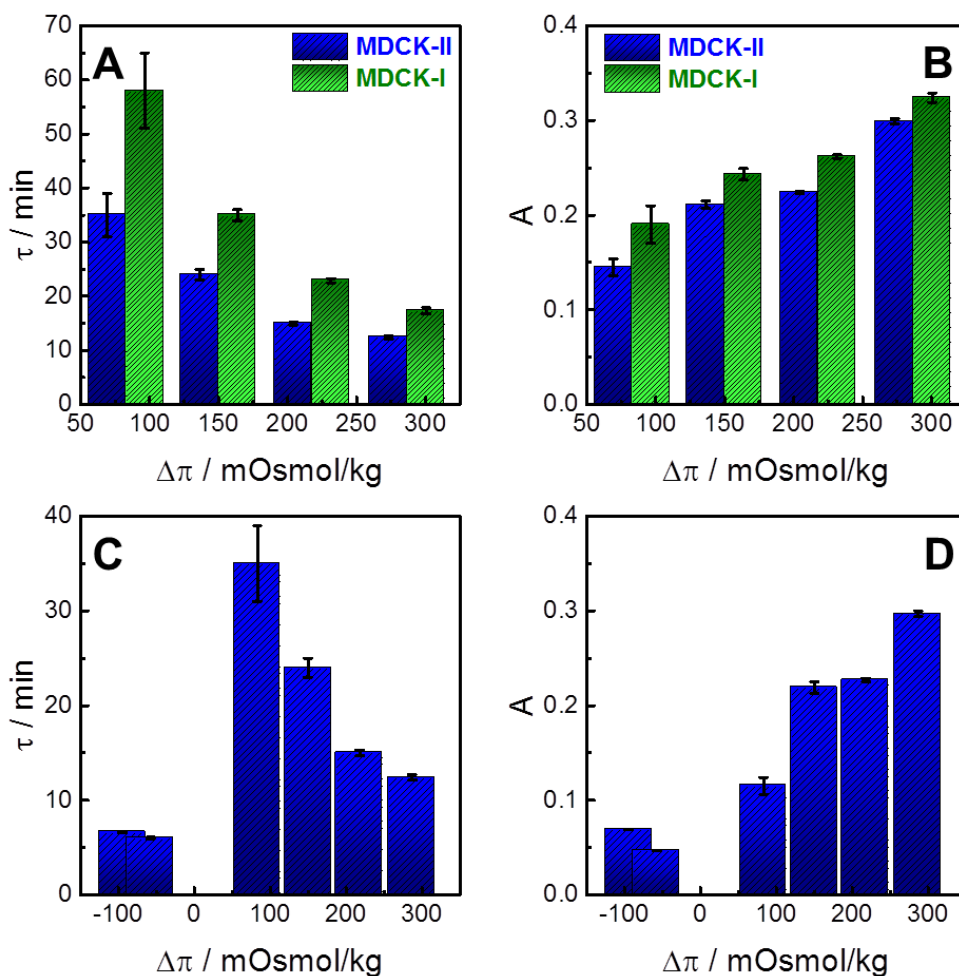


Fig. 6.5: (A) Time-constants τ and (B) amplitudes of fit-function for MDCK-I (mean \pm SE, $n = 2$) and MDCK-II (mean \pm SE, $n = 3$) cells determined for hypertonic stimulations. (C) Time-constants τ and (D) amplitudes of the fit-function for MDCK-II (mean \pm SE, $n = 3$) obtained for hyper- and hypotonic stimulations.

The hypertonic stimulations lead to significantly higher time-constants for MDCK-I layers (Fig. 6.5A). MDCK-II layers react faster to hyperosmotic pressure gradients and are able to compensate the osmotic gradient in a shorter time period. Furthermore, higher osmotic pressure gradients are connected with lower time-constants. The situation is different for the corresponding amplitudes (Fig. 6.5B). MDCK-I cells show slightly increased amplitudes compared to MDCK-II cells for hypertonic stimulations. Higher hyperosmotic pressure gradients are associated with higher amplitudes. The time-constants observed for hyper- and hypotonic stimulations of MDCK-II monolayers are noticeably different (Fig. 6.5C). One of the hypotonic buffers (HYPO B) induces approximately the same but reversed osmotic pressure gradient across MDCK-II cells as a 50 mM sucrose solution. However, transepithelial water permeation appears to be significantly faster for hypotonic stimulations. This is reflected in the time-constants of (6.61 ± 0.06) min for HYPO B or (35 ± 4) min for 50 mM sucrose,

respectively. Another difference between the hyper- and hypotonic experiments is that the two hypotonic buffers reveal similar time-constants, whereas a clear trend is observed for the hypertonic solutions. The amplitudes show also a discrepancy between hyper- and hypotonic stimulations (Fig. 6.5D). The amplitudes are generally higher for hypertonic experiments. However, hyper- and hypotonic simulation experiments were recorded at different readout frequencies making a direct comparison between the amplitudes critical. The cell constant of the device is significantly higher at 10 kHz with a value of $(20 \pm 1) \text{ cm}^{-1}$ compared to the cell constant at 100 kHz $(13.5 \pm 0.9) \text{ cm}^{-1}$.

To the best of our knowledge, the observation that transepithelial water flux occurs faster across filter-grown MDCK-II cells in presence of hypotonic buffers compared to hypertonic buffers has not been reported so far. In contrast, Robelek and Wegener published a SPR-based approach for quantifying cell volume changes (Robelek and Wegener 2010). They observed that water flux across a single plasma membrane is much faster for hypertonic stimulations with a time-constant of $(1.5 \pm 0.1) \text{ min}$ (for 70 mOsmol/kg), whereas hypotonic stimulation yielded a time-constant of approximately 12 minutes (for 135 mOsmol/kg). They explained these differences in the rate of water permeation by particular cellular mechanism denoted as *regulatory volume changes* (RVC). MDCK-II layers are known to exhibit *regulatory volume decrease* (RVD) mechanisms subsequent to hypotonic stimulations. Besides water flux into the cytoplasm, water is simultaneously transported across the plasma membrane into the extracellular space to some extent decelerating the overall water permeation and cell volume changes. The opposing regulatory process referred to as *regulatory volume increase* (RVI) is not reported for MDCK-II cells after hypertonic stimuli (Roy and Sauvé 1987). However, the SPR-based assay detects water flux across only one plasma membrane instead of taking both, the apical and basolateral plasma membrane, into account. The hypothesis that RVD affects the water permeation rate after hypotonic stimulations is not reflected in the results of Fig. 6.5. The impedance-based approach that analyses the apical and basolateral membrane clearly indicates a higher water permeation rate after hypotonic stimuli.

Fluorescence-based transepithelial water flux assays were introduced and performed by Levin et al (Levin *et al.* 2006). They induced hyper- and hypotonic pressure gradients across HBE monolayers. The resulting net water flux was determined by the *fluorophore dilution method* which was described in chapter 1.1.3.3. They found that the (normalized)

fluorescence intensity was decreasing over time after the addition of hypertonic solutions to the apical compartment. This decrease of norm.F is associated with water permeation into the apical compartment that dilutes the fluorophore concentration. Similar to the impedance-based approach, they fitted the parameters of an exponential function of 1st order to the time-course of the fluorescence intensity change. In contrast to the results of Fig. 6.5, they observed no significant differences of the time-constants for hyper- and hypotonic stimulation experiments. Both τ values were approximately 50 minutes for apical and basolateral addition of 300 mM D-mannitol, respectively. However, two experimental details are different for the study of Levin et. al and the here presented assay:

- (I) Levin et. al used a different cell line. HBE monolayers cannot be directly compared to MDCK-II cells. MDCK-II cells have a different molecular composition as HBE cells having certainly an impact on the barrier function to water.
- (II) Whereas we used hypotonic solutions to reverse the osmotic pressure gradient and hence, the direction of water flux, Levin et. al changed the compartment, in which they added D-mannitol, to reverse the direction of water flow. Therefore, the data of the two different approaches may not be compared directly.

A possible explanation for the striking difference in the time-constants of the impedance-based water flux assay may be found in the experimental setup and the direction of transepithelial water flux. The apical addition of a hypertonic solution results in a water flux from the basolateral to the apical side of the cellular barrier. Thus, water has to flow from the lower into the upper compartment against the force of gravity. This may lead to a slight underestimation of the rate of water permeation. In contrast, the apical addition of a hypotonic solution causes water flux from the apical into the basolateral compartment, i.e. from the upper into the lower compartment without being affected but even facilitated by the force of gravity.

Besides the experimental settings, the different time-constants that are observed in hyper- and hypotonic stimulation experiments using MDCK-II cells may be based on biological reasons. A different expression of aquaporins within the apical and basolateral plasma membrane may lead to different water permeation rates after hyper- and hypotonic stimulations.

The results of chapter 6.1.2 and chapter 6.1.3 clearly prove the rationale of the novel water flux assay. However, two drawbacks confine the assay:

- (I) The central position of the electrode pair beneath the cell layer under study permits only local water flux monitoring which is not representative for the entire cell layer.
- (II) The assay with central readout of water flux does not provide the calculation of P_{OS} values. This is associated with the direct placement of the cell-covered filter inserts onto the bottom of the basolateral compartment leading to an undefined basolateral volume V_0 . However, exact knowledge of V_0 is a basic requirement for determining the net water flux J_V and the osmotic water permeability coefficient P_{OS} , respectively (chapter 3.2.2, equations 3.39 and 3.45).

6.1.5 Hypertonic stimulations of MDCK-I-AQP1 monolayers

The impedance-based water flux assay with central readout was performed with confluent monolayers of a transfected MDCK-I cell line that overexpresses the membrane water channel aquaporin 1 (AQP1). This transfected cell line is denoted as MDCK-I-AQP1. The impedance was determined from 10^4 Hz to 10^6 Hz. At $t = 0$ min, different hypertonic sucrose solutions (100 / 150 / 200 mM) were added to the apical compartment. As a reference, the experiments were accompanied by water flux measurements with non-transfected MDCK-I cells. The following paragraphs present the time-courses of the conductance of the basolateral buffer after hypertonic stimulation of MDCK-I and MDCK-I-AQP1 layers as well as the time-constants and amplitudes of the corresponding fit-functions.

The time-courses of the basolateral conductance for MDCK-I-AQP1 and MDCK-I monolayers in response to the addition of variable sucrose solutions are displayed in Fig. 6.6. All conductances are normalized to the conductance recorded at $t = 0$ min. The increase of the conductance of the basolateral buffer is unequivocally discriminable for the AQP1-overexpressing and the wildtype cell line. The addition of 100 mM sucrose (Fig. 6.6A) leads to an an instant increase of (6 ± 1) % after five minutes in presence of AQP1. In contrast, the wildtype cell line shows a lag phase at the beginning of the experiment. In MDCK-I-AQP1 cells the osmotic imbalance is already compensated after 25 minutes, whereas the non-transfected MDCK-I cells require more than 40 minutes for the compensation. A similar trend is observed for 150 mM sucrose (Fig. 6.6B). The initial

conductance increase is clearly steeper for MDCK-I-AQP1 layers. Water permeation is completed after around 25 minutes in case of AQP1-overexpressing cells, whereas the control cells are significantly slower for compensating the osmotic pressure gradient.

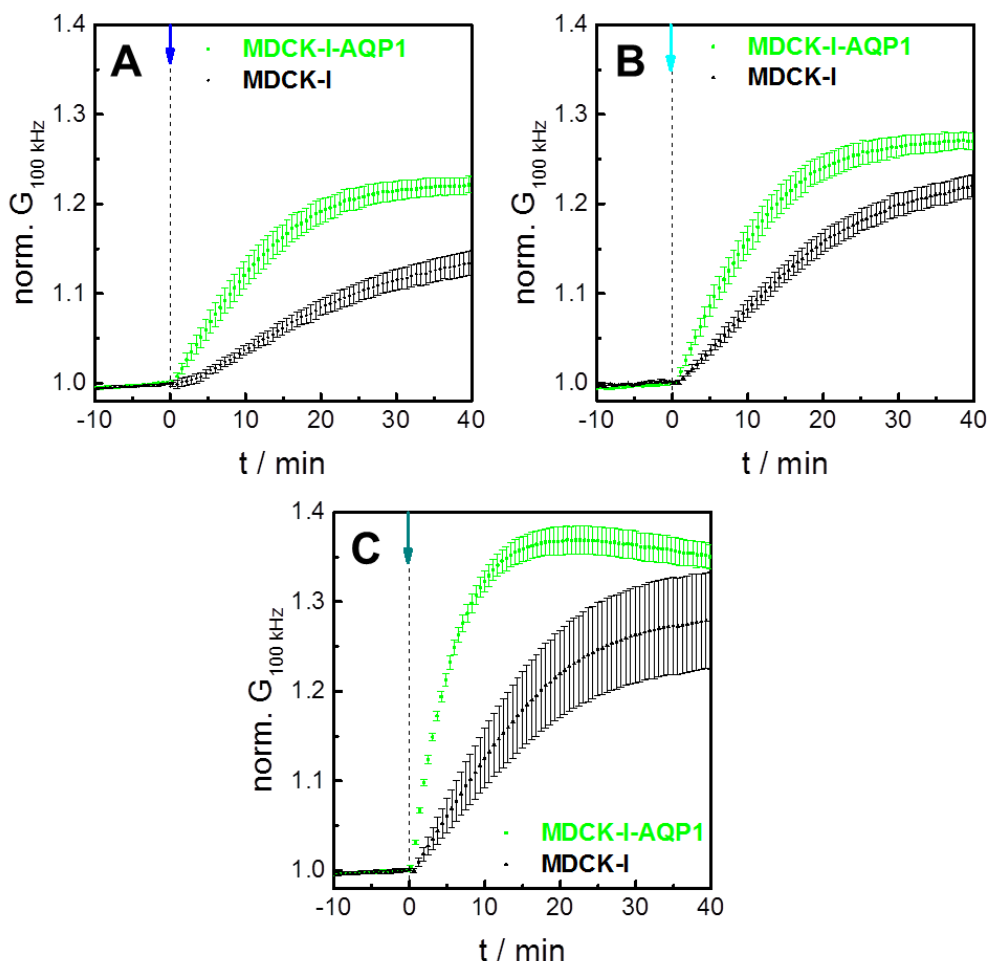


Fig. 6.6: Impedimetric water flux assay with AQP1-overexpressing and wildtype MDCK-I cells recorded with the 1st generation of water flux electrodes (mean \pm SE, $n \geq 5$). The epithelial barriers are apically exposed to variable sucrose solutions inducing a hyperosmotic pressure gradient at time point zero: **(A) 100 mM**, **(B) 150 mM**, **(C) 200 mM**. Transepithelial water flow is followed by monitoring time-dependent (normalized) conductance changes of the basolateral buffer at a frequency of 100 kHz. Absolute conductance at $t = 0$ min: $G_{100\text{kHz}}$ (100 mM, MDCK-I-AQP1) = (1053 ± 19) μS , $G_{100\text{kHz}}$ (150 mM, MDCK-I-AQP1) = (1038 ± 12) μS , $G_{100\text{kHz}}$ (200 mM, MDCK-I-AQP1) = (1073 ± 20) μS , $G_{100\text{kHz}}$ (100 mM, MDCK-I) = (1052 ± 4) μS , $G_{100\text{kHz}}$ (150 mM, MDCK-I) = (1023 ± 12) μS , $G_{100\text{kHz}}$ (200 mM, MDCK-I) = (1100 ± 18) μS .

Tab. 6.7: Overall changes of the basolateral (normalized) conductance in response to hypertonic stimulations of MDCK-I-AQP1 and MDCK-I cell layers (mean \pm SE, $n \geq 5$). The signal changes refer to the time interval between $t = 0$ min and $t = 40$ min.

c (sucrose) / mM	$\Delta\pi$ / mOsmol/kg	$\Delta\text{norm.}G_{100\text{kHz}} / \%$	
		MDCK-I	MDCK-I-AQP1
100	150	13 ± 2	22 ± 1
150	218	22 ± 1	27 ± 1
200	287	28 ± 5	35 ± 1

The strongest osmotic pressure gradient was induced by the addition of 200 mM sucrose (Fig. 6.6C). MDCK-I-AQP1 cells are characterized by an enormous conductance increase immediately after the hypertonic stimulation. At $t = 5$ min, the basolateral conductance increased drastically to (21.3 ± 0.6) %, whereas the control cells indicate only a minor increase to only (6 ± 2) %. The osmotically induced water flux is equilibrated after 15 minutes in presence of AQP1, whereas MDCK-I cells need approximately 40 minutes to completely settle the osmotic gradient. However, a slight signal decrease is observable from 25 minutes to 40 minutes in case of MDCK-I-AQP1. The overall changes of the (normalized) conductance of the basolateral buffer are listed in Tab. 6.7.

As already explained in detail in the previous chapter, the raw data of Fig. 6.6 is analogously analyzed by fitting the time-courses of $\text{norm.G}_{100\text{kHz}}$ by an exponential growth function of 1st order. The associated time-constants τ and amplitudes A of the fit-function (as absolute values) are summarized in Tab. 6.8 and compared in Fig. 6.7.

Fig. 6.7A indicates drastically lower time-constants for MDCK-I-AQP1 cells. All three applied sucrose concentrations allow a distinct discrimination between the two cell lines, but the most striking discrepancy between MDCK-I and MDCK-I-AQP1 layers is observed for 200 mM sucrose. The wildtype cells present almost three times higher time-constants than the transfected cell line. A different trend gets obvious for the amplitudes of conductance change (Fig. 6.7B). With increasing osmotic pressure gradient, the amplitudes are increasing. However, no consistent and significant differences are noticed for the two cell lines.

The differences in time-constants and the similar amplitudes are in perfect agreement to the expectations. The presence of AQP1 in the plasma membrane facilitates water permeation by lowering the activation energy of the process (Hub and Groot 2008; Madeira *et al.* 2016). Thereby, significantly higher water permeation rate across cellular barriers is provided. This accelerated water flow is reflected in the lower time-constants of MDCK-I-AQP1 layers. The overall amount of water which is transported between the apical and basolateral side is not influenced by the presence of additional water channels which is proven by the similar range of the amplitudes for both cell lines. The results of the AQP-studies highlight the immense potential of the new water flux assay, as the presence of aquaporins is unequivocally verified on a functional level by the impedance-based method.

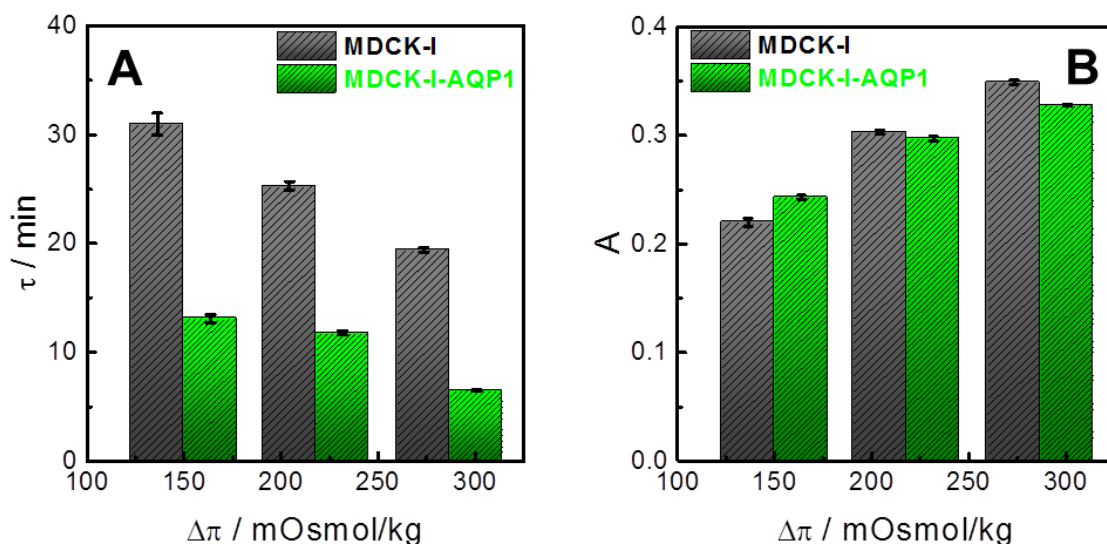


Fig. 6.7: (A) Time constants τ and (B) amplitudes A of the fit-functions of AQP1-overexpressing and wildtype MDCK-I cells in response to hypertonic stimulations (mean \pm SE, $n \geq 5$).

Tab. 6.8: Time-constants τ and amplitudes A of the fit-function for MDCK-I-AQP1 and MDCK-I cell layers determined for hypertonic stimulation experiments (mean \pm SE, $n \geq 5$).

c (sucrose) / mM	$\Delta\pi$ / mOsmol/kg	MDCK-I		MDCK-I-AQP1	
		τ / min	A	τ / min	A
100	150	31 \pm 1	0.220 \pm 0.004	13.1 \pm 0.4	0.243 \pm 0.002
150	218	25.4 \pm 0.3	0.303 \pm 0.002	11.8 \pm 0.1	0.297 \pm 0.002
200	287	19.4 \pm 0.1	0.349 \pm 0.002	6.49 \pm 0.06	0.328 \pm 0.001

6.1.6 AQP-inhibition study with the AQP1-inhibitor $\text{HAuCl}_4 \cdot 3\text{H}_2\text{O}$

Another AQP-based experiment was performed with the novel assay. For this purpose, filter-grown MDCK-I-AQP1 cells were exposed apically ($t = 0$ min) to a hypertonic solution in presence or absence, respectively, of 100 μM $\text{HAuCl}_4 \cdot 3\text{H}_2\text{O}$ that is a well-known AQP1-inhibitor (chapter 1.2.3). Please note that the AQP1-inhibitor was present during the entire assay including baseline recording. The impedance of the device was recorded in a frequency range from 10^4 Hz to 10^6 Hz. A detailed evaluation of potential cytotoxic effects of $\text{HAuCl}_4 \cdot 3\text{H}_2\text{O}$ is provided in chapter 6.5. All conductances were normalized to the conductance measured at $t = 0$ min.

The time courses of the (normalized) basolateral conductance are illustrated in Fig. 6.8. The presence of 100 μM Au^{3+} significantly affects water flux across the epithelial barrier, as indicated by the weakened increase of $\text{norm.G}_{100\text{kHz}}$. In absence of Au^{3+} , a rapid conductance increase of (23 ± 2) % within 10 minutes after sucrose addition is observable and at the end of the experiment the signal changes around (32 ± 1) % in total. In contrast, the

AQP1-inhibitor allows only a slight signal increase of (5.1 ± 0.8) %, before the conductance remains constant. After 40 minutes, a conductance increase of only (6 ± 1) % is measured in presence of $100 \mu\text{M Au}^{3+}$. The overall conductance response as well as the corresponding time-constants and amplitudes (as absolute values) of the exponential fit-functions are listed in Tab.6.9.

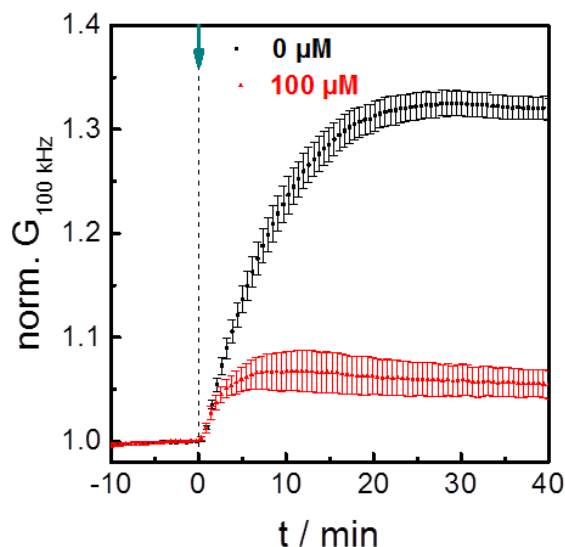


Fig. 6.8: Impedance-based monitoring of transepithelial water flux with MDCK-I-AQP1 cells recorded with a central electrode pair beneath the overlying cell layer (mean \pm SE, $n \geq 5$). At time zero, the cells are exposed to **200 mM sucrose** to induce a hyperosmotic pressure gradient. Either **0 μM** or **100 μM** of the AQP1-inhibitor **$\text{HAuCl}_4 \cdot 3\text{H}_2\text{O}$** are present during the entire measurement. Transepithelial water transport is followed by monitoring the time-dependent increase of (normalized) conductance of the basolateral buffer at a frequency of 100 kHz. Absolute conductance at $t = 0$ min: $G_{100\text{kHz}}(0 \mu\text{M}) = (1018 \pm 15) \mu\text{S}$, $G_{100\text{kHz}}(100 \mu\text{M}) = (1090 \pm 18) \mu\text{S}$.

Tab. 6.9: Overall changes of the (normalized) basolateral conductance after 40 minutes as well as the time-constants τ and amplitudes A of the exponential fit-function determined for the AQP1-inhibition studies (mean \pm SE, $n \geq 5$).

$c(\text{HAuCl}_4 \cdot 3\text{H}_2\text{O}) / \mu\text{M}$	$\Delta \text{norm.} G_{100\text{kHz}} / \%$	τ / min	A
0	32 ± 1	4.47 ± 0.08	0.363 ± 0.001
100	6 ± 1	1.43 ± 0.06	0.091 ± 0.004

However, the experimental data of Fig. 6.8 give reason to question the AQP1-inhibition experiment. The study suggests that the inhibitor affects primarily the overall signal change which is quantified as 75 % amplitude reduction. Otherwise, the time-constant which is the key parameter for describing the rate of water permeation is even decreased in presence of the inhibitor. The presence of AQP1 in the plasma membrane is supposed to accelerate water permeation, but not to have an impact on the overall amount of transported water. Therefore, it is likely that a yet unknown phenomenon has taken place during the experiment

subverting the inhibition study. The impedance-based water flux assay in its current state does not allow a deeper insight into this problematic issue. However, a different version of the impedimetric water flux assay provides an improved information content that may offer a reasonable explanation for this unexpected time-course of the basolateral conductance.

6.2 Spatially resolved monitoring of transepithelial water flux

By integrating three laterally distributed electrode pairs instead of only one central electrode pair at the bottom of the lower compartment, even laterally resolved monitoring of transepithelial water flow is enabled. Each pair is composed of two co-planar, circular electrodes with a diameter of each 500 μm and a distance of 800 μm between the two electrodes (chapter 4.2.1, Fig. 4.6). As proof-of-concept measurements, two different uniform monolayers (MDCK-I, MDCK-I-AQP1) are hypertonically stimulated. An additional water flux measurement is performed with the spatially resolved version of the assay using mixed but segregated cells confluent on one common filter membrane to highlight the lateral resolution of the device.

6.2.1 Hypertonic stimulations of MDCK-I and MDCK-I-AQP1 monolayers

Impedimetric water flux studies with lateral resolution were conducted with confluent monolayers of MDCK-I and MDCK-I-AQP1 cells. The impedance was recorded from 10^4 to 10^6 Hz. A 200 mM sucrose solution was added to the apical solution at $t = 0$ min to induce a hyperosmotic pressure gradient across the cell layer. A mere buffer exchange served as a control measurement (appendix: Fig. 11.14). All conductances are normalized to the conductance recorded at $t = 0$ min. The following paragraphs show exemplary data.

The time-courses of the conductance of the basolateral buffer at different spots beneath the cell layer are summarized in Fig. 6.9. A photograph of the electrode array provides an overview about the filter and electrode orientation during the experiment (Fig. 6.9C). The overall increase of $\text{norm.}G_{100\text{kHz}}$ as well as the corresponding time-constants τ and amplitudes A of the exponential fit-functions (as absolute values) are listed in Tab. 6.10 for the individual electrode pairs.

Fig. 6.9A displays the results for MDCK-I cells. Similar signal responses are observed for **electrode pair 2** and **electrode pair 3** with a conductance increase of 19 % after 40 minutes. **Electrode pair 1** reveals significantly reduced water permeability with a short lag phase after sucrose addition and a reduced conductance increase of only 10 % after 40 minutes. Filter-grown MDCK-I-AQP1 cells display increased water permeability (Fig. 6.9B). All three electrode pairs show a drastic conductance increase instantaneously after sucrose addition. For example, **electrode pair 2** indicates an increase of 31 % within 40 minutes.

Tab. 6.10: Overview about the overall conductance increase after 40 minutes as well as the time-constants τ and amplitudes A of the exponential fit-functions. The data refers to the device for spatially resolved water flux analysis. The errors of the individual time-constants and amplitudes correspond to the standard error of the fit. Additionally, all individual values are averaged (mean \pm SE, n = 3).

electrode pair	MDCK-I			MDCK-I-AQP1		
	$\Delta \text{norm. } G_{100\text{kHz}} / \%$	τ / min	A	$\Delta \text{norm. } G_{100\text{kHz}} / \%$	τ / min	A
1	10	20 ± 1	0.136 ± 0.002	30	8.0 ± 0.2	0.327 ± 0.004
2	19	18.0 ± 0.5	0.267 ± 0.002	31	6.13 ± 0.08	0.378 ± 0.003
3	19	19.7 ± 0.5	0.234 ± 0.001	31	6.5 ± 0.1	0.324 ± 0.003
mean \pm SE	16 ± 3	18.4 ± 0.8	0.21 ± 0.03	30.7 ± 0.3	6.9 ± 0.6	0.34 ± 0.02

The results of Fig. 6.9 demonstrate that simple impedance-based water flux assay is easily scalable to a method that provides information about water permeability across barrier-forming cells with lateral resolution. The laterally resolved analysis of the hypertonic stimulation of the MDCK-I cells results in significantly reduced changes of the basolateral conductance in comparison to the results of chapter 6.1.2. This may be explained by two aspects:

- (I) The MDCK-I monolayers under study differ in both, cell batch and cell passage number. This may cause a variation of their permeability to water, since epithelial barrier function depends on cell age (Srinivasan *et al.* 2015).
- (II) A crucial step of the water flux assay with central readout is the way of filter insertion onto the electrode containing chamber. Reproducible filter positioning is difficult to achieve due to the lack of a spacer that fixes the filter insert. This problem plays a more important role for the modified electrode array that consists of three electrode pairs. The mounting of the filter insert is even harder and may lead to inaccuracies in the detection of transepithelial water flux.

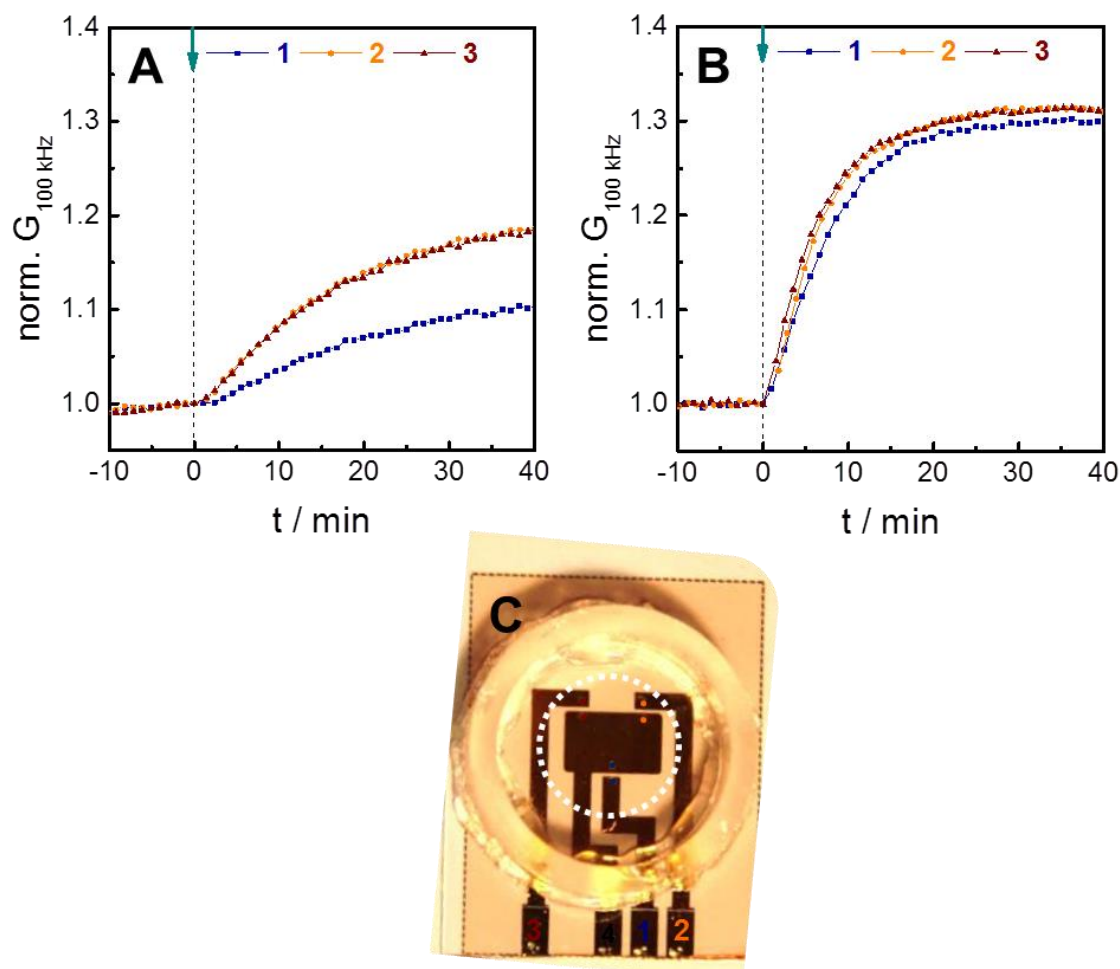


Fig. 6.9: Impedance-based water flux assay providing spatially resolved readout. The measurements are performed with a (A) MDCK-I and (B) MDCK-I-AQP1 covered filter insert. The epithelial monolayers are exposed apically to **200 mM sucrose** at $t = 0$ min to induce a hyperosmotic pressure gradient. Transepithelial water flux is followed by monitoring time-dependent (normalized) conductance changes at locally distributed positions beneath the cell layer at a frequency of 100 kHz. (C) Photograph of the electrode array used in this measurement. The three laterally distributed electrode pairs are color coded and a white, dashed circle indicates roughly the filter position. Absolute conductance at $t = 0$ min: $G_{100\text{ kHz}}$ (1, MDCK-I) = 1482 μS , $G_{100\text{ kHz}}$ (2, MDCK-I) = 2302 μS , $G_{100\text{ kHz}}$ (3, MDCK-I) = 2301 μS , $G_{100\text{ kHz}}$ (1, MDCK-I-AQP1) = 1401 μS , $G_{100\text{ kHz}}$ (2, MDCK-I-AQP1) = 2282 μS , $G_{100\text{ kHz}}$ (3, MDCK-I-AQP1) = 2285 μS .

6.2.2 Hypertonic stimulation of mixed but segregated cell layers

Besides the impedance-based analysis of uniform monolayers, mixed but segregated cell layers were examined with the spatially resolved device. The impedance was recorded from 10^4 Hz to 10^6 Hz. A hypertonic solution containing 200 mM sucrose was added to the apical side at time point zero. All conductances are normalized to the conductance at $t = 0$ min.

Fig. 6.10A presents laterally resolved water flux monitoring across a mixed cell monolayer cultivated on one common filter membrane with segregated areas covered by MDCK-I and MDCK-I-AQP1 cells. The orientation of the two different cell lines above the electrode pairs is

assigned by a color code in Fig. 6.10B. Electrode pair 1 is located beneath an MDCK-I-AQP1-dominated region of the filter support and shows a distinguishable conductance increase compared to the other two electrode pairs. Electrode pair 2 and electrode pair 3 are localized beneath an MDCK-I domain. After ten minutes, a conductance increase of 20 % has been detected by electrode pair 1, whereas a signal increase of only 13 % and 14 % has been recorded for electrode pair 2 or electrode pair 3, respectively. The overall conductance alteration is also discriminable 40 minutes after the hypertonic stimulation with changes of 30 % for electrode pair 1 and 26 % for both, electrode pair 2 and electrode pair 3.

In analogy to the procedure that was described above, the time-courses of $\text{norm.G}_{100\text{kHz}}$ are fitted by an exponential growth function of 1st order revealing the time-constants and amplitudes of the fit-function. Electrode pair 1 that is located beneath AQP1-overexpressing cells provides significant lower time-constants ($8.2 \text{ min} \pm 0.3 \text{ min}$) compared to the other two electrode pairs. This is in perfect agreement with the expectations, since a lower time-constant goes along with a higher water permeation rate. The higher rate for water permeation in the region of the filter support above electrode pair 1 is associated with the overexpression of the membrane water channel AQP1 that favors water flux energetically (Hub and Groot 2008; Madeira *et al.* 2016). The overall conductance changes of the basolateral buffer as well as the time-constants τ and amplitudes A of the exponential fit-functions (as absolute values) are summarized in Tab. 6.11.

Tab. 6.11: Overview about the overall conductance increase recorded with the three locally distributed electrode pairs after 40 minutes of hyperosmotic stimulation as well as the time-constants τ and amplitudes A of the exponential fit-functions. The errors of the individual time-constants and amplitudes are standard errors of the fitting routine.

electrode pair	cell line	$\Delta\text{norm.G}_{100\text{kHz}} / \%$	τ / min	A
1	MDCK-I-AQP1	30	8.2 ± 0.3	0.361 ± 0.006
2	MDCK-I	26	12.9 ± 0.6	0.307 ± 0.005
3	MDCK-I	26	12.3 ± 0.5	0.301 ± 0.004

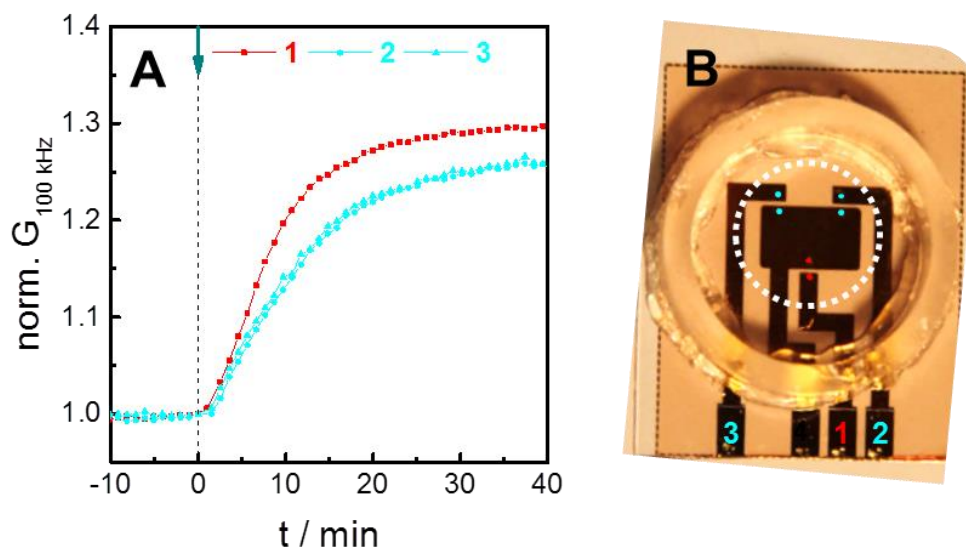


Fig. 6.10: (A) Impedance-based water flux assay with laterally resolved readout of a mixed but segregated epithelial layer cultivated on one common Transwell® filter. A hyperosmotic gradient is induced by applying **200 mM sucrose** to the apical side at time point zero. The associated water flow across the cell layer is followed over time by monitoring time-dependent (normalized) conductance changes of the basolateral buffer at a frequency of 100 kHz. Spatially resolved detection is yielded by using three locally distributed electrode pairs beneath the cell layer. (B) Photograph of the applied electrode array. The position of the filter insert is roughly indicated by a grey, dashed circle. The location of the two different cell types is color coded (**MDCK-I**, **MDCK-I-AQP1**). Absolute conductance at $t = 0 \text{ min}$: $G_{100 \text{ kHz}}$ (1) = 1492 μS , $G_{100 \text{ kHz}}$ (2) = 2424 μS , $G_{100 \text{ kHz}}$ (3) = 2416 μS . The time-courses of $\text{norm. } G_{100 \text{ kHz}}$ that are presented here were obtained by a single measurement.

6.3 Combined impedance-based monitoring of osmotically induced transepithelial water flux and TER ($P_{\text{OS}}\text{TER}$ -assay)

Prior to epithelial water flux studies the transepithelial electrical resistance of the cell layer under study is usually recorded in a separated measurement to ensure barrier integrity. The device presented here intends to combine water flux and resistance measurements across epithelial cell layers by using an impedance-based readout for both, TER and P_{OS} . Interdigitated gold electrodes (chapter 4.2.1, Fig. 4.4) are located beneath most of the cell layer and provide integral monitoring of osmotically induced water flux between two chemical compartments with outstanding time-resolution. By integrating a Teflon® spacer (thickness 100 μm , chapter 4.3.2.1, Fig. 4.12) into the measurement chamber, on which the cell-covered filter insert is placed, the initial donor volume is clearly determined by the thickness and inner diameter of the spacer ($V_0 = 9.85 \cdot 10^{-3} \text{ cm}^3$). Exact knowledge of V_0 is a basic requirement for the calculation of P_{OS} values. Simultaneous monitoring of ionic permeability across the same cell layer is realized by dipping a stainless steel electrode (chapter 4.2.2, Fig. 4.9B) into

the apical solution and by using the interdigitated gold-film electrodes as basolateral counter electrode.

6.3.1 Characterization of the electrode

Frequency spectra of the impedance using PBS⁺⁺/glucose (1 g/L)

Cell-free filter inserts were placed onto the Teflon[®] spacer that was described above. Interdigitated concentric gold electrodes with a width of 400 μm and a gap of 400 μm (IDE-400) were used as co-planar, basolateral electrodes. A stainless steel dipping electrode was dipped into the apical buffer (Fig. 6.11A). The impedance was measured both, in **P_{OS}-mode (1 vs. 2)** and **TER-mode (1 vs. 3)**, from 1 Hz to 10⁵ Hz. Frequency spectra of the impedance magnitude $|Z|$, the conductance G (which is the inverse of the resistance R) and the capacitance C of both measuring modes are illustrated in Fig. 6.11B-D. The recorded spectra are similar in P_{OS}- and TER-mode. The total impedance is dominated by the resistance of the buffer at higher frequencies from 10⁴ Hz to 10⁵ Hz. At frequencies from 1 Hz to 10⁴ Hz, the electrode-electrolyte interface impedance is dominating the signal. In contrast to the impedance spectra of the above described electrode design for water flux measurements (chapter 6.1.1), the interdigitated electrodes indicate no parasitic influences at the high frequency end. By equivalent circuit modeling, the elements of the equivalent circuit presented in chapter 3.1.2 (Fig. 3.3) are assessable and listed in Tab. 6.12. The filter resistance R_{ins} and capacitance C_{ins} are only determined in TER-mode with values of $R_{\text{ins}} = (21 \pm 2) \Omega\text{cm}^2$ and $C_{\text{ins}} = (7.2 \pm 0.6) \mu\text{F}/\text{cm}^2$. The TER values of the cell-covered filter supports need to be corrected for the values of R_{ins} and C_{ins} by applying an expanded equivalent circuit which was described in chapter 3.1.2 (Fig. 3.5). The contribution of the filter insert is irrelevant for P_E-mode as the impact of the cell-free filter insert is only slightly observable in the middle frequency regime. However, transepithelial water flux is followed at a frequency of 100 kHz.

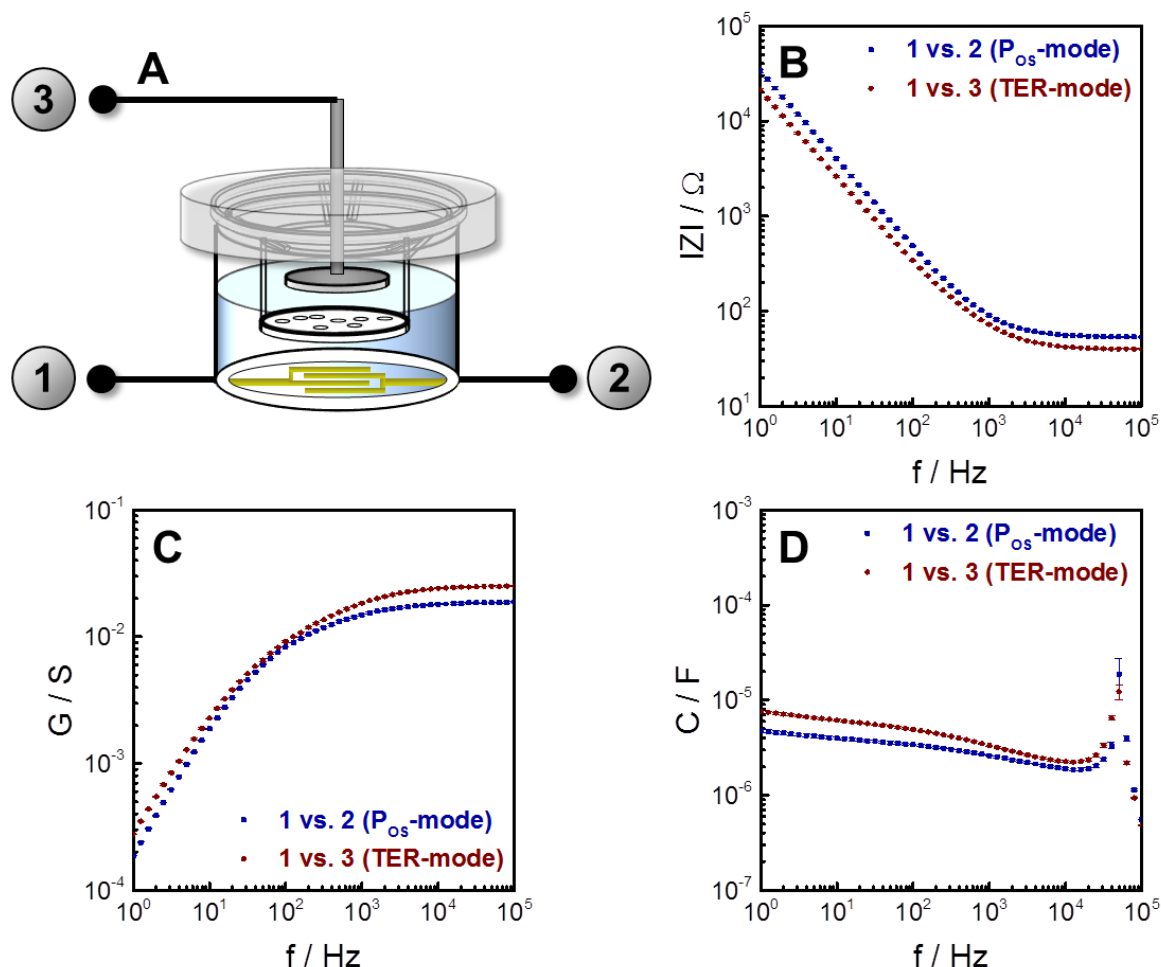


Fig. 6.11: (A) Schematic of the experimental setup for electrode characterization of the P_{OS}TER-device using IDE-400 (width 400 μm / gap 400 μm). A cell-free filter insert is placed onto a Teflon[®] spacer. Spectra are displayed as (B) impedance magnitude $|Z|$, (C) conductance G and (D) capacitance C for both measuring modes (mean \pm SE, $n = 3$).

Tab. 6.12: Values of the different circuit elements after equivalent circuit modeling of the data of Fig. 6.11 (mean \pm SE, $n = 3$). The values are related to IDE-400. The resistance of the filter insert R_{ins} and the filter membrane capacitance C_{ins} are only determined for TER-mode.

parameter	P _{OS} -mode (1 vs. 2)	TER-mode (1 vs. 3)
R_{bulk} / Ω	53.3 ± 0.7	40.0 ± 0.6
$A_{\text{CPE}} / \mu\text{Fs}^{-1}$	4.8 ± 0.2	8.0 ± 0.3
n_{CPE}	0.927 ± 0.003	0.907 ± 0.003
$R_{\text{ins}} / \Omega\text{cm}^2$		21 ± 2
$C_{\text{ins}} / \mu\text{F}/\text{cm}^2$		7.2 ± 0.6

Determination of the cell constant of the device

The impact of altering the ionic concentration of the buffer on the recorded conductance is shown in Fig. 6.12A. The impedance was measured in presence of different concentrations of KCl (25 / 50 / 75 / 100 / 125 / 150 / 175 / 200 mM) to simulate different ionic

concentrations. The specific conductivity γ of the individual KCl concentrations was determined separately by means of a conductivity sensor (chapter 4.1.5, Tab. 4.6). The conductance of the buffer is increased with increasing KCl concentrations. Tab. 6.13 provides an overview about the measured conductances of the individual KCl solutions at a frequency of 100 kHz.

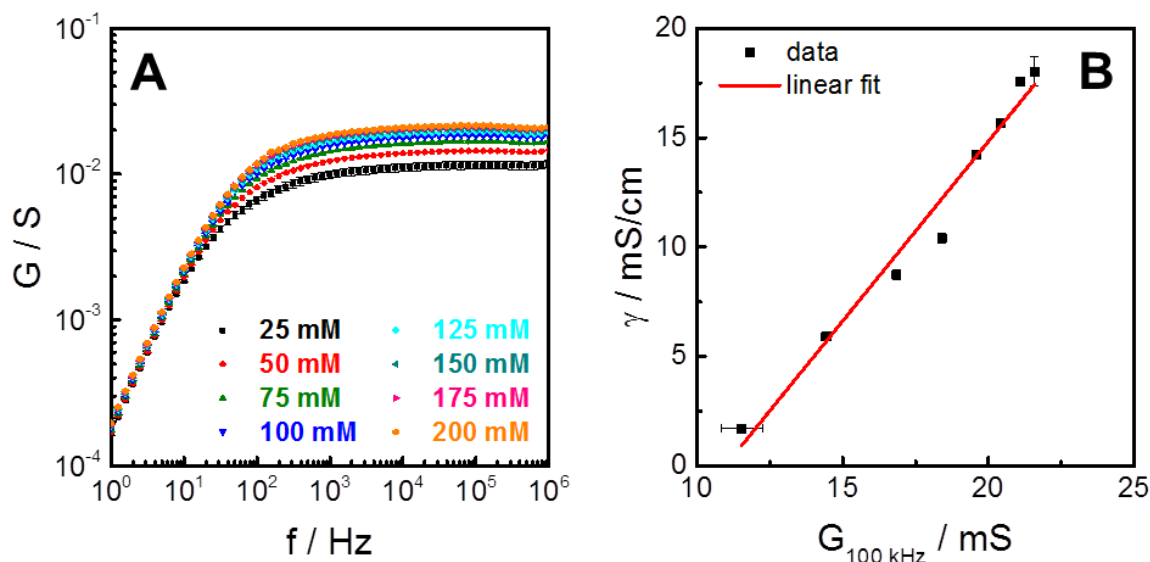


Fig. 6.12: (A) Conductance spectra recorded with IDE-400 (P_{OS} -mode) in presence of variable KCl concentrations (mean \pm SE, $n = 3$) mimicking different ionic concentrations of the buffer. (B) Determination of the cell constant of the P_{OS} TER-device ($K = \gamma/G$). The specific conductivity γ of the KCl solutions are plotted against the measured conductance at a frequency of 100 kHz (both parameters: mean \pm SE, $n = 3$). The individual specific conductivities γ of the different KCl solutions are plotted as a function of the recorded conductance at a frequency of 100 kHz (mean \pm SE, $n = 3$). The linear relationship between the two parameters is analyzed by linear regression revealing a cell constant of $(1.7 \pm 0.1) \text{ cm}^{-1}$. The error is provided by Origin2016 ($R^2 = 0.975$).

Tab. 6.13: Conductances that are recorded by IDE-400 at a frequency of 100 kHz for variable KCl concentrations simulating different ionic concentrations (mean \pm SE, $n = 3$).

c (KCl) / mM	G_{100kHz} / mS	c (KCl) / mM	G_{100kHz} / mS
25	11.5 ± 0.7	125	19.58 ± 0.02
50	14.44 ± 0.04	150	20.41 ± 0.02
75	16.84 ± 0.02	175	21.10 ± 0.01
100	18.41 ± 0.02	200	21.58 ± 0.02

The individual specific conductivities γ of the different KCl solutions are plotted as a function of the conductance ($f = 100 \text{ kHz}$) measured by the impedance measurement (Fig. 6.12B). There is a linear relationship between γ and G_{100kHz} which is analyzed by linear regression. The slope of this linear fit-function provides an electrode-specific parameter that is denoted

as the *cell constant* K ($= \gamma/G$). The cell constant resembles the slope of the linear fit-function and is $(1.7 \pm 0.1) \text{ cm}^{-1}$ for IDE-400.

6.3.2 Hypertonic stimulations of different epithelial monolayers

The $P_{\text{OS}}\text{TER}$ -assay was conducted with confluent monolayers of different epithelial cell lines (MDCK-I, MDCK-II, MDCK-I-AQP1). The impedance was followed at 100 kHz in **P_{OS} -mode** and from 1 Hz to 10^5 Hz in **TER-mode**. At time zero, the cell layers were osmotically stimulated by adding hypertonic solutions (50 mM / 200 mM sucrose) to the apical compartment. A mere buffer exchange does not influence $\text{norm.G}_{100\text{kHz}}$ significantly (appendix: Fig. 11.15). The following paragraphs show exemplary data with typical time-courses of $\text{norm.G}_{100\text{kHz}}$ and TER for all three cell lines.

$P_{\text{OS}}\text{TER}$ -assay using 50 mM sucrose

Simultaneous recording of transepithelial water flux and ionic permeability after the induction of a moderate osmotic pressure gradient (50 mM sucrose) across the different cell layers is illustrated in Fig. 6.13. All conductances are normalized to the conductance measured at $t = 0$ min.

The transepithelial electrical resistance of MDCK-I cells (Fig. 6.13A) is $1627 \text{ } \Omega\text{cm}^2$ at time point zero and reveals a continuous increase between $t = 10$ min and $t = 40$ min to $2421 \text{ } \Omega\text{cm}^2$. After hypertonic stimulation the conductance of the basolateral buffer increases time-dependently about 1.7 % within 40 minutes. However, the signal response is retarded in the beginning of the experiment as no signal response is observed within the first five minutes after the addition of 50 mM sucrose.

Filter-grown MDCK-II cells show a relatively constant TER after the osmotic stimulus with a value of $83 \text{ } \Omega\text{cm}^2$ at $t = 40$ min (Fig. 6.13B). A more pronounced increase of $\text{norm.G}_{100\text{kHz}}$ gets obvious compared to MDCK-I cells. The MDCK-II layer does not indicate a lag phase after the addition of sucrose. At $t = 10$ min, the conductance increased by about 1.2 %. After 40 minutes of incubation, an increase of 2.1 % is reached.

MDCK-I-AQP1 cells (Fig. 6.13C) indicate the strongest response of the conductance of the basolateral buffer after the hypertonic stimulation. The conductance increases instantaneously after sucrose addition. Already after 3.5 minutes, an increase of 2.0 % is

recorded resembling a three times stronger response compared to MDCK-II cells. The time-course of $\text{norm.}G_{100\text{kHz}}$ suggests that the osmotic gradient is compensated only 20 minutes after the osmotic stimulation. After 40 minutes, a conductance change of 5.2 % is measured. The TER of the filter-grown MDCK-I-AQP1 cells is increasing after sucrose addition from $370 \Omega\text{cm}^2$ ($t = 0 \text{ min}$) to $736 \Omega\text{cm}^2$ ($t = 40 \text{ min}$).

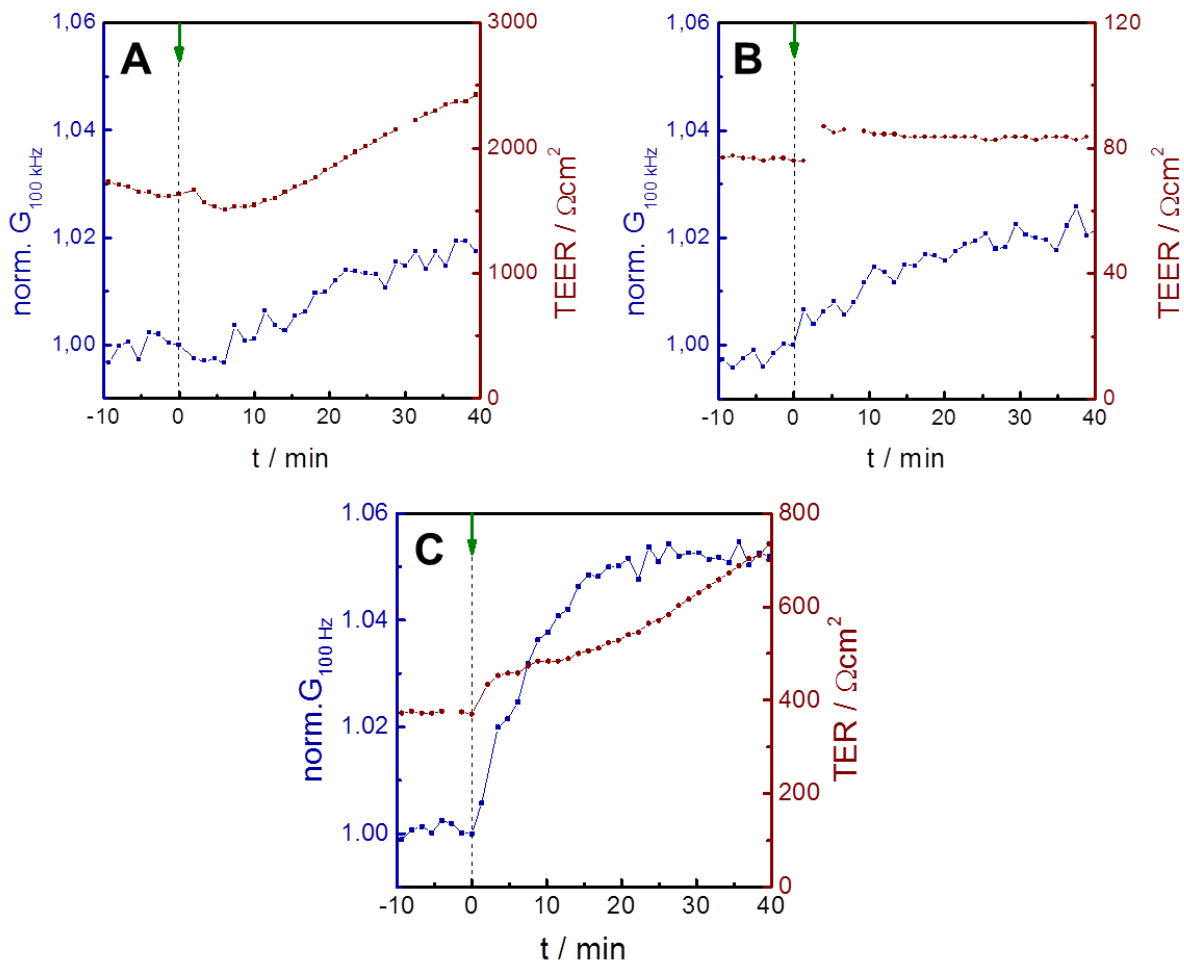


Fig. 6.13: $P_{\text{os}}\text{TER}$ -assay with confluent monolayers of **(A)** MDCK-I, **(B)** MDCK-II and **(C)** MDCK-I-AQP1 cells recorded with IDE-400. The epithelial barriers are exposed apically to a hypertonic solution (**50 mM sucrose**) at $t = 0 \text{ min}$. Transepithelial water flow is followed over time by monitoring (normalized) conductance changes of the basolateral buffer at a frequency of 100kHz (P_{os} -mode). The transfilter measurement (TER -mode) provides time-resolved TER values of the same monolayer simultaneously. Absolute conductance at $t = 0 \text{ min}$: $G_{100\text{kHz}}$ (MDCK-I) = 19.8 mS, $G_{100\text{kHz}}$ (MDCK-II) = 17.8 mS, $G_{100\text{kHz}}$ (MDCK-I-AQP1) = 19.0 mS.

$P_{\text{os}}\text{TER}$ -assay using 200 mM sucrose

Simultaneous monitoring of transepithelial water flux and ionic permeability across different cell layers after the induction of a strong osmotic pressure gradient (200 mM sucrose) is

displayed in Fig. 6.14. All conductances are normalized to the conductance measured at $t = 0$ min.

TER of filter-grown MDCK-I cells is decreasing after hyperosmotic stimulation and levels off at a value of $1128 \Omega\text{cm}^2$ (Fig. 6.14A). However, the TER values show a distinct decrease even at baseline recording. The time-course of the basolateral conductance has a short lag phase of two minutes prior to a significant increase of 2.0 % at $t = 10$ min or 5.2 % at $t = 40$ min, respectively.

The MDCK-II layer that is challenged with a 200 mM sucrose solution shows constant TER values of approximately $62 \Omega\text{cm}^2$ during the entire measurement (Fig. 6.14B). The conductance increase of the basolateral buffer is faster for MDCK-II cells in comparison to MDCK-I cells. After a short lag phase of two minutes, a signal increase of 2.5 % is recorded at $t = 10$ min. The overall change of the basolateral conductance (5.3 %) is similar to the change recorded for MDCK-I cells.

The most striking osmotic water flow is observed for MDCK-I-AQP1 cells (Fig. 6.14C). The basolateral conductance indicates a drastic increase directly after sucrose addition. At $t = 3.6$ min, an increase of 2.1 % is measured. Subsequently, $\text{norm.G}_{100\text{kHz}}$ is increasing about 7.3 % at $t = 17$ min, before a saturation gets obvious. The conductance changed about 7.9 % 40 minutes after the osmotic stimulation. The simultaneously monitored time-course of TER displays a significant addition peak from $531 \Omega\text{cm}^2$ to $776 \Omega\text{cm}^2$, before TER reaches a minimum of $502 \Omega\text{cm}^2$ at $t = 7.7$ min. However, the TER values show an increase even at baseline recording. Afterwards, TER is recovering and stabilizes at a magnitude of $760 \Omega\text{cm}^2$. The total changes of the (normalized) basolateral conductance are summarized in Tab. 6.14.

Tab. 6.14: Total changes of the (normalized) basolateral conductance after hypertonic stimulation with increasing buffer osmolality and the cell lines under study. The signal changes refer to the time interval between $t = 0$ min and $t = 40$ min.

cell line	$\Delta\pi$ / mOsmol/kg	$\Delta\text{norm.G}_{100\text{kHz}}$ / %
MDCK-I	83	1.7
	287	5.2
MDCK-II	83	2.1
	287	5.3
MDCK-I-AQP1	83	5.2
	287	7.9

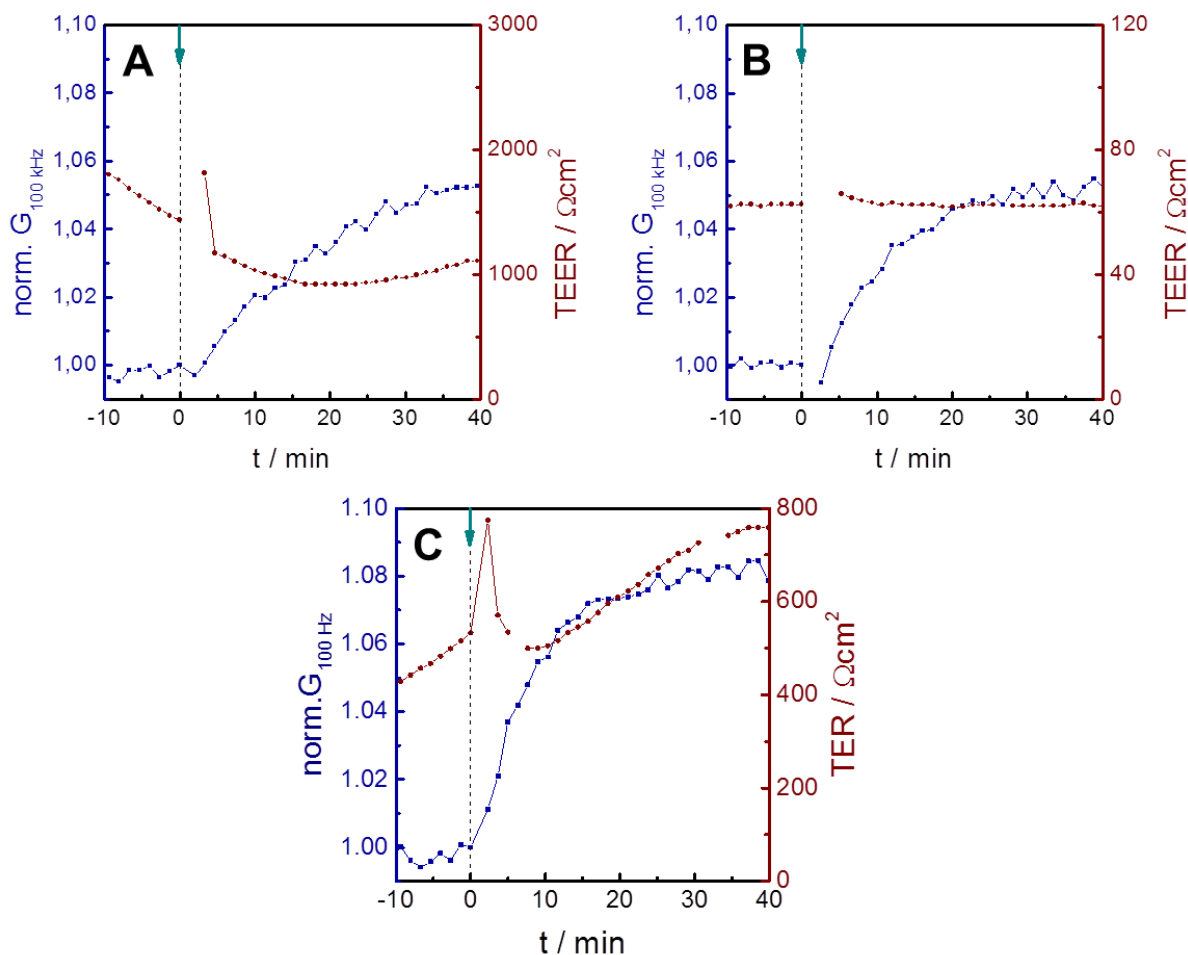


Fig. 6.14: P_{OS}TER-assay with confluent monolayers of **(A)** MDCK-I, **(B)** MDCK-II and **(C)** MDCK-I-AQP1 cells performed with IDE-400. The epithelial barriers are hypertonically stimulated by an apical addition of **200 mM sucrose** at t = 0 min. Transepithelial water flow is followed over time by monitoring (normalized) conductance changes of the basolateral solution at a frequency of 100 kHz (**P_{OS}-mode**). The transfilter measurement (**TER-mode**) provides time-resolved TER values of the same monolayer simultaneously. Absolute conductance at t = 0 min: G_{100kHz} (MDCK-I) = 19.9 mS, G_{100kHz} (MDCK-II) = 17.2 mS, G_{100kHz} (MDCK-I-AQP1) = 19.4 mS.

The TER values that are provided by the P_{OS}TER-device are in a reasonable range and match other reported TER values for the cell lines under study (Tab. 5.4). The trend in barrier function is perfectly reflected by the order of TER (MDCK-I > MDCK-II). Obviously, the transfected MDCK-I cells (MDCK-I-AQP1) form leakier monolayers compared to the wildtype MDCK-I cells, as indicated by a significantly lower transepithelial electrical resistance. However, TER of MDCK-I-AQP1 has still a value that is acceptable for MDCK-I cells.

As already described in chapter 6.1, the conductance of the basolateral solution is coupled to changes of the ionic concentration. After the addition of a hypertonic solution into the apical compartment, water flux without solute flux from the basolateral to the apical side of the cell layer occurs to compensate the osmotic gradient. Thereby, the ionic concentration of the

basolateral buffer is increased resulting in an increase of the basolateral conductance which is exactly mirrored in the time-courses of $\text{norm.G}_{100\text{kHz}}$ that are shown above. In addition, the $\text{P}_{\text{OS}}\text{TER}$ -device is suitable for performing AQP-based studies, as the presence of the water channel AQP1 is clearly detectable. The increase of the basolateral conductance is significantly faster for MDCK-I-AQP1 monolayers compared to the two other cell lines. This is in perfect agreement with the expectations, as the high amount of AQP1 in the plasma membrane lowers the activation energy of transcellular water permeation facilitating transepithelial water flow (Hub and Groot 2008; Madeira *et al.* 2016).

Interestingly, the first version of the impedimetric water flux assay that offers central water flow recording shows a significantly stronger conductance response after osmotic stimulation. Thus, the central readout provides a higher sensitivity for water flux detection in comparison to the $\text{P}_{\text{OS}}\text{TER}$ -approach. The basolateral electrode arrays differ for the two different versions of the assay. A huge difference of the two electrode designs originates from the absolute conductance when the electrodes are immersed with the basolateral buffer. Whereas IDE-400 is characterized by high conductances of around 20 mS in presence of $\text{PBS}^{++}/\text{glucose}$ (1 g/L), the central electrode pair provides significantly reduced basolateral conductance in the range of 1.3 mS. This difference in the absolute conductances might be an explanation for the distinctive discrepancies of the time-resolved conductance changes for the two different assay versions.

6.3.3 Hypotonic stimulations of MDCK-II monolayers

To test the $\text{P}_{\text{OS}}\text{TER}$ -device for its capability of bidirectional monitoring of transepithelial water flux, the osmotic gradient across the cell layer was reversed by adding different hypotonic solutions to the apical compartment at $t = 0$ min. The impedance was measured at 100 kHz in **P_{OS} -mode** and from 1 Hz to 10^5 Hz in **TER-mode**. In contrast to the hypotonic stimulations that were conducted with the centrally located electrode pair (chapter 6.1.3), the $\text{P}_{\text{OS}}\text{TER}$ -device permits the use of a readout frequency of 100 kHz, since no significant parasitic capacitances are observed for IDE-400. Please note that the recorded TER values are denoted as *apparent transepithelial electrical resistance* (TER_{app}) in presence of hypotonic buffers. This is due to the low, non-physiological specific conductivity of the hypotonic buffers applied in this thesis (Tab. 4.11). The results of the $\text{P}_{\text{OS}}\text{TER}$ -assay for the

hypotonic stimulations of different cell lines are summarized in Fig. 6.15. All conductances are normalized to the conductance recorded at $t = 0$ min.

The addition of an isotonic solution does not alter the basolateral conductance sustainably, as no transepithelial water flux occurs (Fig. 6.15A). TER_{app} of the same MDCK-II layer remains constant during the entire measurement. However, the absolute TER_{app} values are relatively high for MDCK-II cells in the range of $190 \Omega\text{cm}^2$.

The apical exposure to a moderate hypotonic buffer (HYPO A) that induces an osmotic pressure gradient of 58 mOsmol/kg results in a slight decrease of TER_{app} from $206 \Omega\text{cm}^2$ at $t = 0$ min to $188 \Omega\text{cm}^2$ at $t = 40$ min (Fig. 6.15B). The simultaneously recorded conductance of the basolateral buffer indicates an unequivocal decrease of 1.5 % at $t = 5$ min or 2.3 % at $t = 40$ min, respectively.

The strongest transepithelial water flux is observed for the addition of a hypotonic buffer (HYPO B) that induces an osmotic pressure gradient of 95 mOsmol/kg (Fig. 6.15C). Here, the basolateral conductance shows a decrease of 2.5 % at $t = 5$ min or 3.9 % at $t = 40$ min, respectively. The apparent transepithelial electrical resistance of the same monolayer remains stable at a value of $185 \Omega\text{cm}^2$ over time with a negligible addition peak. Tab. 6.15 displays an overview about the total changes of $norm.G_{100\text{kHz}}$ after hypotonic stimulations of MDCK-II cells.

The time-courses of $norm.G_{100\text{kHz}}$ presented in Fig. 6.15 prove the rationale of impedance-based water flux monitoring. The induction of a hypoosmotic pressure gradient leads to water flux but no solute flux from the apical into the basolateral compartment. Thereby, the ionic concentration of the basolateral buffer is decreasing. The associated drop of the conductance of the basolateral buffer confirms the direction of water permeation.

The unusually high apparent TER values of the MDCK-II monolayers under study are connected with the low specific conductivity of the hypotonic buffers that were used in this thesis. The overall impedance magnitudes are increased due to the low conductivity pretending higher TER values. This problem is acknowledged by denoting the detected values as apparent transepithelial electrical resistances.

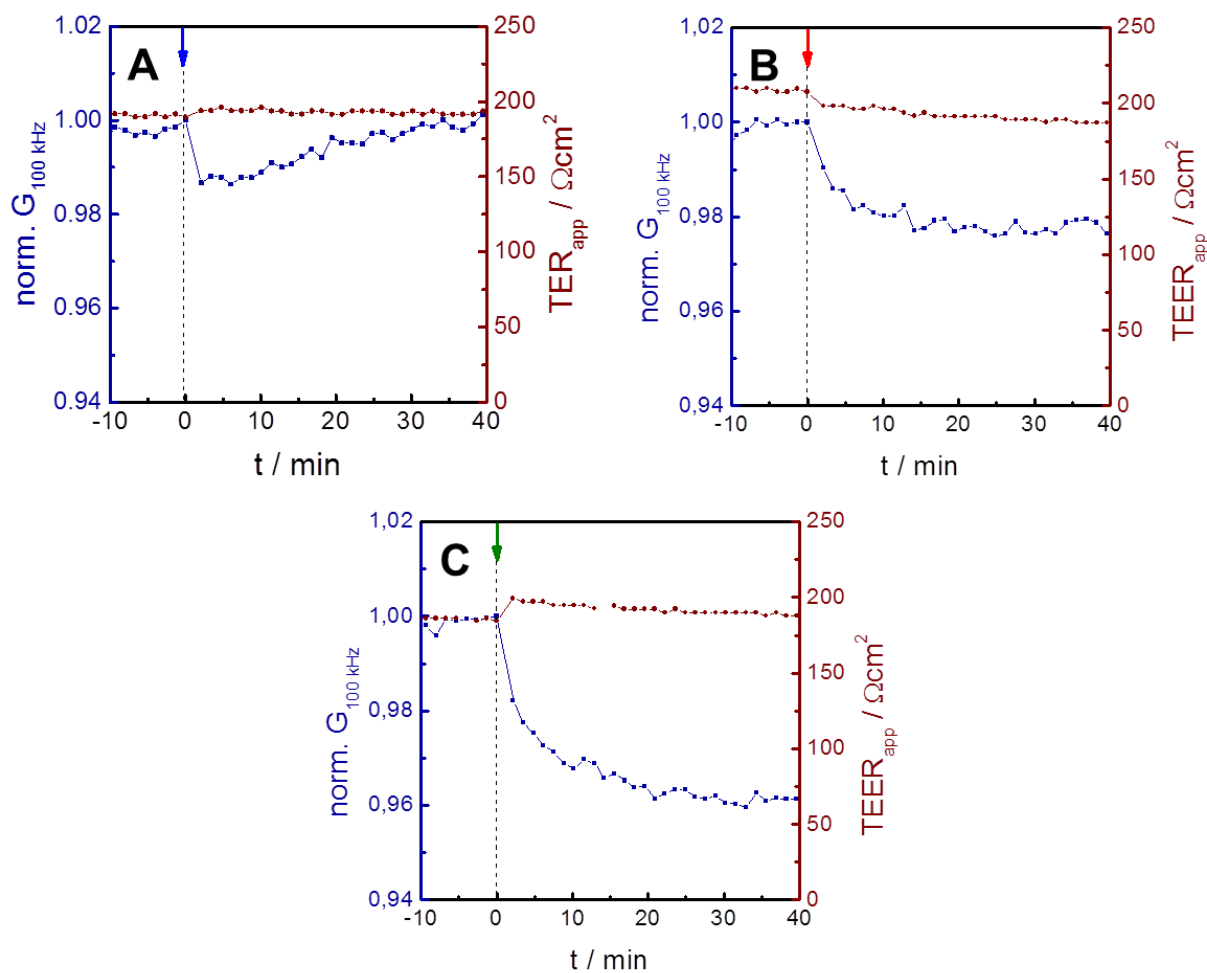


Fig. 6.15: P_{OS} TER-assay with confluent MDCK-II monolayers recorded with IDE-400. At time point zero, different hypotonic stimulations were induced by apical addition of **(A)** an isotonic buffer (**ISO**), **(B)** a moderate hypotonic buffer (**HYPO A**) and **(C)** a strong hypotonic buffer (**HYPO B**). Transepithelial water flow is followed over time by monitoring (normalized) conductance changes of the basolateral solution at a frequency of 100 kHz (**P_{OS} -mode**). The transfilter measurement (**TER-mode**) provides time-resolved apparent TER values of the same monolayer simultaneously. Absolute conductance at $t = 0$ min: $G_{100\text{kHz}}$ (ISO) = 12.1 mS, $G_{100\text{kHz}}$ (HYPO A) = 11.9 mS, $G_{100\text{kHz}}$ (HYPO B) = 12.2 mS.

Tab. 6.15: Total changes of the (normalized) basolateral conductance after different hypotonic stimulations of MDCK-II monolayers. The signal changes refers to the time interval between $t = 0$ min and $t = 40$ min.

buffer	$\Delta\pi$ / mOsmol/kg	$\Delta\text{norm.}G_{100\text{kHz}}$ / %
ISO	0	0.1
HYPO A	58	2.3
HYPO B	95	3.9

6.3.4 Calculation of P_{OS} values

A crucial improvement of the P_{OS} TER-assay over the first approach of impedance-based water flux detection is the ability of calculating osmotic water permeability coefficients (P_{OS}). In contrast to the first assay version introduced in chapter 6.1, the initial basolateral volume

V_0 is now defined by the thickness and the inner diameter of a Teflon[®] spacer ($9.85 \cdot 10^{-3} \text{ cm}^3$) which is an unconditional requirement for the computation of P_{OS} values (chapter 3.2.2, equations 3.39 and 3.45). In analogy to chapter 6.1.4, the time-courses of $\text{norm.G}_{100\text{kHz}}$ are analyzed by fitting the parameters of an exponential growth function of 1st order ($y = A \times \exp\left(\frac{x}{\tau}\right) + y_0$) or exponential decay function of 1st order ($y = A \times \exp\left(\frac{-x}{\tau}\right) + y_0$), respectively, to the experimental raw data. Thereby, the *time-constants* τ and *amplitudes* A of the fit-functions are quantified and expressed as absolute magnitudes. The osmotic water permeability coefficients are calculated according to the protocol of chapter 3.2.2. The fitting procedure was conducted with Origin2016. The results for the hypertonic studies are presented in Tab. 6.16 as well as in Fig. 6.16. The corresponding τ , A and P_{OS} values for the hypotonic stimulation experiments are summarized in Tab. 6.17. The apical addition of 50 mM sucrose induces a moderate osmotic pressure gradient of 83 mOsmol/kg, whereas the addition of 200 mM sucrose to the apical compartment leads to a strong osmotic pressure gradient of 287 mOsmol/kg. The use of HYPO A and HYPO B induces a transepithelial osmotic gradient of 58 mOsmol/kg or 95 mOsmol/kg, respectively.

The time-constants for the cell lines under study show several distinctive features (Fig. 6.16A):

- (I) A decrease of the time-constant goes along with a higher osmotic pressure gradient. Lower time-constants indicate a faster compensation of the transepithelial osmotic gradient.
- (II) The AQP1-overexpressing MDCK-I cells have significantly smaller time-constants indicating a faster equilibration of the osmotic pressure gradient. This facilitated transepithelial water permeation is based on the presence of AQP1 in the plasma membrane which lowers the activation energy of water permeation across epithelial barriers (Hub and Groot 2008; Madeira *et al.* 2016).
- (III) Furthermore, the time-constants for MDCK-II cells are clearly lower than for MDCK-I cells. This trend was also observed with the central water flux assay (chapter 6.1.4).

The corresponding amplitudes of the fit-functions present more uniform magnitudes for the three cell types compared to the time-constants (Fig. 6.16B). No significant discrimination of the amplitudes of the three cell lines under study is possible in presence of 200 mM sucrose. However, MDCK-I-AQP1 cells show moderately increased amplitudes of (0.051 ± 0.004) compared to MDCK-I and MDCK-II cells after the addition of 50 mM sucrose. Moreover, a distinct correlation between the induced osmotic pressure gradient and the resulting amplitudes gets obvious. Higher osmotic pressure gradients result in higher amplitudes due to the increased amount of water that is permeating for the equilibration of the osmotic gradient.

The P_{OS} values for MDCK-I and MDCK-II monolayers are in the same range independent of the osmotic pressure gradient that was induced across the cell layer and range from $0.7 \mu\text{m/s}$ to $2.1 \mu\text{m/s}$ (Fig. 6.16C). A four times higher P_{OS} value is observed for confluent monolayers of MDCK-I-AQP1 cells. The differences of the osmotic water permeability coefficients for the three different cell lines seem to be more intensive for the addition of 50 mM sucrose instead of 200 mM sucrose.

As already observed in chapter 6.1.4, the time-constants and P_{OS} values indicate faster water flux after hypotonic instead of hypertonic stimulations. The time-constants for MDCK-II cells after the addition of hypotonic buffers are significantly lower compared to the time-constants that were found in hypertonic stimulation experiments. A possible explanation for this difference may be due to the different flux directions and the experimental setup and was already discussed in chapter 6.1.4

Tab. 6.16: Overview about the time-constants τ and amplitudes A (both mean \pm SE, $n = 3$) as returned by the fitting procedure and the associated osmotic water permeability coefficients P_{OS} (mean \pm maximal error, $n = 3$) determined for the hypertonic stimulations.

cell line	c (sucrose) / mM	$\Delta\pi$ / mOsmol/kg	τ / min	A	P_{OS} / $\mu\text{m/s}$
MDCK-II	50	83	20 ± 3	0.030 ± 0.004	1.5 ± 0.4
	200	287	12 ± 2	0.076 ± 0.002	1.9 ± 0.2
MDCK-I	50	83	32 ± 5	0.037 ± 0.001	1.4 ± 0.6
	200	287	24 ± 2	0.079 ± 0.005	0.9 ± 0.2
MDCK-I-AQP1	50	83	10 ± 2	0.051 ± 0.004	5.7 ± 0.5
	200	287	8.6 ± 0.3	0.085 ± 0.002	2.9 ± 0.2

Tab. 6.17: Overview about the time-constants τ and amplitudes A (both mean \pm SE, $n = 3$) as returned by the fitting procedure for MDCK-II cell layers and the resulting osmotic water permeability coefficients P_{OS} (mean \pm maximal error, $n = 3$) determined for the hypotonic stimulations.

buffer	$\Delta\pi$ / mOsmol/kg	τ / min	A	P_{OS} / $\mu\text{m/s}$
HYPO A	58	3.4 ± 0.8	0.015 ± 0.005	8 ± 3
HYPO B	95	5.6 ± 0.5	0.031 ± 0.002	4.8 ± 0.8

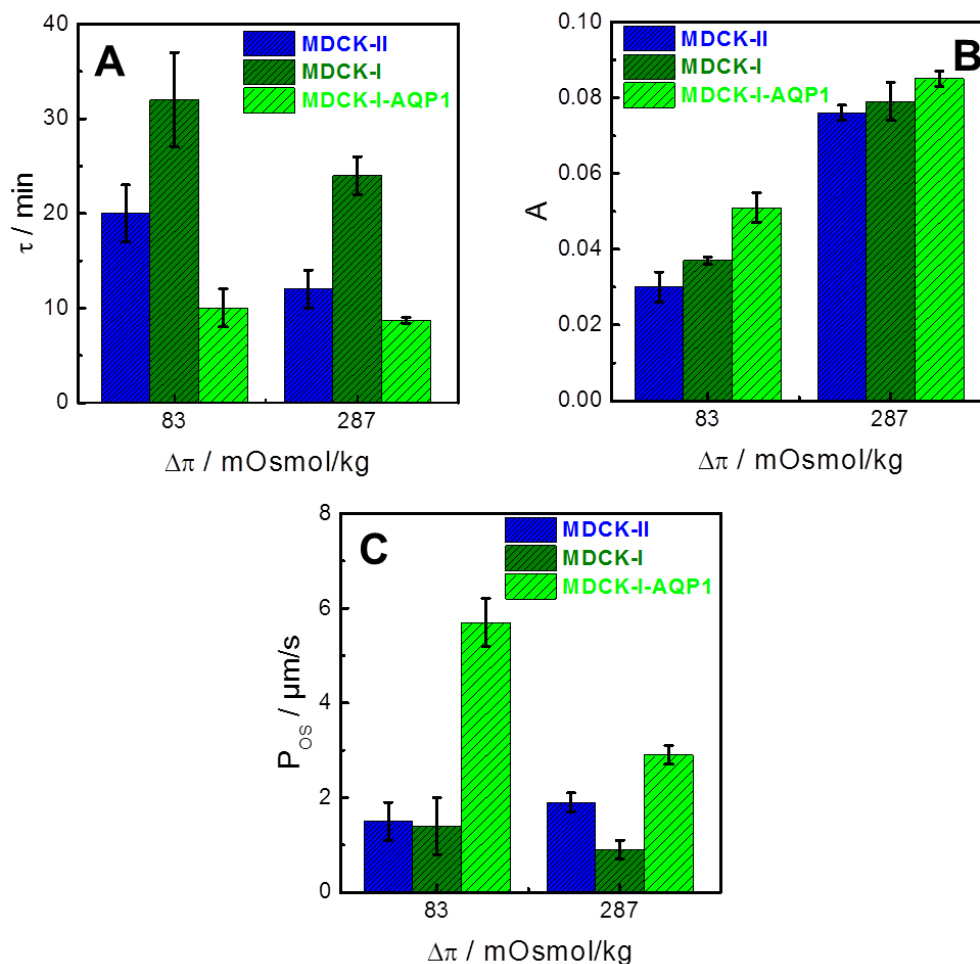


Fig. 6.16: (A) Time-constants τ (mean \pm SE, $n = 3$) and (B) amplitudes A (mean \pm SE, $n = 3$) of the fit-functions for different epithelial cell layers after hypertonic stimulations. (C) Associated osmotic water permeability coefficients P_{OS} (mean \pm maximal error, $n = 3$).

Generally, the results of Fig. 6.16 match the trends of chapter 6.1.4 and chapter 6.1.5. The transfected cell line (MDCK-I-AQP1) is unequivocally discriminable from the wildtype MDCK-I cell line. The time-constants for transepithelial water flux are in a similar range when the results for the electrode arrays, central electrode pair and IDE-400, are compared. In contrast, the amplitudes for water flow are distinctively lower with IDE-400.

Transepithelial water flux is a well-studied topic in literature. Tab. 6.18 provides a selection of P_{OS} values for different epithelial barriers that have been reported by other labs. Since the reported P_{OS} values refer to hypertonic stimulations, only the hypertonic water flux measurements of this work are considered in Tab. 6.18.

Tab. 6.18: Osmotic water permeability coefficients P_{OS} for different epithelial monolayers and variable readout systems. Since the P_{OS} values that are cited here refer to hypertonic stimulations, only the osmotic water permeability coefficients that were determined for the hypertonic stimulations are considered in this table (each mean \pm maximal error, $n = 6$). All P_{OS} values that are cited here refer to transepithelial water flux.

cell line	$P_{OS} / \mu\text{m/s}$	readout	reference
MDCK-I	7 ± 2	scanning ion-selective microelectrode	(Missner <i>et al.</i> 2008)
MDCK-I-AQP1	33 ± 7		
MDCK-I	4 ± 2	spectroscopic using phenol-red	(Deen <i>et al.</i> 1997)
MDCK-I-AQP1	58 ± 1		
MDCK	9 ± 4	fluorophore dilution (standard)	(Alam <i>et al.</i> 2017)
MDCK-AQP5	59 ± 2		
MDCK-II	16 ± 2	fluorophore dilution (standard)	(Matsui <i>et al.</i> 2000)
HBE	169 ± 24	fluorophore dilution (standard)	(Matsui <i>et al.</i> 2000)
FRT	3 ± 1	FT-on-chip	(Jin and Verkman 2017)
FRT-AQP4	9 ± 2		
CHO	12.5 ± 0.1	light microscopy with spatial filtering	(Farinas <i>et al.</i> 1997)
CHO-AQP1	140 ± 1		
MDCK-I	1.1 ± 0.4	impedimetric	this work
MDCK-II	1.7 ± 0.3		
MDCK-I-AQP1	4.3 ± 0.4		

The impedance-based water flux assay provides reliable estimates of P_{OS} , which are very similar to osmotic water permeability coefficients reported in literature. Excellent accordance is observed for P_{OS} values of MDCK-I cells that were determined with the impedimetric approach and a spectroscopic water flux assay reported by Deen *et al.* (1997) with values of $(1.1 \pm 0.4) \mu\text{m/s}$ or $(4 \pm 2) \mu\text{m/s}$, respectively. They used a standard dual chamber similar to the experimental setup of the impedance-based method. The apical compartment was incubated with a phenol-red containing buffer. Two hours after the osmotic stimulation, the content of the apical compartment was analyzed for absorbency at 479 nm which is the isosbestic point for phenol-red. Transepithelial water flux was calculated from the change of absorbency in the apical compartment which was due to the water flux between the two compartments. However, this spectroscopic approach does not provide online information but is a classical end-point assay. Therefore, this approach is highly prone to errors and is less reliable compared to the new P_{OS} TER-assay. Moreover, most of the published osmotic water permeability coefficients are slightly higher compared to the impedimetrically determined

values. In the $P_{OS}TER$ -assay, AQP1-overexpressing MDCK-I cells show a four times increased P_{OS} value compared to wildtype MDCK-I cells. The relative increase of P_{OS} compares favorably with the results published by Missner et. al (2008). They used the identical transfected cell line and reported that the presence of AQP1 gives rise to a 4.7 times increased osmotic water permeability coefficient in comparison to the wildtype MDCK-I cells.

6.3.5 AQP-inhibition study with the AQP1-inhibitor $H AuCl_4 \cdot 3H_2O$

In analogy to chapter 6.1.6, a $P_{OS}TER$ -based AQP-inhibition study was performed using the AQP1-inhibitor $H AuCl_4 \cdot 3H_2O$. At time zero, a confluent monolayer of MDCK-I-AQP1 cells was exposed apically to a 200 mM sucrose solution in presence and absence of 100 μM $H AuCl_4 \cdot 3H_2O$. The impedance of the $P_{OS}TER$ -device was measured at 100 kHz in **P_{OS} -mode** and from 1 Hz to 10^5 Hz in **TER-mode**. All conductances are normalized to the conductance recorded at $t = 0$ min. The results of the inhibition study are presented in Fig. 6.17.

The time-courses of the (normalized) basolateral conductance in presence and absence of Au^{3+} are shown in Fig. 6.17A. In absence of the inhibitor, the filter-grown MDCK-I-AQP1 cells display a drastic conductance increase of (3.7 ± 0.3) % five minutes after the addition of 200 mM sucrose. At $t = 40$ min, $norm.G_{100kHz}$ has increased about (8.0 ± 0.3) %. The time-course of the basolateral conductance is significantly different in presence of the gold compound. The increase of the basolateral conductance is less pronounced directly after the induction of the osmotic pressure gradient. Five minutes after sucrose addition, $norm.G_{100kHz}$ has increased only about (1.7 ± 0.3) %. Thus, the initial signal response is 55 % lower in presence of 100 μM $H AuCl_4 \cdot 3H_2O$ giving a hint for the inhibition of AQP1. After 20 minutes, the basolateral conductance reaches a value of (4.4 ± 0.3) %, before a slight decrease of $norm.G_{100kHz}$ is observed for the last 15 minutes of the experiment.

Fig. 6.17B presents not only typical (not averaged) time-resolved data of water flux monitoring, but also the corresponding TER values of the same cell monolayer. The MDCK-I-AQP1 monolayer which is exposed to 100 μM $H AuCl_4 \cdot 3H_2O$ indicates a severe impact of the inhibitor to barrier function of MDCK-I-AQP1 cells, as indicated by an exponential decay of the TER values. Please note that the inhibitor was present during the complete measurement time, even at baseline recording. The trend of decreasing TER values in presence of 100 μM $H AuCl_4 \cdot 3H_2O$ was confirmed by the pool of our data. In the

particular case of Fig. 6.17B, TER is $200 \Omega\text{cm}^2$ ten minutes prior to the addition of sucrose or $40 \Omega\text{cm}^2$ at $t = 40 \text{ min}$ resembling a barrier breakdown of 60 %. In contrast, barrier function of MDCK-I-AQP1 layers is not affected in absence of $\text{HAuCl}_4 \cdot 3\text{H}_2\text{O}$ (Fig. 6.13C and Fig. 6.14C).

The time-courses of $\text{norm.G}_{100\text{kHz}}$ of Fig. 6.17A suggest an inhibitory effect of the gold compound on AQP1, as indicated by the decreased initial slope of the basolateral conductance change. However, the conductance is decreasing after 25 minutes which is completely unexpected. The inhibition of AQP1 is supposed to lead to a decreased water permeation rate which is reflected in a decreased time-constant. In contrast, the overall amount of permeating water, i.e. the amplitude of the time-dependent conductance change, is not thought to be affected by the presence of the inhibitor. Nevertheless, the total conductance changes in presence and absence of the inhibitor are significantly different. A similar observation was already made in the AQP-inhibition study that was performed with the central water flux assay (chapter 6.1.6). A possible explanation for this unexpected time-course of $\text{norm.G}_{100\text{kHz}}$ is provided by the $P_{\text{OS}}\text{TER}$ -assay. The simultaneously recorded TER values show a drastic impact of $100 \mu\text{M}$ $\text{HAuCl}_4 \cdot 3\text{H}_2\text{O}$ on the barrier function of MDCK-I-AQP1 cells. As a consequence, the osmotic pressure gradient is attenuated, since sucrose that is actually low membrane-permeable is supposed to permeate into the basolateral compartment along the open junctions. Therefore, the driving force for water flow is dissipating over time which might explain the suspicious conductance response. Two conclusions are following from the $P_{\text{OS}}\text{TER}$ -based AQP-inhibition:

- (I) $\text{HAuCl}_4 \cdot 3\text{H}_2\text{O}$ is not appropriate for AQP-inhibition experiments in a concentration of $100 \mu\text{M}$, as barrier function is significantly affected. However, the gold compound is often applied in this concentration in such studies (Misztal *et al.* 2018; Yang *et al.* 2006). A detailed examination of the cytotoxic effects of $\text{HAuCl}_4 \cdot 3\text{H}_2\text{O}$ is presented in chapter 6.5.
- (II) The combined electrochemical detection of P_{OS} and TER offers a powerful tool for aquaporin analysis with enhanced information content. The time-courses of $\text{norm.G}_{100\text{kHz}}$ remained unclear in chapter 6.1.6, whereas the $P_{\text{OS}}\text{TER}$ -assay demonstrated a significant impact of $100 \mu\text{M}$ $\text{HAuCl}_4 \cdot 3\text{H}_2\text{O}$ on barrier function of MDCK-I-AQP1 cell layers which subverts the actual AQP-inhibition study.

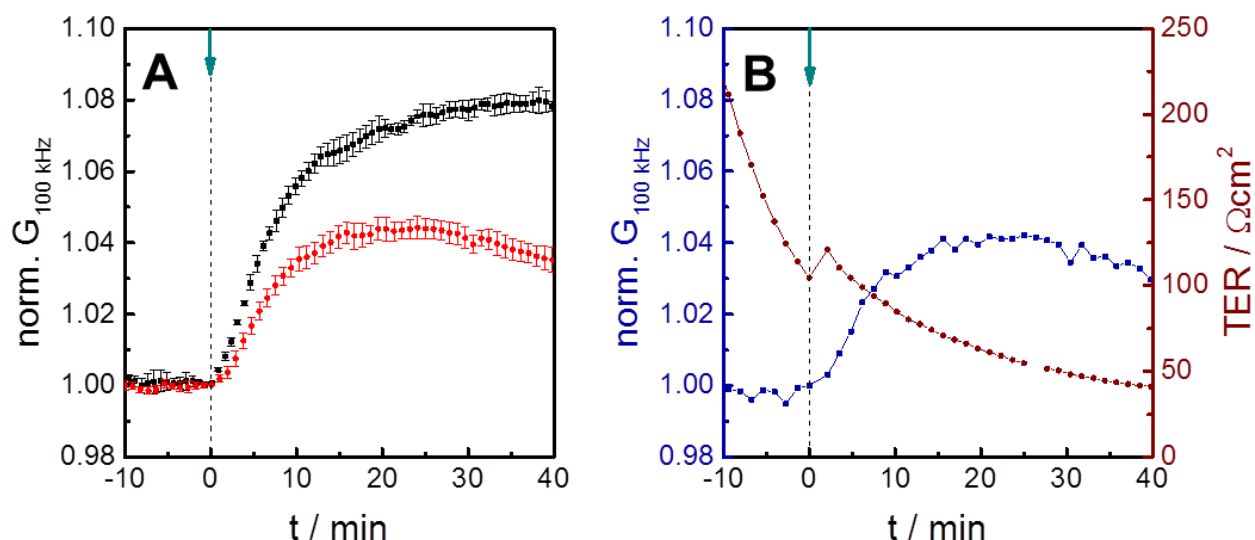


Fig. 6.17: $P_{os}TER$ -based AQP1-inhibition study in MDCK-I-AQP1 cells recorded with IDE-400. **(A)** Transepithelial water flow is followed by monitoring time-dependent changes of the (normalized) basolateral conductance ($f = 100$ kHz) **without the inhibitor** or in presence of **100 μ M HAuCl₄·3H₂O**, respectively (mean \pm SE, $n \geq 3$). At time point zero, a hyperosmotic pressure gradient is induced by the addition of **200 mM sucrose**. **(B)** Besides investigating water permeability (P_{os} -mode), time-resolved and simultaneous recording of TER values (TER -mode) of the same monolayer enhances the information content and demonstrates a significant impact of the gold compound on the barrier function of MDCK-I-AQP1 cells. The graph represents typical data. Absolute conductance at $t = 0$ min: G_{100kHz} (w/o Au³⁺) = (19.4 \pm 0.6) mS, G_{100kHz} (100 μ M Au³⁺) = (19.63 \pm 0.09) mS.

6.4 Water flux measurements using the established fluorophore dilution method as an independent reference

Transepithelial water flux was additionally monitored with a fluorescence-based readout. For this purpose, a confluent monolayer of MDCK-II cells was osmotically stimulated by an apical addition of a dye-containing, hypertonic solution (200 mM sucrose) at time point zero. FITC-dextran ($\beta = 0.25$ mg/ml, 500 kDa) was used as an apical, membrane-impermeable fluorophore. Samples were taken in small aliquots (5 μ L) from the apical compartment and diluted in 1 mL PBS⁺⁺/glucose (1 g/L) at defined time-points ($t = 0 / 10 / 20 / 30 / 40$ min). The fluorescence intensity was followed at an emission wavelength of 515 nm. The results of the fluorophore dilution method are presented in Fig. 6.18. The fluorescence intensity is normalized to the value determined at $t = 0$ min.

The (normalized) fluorescence intensity does not alter significantly after a mere buffer exchange (Fig. 6.18A), as no water flow between the two compartments occurs. All changes

are significantly smaller than the standard error of the measurement and are, thus not significant. However, the recorded fluorescence intensities suffer from relatively high error bars reflecting the low reproducibility of the fluorophore dilution method.

The signal is decreasing time-dependently after the apical addition of 200 mM sucrose (Fig. 6.18B). After ten minutes, the fluorescence intensity decreases by about $(6 \pm 2) \%$. The signal reaches a fluorescence intensity change of $(11 \pm 2) \%$ after 40 minutes.

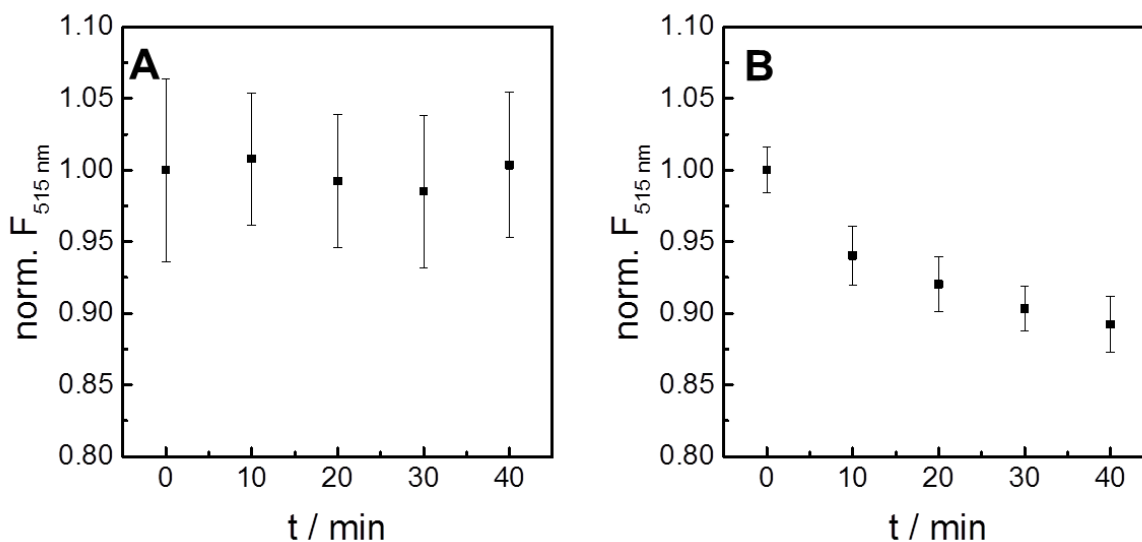


Fig. 6.18: Water flux monitoring after hypertonic stimulations of filter-grown MDCK-II cells using the established fluorophore dilution method. The graphs show time-dependent changes of the (normalized) fluorescence intensity of an apical, membrane-impermeable fluorophore after the addition of **(A)** PBS⁺⁺/glucose (1 g/L) or **(B)** 200 mM sucrose (mean \pm SE, $n \geq 4$).

Tab. 6.19: Comparison between the time-constants τ and amplitudes A of the fit-functions and the corresponding osmotic water permeability coefficients P_{OS} provided by the impedance-based P_{OS} TER-assay and the fluorophore dilution method. The time-constants τ (mean \pm SE, $n \geq 3$), the amplitudes A (mean \pm SE, $n \geq 3$) and the P_{OS} values (mean \pm maximal error, $n \geq 3$) refer to hypertonic stimulations (200 mM sucrose) of filter-grown MDCK-II cells.

readout	τ / min	A	P_{OS} / $\mu\text{m/s}$
impedimetric	12 ± 2	0.076 ± 0.002	1.9 ± 0.2
fluorophore dilution	15 ± 3	0.112 ± 0.007	70 ± 16

The time-course of fluorescence intensity after hypertonic stimulation (Fig. 6.18B) agrees with the expectations. The addition of a hypertonic solution to the apical side of a MDCK-II cell layer induces a transepithelial osmotic pressure gradient. To compensate this osmotic gradient, water flux from the basolateral into the apical compartment takes place. Thus, the fluorophore concentration in the apical compartment is diluted causing a decrease of

norm. $F_{515\text{nm}}$. For an in depth-analysis, the parameters of an exponential decay function of 1st order ($y = A \times \exp\left(\frac{-x}{\tau}\right) + y_0$) are fitted to the experimental raw data of Fig. 6.18B. Thereby, the time-constant τ and the amplitude A of the fit-function get accessible making the calculation of P_{OS} possible (chapter 3.2.2, equations 3.39 and 3.45).

The initial volume of the donor compartment V_0 is 0.2 cm^3 . The fitting procedure reveals a time-constant τ of $(15 \pm 3) \text{ min}$, an amplitude A of (0.112 ± 0.007) and a P_{OS} value of $(70 \pm 16) \mu\text{m/s}$. The time-constants for the fluorescence-based and impedance-based water flux assays are similar and cannot be distinguished from each other under consideration of the individual errors. However, the amplitudes that are observed with the fluorophore dilution method are higher than for the $P_{\text{OS}}\text{TER}$ -assay, but lower as for the first version of the impedimetric water flux assay with central readout. It is striking that the fluorescence-based water flux assay provides a significant higher P_{OS} value for MDCK-II cells than the impedance-based approach. The individual values are opposed in Tab. 6.19.

As already shown in chapter 6.3.4, the P_{OS} values of MDCK-II cells determined with the impedimetric $P_{\text{OS}}\text{TER}$ -assay match reported osmotic water permeability coefficients (Tab. 6.18). In contrast, the fluorophore dilution assay that was performed in this thesis indicates distinctively increased P_{OS} values after osmotic stimulation as usual. Due to the error-proneness of the fluorophore dilution method and due to the constant perturbation of the cell layer during the measurement, the fluorescence-based osmotic water permeability coefficients have to be considered with caution and are less reliable than the impedimetrically determined P_{OS} values.

6.5 Evaluation of the cytotoxic potential of the AQP1-inhibitor $\text{HAuCl}_4 \cdot 3\text{H}_2\text{O}$

The AQP1-inhibitor $\text{HAuCl}_4 \cdot 3\text{H}_2\text{O}$ was used as a $100 \mu\text{M}$ solution in the water flux measurements (chapter 6.1.6 and chapter 6.3.5), as it was performed in other published studies (Misztal *et al.* 2018; Yang *et al.* 2006). To attribute altered water permeation to an inhibitory effect of $\text{HAuCl}_4 \cdot 3\text{H}_2\text{O}$, possible cytotoxic effects of the gold compound have to be excluded. Therefore, two different cytotoxicity studies were conducted:

- (I) Potential effects on the mitochondrial activity were examined by means of a PrestoBlue[®]-assay that is classified as a typical end-point assay.
- (II) More detailed information about cytotoxicity of the inhibitor is provided by ECIS-measurements that permit online monitoring with excellent time-resolution.

The results of these two different approaches are presented in the following paragraphs.

PrestoBlue[®]-assays using MDCK-I-AQP1 cells

Confluent monolayers of MDCK-I-AQP1 cells were exposed for one hour to six different concentrations of H_{Au}Cl₄·3H₂O (10 / 50 / 100 / 200 / 500 / 1000 μM). Please note that the cell layers were exposed to H_{Au}Cl₄·3H₂O for approximately one hour in total in the water flux studies under consideration of baseline recording. The PrestoBlue[®]-assay included a negative control (PBS⁺⁺/glucose (1 g/L)) and a positive control (0.5 % (v/v) Triton-X-100 in PBS⁺⁺/glucose (1 g/L)). The final readout parameter is denoted as *cytotoxicity index CI* [in %]. The exact calculation protocol of CI was already described in chapter 5.3.

The cytotoxicity index CI is plotted as a function of the inhibitor concentration (Fig. 6.19). The exposure to a 10 mM or 50 mM concentration, respectively, leads to CI values from (4 - 10) %. The concentration of 100 μM, as applied in water flux experiments, causes a moderately increased CI of (19 ± 5) %. The incubation with a 200 μM H_{Au}Cl₄·3H₂O solution leads to a higher CI value of (53 % ± 22 %). The two highest concentrations cause tremendous damage to the mitochondrial activity of the AQP1-overexpressing cells, as indicated by high cytotoxic indices that are in the same range as the CI value of the positive control (90 % ± 27 %). For an in-depth analysis, the parameters of a Boltzmann function ($y = A2 + \frac{A1-A2}{1+\exp\left(\frac{x-x_0}{dx}\right)}$) are fitted to the experimental raw data. The fitting procedure was performed by Origin2016. Tab 6.20 summarizes the results of the fitting procedure. The fit-parameter x_0 equals the EC₅₀ value of H_{Au}Cl₄·3H₂O and is (175 ± 15) μM.

The results of the PrestoBlue[®]-assay justify the application of a 100 μM H_{Au}Cl₄·3H₂O solution for AQP1-inhibition studies in MDCK-I-AQP1 cells, since this concentration is lower than the EC₅₀ value. Nevertheless, a minor impact of the inhibitor in a concentration of 100 μM on MDCK-I-AQP1 cells is visible, as indicated by a slightly increased CI of (19 ± 5) %.

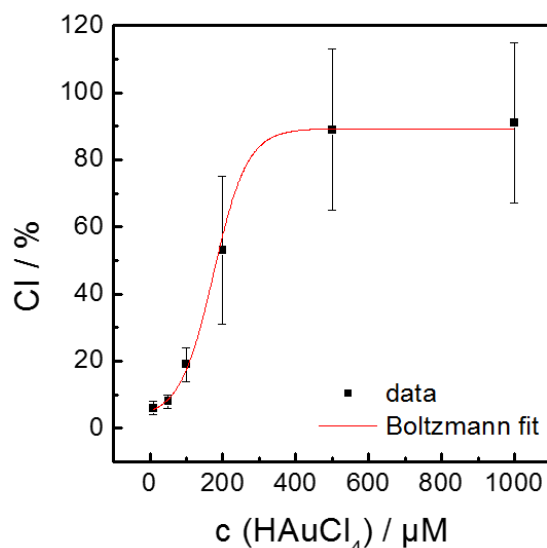


Fig. 6.19: The cytotoxicity index CI is plotted as a function of $\text{HAuCl}_4 \cdot 3\text{H}_2\text{O}$ concentrations (mean \pm SE, $n = 6$) when MDCK-I-AQP1 cells are exposed to the inhibitor for one hour. The parameters of a Boltzmann function are fitted to the data providing an EC_{50} value of $(175 \pm 15) \mu\text{M}$. The positive control has a CI of $(90 \pm 27) \%$.

Tab. 6.20: Results of the Boltzmann fitting process of the data of Fig. 6.19.

fit-parameter	value
A1 / %	3 ± 2
A2 / %	89 ± 7
x_0 / μM	175 ± 15
dx	46 ± 10

ECIS-cytotoxicity test using MDCK-I-AQP1 cells

For an enhanced evaluation of the cytotoxic potential of the AQP1-inhibitor, additional ECIS-cytotoxicity studies were performed. Therefore, $100 \mu\text{M}$ $\text{HAuCl}_4 \cdot 3\text{H}_2\text{O}$ were added to confluent monolayers of MDCK-I-AQP1 cells at time point zero. The impedance magnitude IZI was followed over time at a single frequency of 16 kHz. Determination of the appropriate frequency is presented in the supplementary information (appendix: Fig. 11.16). The results of the ECIS-studies are illustrated in Fig. 6.20.

The control measurement indicates constant impedance magnitudes during the entire incubation time. The signal starts with $(1376 \pm 79) \Omega$ at $t = 0$ h and ends with $(1345 \pm 74) \Omega$ at $t = 3$ h. In contrast, the time-course of $\text{IZI}_{16\text{kHz}}$ is different in presence of the gold compound. Instantaneously after the addition, the impedance magnitude is decreasing to a minimum of $(1276 \pm 15) \Omega$ at $t = 0.3$ h. However, $\text{IZI}_{16\text{kHz}}$ is recovering and reaches a maximum of

(1406 ± 15) Ω after 0.8 h. From 1.2 h to 3 h, the impedance magnitude is linearly increasing to a magnitude of (1563 ± 10) Ω at $t = 3$ h.

The ECIS-measurement demonstrates a minor impact of 100 μM $\text{HAuCl}_4 \cdot 3\text{H}_2\text{O}$ on confluent monolayers of MDCK-I-AQP1. The time-course of $|Z|_{16\text{kHz}}$ is clearly affected by the presence of the AQP1-inhibitor. However, there is no complete damage of the cells under study which is consistent with the findings of the PrestoBlue[®]-assay.

The results of Fig. 6.19 and Fig. 6.20 indicate a considerable cytotoxic potential of the AQP1-inhibitor $\text{HAuCl}_4 \cdot 3\text{H}_2\text{O}$ on MDCK-I-AQP1 cells. However, the use of the gold compound in a concentration of 100 μM shows only slight cytotoxic impact on MDCK-I-AQP1 cells. Both, a moderately increased cytotoxic index and a rather moderate non-monotonic response of the impedance magnitude support this claim. Otherwise, no acute cytotoxicity is observed, as the concentration applied in water flux assays is still lower than the EC_{50} -value determined from PrestoBlue[®]-assays. In addition, the impedance magnitude is not entirely breaking down, but recovers in course of the incubation time. From this point of view, a concentration of 100 μM for the inhibition experiments is justified. However, time-resolved monitoring of TER (chapter 6.3.5) proved a drastic impact of 100 μM $\text{HAuCl}_4 \cdot 3\text{H}_2\text{O}$ on the barrier function of confluent MDCK-I-AQP1 cell layers. Taking all these aspects into consideration, a reduced inhibitor concentration of 50 μM is highly recommended for future aquaporin inhibition studies to reduce the probability of measuring artefacts instead of real inhibitory effects.

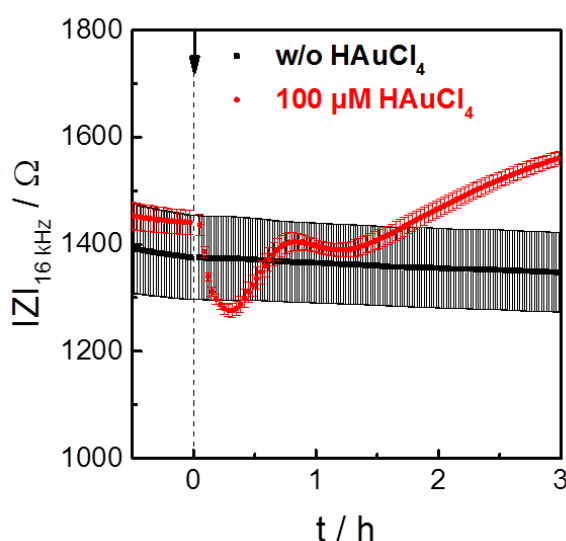


Fig. 6.20: ECIS-measurements for the investigation of possible cytotoxic effects of 100 μM $\text{HAuCl}_4 \cdot 3\text{H}_2\text{O}$ on MDCK-I-AQP1 monolayers (mean \pm SE, $n \geq 3$) recorded with an 8W10E+ array. The impedance magnitude is monitored over time at a fixed frequency of 16 kHz. The AQP1-inhibitor is added at $t = 0$ h. The addition of PBS^{++} /glucose (1 g/L) serves as a control measurement.

6.6 Advantages and limitations of the impedance-based water flux assay in comparison to established methods

The novel impedance-based water flux assay enables monitoring of transepithelial water flux in a superior quality compared to the conventional epithelial water flux assays. The following chapters provide a detailed discussion about the benefits and limitations of the new method.

6.6.1 Automated monitoring of water flux with excellent time-resolution

Water permeation across filter-grown cell layers is commonly monitored via fluorescence-based readouts (Levin *et al.* 2006) or by means of connecting glass capillaries to one of the two fluid compartments (Dorr *et al.* 1997). Although the use of capillaries is a very straightforward approach with outstanding precision, the elaborate experimental setup and the involved high monetary efforts preclude the application in pharmaceutical studies. The fluorophore dilution method, which is the most often performed epithelial water flux assay, has several drawbacks. Samples have to be taken from the dye-containing compartment at specific time-points to monitor transepithelial water flux. In a separated experiment, the fluorescence intensities of the individual aliquots are determined to calculate back on P_{OS} values. Consequently, fluorescence-based recording of water flux across epithelial layers always contains two different experimental steps: (I) The actual water flux experiment comprising the osmotic stimulation of the cell layer under study and the liquid handling to provide aliquots at specific time-points. (II) Determination of the fluorescence intensity of the taken aliquots. This leads to an inevitable increased experimental effort. Another disadvantage of the fluorophore dilution assay is provided by the sequential sampling as it may lead to an interference with the epithelial layer. Thus, the water flux measurement may become more invasive. Time-resolution is often neglected in such kind of assays and only very few data points are analyzed (Deen *et al.* 1997) to reduce the invasiveness of the method. As a consequence, such experiments suffer from a high susceptibility to errors and do not allow any online information. The impedance-based water flux assay provides an immense improvement concerning the liquid handling and the associated low time-resolution. Once the osmotic pressure gradient across the cell layer is induced, transepithelial water flux is recorded completely automated without any liquid handling. Therefore, the novel method

guarantees non-invasive examination of epithelial water permeability. Besides, the automated nature of impedance spectroscopy enables an easy-to-handle assay that is not restricted to experts. In addition, the impedance-based approach excels the conventional water flux assays by far in terms of time-resolution. The $P_{OS}TER$ -assay provides time-resolved recording of water flux in the range of 1.3 minutes. Even better time-resolution (0.6 min) is yielded by focusing on P_{OS} and neglecting TER. Thus, the $P_{OS}TER$ -assay provides not only P_{OS} values, but also online monitoring of transepithelial water flux.

Besides $P_{OS}TER$, an improved fluorescence-based water flux assay, which is referred to as *fluid transport on a chip* (FT-on-chip), was recently published by Jin and Verkman (Jin and Verkman 2017). They fabricated a microfluidics platform on which they placed cell-covered filter inserts. They induced osmotic pressure gradients across epithelial cell layers by adding a non-isotonic solution to the apical compartment. In contrast to conventional fluorophore dilution assays, the perfusate in the microfluidic channel beneath the cell layer contained a membrane-impermeable fluorescent dye (500 kDa FITC-dextran) instead of adding the fluorophore to the apical buffer. The measurement of transepithelial water flux required only a single fluorescence image without sequential sampling. P_{OS} values were deduced from the steady-state concentration profile along the length of the microfluidic channel of the fluorophore in the perfusate. FT-on-chip allows for rapid and accurate measurements of transepithelial water permeability. In the current device, they estimate approximately 0.1 $\mu\text{m/s}$ as the lowest detectable P_{OS} value. However, the method suffers from some limitations that may be overcome by the impedance-based water flux assay:

- (I) FT-on-chip averages heterogeneities in water permeability within one cell layer, as the fluorescence profile is determined from the properties of all cells overlying the microfluidic channel. In contrast, the impedance-based water flux assay provides spatially resolved monitoring of water flux when laterally distributed electrode pairs are integrated into the bottom of the basolateral chamber (chapter 6.2). Thereby, differences of water permeability within one single cell layer may be quantified.
- (II) Although FT-on-chip provides online water flux monitoring with a time-resolution that is strongly improved compared to the standard fluorophore dilution method, the time-resolution of the impedance-based water flux assay is even better. The time-resolution of the FT-on-chip method is related to the time that is required to generate a steady-state fluorescence profile which may take up to several minutes.

However, the impedimetric water flux assay may be performed in a time-resolution in the range of seconds when measuring at one discrete frequency of 100 kHz and neglecting the internal TER-control. Even the combined detection of P_{OS} and TER permits a time-resolution of approximately one minute.

- (III) Parallel measurements in separate wells are not easily implemented in FT-on-chip assays. In contrast, the impedance-based water flow assay is easily scalable to multi-well formats and offers the potential for higher throughput analysis.
- (IV) FT-on-chip includes no internal TER-control and hence, requires separated TER-measurements to ensure barrier integrity. In contrast, the P_{OS} TER-device provides online recording of TER which saves measuring time and allows for an improved experimental control.

On the other hand, FT-on-chip has two major benefits compared to the impedimetric approach:

- (I) The method is applicable to *in vivo* transepithelial permeability measurements using tissues, such as urinary bladder or intestine, in which the apical surface contacts the microfluidic channel and basolateral perfusion is unnecessary due to blood flow. The impedimetric method in its current version is restricted to two dimensional cell monolayers cultivated onto standard filter inserts.
- (II) FT-on-chip allows not only for the determination of osmotically induced transepithelial water permeability (P_{OS}), but also for diffusional movement of water across epithelial monolayers in absence of an osmotic pressure gradient (P_D). P_D determination was achieved by identical experimental settings consisting of the microfluidics platform and an overlying cell-covered filter insert. The crucial point was that the perfusate contained now a D_2O -sensitive fluorescent dye (e.g. aminonaphthalene trisulfonic acid, ANTS). An isotonic D_2O solution was added to the apical compartment to drive diffusional water flux. P_D values were deduced from ANTS fluorescence images in the microfluidic channel. Up to now, the impedance-based water flux assay does not provide P_D determination.

6.6.2 Determination of P_{OS} values with internal TER-control

Usually, water flux studies are accompanied by TER-assays to ensure barrier integrity (Alam *et al.* 2017; Missner *et al.* 2008). This additional experiments cause an increase in both, measuring time and experimental costs. To the best of our knowlegde, all epithelial water flux assays that have been published lack the ability to record P_{OS} and TER simultaneously within one single experimental setup. The novel water flux assay solves this problem by reading out both parameters – P_{OS} and TER – impedimetrically. The transepithelial electrical resistance is monitored online and automated during the entire measurement, providing an internal and continuous control of barrier function. Damaged monolayers or cytotoxic influences of test compounds are comfortably identified by the internal TER-control.

6.6.3 Laterally resolved recording of transepithelial water permeation

A major drawback of cultivating epithelial cells on filter membranes is the heterogeneous barrier function of filter-grown monolayers (Klusmeier *et al.* 2019; Wegener and Seebach 2014). Although a small pool of assays for spatially resolved monitoring of tracer permeation exists, no methods have been reported yet that permit transepithelial water flux monitoring with lateral resolution. The impedance-based assay offers next to an integral or central readout also a spatially resolved readout which grants the new device a unique feature. However, the level of lateral resolution is restricted to the number of integrated electrode pairs at the bottom of the measurement chamber. The device as it has been presented in this thesis is composed of only three electrode pairs, but is easily scalable to a higher amount of electrode pairs providing “water flux mapping” within one single cell layer or even within one single cell.

6.7 Summary and outlook

Conventional water flux measurements of epithelial cells tend to be error-prone and are limited to low-throughput. The second project of this thesis displays a novel, impedance-based assay for detecting osmotically induced water permeation across epithelial layers. A first version of the assay enabled very sensitive and central water flux monitoring, but had the disadvantage of an undefined basolateral volume. Therefore, this approach was not suitable for calculating osmotic water permeability coefficients (P_{OS}). Besides, the

associated change of the basolateral conductance was not representative for the entire cell layer due to the very local readout. A second version of the assay solved these problems by using a well-defined basolateral volume and by depositing interdigitated electrodes beneath most of the cell layer. The impedimetrically determined P_{OS} values were in a similar range as literature data. However, the fluorescence-based P_{OS} values, that were determined as an independent reference, were found to have significantly higher values compared to the impedimetrically determined P_{OS} values and literature data. The most important advantage of the second version of the assay was the ability to simultaneously monitor transepithelial water flux (P_{OS}) and the resistance (TER) of one single cell monolayer and was referred to as P_{OS} TER-assay. Furthermore, the new device allowed for laterally resolved recording of water flux across epithelial cell layers by increasing the number of basolateral electrode pairs. Thereby, heterogeneities in water permeability of one single cell layer and of mixed but segregated epithelial layers became accessible. Moreover, the impedimetric water flux assay was not restricted to a uniform flow direction, but permits bidirectional monitoring. Several aquaporin studies highlighted the immense potential of the novel method.

So far, the novel water flux assay was only performed with three different cell lines. Therefore, the next step is the investigation of other relevant epithelial cell lines (e.g. FRT cells). Although several aquaporin studies have been already conducted, further investigations would be useful as for example AQP-studies with other inhibitors or the application of $HAuCl_4 \cdot 3H_2O$ in a non-cytotoxic concentration, respectively. Immunological detection of AQP1 in MDCK-I-AQP1 cells by conducting a Western blot or by immunological staining are important to validate the AQP-studies of this thesis and to quantify the copy number of AQP1 in MDCK-I-AQP1 cells. The experimental setup of the first version of the assay might be modified to create a defined initial donor volume enabling the calculation of osmotic water permeability coefficients.

7 Transepithelial impedance analysis using PEDOT-electrodes

The prevailing parameter to describe epithelial and endothelial barrier function is the *transepithelial and –endothelial electrical resistance* (TER). However, under certain circumstances TER-readings may become inaccurate and result in misinterpretations. The impedance-based TER-approach faces its limits when investigating extremely tight monolayers or cellular barriers with highly folded plasma membranes due to the special characteristics of the interface impedance of stainless steel and gold electrodes, respectively.

The third project of this thesis introduces a new concept to overcome these limitations in impedance-based TER-assays. The conventional electrode material is substituted or coated by a well-established conductive polymer: poly-3,4-ethylenedioxythiophene (PEDOT). A cell-covered filter insert is sandwiched between two PEDOT-electrodes and impedance is recorded as a function of frequency as in regular setups. TER is extracted from the impedance spectra as described above. Due to the very high interface capacitance of PEDOT, the impact of the electrode-electrolyte interface is shifted significantly to lower frequencies in the impedance spectra improving the sensitivity and accuracy of the TER-detection. The novel setup is applied in first proof-of-concept studies analyzing well-known epithelial monolayers (MDCK-I, MDCK-II). Furthermore, the relevance of the new setup is illustrated with simulated frequency spectra of Caco-2 cell layers that are known to express strongly folded plasma membranes, hence, high cell layer capacitances, and that represent a widespread barrier model in drug absorption studies. The robustness and stability of the PEDOT-electrodes are examined by long-term measurements with a cell-free filter insert. In addition, long-term studies of different epithelial barriers (MDCK-I, MDCK-II) with subsequent barrier manipulation are conducted.

7.1 Comparative TER-studies of MDCK cells using PEDOT and stainless steel electrodes

The PEDOT-based setup for TER measurements comprises a basolateral PEDOT-foil that is coated with a thin gold film outside the measurement chamber to reduce the lead resistance

(chapter 4.2.3, Fig. 4.10A) and an apical stainless steel electrode covered with a thin layer of PEDOT (chapter 4.2.3, Fig. 4.10B). All PEDOT-based measurements of the transepithelial electrical resistance are compared to an established TER-device based on stainless steel electrodes (chapter 4.2.2, Fig. 4.9).

Transfilter measurements using cell-free filter inserts

Cell-free filter inserts were placed into a PEDOT (3 vs. 4, Fig. 7.1D) and a stainless steel configuration (1 vs. 2, Fig. 7.1A). The complex impedance of the different electrode arrangements was recorded from 1 Hz to 10^5 Hz. Fig. 7.1 displays the corresponding frequency spectra of the impedance magnitude $|Z|$, the resistance R , the capacitance C and the phase shift Φ .

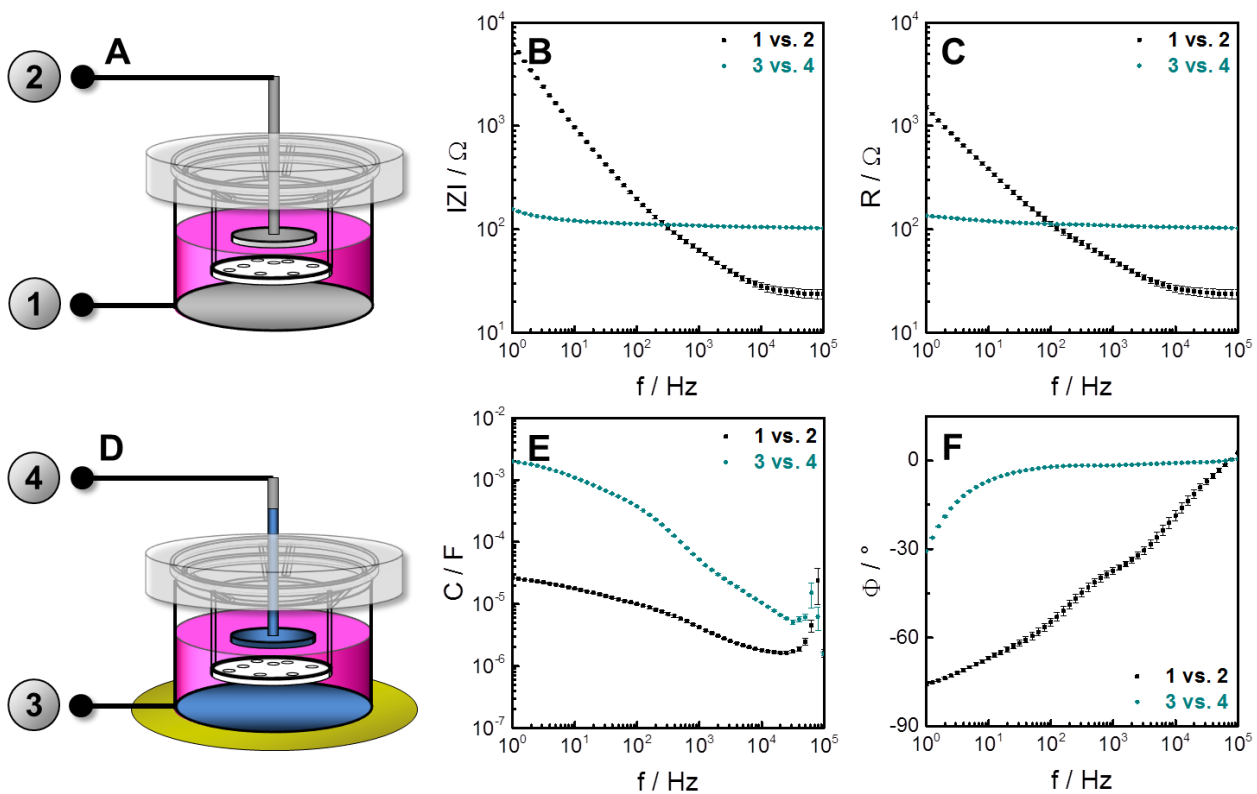


Fig. 7.1: A cell-free filter insert is placed into **(A) a TER setup based on stainless steel electrodes (1 vs. 2)** or **(D) a similar setup using PEDOT-electrodes (3 vs. 4)**. The complex impedance is measured from 1 Hz to 10^5 Hz (mean \pm SE, $n = 3$) and displayed as **(B)** the impedance magnitude $|Z|$, **(C)** the resistance R , **(E)** the capacitance C and **(F)** the phase shift Φ as a function of frequency, respectively.

The impedance spectra reveal a distinct difference between the two setups (Fig. 7.1B). For the stainless steel electrodes a narrow frequency window from 10^4 Hz to 10^5 Hz is dominated by the bulk resistance. For stainless steel electrodes lead resistance between the

measurement chamber and hardware is negligible. Thus, the impedance magnitude is low with a value of $(24 \pm 1) \Omega$ at 10^5 Hz. The impact of the electrode-electrolyte double layer capacitance is strongly emphasized ranging from 1 Hz to 10^4 Hz. At 1 Hz, an impedance magnitude of $(6230 \pm 85) \Omega$ is measured. Additionally, a slight contribution of the filter support is visible in the mid frequency range. In contrast, the PEDOT-device gives rise to an extended frequency section from 10 Hz to 10^5 Hz which is dominated by R_{bulk} and the significant lead resistance. The impedance magnitudes are four times higher with values of $(101.2 \pm 0.7) \Omega$ compared to established electrodes. The influence of the electrode-electrolyte interface is only observable below 10 Hz reaching a $|Z|_{1\text{Hz}}$ -value of $(156.9 \pm 0.9) \Omega$. A similar trend is observed for the resistance spectra (Fig. 7.1C). The capacitance spectra directly indicate the enormous difference of the interface capacitances of PEDOT and stainless steel electrodes (Fig. 7.1E). The PEDOT-system yields a capacitance value of $(1989 \pm 8) \mu\text{F}$ at 1 Hz, whereas a capacitance of $(26.3 \pm 0.4) \mu\text{F}$ is obtained at the same frequency for stainless steel. Thus, the value is 76 times higher for the PEDOT-electrodes. The phase shift spectra show also interesting behavior (Fig. 7.1F). In case of the stainless steel electrodes, the higher frequencies are dominated by resistive contributions causing a phase shift of almost zero. With decreasing frequencies, capacitive influences become more and more important resulting in a phase shift of around -75° at 1 Hz. The mid frequency area uncovers clearly the contribution of the filter support. The frequency-dependent phase shift response is strikingly different with the PEDOT-setup. No phase shift is observed in the frequency window from 10^2 Hz to 10^5 Hz arguing for the prevailing influence of R_{bulk} and the lead resistance. From 100 Hz on the signal is slightly decreasing, but a significant phase shift is only measurable beneath 10 Hz. A phase shift of $(-30.7 \pm 0.4)^\circ$ is detected at 1 Hz. It is also striking that the electric properties of filter support are less visible with the PEDOT-system.

Transfilter measurements using MDCK-II- and MDCK-I-covered filter inserts

MDCK-II- and MDCK-I-covered filter inserts were placed into a PEDOT (3 vs. 4, Fig. 7.2D and Fig. 7.3D) and a stainless steel setup (1 vs. 2, Fig. 7.2A and Fig. 7.3A). The frequency-dependent complex impedance was measured as before. The resulting spectra of the impedance magnitude $|Z|$, the resistance R , the capacitance C and the phase shift Φ are presented in Fig. 7.2 and Fig. 7.3.

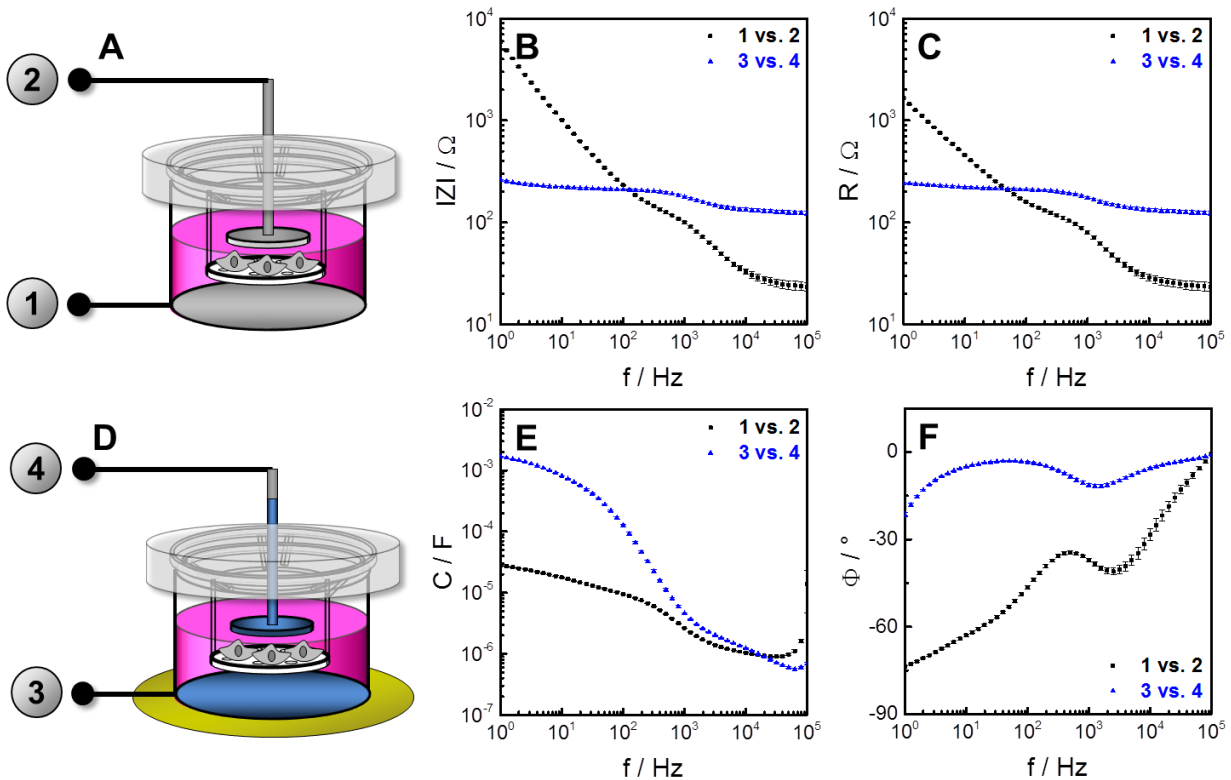


Fig. 7.2: A MDCK-II-covered filter insert is placed into (A) a TER-setup based on stainless steel electrodes (1 vs. 2) or (D) a similar setup using PEDOT-electrodes (3 vs. 4). The complex impedance is recorded from 1 Hz to 10⁵ Hz (mean ± SE, n = 3) and displayed as the frequency-dependent (B) impedance magnitude $|Z|$, (C) resistance R , (E) capacitance C and (F) phase shift Φ , respectively.

Significant differences are visible in the impedance spectra obtained for MDCK-II monolayers (Fig. 7.2B). The higher frequencies from 10⁴ Hz to 10⁵ Hz are dominated by the bulk resistance when using the stainless steel electrodes. The impact of the barrier-forming MDCK-II cells is obvious from 250 Hz to 10⁴ Hz and it is characterized by a plateau. The height of this plateau determines the TER and the plateau width is associated with the cell layer capacitance C_{cl} . The frequency-dependent impedance response is different with PEDOT-electrodes. The overall impedance magnitudes are higher, but the impact of the electrode-electrolyte interface is shifted to frequencies beneath 10 Hz. However, the impedance magnitude at 10⁵ Hz is slightly increased in comparison to the analysis of a cell-free filter insert. The resistance spectra show a similar behavior (Fig. 7.2C). The spectra of the capacitance indicate a drastic difference with respect to the interface capacitances for both electrode configurations (Fig. 7.2E). The PEDOT-setup shows a 60 fold higher capacitances than the stainless steel electrodes at a frequency of 1 Hz. The cell layer influence is observable at mid and higher frequencies in both setups. The cell impact is dominating from 100 Hz to 2000 Hz in the phase shift spectrum of stainless steel electrodes

(Fig. 7.2F). Similar observations apply for the PEDOT-setup, but with clearly lower absolute phase shifts.

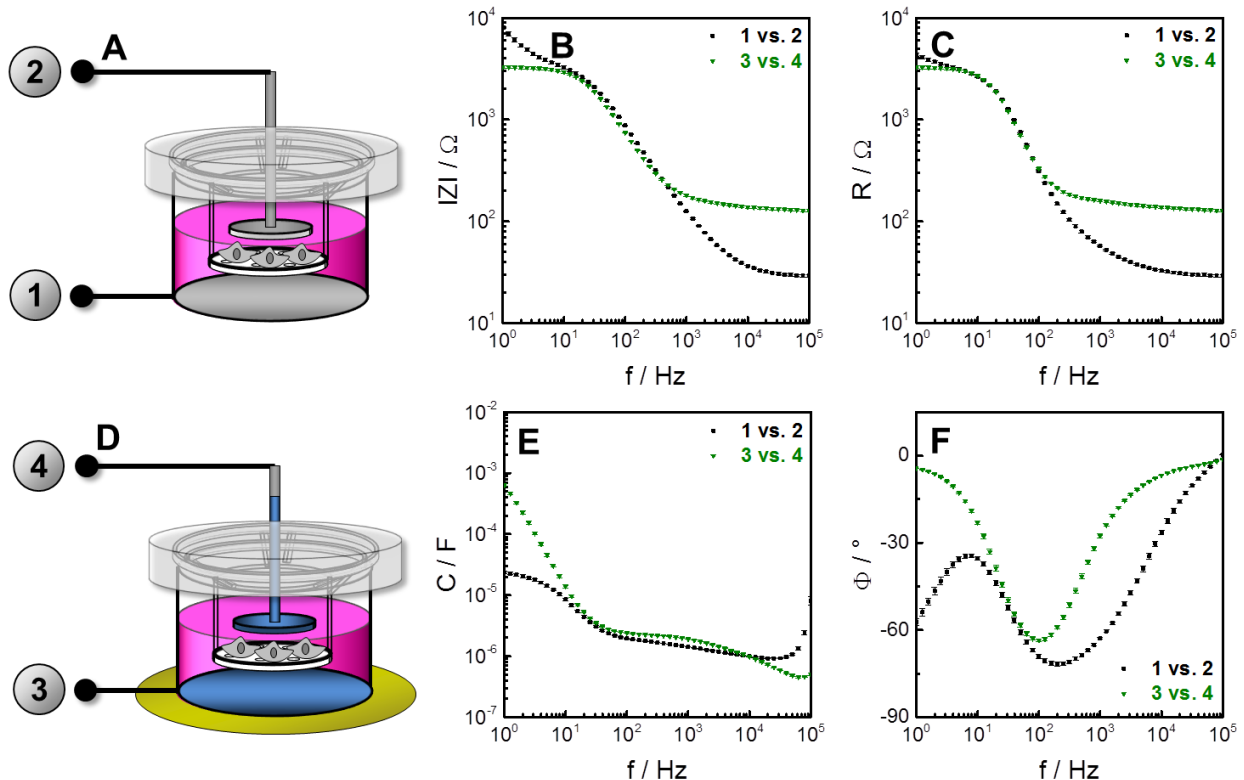


Fig. 7.3: A MDCK-I-covered filter insert is placed into (A) a TER-setup based on stainless steel electrodes (1 vs. 2) or (D) a similar setup using PEDOT-electrodes (3 vs. 4). The complex impedance is monitored from 1 Hz to 10^5 Hz (mean \pm SE, $n = 3$) and presented as the frequency-dependent (B) impedance magnitude $|Z|$, (C) resistance R , (E) capacitance C and (F) phase shift Φ , respectively.

The impedance spectra obtained with the two setups for MDCK-I cells differ at frequencies lower than 10 Hz and at the frequencies in the range from 10^3 Hz to 10^5 Hz (Fig. 7.3B). The PEDOT-setup shows four times higher impedance magnitudes at higher frequencies. The crucial difference of the spectra is obtained in the frequency window from 1 Hz to 10 Hz. After reaching the plateau, the signal is increasing at very low frequencies when using a stainless steel configuration. In this case, an impedance magnitude of $(8065 \pm 364) \Omega$ is detected at 1 Hz. In contrast, the PEDOT-electrodes reveal a constant plateau without a signal increase at low frequencies. Here, the impedance magnitude is $(3298 \pm 110) \Omega$ at 1 Hz. Furthermore, the impact of filter-grown MDCK-I cells ranges from 1 Hz to 10^4 Hz. The frequency-dependent resistance is similar (Fig. 7.3C). The influence of the very tight MDCK-I monolayers is also visible in the capacitance spectra (Fig. 7.3E). In both setups, the capacitances are influenced by the MDCK-I cells in a broad frequency window from 40 Hz to

10^5 Hz. The different interface capacitances of PEDOT and stainless steel are in turn obvious at low frequencies with a $C_{1\text{Hz}}$ -value of (643 ± 18) μF for PEDOT and (24 ± 1) μF for stainless steel. Besides, the phase shift spectra are strongly influenced by MDCK-I barriers (Fig. 7.3F). The crucial difference between the two electrode configurations is determined at frequencies lower than 10 Hz. Whereas the phase shift is decreasing to a final value of $(-57.3 \pm 0.9)^\circ$ at 1 Hz for stainless steel electrodes, the phase shift is dominated by the resistive contribution of the cell layer for PEDOT-electrodes. The phase shift is almost zero at 1 Hz indicating the predominance of an ohmic resistor.

The frequency spectra of all four impedance-based quantities are pooled for cell-covered (MDCK-I, MDCK-II) and cell-free inserts in Fig. 7.4 for better comparison. Fig. 7.4 demonstrates that the use of PEDOT-electrodes offers significant advantages in particular at the low frequency end as the impedance of the electrode-electrolyte interface does not contribute and mask the cell-based impedance contribution.

The results of Fig. 7.1, Fig. 7.2 and Fig. 7.3 convincingly confirm the rationale of the PEDOT-based setup for TER determination. By substituting stainless steel by PEDOT, the interface capacitance is drastically increased. This is due to the porous structure of PEDOT providing a significantly enlarged effective surface area and hence, providing a dramatically higher number of sites with which ions may interact (Bobacka *et al.* 2000; Cui *et al.* 2001; Cui and Martin 2003; Koutsouras *et al.* 2017; Martin and Malliaras 2016). The higher interfacial surface leads to a shift of the CPE-dominated impedance to very low frequencies. Thus, the window for the actual cell impact in the frequency spectra is widened by using PEDOT-electrodes. Investigation of a cell-free insert reveals a contribution of the interface impedance only at frequencies lower than 10 Hz which is a tremendous improvement in comparison to stainless steel electrodes (Fig. 7.1B). On the other hand, PEDOT ($\gamma = 0.4$ S/cm – 400 S/cm (Groenendaal *et al.* 2000; Gustafsson *et al.* 2008; Ouyang *et al.* 2005) suffers from a significantly lower intrinsic conductivity than stainless steel ($\gamma = 1.45 \cdot 10^4$ S/cm, (Serway and Jewett 1998) forcing the overall impedance magnitudes to higher values in the high frequency regime. The impedance magnitudes at high frequencies that are dominated by the bulk resistance and the lead resistance are around four times higher using PEDOT-electrodes. This loss in conductivity impairs the sensitivity of the TER-measurement and may constitute a problem when analyzing leaky monolayers. However, the PEDOT-approach is especially suitable for monitoring the transepithelial

electrical resistance of (extremely) tight barriers. The impedance spectrum of MDCK-I cells recorded with the stainless steel electrodes shows a signal increase due to the high interface impedance at very low frequencies rendering the fitting procedure susceptible to errors (Fig. 7.3B). In general, in order to determine the parameters of a constant phase element by fitting the experimental data, it takes a portion of the spectrum to be linear to guarantee a proper fitting process. From experience, it takes linearity of the impedance for at least a frequency decade or the slope of the curve, that determines n_{CPE} , is insufficiently determined. In case of MDCK-I cells, this frequency window has to be narrowed significantly. In extreme cases, only a third of a decade is available for this fitting procedure. This problem is solved by the use of PEDOT-electrodes. Due to the low interface impedance, the MDCK-I-plateau remains stable and is not affected by the electrode-electrolyte interface. Thus, the experimental data is easily fitted by an appropriate equivalent circuit. The determination of the corresponding transepithelial electrical resistances is illustrated later in this chapter.

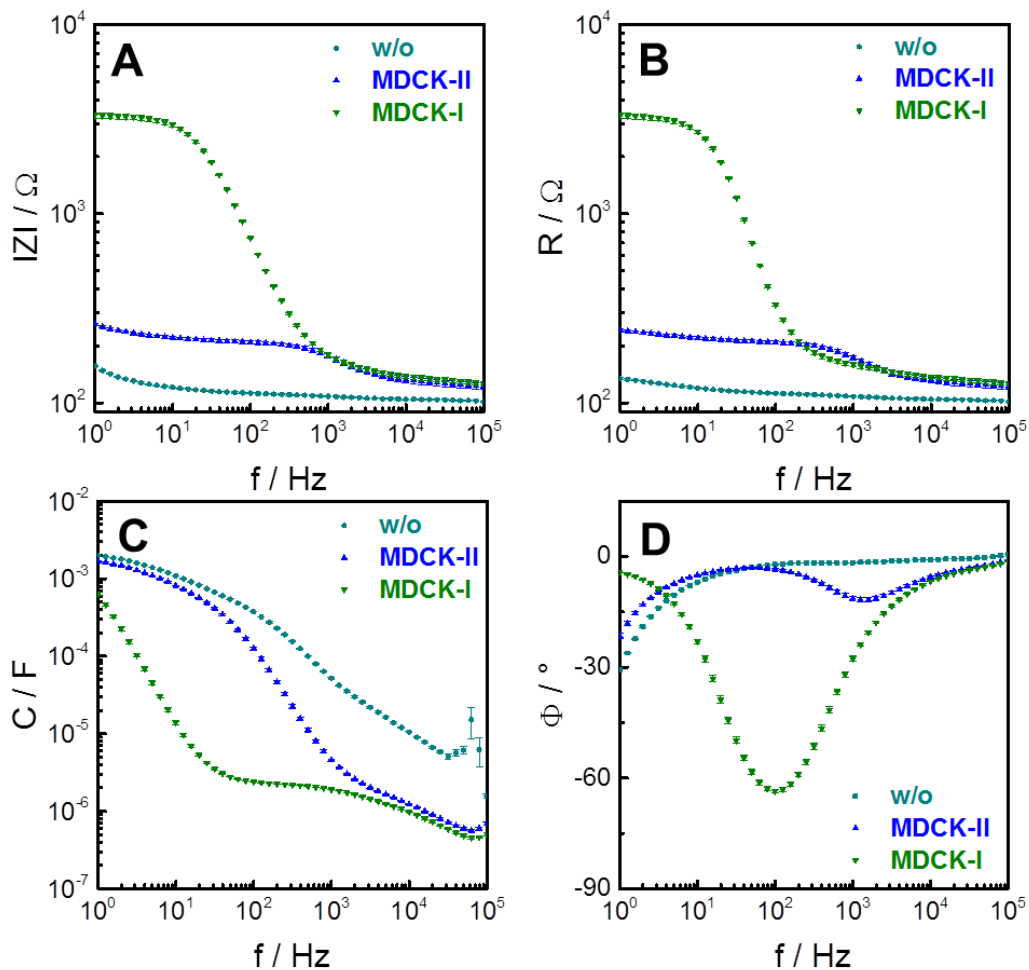


Fig. 7.4: Frequency spectra of the impedimetric parameters recorded for **cell-free inserts** as well as for **MDCK-II-** and **MDCK-I-**covered filter inserts using PEDOT-electrodes (mean \pm SE, $n = 3$). The complex impedance is displayed as the frequency-dependent **(A)** impedance magnitude $|Z|$, **(B)** resistance R , **(C)** capacitance C and **(D)** phase shift Φ , respectively.

Sensitivity improvement of TER-measurements using PEDOT-electrodes

Besides the improved fitting procedure, the sensitivity of the TER-determination is also improved by using PEDOT-electrodes which is mirrored in the normalized impedance magnitude spectra (Fig. 7.5). The sensitivity of the TER-measurement is defined as the maximum of the frequency-dependent normalized impedance. Whereas moderately tight monolayers like MDCK-II cells reveal no significant sensitivity enhancement (Fig. 7.5B), the normalized impedance ($|Z|/|Z|_0$) maximum is five times higher in case of very tight MDCK-I layers (Fig. 7.5D). Additionally, the frequency of the maximal normalized impedance magnitude is shifted from 40 Hz to 5 Hz when using PEDOT-electrodes. It is also striking that the PEDOT-configuration yields a broader sensitive frequency window compared to measurements using stainless steel electrodes for MDCK-II cell layers.

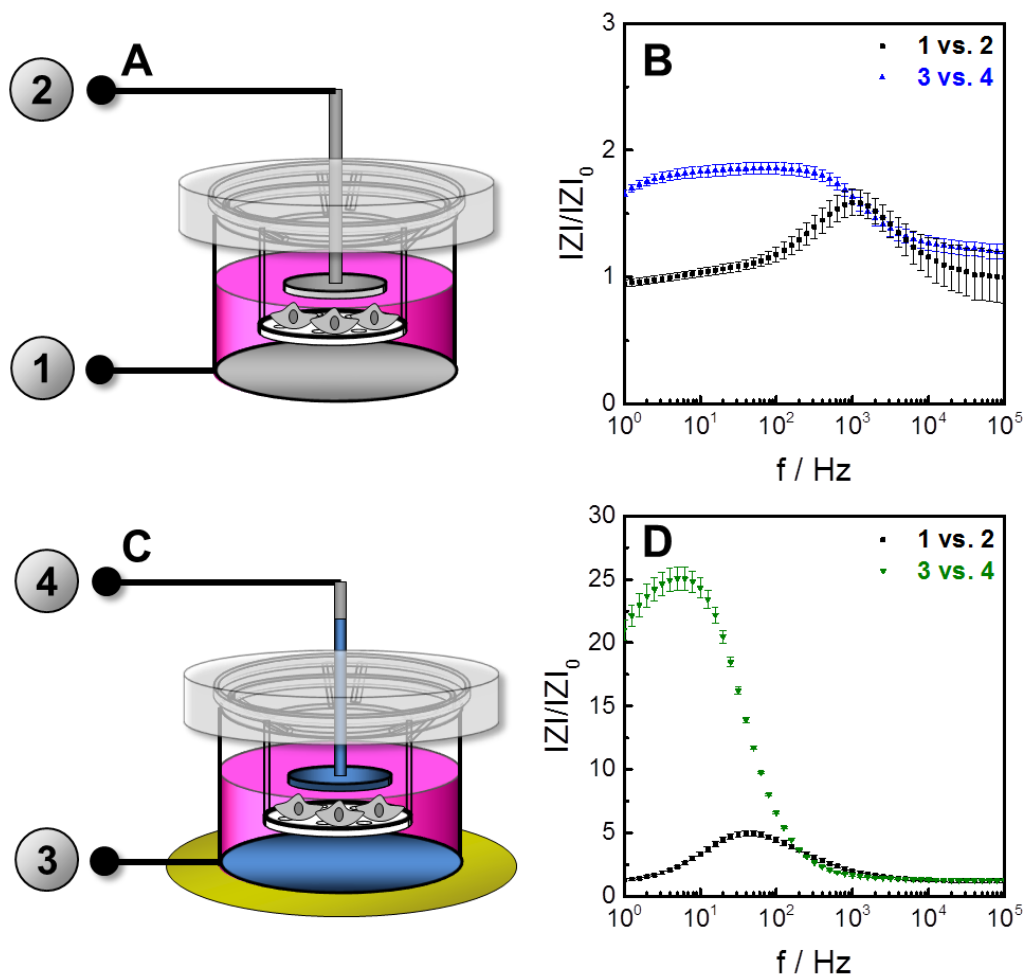


Fig. 7.5: Comparison of the normalized impedance of TER-measurements performed with **(A)** stainless steel electrodes (1 vs. 2) and **(C)** PEDOT-electrodes (3 vs. 4). The normalized impedance spectra ($|Z|/|Z|_0$) are displayed for **(B)** MDCK-II and **(D)** MDCK-I (mean \pm maximal error, $n = 3$).

Extracting the parameters TER and C_{cl} from the impedance spectra

The parameters of the established electric equivalent circuit (chapter 3.1.2, Fig. 3.5) are fitted to the experimental data of Fig. 7.2 and Fig. 7.3. To account for the contribution of a cell-free filter insert, the values for the filter insert resistance R_{ins} and capacitance C_{ins} are determined by analyzing the results of Fig. 7.1 with a more simple equivalent circuit (chapter 3.1.2, Fig. 3.3). The here determined values for R_{ins} and C_{ins} are used for filter correction. The filter-corrected transepithelial electrical resistances and cell layer capacitances of MDCK-II and MDCK-I cells for both electrode arrangements are summarized in Fig. 7.6. Please note that exactly the same monolayers were examined with both, the PEDOT- and stainless steel electrodes.

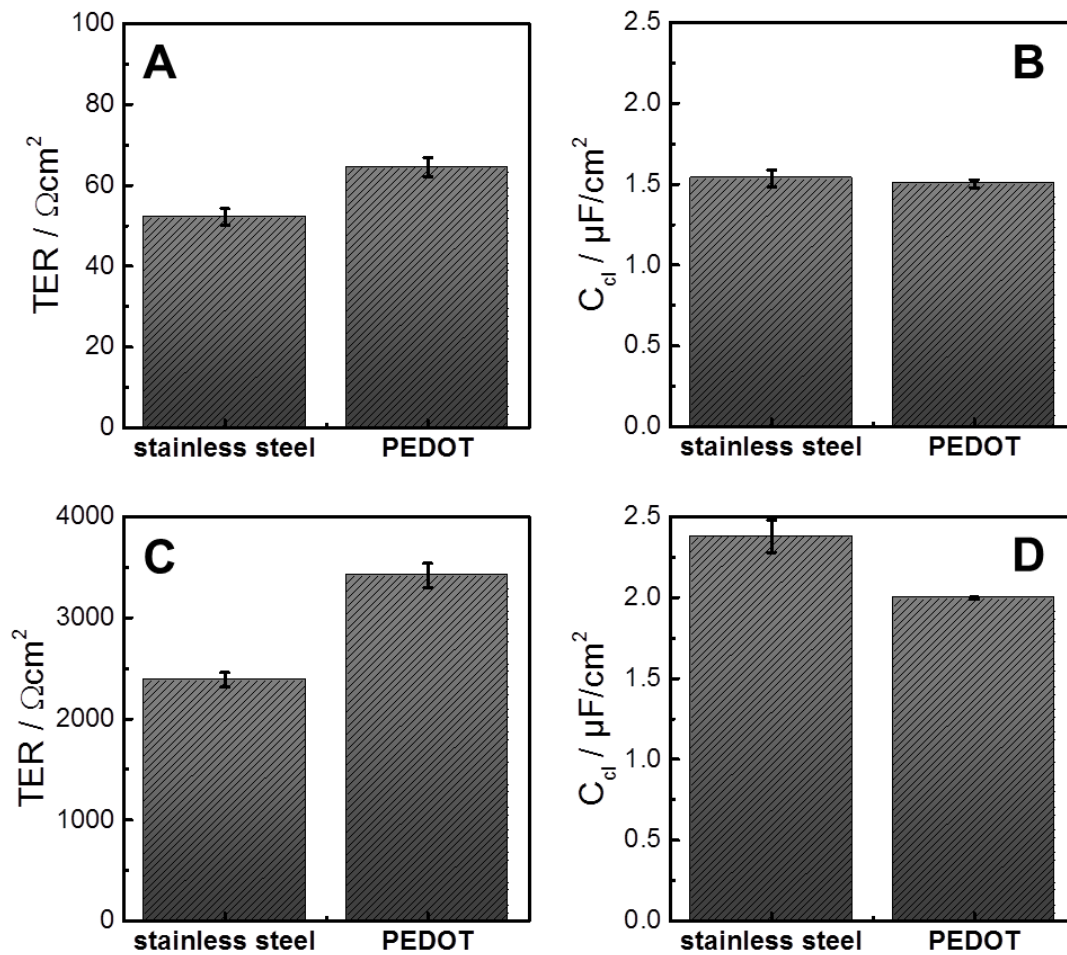


Fig. 7.6: Filter-corrected results of the fitting procedure of the experimental data of the cell-covered filter inserts (Fig. 7.2 and Fig. 7.3). Exactly the same cell-covered filter inserts are used for the transfilter impedance measurements. The bar charts present the transepithelial electrical resistances TER and cell layer capacitances C_{cl} determined with both, the stainless steel and the PEDOT-electrodes (mean \pm SE, $n = 3$). **(A)** TER of MDCK-II, **(B)** C_{cl} of MDCK-II, **(C)** TER of MDCK-I and **(D)** C_{cl} of MDCK-I.

The PEDOT-based setup yields transepithelial electrical resistances of $(64 \pm 2) \Omega\text{cm}^2$ for MDCK-II barriers (Fig. 7.6A). TER provided by the stainless steel electrodes is lower with a value of $(52 \pm 2) \Omega\text{cm}^2$ which is about 14 % smaller. The corresponding cell layer capacitance cannot be distinguished for the two different approaches ranging from $(1.48 - 1.59) \mu\text{F}/\text{cm}^2$ (Fig. 7.6B). A stronger divergence is observed for the TER of MDCK-I monolayers (Fig. 7.6C). The PEDOT-approach reveals TER values of $(3419 \pm 119) \Omega\text{cm}^2$, whereas the stainless steel device results in transepithelial electrical resistances of $(2389 \pm 69) \Omega\text{cm}^2$. Consequently, TER is 30 % reduced when applying stainless steel as the electrode material. Otherwise, experiments using stainless steel electrodes provide higher cell layer capacitances $(2.4 \mu\text{F}/\text{cm}^2 \pm 0.1 \mu\text{F}/\text{cm}^2)$ compared to the PEDOT-based measurement $(1.997 \mu\text{F}/\text{cm}^2 \pm 0.007 \mu\text{F}/\text{cm}^2)$. Thus, the C_{cl} values differ by 17 % (Fig. 7.6D).

In general, the range of the determined TER values is comparable to reported transepithelial electrical resistances of MDCK-I and MDCK-II cells, respectively, indicating the reliability of the PEDOT-based approach (Tab. 5.4). However, the TER values that are determined with the PEDOT-electrodes are significantly higher compared to the TER values provided by the stainless steel electrodes. This trend is observed for both, MDCK-I and MDCK-II cells. Possible explanations for this observation are provided by the following paragraphs:

- (I) The discrepancies in TER and C_{cl} may be due to the different sensitivities of the two approaches. The PEDOT-configuration reads higher transepithelial electrical resistances for both, MDCK-II and MDCK-I cells. As indicated by Fig. 7.5, the sensitivity for TER-determination is enhanced by PEDOT-electrodes for both cell lines. This might be the reason for getting higher TER values using PEDOT-electrodes compared to stainless steel electrodes.
- (II) Otherwise, the high interface impedance of stainless steel electrodes might impede the fitting process of the impedance spectra and hence, lead to an underestimation of TER. The electrode-electrolyte interface capacitance is described by the constant phase element (CPE) which might be the problematic parameter of the fitting procedure.

7.2 Simulated impedance spectra of Caco-2 monolayers for PEDOT and stainless steel as electrode material

The established impedimetric TER-readout shows two weak points:

- (I) Very tight monolayers leading to high transepithelial electrical resistances may cause error-prone fitting processes.
- (II) Another pitfall arises for epithelial layers with highly folded plasma membranes. Such barriers significantly enlarge the interface between the plasma membrane and the surrounding solution resulting in increased cell layer capacitances which are associated with the plateau width in the impedance spectrum. The widespread and pharmaceutically relevant Caco-2 (heterogeneous human epithelial colorectal adenocarcinoma) cells are famous for establishing barrier-forming monolayers with an enormous level of membrane foldings which is commonly described as a brush border structure (Lea 2015; Sambuy *et al.* 2005).

In this chapter, frequency spectra of filter-grown Caco-2 monolayers are simulated for the novel PEDOT-setup and the established stainless steel TER-assay. The frequency-dependent complex impedance is simulated by means of the established electric equivalent circuit (chapter 3.1.2, Fig. 3.3) and the corresponding transfer function. The values of the different circuit elements (R_{bulk} , A_{CPE} , n_{CPE} , TER, C_{cl}) as used in this simulation are listed in Tab. 7.1. The electrode-specific parameters are extracted from transfilter measurements of this work. TER and C_{cl} values of Caco-2 cells are based on reported data (Schäfer *et al.* 2013).

Tab. 7.1: Preset values of the circuit elements of the equivalent circuit applied to simulate frequency-dependent impedance spectra. The electrode-specific parameters are estimated values based on transfilter measurements performed in this work. The transepithelial electrical resistance and the cell layer capacitance of filter-grown Caco-2 cells rely on published data (Schäfer *et al.* 2013).

circuit element	PEDOT	stainless steel
R_{bulk} / Ω	100	25
$A_{\text{CPE}} / \text{s}^{n-1} \mu\text{F}/\text{cm}^2$	2650	60
n_{CPE}	0.76	0.90
TER / Ωcm^2		260
$C_{\text{cl}} / \mu\text{F}/\text{cm}^2$		4.0

The simulated frequency spectra of the complex impedance for a cell-free filter insert and filter-grown Caco-2 cells are displayed as the impedance magnitude $|Z|$, the resistance R , the capacitance C and the phase shift Φ , respectively. The results for the two different electrode materials are compared in Fig. 7.7.

The impedance spectra recorded with stainless steel electrodes indicate a distinct cell impact from 10 Hz to 10^4 Hz (Fig. 7.7A). The PEDOT-electrodes provide discrimination between the cell-covered and the cell-free device from 1 Hz to 10^3 Hz (Fig. 7.7B). As already seen in chapter 7.1, the impedance magnitude is only slightly increasing below 10 Hz, whereas the stainless steel electrodes show the predominance of the electrode-electrolyte interface impedance at these frequencies.

The frequency-dependent resistance that is recorded for PEDOT-electrodes (Fig. 7.7D) is similar to the frequency dependence of the corresponding impedance magnitude. However, the stainless steel electrodes show differences in their impedance and resistance spectra (Fig. 7.7C). The resistance is dominated by the bulk resistance and the lead resistance at higher frequencies from 10^3 Hz to 10^5 Hz, whereas the impact of Caco-2 cells gets obvious between 10 Hz and 10^3 Hz. The resistances at frequencies lower than 10 Hz are dominated by the electrode-electrolyte interface impedance.

The capacitance spectra simulated for stainless steel electrodes shows a cell impact from 10^2 Hz to 10^5 Hz (Fig. 7.7E). The obtained value at 1 Hz is 48 fold higher for the PEDOT-electrodes (Fig. 7.7F). In addition, Caco-2 cells exert a significantly stronger influence on the capacitance spectra of the PEDOT-electrodes.

The simulated spectra of the phase shift for stainless steel electrodes reveal a cell impact in the frequency window from 1 Hz to 10^3 Hz (Fig. 7.7G). Due to the dominance of the electrode-electrolyte double layer capacitance at frequencies in the range of 1 Hz, the phase shift is almost -90° . The PEDOT-electrodes show a cell signal from 1 Hz to 10^4 Hz with a maximal phase shift in the range of -30° at a frequency of 320 Hz (Fig. 7.7H).

The impact of Caco-2 cells to the frequency-dependent impedance is clearly observable for both, the stainless steel and the PEDOT-electrodes. To analyze the TER-sensitivity of both electrode arrangements, the normalized impedance ($|Z|/|Z|_0$) spectra are compiled to provide a more detailed evaluation of the sensitivities (Fig. 7.8).

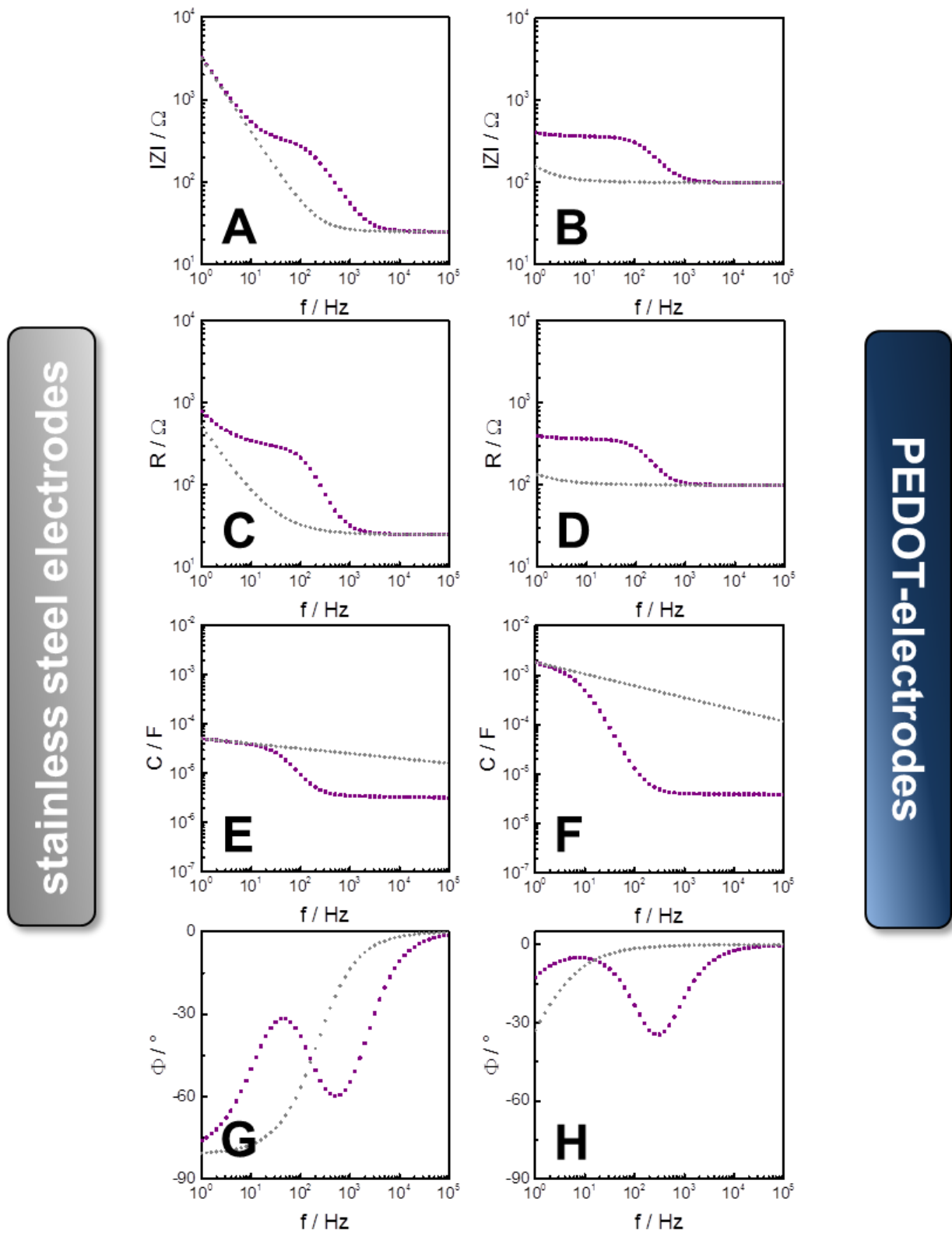


Fig. 7.7: Simulated frequency-dependent complex impedance for transfilter measurements of a cell-free insert and filter-grown **Caco-2 cells** using either PEDOT or stainless steel electrodes, respectively. The complex impedance is displayed as the frequency-dependent **(A)** impedance magnitude $|Z|$ (stainless steel), **(B)** impedance magnitude $|Z|$ (PEDOT), **(C)** resistance R (stainless steel), **(D)** resistance R (PEDOT), **(E)** capacitance C (stainless steel), **(F)** capacitance C (PEDOT), **(G)** phase shift Φ (stainless steel) and **(H)** phase shift Φ (PEDOT). The preset values for the parameters of the corresponding equivalent circuit are presented in Tab. 7.1.

The normalized impedance spectrum of the stainless steel electrodes has a maximum of 5 at a frequency of 160 Hz. The impedance of a cell-free and Caco-2-covered filter insert is not discriminable from each other at low frequencies from 1 Hz to 10 Hz and at the high frequency end from 10^4 Hz to 10^5 Hz. The PEDOT-electrodes show a different normalized impedance spectrum. In contrast to the stainless steel electrodes, $|Z|/|Z|_0$ of the PEDOT-approach has a broadened frequency window from 1 Hz to 10^3 Hz in which the impact of Caco-2 cells gets obvious. The maximum normalized impedance of 3.5 is determined at 25 Hz. Thus, the stainless steel electrodes show a better sensitivity for filter-grown Caco-2 cells compared to the PEDOT-electrodes in terms of the maximum of the normalized impedance magnitude. A second method for quantifying TER-sensitivity is provided by the area under curve (AUC) which is analyzed by Origin2016. AUC for both electrode arrangements has approximately the same value indicating no significant differences in TER-sensitivity.

The bottom line is that the use of PEDOT-electrodes does not provide improved sensitivity for TER-readings of filter-grown Caco-2 cells. The established stainless steel electrodes show even higher maximal normalized impedances indicating higher sensitivity for TER-analysis of Caco-2 cells compared to PEDOT-electrodes. Actually, the use of PEDOT for transepithelial impedance analysis was thought to be especially useful for the analysis of epithelial cell layers with extremely high cell layer capacitances. Caco-2 cells have very high C_{cl} values due to high level of plasma membrane foldings. However, the simulation presented in Fig. 7.7 and Fig. 7.8 clearly shows that PEDOT-electrodes do not improve the sensitivity of TER-measurements of Caco-2 cells.

Nevertheless, PEDOT-electrodes yielded a significant improvement for the TER-measurements of extremely tight barriers (e.g. MDCK-I cell layers), as shown in the previous chapter. In case of MDCK-I cells, the maximal normalized impedance is five times higher for PEDOT-electrodes compared to the stainless steel setup (Fig. 7.5D). Therefore, the PEDOT-based approach has its benefits for the analysis of cell layers with high TER values rather than for the investigation of cell layers with high C_{cl} values. No significant enhancement is obtained by the use of PEDOT-electrodes for TER-analysis with moderately tight cell layers (e.g. MDCK-II cell layers). The maximal normalized impedance magnitudes are in the same range for both electrode arrangements, but the frequency window, in which the cell impact is visible, is broadened using PEDOT-electrodes. However, the high lead resistance of the PEDOT-based setup may mask the cell impact of moderately tight or leaky

monolayers. The significantly higher lead resistance of the novel setup is connected to the lower intrinsic conductivity of PEDOT in comparison to stainless steel and constitutes an inherent limitation of the use of PEDOT as electrodes in transepithelial impedance studies.

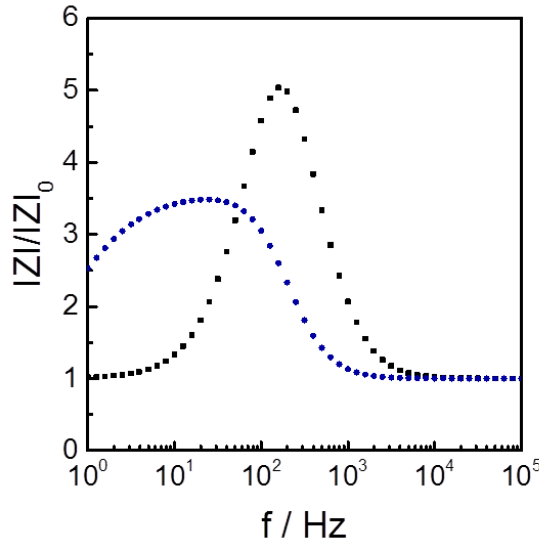


Fig. 7.8: Normalized impedance spectra ($|Z|/|Z|_0$) of the simulated transfilter measurements of Caco-2 cells using either **PEDOT** or **stainless steel electrodes**.

7.3 Long-term stability measurements

The most critical issue of PEDOT-based electrodes is their long-term stability. Most studies on TER are run over several hours or even days and hence, require a robust setup providing reliable data at any time point. Therefore, the long-term stability of the PEDOT-based device is examined by two different approaches:

- (I) Robustness and stability are checked by long-term measurements on cell-free filter inserts.
- (II) Long-term TER-monitoring of MDCK cells is performed including barrier manipulation.

7.3.1 Stability study of the PEDOT-electrodes in absence of epithelial cells

A cell-free filter insert was integrated into the novel TER-device. The complex impedance was recorded from 1 Hz to 10^5 Hz for 40 hours. The resulting frequency- and time-dependent impedance magnitude $|Z|$ and capacitance C are presented in Fig. 7.9.

The impedance magnitude shows similar frequency-dependency as observed in chapter 7.1 (Fig. 7.1B). The main part is dominated by the bulk resistance and the lead resistance, whereas only frequencies lower than 10 Hz reveal the impact of the electrode-electrolyte interface impedance (Fig. 7.9A). However, fluctuations of the overall impedance magnitudes are visible within the first ten hours. At $f = 10^5$ Hz, the value starts with 104 Ω , before a minimal magnitude of 90 Ω is reached after 1.2 hours. Subsequently, the impedance magnitude is increasing to a maximum of 97 Ω at $t = 5.3$ h. Afterwards, the signal indicates a slight, but constant decrease towards a final value of 88 Ω at $t = 40$ h. The same trend is observed for the mid and low frequency area, but with higher absolute impedance magnitudes.

The frequency-dependent capacitance is similar to what has been described (chapter 7.1, Fig. 7.1E). The signal exhibits a continuous increase from higher to lower frequencies (Fig. 7.9B). Moreover, the capacitance suffers from artefacts at high frequencies close to 10^5 Hz which is due to the much smaller reactance relative to the resistance. However, reactance is the basis for calculating the capacitance. The interesting information of this experiment is that the capacitance presents almost constant time-courses. At a frequency of 1 Hz, the value is 2000 μF at the beginning and 1870 μF after 40 hours indicating an insignificant capacitance decrease of only 6 %.

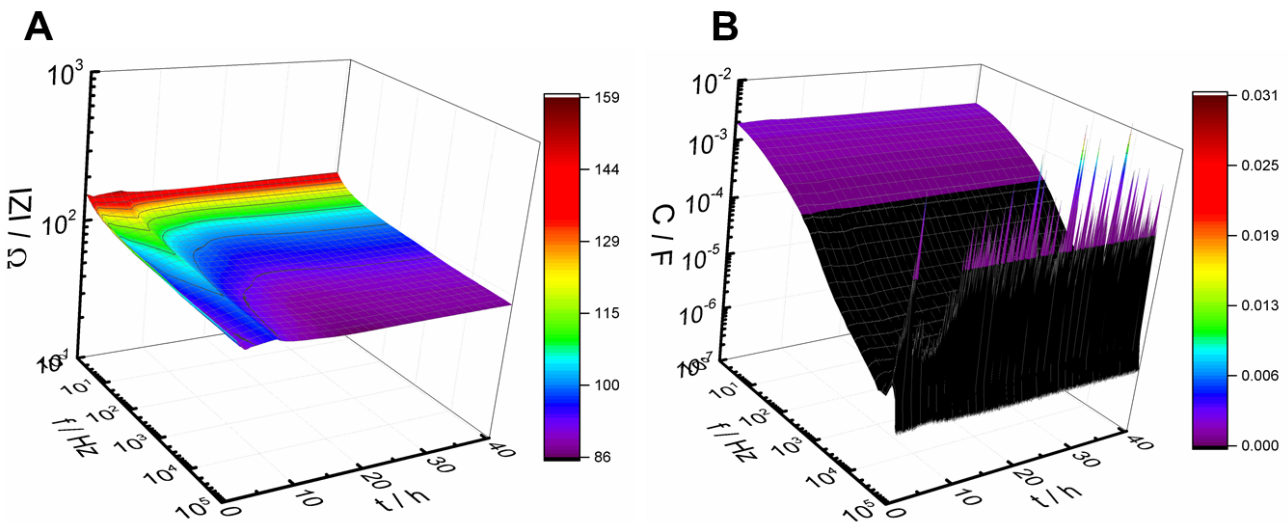


Fig. 7.9: 3D-plots of the long-term stability test of PEDOT-electrodes in absence of barrier-forming cells. The complex impedance is recorded and presented as **(A)** the frequency- and time-dependent impedance magnitude $|Z|$ and **(B)** capacitance C . The graphs represent typical data.

The commercially available, basolateral PEDOT-foil is robust and is supposed to provide adequate long-term stability. Preparation of the apical PEDOT-electrode is the experimental challenge. For this purpose, a stamp-like stainless steel electrode is covered by a thin film of the conductive polymer. The subsequent treatment with ethylene glycol is the crucial point in the fabrication process. Thereby, PSS is dissolved from the films inducing a conformational change of the PEDOT-chains which is directly coupled to a reduced water solubility (Ouyang *et al.* 2004). An initial removal of PSS is not possible, because it is needed to get PEDOT into solution and to allow coating of the stainless steel electrode with the conductive polymer. The results of Fig. 7.9 indicate minor signal fluctuations, but unequivocally prove that the PEDOT-electrodes maintain their stability within a measuring time of 40 hours. Thus, the PEDOT-layer remains stable and does not dissolve from the stainless steel electrode to a higher extent. Nevertheless, the mechanical robustness of the apical PEDOT-electrode needs improvement as touching the glass ring of the measurement chamber is sufficient to induce removal of the PEDOT-layer. As a consequence, the PEDOT-electrodes allow single long-term measurements, but are not suitable for several applications in series. In the current form they must be considered to be more consumable than a stable long-term device.

7.3.2 Manipulation of barrier function of MDCK cells

MDCK-II- and MDCK-I-covered filter inserts were placed into the novel PEDOT-setup. The complex impedance was recorded over a frequency range from 1 Hz to 10^5 Hz for 4.5 hours. After three hours, barrier function of the confluent monolayers was artificially challenged by the apical addition of 5 μ M cytochalasin-D acting as an inhibitor of actin polymerization, as already described in chapter 5. Fig. 7.10 displays the frequency- and time-dependent impedance magnitude $|Z|$ recorded for MDCK-II and MDCK-I cells.

The frequency-dependent impedance of filter-grown MDCK-II cells (Fig. 7.10A) has similar shape as observed in chapter 7.1 (Fig. 7.2B). At the beginning of the experiment, a short increase of the overall impedance magnitudes is observed before stable values are established. At time zero, impedance magnitudes of 217 Ω ($f = 1$ Hz) and of 85 Ω ($f = 100$ kHz) are determined. Evidently, the cell impact remains consistent within three hours of measuring time. Prior to barrier disruption by cytochalasin-D, the impedance magnitudes are 214 Ω at 1 Hz and 86 Ω at 100 kHz. After the apical addition of 5 μ M cytochalasin-D, two phenomena occur:

- (I) The cell-related signal is successively decreasing. At a frequency of 1 Hz, the value is declining from 213 Ω ($t = 2.9$ h) to 171 Ω ($t = 3.4$ h). At the end of the measurement, an impedance magnitude of 167 Ω is detected at the same frequency.
- (II) Values for the high frequency impedance, dominated by the bulk resistance and the lead resistance, reveal slightly increasing impedance magnitudes. After one hour of cytochalasin-D incubation, $|Z|_{100\text{kHz}}$ increases from 86 Ω to 96 Ω .

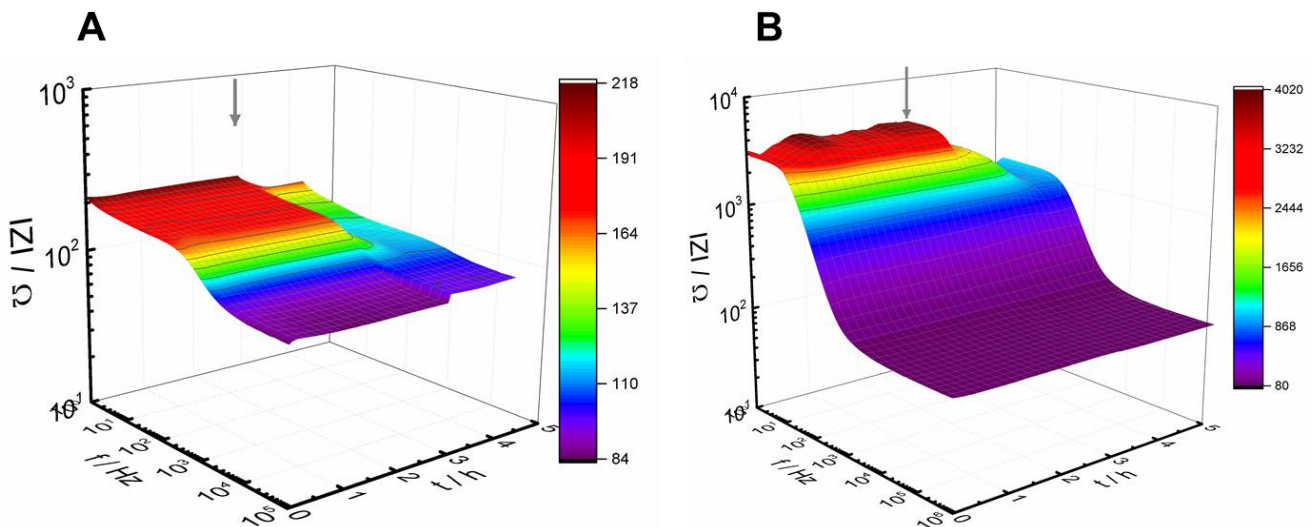


Fig. 7.10: 3D-plots of the long-term stability tests of the PEDOT-electrodes. The complex impedance is recorded in presence of filter-grown **(A)** MDCK-II and **(B)** MDCK-I monolayers and displayed as the frequency- and time-dependent impedance magnitude $|Z|$. The addition of the actin polymerization inhibitor ($5 \mu\text{M}$ cytochalasin-D) to the apical compartment is marked by a grey arrow. The graphs represent typical data.

The frequency-dependent impedance magnitudes of confluent MDCK-I monolayers (Fig. 7.10B) resemble the findings of chapter 7.1 (Fig. 7.3B). The impact of the MDCK-I cells is visible from 1 Hz to 10^3 Hz. At the beginning of the measurement, values of 3259 Ω at 1 Hz and 98 Ω at 100 kHz are recorded. Especially the impedance magnitudes lower than 10 Hz, which are dominated by the cell layer resistance, show fluctuations. For instance, the values are increasing from 2788 Ω ($t = 0$ h) to 4005 Ω ($t = 0.8$ h). This fidgety time-course of barrier function is typical for filter-grown MDCK-I monolayers and often observed in this thesis. After the exposure to the actin polymerization inhibitor the cell impact is diminishing. As a consequence, the impedance magnitude decreases from 3766 Ω ($t = 3.1$ h) to 2237 Ω ($t = 3.6$ h) and reaches a final value of 1118 Ω at a frequency of 1 Hz. In contrast to the

long-term test of MDCK-II cells, the impedance magnitudes at the high frequency end stay constant after the addition of cytochalasin-D.

The corresponding time courses of the transepithelial electrical resistance are extracted from the pool of long-term stability tests using MDCK-II and MDCK-I cells by fitting the parameters of the established equivalent circuit to the experimental data (chapter 3.1.2, Fig. 3.5). The time-dependent changes of the transepithelial electrical resistance are displayed in Fig. 7.11. The time-course of TER is normalized to the time-point of the addition of 5 μM cytochalasin-D.

MDCK-II barriers show constant values prior to the barrier manipulation (Fig. 7.11A). A value of $(99 \pm 14) \Omega\text{cm}^2$ is measured at $t = -3$ h. Only a slight decline is observed during the next three hours towards a TER of $(83 \pm 8) \Omega\text{cm}^2$ at $t = 0$ h. The addition of cytochalasin-D results in an instant break down of TER. After 0.5 hours, the value is only $(30 \pm 8) \Omega\text{cm}^2$. Subsequently, TER is decreasing to $(9 \pm 11) \Omega\text{cm}^2$ at the end of the experiment. Thus, the presence of the actin polymerization inhibitor reduces barrier function of MDCK-II cells about 90 % which indicates complete disruption of the cellular barrier.

Time-resolved TER-monitoring of filter-grown MDCK-I cells (Fig. 7.11B) reflects the fluctuations of barrier function which are observed in Fig. 7.10B. The transepithelial electrical resistance is initially increasing from $(2729 \pm 199) \Omega\text{cm}^2$ at $t = -3$ h to a maximum of $(3860 \pm 498) \Omega\text{cm}^2$ at $t = -2.2$ h. Subsequently, barrier function is in turn reduced establishing a minimum of $(3270 \pm 423) \Omega\text{cm}^2$ at $t = -1.4$ h. The apical exposure to cytochalasin-D leads to an instantaneous TER-reduction from $(3377 \pm 491) \Omega\text{cm}^2$ to $(1915 \pm 665) \Omega\text{cm}^2$ within 0.2 hours. TER of MDCK-I levels off at a plateau of $(1716 \pm 648) \Omega\text{cm}^2$, before a second drop in barrier function is observed. At the end of the experiment, a TER value of $(951 \pm 408) \Omega\text{cm}^2$ is determined indicating a loss in barrier function by about 70 %. However, the addition of 5 μM cytochalasin-D is not sufficient to completely destroy barrier function of MDCK-I cells which is contrary to the findings of the MDCK-II monolayers.

The results of Fig. 7.10 and Fig. 7.11 give rise to several conclusions:

- (I) The PEDOT-electrodes do not affect barrier integrity of MDCK-I and MDCK-II cells within three hours. Prior to the intentional destruction of barrier function the TER values remain stable. The TER-fluctuations of filter-grown MDCK-I monolayers are cell-specific and not a consequence of using PEDOT as the electrode material.

- (II) Besides the non-invasiveness of the PEDOT-based setup, the findings support additionally the long-term stability of the PEDOT-electrodes, as the time-courses of the impedance magnitude and capacitance are stable in presence of cell culture medium.
- (III) TER values recorded with PEDOT-electrodes match published data (Tab. 5.4) validating the new technique.
- (IV) The addition of cytochalasin-D leads to inhibition of actin polymerization which is directly affecting barrier function. The loss in barrier function is reflected in the decline of the transepithelial electrical resistance after the addition of cytochalasin-D. Thus, the PEDOT-based setup provides a powerful and sensitive tool for analyzing potential effects of barrier-opening or barrier-strengthening compounds.

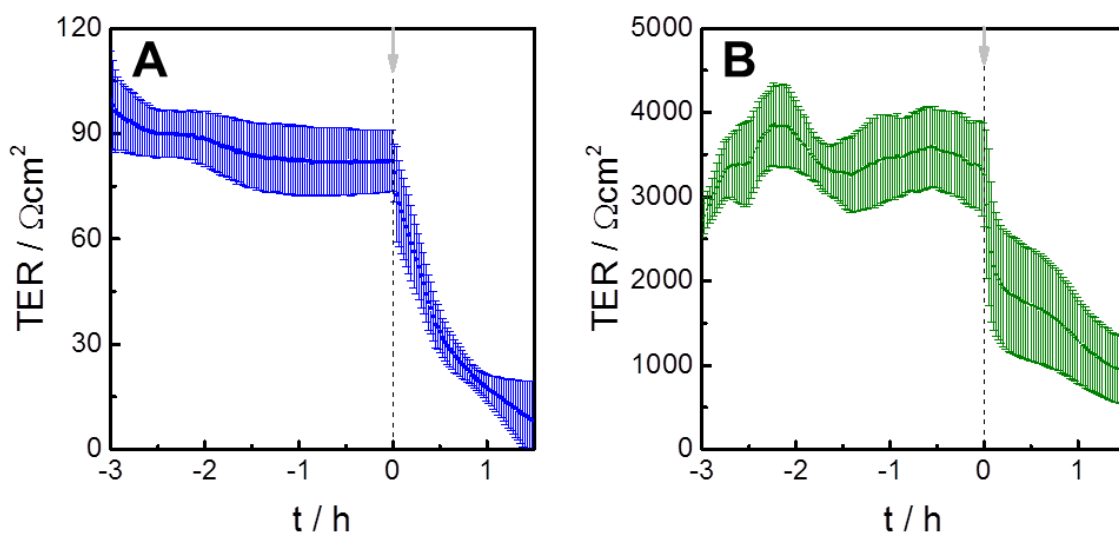


Fig. 7.11: Time-dependent TER-response of filter-grown (A) MDCK-II and (B) MDCK-I monolayers recorded with the PEDOT-electrodes (mean \pm SE, n = 3). After three hours, 5 μM cytochalasin-D are applied apically to challenge barrier function. The transepithelial electrical resistances are extracted from the pool of long-term stability tests using MDCK-II and MDCK-I cells by fitting the parameters of an established electric equivalent circuit (chapter 3.1.2, Fig. 3.5) to the experimental data.

7.4 Summary and outlook

The transepithelial- and endothelial electrical resistance (TER) is the most often studied parameter to describe epithelial and endothelial barrier function. In general, the impedimetric TER-detection is a robust and reliable method. However, the parameter may become error-prone under particular circumstances (i.e. very tight barriers, highly folded plasma membranes). The third project of this thesis introduces a new experimental setup for conventional transfilter measurements overcoming these limitations. By substituting the established electrode materials like stainless steel or gold with poly-3,4-ethylenedioxythiophene (PEDOT), the shape of the recorded frequency spectra was significantly altered. The very high interfacial capacitance of the conductive polymer reduced any masking of the cell layer resistance and cell layer capacitance by the electrode and shifted the influence of the electrode-electrolyte capacitance to frequencies lower than 10 Hz. The apical PEDOT-electrode was treated with ethylene glycol to remove PSS. Thereby, the PEDOT-layer became water insoluble. The contacting pad of the basolateral PEDOT-foil was sputter-coated with a 100 nm thick gold layer to increase the conductivity of the device. First proof-of-concept studies with MDCK-I and MDCK-II barriers proved the rationale of the novel approach and indicated a significant improvement of TER-sensitivity for very tight barriers like MDCK-I layers. Simulated frequency spectra of the complex impedance for filter-grown Caco-2 cells showed that the PEDOT-based approach does not provide significant improvement of TER-measurements for cell layers with highly folded plasma membranes compared to the established, impedance-based TER-setups. Furthermore, the new device was applied in barrier-opening studies demonstrating its potential for the investigation of barrier-influencing substances. In addition, the long-term stability of PEDOT-electrodes was examined in absence of cellular barriers.

So far, the application of PEDOT-electrodes is limited to moderately tight or very tight cell layers due to the relatively high lead resistance of the device. Hence, a more pronounced reduction of the lead resistance, e.g. by the integration of stainless steel into the basolateral PEDOT-film electrode, may be desirable and enable the analysis of leaky barriers. A further optimization of the PEDOT-based setup might be achieved by fostering the mechanical stability of the apical PEDOT-electrode. By means of electrografting (Bélanger and Pinson 2011; Palacin *et al.* 2004) a covalent bond between PEDOT and stainless steel might be formed rendering the PEDOT-electrode more robust. Furthermore, other electrode materials

exhibiting high interface capacitances due to an enlarged active electrode surface (e.g. LSG (laser scribed graphene) electrodes (Fenzl *et al.* 2017; Nayak *et al.* 2016)) might be tested for transfilter measurements. Besides changing the electrode material, a modification of the filter inserts may also lead to the same goal of debilitating the impact of the electrode-electrolyte interface capacitance. By significantly reducing the filter membrane area, the influence of the cell layer resistance R_{cl} and capacitance C_{cl} might be drastically increased and may cover the CPE-dominated impedance magnitudes in the relevant frequency regimes.

8 Summary

Epithelial and endothelial barrier function is studied *in vitro* by cultivating cellular monolayers on porous filter membranes mimicking the physiological situation of an interfacial cell layer between two fluid compartments. In general, the permeability across such barriers is quantified by three parameters:

- (I) The transepithelial electrical resistance (TER) is a measure for the permeability to small inorganic ions and represents the most popular parameter to describe epithelial and endothelial barrier function.
- (II) The permeation of (macro-)molecular probes across barrier-forming layers is described by the molecular permeability coefficient (P_E).
- (III) The osmotic water permeability coefficient (P_{OS}) quantifies barrier function to water flux as a response to an osmotic pressure gradient.

So far, only TER is recorded via impedance spectroscopy, whereas the parameters P_E and P_{OS} are commonly measured by non-impedimetric techniques. The present study contained three projects dealing with the development of new impedance-based assays and devices for a comprehensive analysis of epithelial barrier function.

The first project of this thesis introduced a device to quantify molecular permeability coefficients (P_E) by means of impedance analysis. The permeation of redox-active compounds ($[Fe(CN)_6]^{3-/4-}$, FcMeOH) across epithelial monolayers of different tightness was followed via different electrode arrangements deposited at the bottom of the receiver compartment. The presence of redox tracers induced two faradaic phenomena at the electrode-electrolyte interface (charge-transfer resistance R_{CT} , Warburg impedance Z_W) which provided a linear correlation between $1/|Z|_{1Hz}$ and tracer concentration. Thereby, time-dependent changes of the inverse impedance magnitude at a frequency of 1 Hz were used to report on the time-resolved tracer accumulation in the receiver compartment. Finally, the rate of permeation enabled the calculation of P_E values. Due to the common impedance-based readout, the two parameters P_E and TER have been recorded simultaneously within one single device (P_E TER-assay). The idea was realized by the application of a three electrode configuration. Two co-planar, interdigitated gold electrodes

provided information about substrate permeability, whereas an apical stainless steel electrode was needed in combination with one of the two basolateral electrodes for recording TER values. Besides, a second electrode system was developed that permits spatially resolved monitoring of the permeation of redox-active tracers across different tight cell layers. This second $P_{E}TER$ -version reflects local heterogeneities in epithelial barrier function. For this purpose, the number of working electrodes in the receiver compartment was increased. Compared to the other *in vitro* permeability assays which predominantly rely on fluorescence-based or radio analytical readouts, the assay as presented here was found to be superior in terms of time-resolution, high-throughput potential, automation and handling. The internal TER-control offered continuous observation of barrier integrity and implicates an immense saving of time and costs compared to the established permeability assays.

The second project addressed the development of an impedance-based assay for quantification of transepithelial water permeation. Experimental generation of an osmotic gradient across an epithelial monolayer causes water flux between the two compartments. As a consequence, the ionic concentration changes in the basolateral buffer resulting in an altered conductance. By creating a very small basolateral volume, the signal change was sensitive enough to record these conductivity changes at a frequency of 100 kHz. The time-resolved conductance response provided calculation of osmotic water permeability coefficients (P_{OS}). A first generation of gold electrodes consisting of one central electrode couple enabled very sensitive, but local water flux monitoring. A second version of the novel assay made use the experimental $P_{E}TER$ -setup. By applying two co-planar interdigitated gold electrodes and an apical stainless steel electrode, simultaneous and integral recording of the two barrier-describing parameters – P_{OS} and TER – became possible ($P_{OS}TER$ -assay). In addition, transepithelial water flow was measured with lateral resolution by using three locally distributed electrode pairs beneath the filter membrane. Whereas the conventional water flux assays are supposed to be error-prone and elaborate, the new device offered an automated and easy-to-use approach with high-throughput potential as well as time- and spatially resolved water flux monitoring. The online TER-detection served as an internal control of barrier integrity and led to an enormous saving of time in comparison to standard *in vitro* water flux assays.

The last project of this thesis was targeted on the transepithelial electrical resistance (TER). Conventional impedimetric TER-readings of extremely tight barriers or cell types with a high level of membrane folding easily become error-prone since the impedance of the

electrode-electrolyte interface is increasingly difficult to separate from the cell impedance. By substituting the typical electrode materials (stainless steel, gold) by poly-3,4-ethylenedioxythiophene (PEDOT), the influence of the interface impedance was almost completely removed from the impedance spectra. This was due to the large effective electrode area and the associated high interface capacitance of PEDOT. As a consequence, the sensitivity of TER-measurements for tight barriers was drastically improved. The PEDOT-setup consisted of two elements: (I) A commercially available PEDOT-foil served as a basolateral electrode. The contact pads and leads were covered by a 100 nm thick gold layer to improve the general conductivity of the device. (II) A stamp-like stainless steel electrode was covered by a thin PEDOT:PSS-film and was applied as an apical electrode. A crucial step of the electrode fabrication has been the treatment of the apical PEDOT-electrode with ethylene glycol dissolving PSS from the electrodes and hence, rendering the PEDOT-layer water insoluble and long-term stable.

9 Zusammenfassung

Die Barriereigenschaften von epithelialen und endothelialen Zellschichten werden *in vitro* unter Zuhilfenahme sogenannter Transwell® Filter untersucht. Dabei werden barrierebildenden Zellen konfluent auf diesen permeablen Wachstumssubstraten kultiviert, wodurch die physiologischen Bedingungen zweier voneinander abgetrennter Flüssigkeitshalbräume nachgestellt werden. Generell wird die Permeabilität von Epithelschichten mit Hilfe von drei Parametern beschrieben:

- (I) Der transepitheliale elektrische Widerstand (TER) dient als Maß für die Permeabilität kleiner, anorganischer Ionen und repräsentiert den populärsten Parameter in Studien zur epithelialen und endothelialen Barrier-Funktion.
- (II) Die Permeation (makro-)molekularer Sonden über eine Zellbarriere wird durch den molekularen Permeabilitätskoeffizienten (P_E) charakterisiert.
- (III) Der osmotische Wasserpermeabilitätskoeffizient (P_{OS}) ist ein Maß für die Permeabilität von Wasser über eine Epithelschicht als Reaktion auf einen osmotischen Stimulus.

Bisher werden lediglich TER-Studien impedimetrisch durchgeführt, während die Parameter P_E und P_{OS} durch nicht-impedimetrische Ausleseverfahren bestimmt werden. Die hier vorliegende Studie widmete sich der Entwicklung neuer, impedanzbasierter Messmethoden zur umfassenden Analyse der Barrierefunktion von Epithelzellen.

Das erste Projekt dieser Arbeit stellt einen verbesserten Aufbau zur impedimetrischen Bestimmung von molekularen Permeabilitätskoeffizienten vor. Die Permeation redox-aktiver Sonden ($[\text{Fe}(\text{CN})_6]^{3-/4-}$, FcMeOH) über unterschiedlich dichte Epithelschichten wurde mittels verschiedener Elektrodenstrukturen verfolgt, welche am Boden des Empfänger-Kompartiments integriert wurden. Die Anwesenheit der Redoxsonden induzierte zwei faradaysche Phänomene an der Elektroden-Elektrolyt-Grenzfläche (Ladungsübertragungswiderstand R_{CT} , Warburg-Impedanz Z_W), welche einen linearen Zusammenhang zwischen $1/|Z|_{1\text{Hz}}$ und der anwesenden Konzentration der Permeabilitätssonde ermöglichen. Dadurch konnte der Zeitverlauf des Messsignals (reziproker Betrag der Impedanz bei 1 Hz) dazu verwendet werden, die Anhäufung der

Sonde im Empfänger-Kompartiment zeitaufgelöst darzustellen. Aus der Rate dieser Permeation wurden P_E -Werte berechnet. Durch das gemeinsame, impedanzbasierte Auslesen von P_E und TER konnten beide Parameter simultan und mit nur einem experimentellen Aufbau gemessen werden (P_E TER-Assay). Die Idee wurde mit Hilfe eines Drei-Elektroden-Systems realisiert. Zwei co-planare, interdigitierte Gold-Elektroden erlaubten das Aufzeichnen der Substratpermeabilität, während eine apikale Edelstahl-Elektrode in Kombination mit den Bodenelektroden für die Bestimmung des TER benötigt wurde. Darüber hinaus wurde ein zweites Setup entwickelt, welches ein orts aufgelöstes Aufzeichnen der Permeation redox-aktiver Sonden erlaubte. Hierfür wurde die Anzahl an Gold-Elektroden auf dem Boden des Empfänger-Kompartimentes erhöht. Dadurch konnten lokale Unterschiede in der Barriere-Funktion innerhalb einer gemeinsamen Zellschicht aufgedeckt werden. Verglichen mit den etablierten *in vitro* Permeabilitätsmessungen, welche in erster Linie auf fluoreszenzbasierten oder radioanalytischen Techniken beruhen, war der hier vorgestellte P_E TER-Assay überlegen in Sachen Zeitauflösung, Durchsatzpotential, Automatisierbarkeit und experimenteller Handhabung. Die integrierte TER-Kontrolle ermöglichte eine kontinuierliche Überwachung der Barriereintegrität und brachte eine immense Zeitersparnis im Vergleich zu etablierten *in vitro* Permeabilitätsassays.

Das zweite Projekt adressierte die Entwicklung einer impedimetrischen Messmethode zur Detektion transepithelialen Wasserflusses. Das Anlegen eines osmotischen Gradienten über eine Epithelschicht verursacht einen Wasserstrom zwischen den beiden Kompartimenten. Daraus resultiert eine veränderte Ionenkonzentration im basolateralen Puffer, was wiederum zu einer Beeinflussung der gemessenen Leitfähigkeit führt. Durch das Erzeugen eines sehr kleinen basolateralen Volumens konnte die Leitfähigkeitsänderung bei 100 kHz sensitiv aufgezeichnet werden. Die zeitaufgelöste Leitfähigkeitsänderung ermöglichte die Berechnung des osmotischen Wasserpermeabilitätskoeffizienten (P_{OS}). Eine erste Generation von Gold-Elektroden, welche aus einem zentralen Elektroden-Paar bestand, erlaubte ein äußerst nachweisstarkes, aber lokales Aufzeichnen der über die Zellschicht fließenden Wassermenge. Eine zweite Version des neuen Assays machte sich den experimentellen P_E TER-Messaufbau zunutze. Durch die Verwendung von zwei co-planaren, interdigitierten Gold-Elektroden und einer apikalen Edelstahl-Elektrode wurde eine simultane und integrale Bestimmung der beiden Messgrößen zugänglich. Zusätzlich konnte der Wassertransport über eine zelluläre Barriere mit einer lateralen Auflösung aufgezeichnet werden, indem drei räumlich verteilte Elektroden-Paare unter der Filtermembran integriert

wurden. Während die konventionellen *in vitro* Wasserflussassays im Verdacht stehen, fehleranfällig und aufwändig zu sein, präsentierte das neue System eine hoch automatisierte und einfache Herangehensweise, die neben ihrem hohen Durchsatzpotential zusätzlich zeit- und orts aufgelöste Informationen lieferte. Die mitlaufende TER-Messung diente als interne Kontrolle der Barriereintegrität und führte zu einer enormen Zeitersparnis im Vergleich zu gängigen Wasserfluss-Studien.

Das letzte Kapitel dieser Arbeit war auf den transepithelialen elektrischen Widerstand (TER) gerichtet. TER-Messungen von extrem dichten Barrieren oder von Zellschichten mit stark gefalteter Plasmamembran können mit der üblichen, impedanzbasierten Methode schnell zu fehlerhaften Ergebnissen führen, da sich die Impedanz der Elektroden-Elektrolyt-Grenzfläche nur noch unzureichend von der Impedanz der Zellschicht trennen lässt. Durch das Ersetzen der typischen Elektrodenmaterialien (Edelstahl, Gold) durch Poly-3,4-ethylendioxythiophen (PEDOT) konnte der Einfluss der Grenzflächenkapazität nahezu vollständig aus den Impedanzspektren entfernt werden. Dies lässt sich auf die große effektive Elektrodenfläche und der damit verbundenen hohen Grenzflächenkapazität von PEDOT zurückführen. Dadurch konnte die Sensitivität von TER-Bestimmungen sehr dichter Zellschichten drastisch verbessert werden. Der neue TER-Messaufbau bestand aus zwei Elementen: (I) Eine kommerziell erhältliche PEDOT-Folie diente als basolaterale Elektrode. Die Kontaktstellen und Zuleitungen dieser PEDOT-Filmelektrode wurden mit einer 100 nm dicken Goldschicht versehen, um die allgemeine Leitfähigkeit des Systems zu optimieren. (II) Eine stempelförmige Edelstahl-Elektrode wurde mit einer dünnen PEDOT:PSS-Schicht überzogen und wurde als apikale Elektrode eingesetzt. Einen äußerst wichtigen Schritt in der Elektrodenherstellung stellte die Behandlung der apikalen PEDOT-Elektrode mit Ethylenglykol dar, um PSS aus der Polymerschicht zu lösen und dadurch die PEDOT-Schicht wasserunlöslich und damit langzeitstabil zu machen.

10 References

A

- Alam, J., Koh, J. H., Kwok, S.-K., Park, S.-H., Park, K. and Choi, Y. (2017): Functional Epitopes for Anti-Aquaporin 5 Antibodies in Sjögren Syndrome. – *Journal of dental research* **96**(12): 1414–1421.
- Alberts, B. (2017): *Molecular Biology of the Cell*. CRC Press.
- Almeida, A. de, Soveral, G. and Casini, A. (2014): Gold compounds as aquaporin inhibitors: New opportunities for therapy and imaging. – *Med. Chem. Commun.* **5**(10): 1444–1453.
- Amidon, G. L., Lee, P. I. and Topp, E. M. (1999): *Transport Processes in Pharmaceutical Systems*. Taylor & Francis.
- Anderson, J. M. (2001): Molecular structure of tight junctions and their role in epithelial transport. – *News in physiological sciences : an international journal of physiology produced jointly by the International Union of Physiological Sciences and the American Physiological Society* **16**: 126–130.
- Anderson, J. M. and van Itallie, C. M. (2009): Physiology and function of the tight junction. – *Csh. Perspect. Biol.* **1**(2): a002584.
- Balda, M. S., Whitney, J. A., Flores, C., González, S., Cerejido, M. and Matter, K. (1996): Functional dissociation of paracellular permeability and transepithelial electrical resistance and disruption of the apical-basolateral intramembrane diffusion barrier by expression of a mutant tight junction membrane protein. – *The Journal of cell biology* **134**(4): 1031–1049.

B

- Balimane, P. V., Han, Y.-H. and Chong, S. (2006): Current industrial practices of assessing permeability and P-glycoprotein interaction. – *The AAPS journal* **8**(1): E1-13.
- Balint, R., Cassidy, N. J. and Cartmell, S. H. (2014): Conductive polymers: towards a smart biomaterial for tissue engineering. – *Acta biomaterialia* **10**(6): 2341–2353.
- Bard, A. J. and Faulkner, L. R. (2001): *Electrochemical methods: Fundamentals and applications*. Wiley, Hoboken, NJ, 833 pp.
- Barsoukov, E. and Macdonald, J. R. (2005): *Impedance Spectroscopy*. John Wiley & Sons, Inc, Hoboken, NJ, USA.
- Basu, A., Biswas, D. and Mukherjee, A. (2013): Genotoxicity Testing of Two Anticaking Agents: Sodium and Potassium Ferrocyanide in vitro.
- Baumgarten, S. and Robelek, R. (2011): Surface plasmon resonance (SPR) sensors for the rapid, sensitive detection of the cellular response to osmotic stress. – *Sensors and Actuators B: Chemical* **156**(2): 798–804.
- Baylis, P. H. (1988): Water movement through lipid bilayers, pores and plasma membranes: Theory and reality. (Distinguished Lecture Series of the Society of General Physiologists, Volume 4). Alan Finkelstein, John Wiley and Sons Ltd: New York. 228 pages, £38.45 (1987). – *Cell Biochem. Funct.* **6**(3): 223.
- Bazzoni, G., Martinez-Estrada, O. M., Orsenigo, F., Cordenonsi, M., Citi, S. and Dejana, E. (2000): Interaction of junctional adhesion molecule with the tight junction components ZO-1, cingulin, and occludin. – *The Journal of biological chemistry* **275**(27): 20520–20526.
- Beasley, S., El-Sherbiny, M., Megyerdi, S., El-Shafey, S., Choksi, K., Kaddour-Djebbar, I., Sheibani, N., Hsu, S. and Al-Shabrawey, M. (2014): Caspase-14 expression impairs retinal pigment epithelium barrier function: potential role in diabetic macular edema. – *BioMed. Res.* **2014**: 417986.
- Bélanger, D. and Pinson, J. (2011): Electrografting: A powerful method for surface modification. – *Chemical Society reviews* **40**(7): 3995–4048.
- Bergner, S., Wegener, J. and Matysik, F.-M. (2012): Monitoring passive transport of redox mediators across a confluent cell monolayer with single-cell resolution by means of scanning electrochemical microscopy. – *Anal. Methods* **4**(3): 623–629.

References

- Berry, V., Francis, P., Kaushal, S., Moore, A. and Bhattacharya, S. (2000): Missense mutations in MIP underlie autosomal dominant 'polymorphic' and lamellar cataracts linked to 12q. – *Nature genetics* **25**(1)
- Bevington, P. R. and Robinson, D. K. (2003): *Data reduction and error analysis for the physical sciences*. McGraw-Hill, Boston, Mass., 320 pp.
- Beyer, E. C., Paul, D. L. and Goodenough, D. A. (1990): Connexin family of gap junction proteins. – *The Journal of membrane biology* **116**(3): 187–194.
- Bobacka, J., Lewenstam, A. and Ivaska, A. (2000): Electrochemical impedance spectroscopy of oxidized poly(3,4-ethylenedioxythiophene) film electrodes in aqueous solutions. – *Journal of Electroanalytical Chemistry* **489**(1): 17–27.
- Borradori, L. and Sonnenberg, A. (1996): Hemidesmosomes: Roles in adhesion, signaling and human diseases. – *Current opinion in cell biology* **8**(5): 647–656.
- Boyer, J. S. (1985): Water Transport. – *Annu. Rev. Plant. Physiol.* **36**(1): 473–516.
- Brooks, H. L., Regan, J. W. and Yool, A. J. (2000): Inhibition of aquaporin-1 water permeability by tetraethylammonium: involvement of the loop E pore region. – *Molecular pharmacology* **57**(5): 1021–1026.

C

- Carpi-Medina, P. and Whitembury, G. (1988): Comparison of transcellular and transepithelial water osmotic permeabilities (Pos) in the isolated proximal straight tubule (PST) of the rabbit kidney. – *Pflügers Archiv European Journal of Physiology* **412**(1-2): 66–74.
- Carr, G., Wright, J. A. and Simmons, N. L. (2010): Epithelial barrier resistance is increased by the divalent cation zinc in cultured MDCKII epithelial monolayers. – *J. Membrane Biol.* **237**(2-3): 115–123.
- Chepelinsky, A. B. (2009): Structural function of MIP/aquaporin 0 in the eye lens; genetic defects lead to congenital inherited cataracts. – *Handbook of experimental pharmacology* (190): 265–297.
- Cho, M. J., Thompson, D. P., Cramer, C. T., Vidmar, T. J. and Scieszka, J. F. (1989): The Madin Darby Canine Kidney (MDCK) Epithelial Cell Monolayer as a Model Cellular Transport Barrier. – *Pharm. Res.* **6**(1): 71–77.
- Cohen, A. W., Carbajal, J. M. and Schaeffer, R. C. (1999): VEGF stimulates tyrosine phosphorylation of beta-catenin and small-pore endothelial barrier dysfunction. – *The American journal of physiology* **277**(5): H2038-49.
- Conway, B. E., Bockris, J. O'M. and White, R. E. (2002): *Modern Aspects of Electrochemistry*. – Modern Aspects of Electrochemistry, No. 32. Kluwer Academic Publishers, Boston, MA.
- Cui, X., Lee, V. A., Raphael, Y., Wiler, J. A., Hetke, J. F., Anderson, D. J. and Martin, D. C. (2001): Surface modification of neural recording electrodes with conducting polymer/biomolecule blends. – *J. Biomed. Mater. Res.* **56**(2): 261–272.
- Cui, X. and Martin, D. C. (2003): Electrochemical deposition and characterization of poly(3,4-ethylenedioxythiophene) on neural microelectrode arrays. – *Sensors and Actuators B: Chemical* **89**(1-2): 92–102.

D

- Dai, L. (2004): *Intelligent Macromolecules for Smart Devices: From Materials Synthesis to Device Applications*. – Engineering Materials and Processes. Springer-Verlag London Limited, London.
- Dainty, J. (1976): *Water Relations of Plant Cells*. – In: Lüttge, U. and Pitman, M. G. (eds): *Transport in Plants II: Part A Cells*. Encyclopedia of Plant Physiology, 2 / A. Springer Berlin Heidelberg, Berlin, Heidelberg, pp. 12–35.
- Davignon, J. and Ganz, P. (2004): Role of endothelial dysfunction in atherosclerosis. – *Circulation* **109**(23 Suppl 1)
- Deen, P. M., Nielsen, S., Bindels, R. J. and van Os, C. H. (1997): Apical and basolateral expression of aquaporin-1 in transfected MDCK and LLC-PK cells and functional evaluation of their transcellular osmotic water permeabilities. – *Eur J Physiol* **433**(6): 780–787.
- Detmers, F. J. M., Groot, B. L. de, Müller, E. M., Hinton, A., Konings, I. B. M., Sze, M., Flitsch, S. L., Grubmüller, H. and Deen, P. M. T. (2006): Quaternary ammonium compounds as water channel blockers. Specificity, potency, and site of action. – *The Journal of biological chemistry* **281**(20): 14207–14214.

References

- Diaz, A. F., Kanazawa, K. K. and Gardini, G. P. (1979): Electrochemical polymerization of pyrrole. – *J. Chem. Soc., Chem. Commun.* (14)
- Dorr, R. A., Kierbel, A., Vera, J. and Parisi, M. (1997): A new data-acquisition system for the measurement of the net water flux across epithelia. – *Comput. Meth. Prog. Bio.* **53**(1): 9–14.
- Dubrovskiy, O., Birukova, A. A. and Birukov, K. G. (2013): Measurement of local permeability at subcellular level in cell models of agonist- and ventilator-induced lung injury. – *Laboratory investigation; a journal of technical methods and pathology* **93**(2): 254–263.

E

- Eurell, J.A.C., Frappier, B. L. and Dellmann, H. D. (2006): *Dellmann's Textbook of Veterinary Histology, with CD*. Wiley.

F

- Fan, B., Mei, X. and Ouyang, J. (2008): Significant Conductivity Enhancement of Conductive Poly(3,4-ethylenedioxythiophene):Poly(styrenesulfonate) Films by Adding Anionic Surfactants into Polymer Solution. – *Macromolecules* **41**(16): 5971–5973.
- Fanning, A. S., Jameson, B. J., Jesaitis, L. A. and Anderson, J. M. (1998): The tight junction protein ZO-1 establishes a link between the transmembrane protein occludin and the actin cytoskeleton. – *The Journal of biological chemistry* **273**(45): 29745–29753.
- Farinas, J., Kneen, M., Moore, M. and Verkman, A. S. (1997): Plasma Membrane Water Permeability of Cultured Cells and Epithelia Measured by Light Microscopy with Spatial Filtering. – *J Gen Physiol* **110**(3): 283–296.
- Farinas, J. and Verkman, A. S. (1996): Cell volume and plasma membrane osmotic water permeability in epithelial cell layers measured by interferometry. – *Biophys J* **71**(6): 3511–3522.
- Fenzl, C., Nayak, P., Hirsch, T., Wolfbeis, O. S., Alshareef, H. N. and Baeumner, A. J. (2017): Laser-Scribed Graphene Electrodes for Aptamer-Based Biosensing. – *ACS sensors* **2**(5): 616–620.
- Fischbarg, J. (2010): Fluid transport across leaky epithelia: Central role of the tight junction and supporting role of aquaporins. – *Physiological reviews* **90**(4): 1271–1290.
- Fischbarg, J., Diecke, F. P. J., Iserovich, P. and Rubashkin, A. (2006): The Role of the Tight Junction in Paracellular Fluid Transport across Corneal Endothelium. Electro-osmosis as a Driving Force. – *The Journal of membrane biology* **210**(2): 117–130.
- Freshney, R. I. (ed.) (2010): *Culture of animal cells: A manual of basic technique and specialized applications*. Wiley-Blackwell, Hoboken, N.J, Online-Ressource.
- Fromm, M., Krug, S. M., Zeissig, S., Richter, J. F., Rosenthal, R., Schulzke, J.-D. and Günzel, D. (2009): High-resolution analysis of barrier function. – *Annals of the New York Academy of Sciences* **1165**: 74–81.
- Fuller, S., Bonsdorff, C. H. von and Simons, K. (1984): Vesicular stomatitis virus infects and matures only through the basolateral surface of the polarized epithelial cell line, MDCK. – *Cell* **38**(1): 65–77.
- Furuse, M., Itoh, M., Hirase, T., Nagafuchi, A., Yonemura, S. and Tsukita, S. (1994): Direct association of occludin with ZO-1 and its possible involvement in the localization of occludin at tight junctions. – *The Journal of cell biology* **127**(6 Pt 1): 1617–1626.

G

- Gallicano, G. I., Kouklis, P., Bauer, C., Yin, M., Vasioukhin, V., Degenstein, L. and Fuchs, E. (1998): Desmoplakin is required early in development for assembly of desmosomes and cytoskeletal linkage. – *The Journal of cell biology* **143**(7): 2009–2022.
- Ghandehari, H., Smith, P. L., Ellens, H., Yeh, P. Y. and Kopecek, J. (1997): Size-dependent permeability of hydrophilic probes across rabbit colonic epithelium. – *J. Pharmacol. Exp. Ther.* **280**(2): 747–753.

References

- Giaever, I. (1993): Correction: Micromotion of Mammalian Cells Measured Electrically. – *Proceedings of the National Academy of Sciences of the United States of America* **90**(4): 1634b-1634.
- Giaever, I. and Keese, C. R. (1984): Monitoring fibroblast behavior in tissue culture with an applied electric field. – *Proceedings of the National Academy of Sciences of the United States of America* **81**(12): 3761–3764.
- Giaever, I. and Keese, C. R. (1991): Micromotion of mammalian cells measured electrically. – *Proceedings of the National Academy of Sciences of the United States of America* **88**(17): 7896–7900.
- Gitter, A. H., Bertog, M., Schulzke, J.-D. and Fromm, M. (1997): Measurement of paracellular epithelial conductivity by conductance scanning. – *Pflügers Archiv European Journal of Physiology* **434**(6): 830–840.
- Gitter, A. H., Wullstein, F., Fromm, M. and Schulzke, J. D. (2001): Epithelial barrier defects in ulcerative colitis: Characterization and quantification by electrophysiological imaging. – *Gastroenterology* **121**(6): 1320–1328.
- Gonzalez-Mariscal, L., Chávez de Ramírez, B. and Cereijido, M. (1985): Tight junction formation in cultured epithelial cells (MDCK). – *J. Membrane Biol.* **86**(2): 113–125.
- González-Mariscal, L., Nava, P. and Hernández, S. (2005): Critical role of tight junctions in drug delivery across epithelial and endothelial cell layers. – *The Journal of membrane biology* **207**(2): 55–68.
- Groenendaal, L., Jonas, F., Freitag, D., Pielartzik, H. and Reynolds, J. R. (2000): Poly(3,4-ethylenedioxythiophene) and Its Derivatives: Past, Present, and Future. – *Adv. Mater.* **12**(7): 481–494.
- Groot, B. L. de and Grubmüller, H. (2005): The dynamics and energetics of water permeation and proton exclusion in aquaporins. – *Current opinion in structural biology* **15**(2): 176–183.
- Groschwitz, K. R., Ahrens, R., Osterfeld, H., Gurish, M. F., Han, X., Abrink, M., Finkelman, F. D., Pejler, G. and Hogan, S. P. (2009): Mast cells regulate homeostatic intestinal epithelial migration and barrier function by a chymase/Mcpt4-dependent mechanism. – *Proceedings of the National Academy of Sciences of the United States of America* **106**(52): 22381–22386.
- Guimard, N. K., Gomez, N. and Schmidt, C. E. (2007): Conducting polymers in biomedical engineering. – *Progress in Polymer Science* **32**(8-9): 876–921.
- Gumbiner, B., Lowenkopf, T. and Apatira, D. (1991): Identification of a 160-kDa polypeptide that binds to the tight junction protein ZO-1. – *Proceedings of the National Academy of Sciences of the United States of America* **88**(8): 3460–3464.
- Günzel, D., Krug, S. M., Rosenthal, R. and Fromm, M. (2010): *Biophysical Methods to Study Tight Junction Permeability*. – In: Yu, A. (ed.): *Claudins. Current Topics in Membranes*, v. 65. Elsevier textbooks, s.l., pp. 39–78.
- Günzel, D. and Yu, A. S. L. (2013): Claudins and the modulation of tight junction permeability. – *Physiological reviews* **93**(2): 525–569.
- Günzel, D., Zakrzewski, S. S., Schmid, T., Pangalos, M., Wiedenhoef, J., Blasse, C., Ozboda, C. and Krug, S. M. (2012): From TER to trans- and paracellular resistance: Lessons from impedance spectroscopy. – *Annals of the New York Academy of Sciences* **1257**: 142–151.
- Gustafsson, H., Kvarnström, C. and Ivaska, A. (2008): Comparative study of n-doping and p-doping of poly(3,4-ethylenedioxythiophene) electrosynthesised on aluminium. – *Thin Solid Films* **517**(2): 474–478.

H

- Hajek Kathrin, W. J. (2017): *Disseration_KathrinHajek*.
- Hakvoort, A., Haselbach, M., Wegener, J., Hoheisel, D. and Galla, H. J. (1998): The polarity of choroid plexus epithelial cells in vitro is improved in serum-free medium. – *J. Neurochem.* **71**(3): 1141–1150.
- Hamann, S., Kiilgaard, J. F., Litman, T., Alvarez-Leefmans, F. J., Winther, B. R. and Zeuthen, T. (2002): Measurement of Cell Volume Changes by Fluorescence Self-Quenching. – *J Fluoresc* **12**(2): 139–145.
- Hara, M., Ma, T. and Verkman, A. S. (2002): Selectively reduced glycerol in skin of aquaporin-3-deficient mice may account for impaired skin hydration, elasticity, and barrier recovery. – *J Biol Chem* **277**(48): 46616–46621.

References

- Hara-Chikuma, M., Sohara, E., Rai, T., Ikawa, M., Okabe, M., Sasaki, S., Uchida, S. and Verkman, A. S. (2005): Progressive adipocyte hypertrophy in aquaporin-7-deficient mice: adipocyte glycerol permeability as a novel regulator of fat accumulation. – *J Biol Chem* **280**(16): 15493–15496.
- Harburger, D. S. and Calderwood, D. A. (2009): Integrin signalling at a glance. – *Journal of cell science* **122**(Pt 2): 159–163.
- Haskins, J., Gu, L., Wittchen, E. S., Hibbard, J. and Stevenson, B. R. (1998): ZO-3, a novel member of the MAGUK protein family found at the tight junction, interacts with ZO-1 and occludin. – *The Journal of cell biology* **141**(1): 199–208.
- Heijink, I. H., Kies, P. M., Kauffman, H. F., Postma, D. S., van Oosterhout, A. J. M. and Vellenga, E. (2007): Down-regulation of E-cadherin in human bronchial epithelial cells leads to epidermal growth factor receptor-dependent Th2 cell-promoting activity. – *Journal of immunology (Baltimore, Md. : 1950)* **178**(12): 7678–7685.
- Hibuse, T., Maeda, N., Funahashi, T., Yamamoto, K., Nagasawa, A., Mizunoya, W., Kishida, K., Inoue, K., Kuriyama, H., Nakamura, T., Fushiki, T., Kihara, S. and Shimomura, I. (2005): Aquaporin 7 deficiency is associated with development of obesity through activation of adipose glycerol kinase. – *P Natl Acad Sci USA* **102**(31): 10993–10998.
- Hillgren, K. M., Kato, A. and Borchardt, R. T. (1995): In vitro systems for studying intestinal drug absorption. – *Med. Res. Rev.* **15**(2): 83–109.
- Hu, J. and Verkman, A. S. (2006): Increased migration and metastatic potential of tumor cells expressing aquaporin water channels. – *FASEB journal : official publication of the Federation of American Societies for Experimental Biology* **20**(11): 1892–1894.
- Hua, S. Z. and Pennell, T. (2009): A microfluidic chip for real-time studies of the volume of single cells. – *Lab on a chip* **9**(2): 251–256.
- Huang, Z.-B., Yin, G.-F., Liao, X.-M. and Gu, J.-W. (2014): Conducting polypyrrole in tissue engineering applications. – *Front. Mater. Sci.* **8**(1): 39–45.
- Hub, J. S. and Groot, B. L. de (2008): Mechanism of selectivity in aquaporins and aquaglyceroporins. – *Proceedings of the National Academy of Sciences of the United States of America* **105**(4): 1198–1203.
- Hynes, R. O. (2002): Integrins: Bidirectional, allosteric signaling machines. – *Cell* **110**(6): 673–687.

I

- Ikenouchi, J., Furuse, M., Furuse, K., Sasaki, H., Tsukita, S. and Tsukita, S. (2005): Tricellulin constitutes a novel barrier at tricellular contacts of epithelial cells. – *The Journal of cell biology* **171**(6): 939–945.
- Inai, T., Kobayashi, J. and Shibata, Y. (1999): Claudin-1 contributes to the epithelial barrier function in MDCK cells. – *Eur. J. Cell Biol.* **78**(12): 849–855.
- Ishibashi, K., Hara, S. and Kondo, S. (2009): Aquaporin water channels in mammals. – *Clinical and experimental nephrology* **13**(2): 107–117.
- Ishibashi, K., Tanaka, Y. and Morishita, Y. (2014): The role of mammalian superaquaporins inside the cell. – *Biochimica et biophysica acta* **1840**(5): 1507–1512.
- Itoh, M., Furuse, M., Morita, K., Kubota, K., Saitou, M. and Tsukita, S. (1999): Direct binding of three tight junction-associated MAGUKs, ZO-1, ZO-2, and ZO-3, with the COOH termini of claudins. – *The Journal of cell biology* **147**(6): 1351–1363.

J

- Janshoff, A., Wegener, J., Sieber, M. and Galla, H.-J. (1996): Double-mode impedance analysis of epithelial cell monolayers cultured on shear wave resonators. – *European Biophysics Journal* **25**(2): 93–103.
- Jin, B.-J. and Verkman, A. S. (2017): Microfluidic platform for rapid measurement of transepithelial water transport. – *Lab Chip* **17**(5): 887–895.
- Johnson, A. W. and Harley, B. (2011): *Mechanobiology of Cell-Cell and Cell-Matrix Interactions*. Springer US.

References

Jovov, B., Wills, N. K. and Lewis, S. A. (1991): A spectroscopic method for assessing confluence of epithelial cell cultures. – *Am. J. Physiol.* **261**(6 Pt 1): C1196-203.

K

Kadam, R. S., Scheinman, R. I. and Kompella, U. B. (2012): Pigmented-MDCK (P-MDCK) cell line with tunable melanin expression: an in vitro model for the outer blood-retinal barrier. – *Mol. Pharm.* **9**(11): 3228–3235.

Kaiser, M., Pereira, S., Pohl, L., Ketelhut, S., Kemper, B., Gorzelanny, C., Galla, H.-J., Moerschbacher, B. M. and Goycoolea, F. M. (2015): Chitosan encapsulation modulates the effect of capsaicin on the tight junctions of MDCK cells. – *Sci. Rep.* **5**: 10048.

Kaneto, K., Yoshino, K. and Inuishi, Y. (1983): Electrical and optical properties of polythiophene prepared by electrochemical polymerization. – *Solid State Communications* **46**(5): 389–391.

Karimi Shervedani, R., Akrami, Z. and Sabzyan, H. (2011): Nanostructure Molecular Assemblies Constructed Based on Ex-Situ and In-Situ Layer-by-Layer Ferrioxamation Characterized by Electrochemical and Scanning Tunneling Microscopy Methods. – *J. Phys. Chem. C* **115**(16): 8042–8055.

Kasem, K. (2006): *Electrochemical Behavior of Hexacyano Iron (III/II) in Frozen Aqueous Electrolytes*.

Kaur, G., Adhikari, R., Cass, P., Bown, M. and Gunatillake, P. (2015): Electrically conductive polymers and composites for biomedical applications. – *RSC Adv.* **5**(47): 37553–37567.

Kedem, O. and Katchalsky, A. (1958): Thermodynamic analysis of the permeability of biological membranes to non-electrolytes. – *undefined*.

Keese, C. R., Wegener, J., Walker, S. R. and Giaever, I. (2004): Electrical wound-healing assay for cells in vitro. – *Proceedings of the National Academy of Sciences of the United States of America* **101**(6): 1554–1559.

Kennedy, M. B. (1995): Origin of PDZ (DHR, GLGF) domains. – *Trends in biochemical sciences* **20**(9): 350.

Kim, Y. H., Sachse, C., Machala, M. L., May, C., Müller-Meskamp, L. and Leo, K. (2011): Highly Conductive PEDOT: PSS Electrode with Optimized Solvent and Thermal Post-Treatment for ITO-Free Organic Solar Cells. – *Adv. Funct. Mater.* **21**(6): 1076–1081.

Kim Kit Lee, M. (2014): Drug Development in Cell Culture: Crosstalk from the Industrial Prospects. – *J. Bioequiv. Availab.* **06**(03): 96–114.

Kimelberg, H. K., O'Connor, E. R., Sankar, P. and Keese, C. (1992): Methods for determination of cell volume in tissue culture. – *Canadian journal of physiology and pharmacology* **70 Suppl**: S323-33.

Klusmeier, N., Schnittler, H.-J. and Seebach, J. (2019): A novel microscopic assay reveals heterogeneous regulation of local endothelial barrier function. – *Biophys. J.*

Kotra, G., Haase, W. and Frömter, E. (1993): Tight-junction tightness of Necturus gall bladder epithelium is not regulated by cAMP or intracellular Ca²⁺. I. Microscopic and general electrophysiological observations. – *Pflügers Archiv European Journal of Physiology* **425**(5-6): 528–534.

Koutsouras, D. A., Gkoupidenis, P., Stolz, C., Subramanian, V., Malliaras, G. G. and Martin, D. C. (2017): Impedance Spectroscopy of Spin-Cast and Electrochemically Deposited PEDOT:PSS Films on Microfabricated Electrodes with Various Areas. – *ChemElectroChem* **4**(9): 2321–2327.

K'Owino, I. O. and Sadik, O. A. (2005): Impedance Spectroscopy: A Powerful Tool for Rapid Biomolecular Screening and Cell Culture Monitoring. – *Electroanalysis* **17**(23): 2101–2113.

Krug, S. M., Amasheh, S., Richter, J. F., Milatz, S., Günzel, D., Westphal, J. K., Huber, O., Schulzke, J. D. and Fromm, M. (2009a): Tricellulin forms a barrier to macromolecules in tricellular tight junctions without affecting ion permeability. – *Mol. Biol. Cell* **20**(16): 3713–3724.

Krug, S. M., Fromm, M. and Günzel, D. (2009b): Two-path impedance spectroscopy for measuring paracellular and transcellular epithelial resistance. – *Biophys. J.* **97**(8): 2202–2211.

Krug, S. M., Günzel, D., Conrad, M. P., Lee, I.-F. M., Amasheh, S., Fromm, M. and Yu, A. S. L. (2012): Charge-selective claudin channels. – *Annals of the New York Academy of Sciences* **1257**: 20–28.

L

- Lall, N., Henley-Smith, C. J., Canha, M. N. de, Oosthuizen, C. B. and Berrington, D. (2013): Viability Reagent, PrestoBlue, in Comparison with Other Available Reagents, Utilized in Cytotoxicity and Antimicrobial Assays. – *International journal of microbiology* **2013**: 420601.
- Larco, J. E. de and Todaro, G. J. (1978): Epithelioid and fibroblastic rat kidney cell clones: epidermal growth factor (EGF) receptors and the effect of mouse sarcoma virus transformation. – *Journal of cellular physiology* **94**(3): 335–342.
- Lasia, A. (2002): *Electrochemical Impedance Spectroscopy and its Applications*. – In: Conway, B. E., Bockris, J. O'M. and White, R. E. (eds): *Modern Aspects of Electrochemistry*. Modern Aspects of Electrochemistry. Kluwer Academic Publishers, Boston, pp. 143–248.
- Laukoetter, M. G., Nava, P., Lee, W. Y., Severson, E. A., Capaldo, C. T., Babbin, B. A., Williams, I. R., Koval, M., Peatman, E., Campbell, J. A., Dermody, T. S., Nusrat, A. and Parkos, C. A. (2007): JAM-A regulates permeability and inflammation in the intestine in vivo. – *Journal of Experimental Medicine* **204**(13): 3067–3076
- Lea, T. (2015): *Caco-2 Cell Line*. – In: Swiatecka, D. and Mackie, A. (eds): *The Impact of Food Bioactives on Health: In Vitro and Ex Vivo Models*. Springer, S.L., pp. 103–111.
- Lee, H.-J., Kim, B., Im, N.-R., Lee, D. Y., Kim, H. K., Lee, S. H., Lee, H.-M., Lee, S. H., Baek, S.-K. and Kim, T. H. (2016): Decreased expression of E-cadherin and ZO-1 in the nasal mucosa of patients with allergic rhinitis: Altered regulation of E-cadherin by IL-4, IL-5, and TNF-alpha. – *American journal of rhinology & allergy* **30**(3): 173–178.
- Lennon, V. A., Kryzer, T. J., Pittcock, S. J., Verkman, A. S. and Hinson, S. R. (2005): IgG marker of optic-spinal multiple sclerosis binds to the aquaporin-4 water channel. – *The Journal of experimental medicine* **202**(4): 473–477.
- Levin, M. H., La Fuente, R. de and Verkman, A. S. (2007): Urearetics: A small molecule screen yields nanomolar potency inhibitors of urea transporter UT-B. – *FASEB journal : official publication of the Federation of American Societies for Experimental Biology* **21**(2): 551–563.
- Levin, M. H., Sullivan, S., Nielson, D., Yang, B., Finkbeiner, W. E. and Verkman, A. S. (2006): Hypertonic saline therapy in cystic fibrosis: Evidence against the proposed mechanism involving aquaporins. – *J. Biol. Chem.* **281**(35): 25803–25812.
- Li, J., Patil, R. V. and Verkman, A. S. (2002): Mildly abnormal retinal function in transgenic mice without Müller cell aquaporin-4 water channels. – *Invest Ophth Vis Sci* **43**(2): 573–579.
- Li, J. and Verkman, A. S. (2001): Impaired hearing in mice lacking aquaporin-4 water channels. – *J Biol Chem* **276**(33): 31233–31237.
- Li, X. and Bard, A. J. (2009): Scanning electrochemical microscopy of HeLa cells – Effects of ferrocene methanol and silver ion. – *Journal of Electroanalytical Chemistry* **628**(1-2): 35–42.
- Limonciel, A., Wilmes, A., Aschauer, L., Radford, R., Bloch, K. M., McMorrow, T., Pfaller, W., van Delft, J. H., Slattery, C., Ryan, M. P., Lock, E. A. and Jennings, P. (2012): Oxidative stress induced by potassium bromate exposure results in altered tight junction protein expression in renal proximal tubule cells. – *Arch. Toxicol.* **86**(11): 1741–1751.
- Litjens, S. H. M., Pereda, J. M. de and Sonnenberg, A. (2006): Current insights into the formation and breakdown of hemidesmosomes. – *Trends in cell biology* **16**(7): 376–383.
- Liu, M., Yang, X., Fan, J., Zhang, R., Wu, J., Zeng, Y., Nie, J. and Yu, X. (2012): Altered tight junctions and fence function in NRK-52E cells induced by aristolochic acid. – *Human & experimental toxicology* **31**(1): 32–41.
- Lo, C. M., Keese, C. R. and Giaever, I. (1999): Cell-substrate contact: Another factor may influence transepithelial electrical resistance of cell layers cultured on permeable filters. – *Exp. Cell Res.* **250**(2): 576–580.
- Lu, D. C., Zhang, H., Zador, Z. and Verkman, A. S. (2008): Impaired olfaction in mice lacking aquaporin-4 water channels. – *FASEB J* **22**(9): 3216–3223.
- Ludwig, K. A., Uram, J. D., Yang, J., Martin, D. C. and Kipke, D. R. (2006): Chronic neural recordings using silicon microelectrode arrays electrochemically deposited with a poly(3,4-ethylenedioxythiophene) (PEDOT) film. – *Journal of neural engineering* **3**(1): 59–70.
- Luissint, A.-C., Artus, C., Glacial, F., Ganeshamoorthy, K. and Couraud, P.-O. (2012): Tight junctions at the blood brain barrier: Physiological architecture and disease-associated dysregulation. – *Fluids and barriers of the CNS* **9**(1): 23.

M

- Ma, T., Hara, M., Sougrat, R., Verbavatz, J.-M. and Verkman, A. S. (2002): Impaired stratum corneum hydration in mice lacking epidermal water channel aquaporin-3. – *J Biol Chem* **277**(19): 17147–17153.
- Macdonald, J. R. (1992): Impedance spectroscopy. – *Annals of biomedical engineering* **20**(3): 289–305.
- Madeira, A., Moura, T. F. and Soveral, G. (2016): Detecting Aquaporin Function and Regulation. – *Front Chem* **4**: 3.
- Maeda, S., Nakagawa, S., Suga, M., Yamashita, E., Oshima, A., Fujiyoshi, Y. and Tsukihara, T. (2009): Structure of the connexin 26 gap junction channel at 3.5 Å resolution. – *Nature* **458**(7238): 597.
- Magdić, K., Horvat-Radošević, V. and Kvastek, K. (2016): Impedance aspect of charge storage at graphite and glassy carbon electrodes in potassium hexacyanoferrate (II) redox active electrolyte. – *J. Electrochem. Sci. Eng.* **6**(1): 37.
- Martin, D. C. and Malliaras, G. G. (2016): Interfacing Electronic and Ionic Charge Transport in Bioelectronics. – *ChemElectroChem* **3**(5): 686–688.
- Matsuhisa, K., Kondoh, M., Takahashi, A. and Yagi, K. (2009): Tight junction modulator and drug delivery. – *Expert opinion on drug delivery* **6**(5): 509–515.
- Matsui, H., Davis, C. W., Tarran, R. and Boucher, R. C. (2000): Osmotic water permeabilities of cultured, well-differentiated normal and cystic fibrosis airway epithelia. – *Journal of Clinical Investigation* **105**(10): 1419–1427.
- Matula, R. A. (1979): Electrical resistivity of copper, gold, palladium, and silver. – *Journal of Physical and Chemical Reference Data* **8**(4): 1147–1298.
- McCarthy, K. M., Skare, I. B., Stankewich, M. C., Furuse, M., Tsukita, S., Rogers, R. A., Lynch, R. D. and Schneeberger, E. E. (1996): Occludin is a functional component of the tight junction. – *Journal of cell science* **109** (Pt 9): 2287–2298.
- Michaelis, S., Rommel, C. E., Endell, J., Göring, P., Wehrspohn, R., Steinem, C., Janshoff, A., Galla, H.-J. and Wegener, J. (2012): Macroporous silicon chips for laterally resolved, multi-parametric analysis of epithelial barrier function. – *Lab Chip* **12**(13): 2329–2336.
- Michaelis, S., Wegener, J. and Robelek, R. (2013): Label-free monitoring of cell-based assays: combining impedance analysis with SPR for multiparametric cell profiling. – *Biosensors & bioelectronics* **49**: 63–70.
- Missner, A., Kügler, P., Saparov, S. M., Sommer, K., Mathai, J. C., Zeidel, M. L. and Pohl, P. (2008): Carbon Dioxide Transport through Membranes*. – *The Journal of biological chemistry* **283**(37): 25340–25347.
- Misztal, T., Rusak, T., Brańska-Januszewska, J., Gąsowska, M., Szyńska, B., Gołaszewska, A., Bruczko, M. and Tomasiak, M. (2018): Aquaporins in human platelets: intracellular localization and possible role in granule and lysosome secretion. – *Acta biochimica Polonica* **65**(4): 555–566.
- Mitic, L. L., van Itallie, C. M. and Anderson, J. M. (2000): Molecular physiology and pathophysiology of tight junctions I. Tight junction structure and function: Lessons from mutant animals and proteins. – *American journal of physiology. Gastrointestinal and liver physiology* **279**(2): G250-4.
- Mohamed, R., Sharma, I., Ibrahim, A. S., Saleh, H., Elsherbiny, N. M., Fulzele, S., Elmasry, K., Smith, S. B., Al-Shabrawey, M. and Tawfik, A. (2017): Hyperhomocysteinemia Alters Retinal Endothelial Cells Barrier Function and Angiogenic Potential via Activation of Oxidative Stress. – *Scientific Reports* **7**(1): 11952.
- Muñoz-Berbel, X., Godino, N., Laczka, O., Baldrich, E., Muñoz, F. X. and del Campo, F. J. (2008): *Impedance-Based Biosensors for Pathogen Detection*. – In: Zourob, M. (ed.): Principles of bacterial detection: Biosensors, recognition receptors and microsystems. Springer Science+Business Media, New York, pp. 341–376.
- Murata, K., Mitsuoka, K., Hirai, T., Walz, T., Agre, P., Heymann, J. B., Engel, A. and Fujiyoshi, Y. (2000): Structural determinants of water permeation through aquaporin-1. – *Nat Rev Drug Discov* **407**(6804): 599–605.

N

- Nakagawa, S., Maeda, S. and Tsukihara, T. (2010): Structural and functional studies of gap junction channels. – *Current opinion in structural biology* **20**(4): 423–430.
- Nayak, P., Kurra, N., Xia, C. and Alshareef, H. N. (2016): Highly Efficient Laser Scribed Graphene Electrodes for On-Chip Electrochemical Sensing Applications. – *Adv. Electron. Mater.* **2**(10): 1600185.
- Neuhaus, W., Bogner, E., Wirth, M., Trzeciak, J., Lachmann, B., Gabor, F. and Noe, C. R. (2006): A novel tool to characterize paracellular transport: The APTS-dextran ladder. – *Pharmaceutical research* **23**(7): 1491–1501.
- Niemietz, C. M. and Tyerman, S. D. (2002): New potent inhibitors of aquaporins: silver and gold compounds inhibit aquaporins of plant and human origin. – *FEBS Letters* **531**(3): 443–447.
- Nkosi, D., Pillay, J., Ozoemena, K. I., Nouneh, K. and Oyama, M. (2010): Heterogeneous electron transfer kinetics and electrocatalytic behaviour of mixed self-assembled ferrocenes and SWCNT layers. – *Physical chemistry chemical physics : PCCP* **12**(3): 604–613.

O

- O'Connor, E. R., Kimelberg, H. K., Keese, C. R. and Giaever, I. (1993): Electrical resistance method for measuring volume changes in monolayer cultures applied to primary astrocyte cultures. – *The American journal of physiology* **264**(2 Pt 1): C471-8.
- Ordoñez, C. L., Khashayar, R., Wong, H. H., Ferrando, R., Wu, R., Hyde, D. M., Hotchkiss, J. A., Zhang, Y., Novikov, A., Dolganov, G. and Fahy, J. V. (2001): Mild and moderate asthma is associated with airway goblet cell hyperplasia and abnormalities in mucin gene expression. – *American journal of respiratory and critical care medicine* **163**(2): 517–523.
- Ouyang, J., Chu, C.-W., Chen, F.-C., Xu, Q. and Yang, Y. (2005): High-Conductivity Poly(3,4-ethylenedioxythiophene):Poly(styrene sulfonate) Film and Its Application in Polymer Optoelectronic Devices. – *Adv. Funct. Mater.* **15**(2): 203–208.
- Ouyang, J., Xu, Q., Chu, C.-W., Yang, Y., Li, G. and Shinar, J. (2004): On the mechanism of conductivity enhancement in poly(3,4-ethylenedioxythiophene): Poly(styrene sulfonate) film through solvent treatment. – *Polymer* **45**(25): 8443–8450.

P

- Pajkossy, T. (1994): Impedance of rough capacitive electrodes. – *Journal of Electroanalytical Chemistry* **364**(1-2): 111–125.
- Palacin, S., Bureau, C., Charlier, J., Deniau, G., Mouanda, B. and Viel, P. (2004): Molecule-to-metal bonds: Electrografting polymers on conducting surfaces. – *Chemphyschem : a European journal of chemical physics and physical chemistry* **5**(10): 1468–1481.
- Patra, A., Bendikov, M. and Chand, S. (2014): Poly(3,4-ethylenedioxythiophene) and its derivatives: Novel organic electronic materials. – *Accounts of chemical research* **47**(5): 1465–1474.
- Patton, K. T. (2015): *PART - Anatomy and Physiology*. Elsevier Health Sciences.
- Pereda, A. E., Curti, S., Hoge, G., Cachope, R., Flores, C. E. and Rash, J. E. (2013): Gap junction-mediated electrical transmission: Regulatory mechanisms and plasticity. – *Biochimica et biophysica acta* **1828**(1): 134–146.
- Pfannkuch, F., Suter-Dick, L., Mannhold, R., Kubinyi, H. and Folkers, G. (2014): *Predictive Toxicology: From Vision to Reality*. Wiley.
- Phelps, J. E. and DePaola, N. (2000): Spatial variations in endothelial barrier function in disturbed flows in vitro. – *Am. J. Physiol.-Heart C.* **278**(2): H469-76.
- Platzer, W. and Spitzer, G. (2009): *Locomotor System*. Thieme.
- Preston, G. M., Carroll, T. P., Guggino, W. B. and Agre, P. (1992): Appearance of water channels in *Xenopus* oocytes expressing red cell CHIP28 protein. – *Science (New York, N.Y.)* **256**(5055): 385–387.

References

Preston, G. M., Jung, J. S., Guggino, W. B. and Agre, P. (1993): The mercury-sensitive residue at cysteine 189 in the CHIP28 water channel. – *The Journal of biological chemistry* **268**(1): 17–20.

Prozialeck, W. C., Edwards, J. R., Lamar, P. C. and Smith, C. S. (2006): Epithelial barrier characteristics and expression of cell adhesion molecules in proximal tubule-derived cell lines commonly used for in vitro toxicity studies. – *Toxicol. In Vitro* **20**(6): 942–953.

R

Rasmussen, S. C. (2010): Handbook of Thiophene-Based Materials. Applications in Organic Electronics and Photonics. 2 volumes. Edited by Igor F. Perepichka and Dmitrii F. Perepichka. – *Angewandte Chemie International Edition* **49**(11): 1916–1917.

Ravelli, A. M., Villanacci, V., Ruzzenenti, N., Grigolato, P., Tobanelli, P., Klersy, C. and Rindi, G. (2006): Dilated intercellular spaces: A major morphological feature of esophagitis. – *Journal of pediatric gastroenterology and nutrition* **42**(5): 510–515.

Reiss, B. and Wegener, J. (2015): Impedance analysis of different cell monolayers grown on gold-film electrodes. – *IEEE Eng. Med. Bio.* **2015**: 7079–7082.

Richardson, J.C.W., Scalera, V. and Simmons, N. L. (1981): Identification of two strains of MDCK cells which resemble separate nephron tubule segments. – *Biochimica et Biophysica Acta (BBA) - General Subjects* **673**: 26–36.

Robelek, R. and Wegener, J. (2010): Label-free and time-resolved measurements of cell volume changes by surface plasmon resonance (SPR) spectroscopy. – *Biosensors & bioelectronics* **25**(5): 1221–1224.

Rosenthal, R., Milatz, S., Krug, S. M., Oelrich, B., Schulzke, J.-D., Amasheh, S., Günzel, D. and Fromm, M. (2010): Claudin-2, a component of the tight junction, forms a paracellular water channel. – *Journal of cell science* **123**(Pt 11): 1913–1921.

Roy, G. and Sauvé, R. (1987): Effect of anisotonic media on volume, ion and amino-acid content and membrane potential of kidney cells (MDCK) in culture. – *The Journal of membrane biology* **100**(1): 83–96.

Runswick, S., Mitchell, T., Davies, P., Robinson, C. and Garrod, D. R. (2007): Pollen proteolytic enzymes degrade tight junctions. – *Respirology (Carlton, Vic.)* **12**(6): 834–842.

S

Sambuy, Y., Angelis, I. de, Ranaldi, G., Scarino, M. L., Stamatii, A. and Zucco, F. (2005): The Caco-2 cell line as a model of the intestinal barrier: influence of cell and culture-related factors on Caco-2 cell functional characteristics. – *Cell biology and toxicology* **21**(1): 1–26.

Sanders, S. E., Madara, J. L., McGuirk, D. K., Gelman, D. S. and Colgan, S. P. (1995): Assessment of inflammatory events in epithelial permeability: A rapid screening method using fluorescein dextrans. – *Epithelial Cell Biol.* **4**(1): 25–34.

Schafer, J. A., Patlak, C. S., Troutman, S. L. and Andreoli, T. E. (1978): Volume absorption in the pars recta. II. Hydraulic conductivity coefficient. – *The American journal of physiology* **234**(4): F340-8.

Schäfer, C., Schröder, K. R., Höglinger, O., Tollabimazraehno, S. and Lornejad-Schäfer, M. R. (2013): Acetaminophen changes intestinal epithelial cell membrane properties, subsequently affecting absorption processes. – *Cellular physiology and biochemistry : international journal of experimental cellular physiology, biochemistry, and pharmacology* **32**(2): 431–447.

Schleimer, R. P. and Berdnikovs, S. (2017): Etiology of epithelial barrier dysfunction in patients with type 2 inflammatory diseases. – *The Journal of allergy and clinical immunology* **139**(6): 1752–1761.

Schneeberger, E. and Lynch, R. (2004): The tight junction: A multifunctional complex. – *Am. J. Physiol.* **286**(6): C1213-28.

Serway, R. A. and Jewett, J. W. (1998): *Principles of physics*. – Saunders golden sunburst series. Saunders College Publ, Fort Worth, Tex., xxxii, 954, 50, 20 s.

Sheller, R. A., Cuevas, M. E. and Todd, M. C. (2017): Comparison of transepithelial resistance measurement techniques: Chopsticks vs. Endohm. – *Biol. Proced. Online* **19**: 4.

References

- Shin, K., Fogg, V. C. and Margolis, B. (2006): Tight junctions and cell polarity. – *Annu. Rev. Cell Dev. Bi.* **22**: 207–235.
- Solenov, E., Watanabe, H., Manley, G. T. and Verkman, A. S. (2004): Sevenfold-reduced osmotic water permeability in primary astrocyte cultures from AQP-4-deficient mice, measured by a fluorescence quenching method. – *American journal of physiology. Cell physiology* **286**(2): C426-32.
- Solomon, A. K. (1989): Water channels across the red blood cell and other biological membranes. – *Methods in enzymology* **173**: 192–222.
- Soveral, G., Macey, R. I. and Moura, T. F. (1997): Water permeability of brush border membrane vesicles from kidney proximal tubule. – *J Membrane Biol* **158**(3): 219–228.
- Soveral, G., Madeira, A., Loureiro-Dias, M. C. and Moura, T. F. (2007): Water transport in intact yeast cells as assessed by fluorescence self-quenching. – *Applied and environmental microbiology* **73**(7): 2341–2343.
- Soveral, G., Madeira, A., Loureiro-Dias, M. C. and Moura, T. F. (2008): Membrane tension regulates water transport in yeast. – *Biochim Biophys Acta* **1778**(11): 2573–2579.
- Spring, K. R. (1998): Routes and mechanism of fluid transport by epithelia. – *Annual review of physiology* **60**: 105–119.
- Srinivasan, B., Kolli, A. R., Esch, M. B., Abaci, H. E., Shuler, M. L. and Hickman, J. J. (2015): TEER measurement techniques for in vitro barrier model systems. – *Journal of laboratory automation* **20**(2): 107–126.
- Steinem, C., Janshoff, A., Wegener, J., Ulrich, W.-P., Willenbrink, W., Sieber, M. and Galla, H.-J. (1997): Impedance and shear wave resonance analysis of ligand–receptor interactions at functionalized surfaces and of cell monolayers. – *Biosensors and Bioelectronics* **12**(8): 787–808.
- Stedle, E. (1989): [16] *Water flow in plants and its coupling to other processes: An overview*: Methods in Enzymology : Biomembranes Part U: Cellular and Subcellular Transport: Eukaryotic (Nonepithelial) Cells. Academic Press, pp. 183–225.
- Stevenson, B. R., Anderson, J. M., Goodenough, D. A. and Mooseker, M. S. (1988): Tight junction structure and ZO-1 content are identical in two strains of Madin-Darby canine kidney cells which differ in transepithelial resistance. – *undefined*.
- Stevenson, B. R. and Begg, D. A. (1994): Concentration-dependent effects of cytochalasin D on tight junctions and actin filaments in MDCK epithelial cells. – *J. Cell Sci.* **107**: 367–375.
- Stevenson, B. R., Siliciano, J. D., Mooseker, M. S. and Goodenough, D. A. (1986): Identification of ZO-1: A high molecular weight polypeptide associated with the tight junction (zonula occludens) in a variety of epithelia. – *The Journal of cell biology* **103**(3): 755–766.
- Stolwijk, J. A., Hartmann, C., Balani, P., Albermann, S., Keese, C. R., Giaever, I. and Wegener, J. (2011): Impedance analysis of adherent cells after in situ electroporation: Non-invasive monitoring during intracellular manipulations. – *Biosensors & bioelectronics* **26**(12): 4720–4727.
- Sukma Dewi, I., Celik, S., Karlsson, A., Hollander, Z., Lam, K., McManus, J.-W., Tebbutt, S., Ng, R., Keown, P., McMaster, R., McManus, B., Öhman, J. and Gidlöf, O. (2017): Exosomal miR-142-3p is increased during cardiac allograft rejection and augments vascular permeability through down-regulation of endothelial RAB11FIP2 expression. – *Cardiovas. Res.* **113**(5): 440–452.
- Sun, P. and Mirkin, M. V. (2006): Kinetics of electron-transfer reactions at nanoelectrodes. – *Analytical chemistry* **78**(18): 6526–6534.
- Sweerus, K., Lachowicz-Scroggins, M., Gordon, E., LaFemina, M., Huang, X., Parikh, M., Kanegai, C., Fahy, J. V. and Frank, J. A. (2017): Claudin-18 deficiency is associated with airway epithelial barrier dysfunction and asthma. – *The Journal of allergy and clinical immunology* **139**(1): 72-81.

T

- Thyssen, J. P. and Kezic, S. (2014): Causes of epidermal filaggrin reduction and their role in the pathogenesis of atopic dermatitis. – *The Journal of allergy and clinical immunology* **134**(4): 792–799.
- Torras, N., García-Díaz, M., Fernández-Majada, V. and Martínez, E. (2018): Mimicking Epithelial Tissues in Three-Dimensional Cell Culture Models. – *Front. Bioeng. Biotechnol.* **6**: 197.

References

- Tripathi, S. and Boulpaep, E. L. (1989): Mechanisms of water transport by epithelial cells. – *Quarterly journal of experimental physiology (Cambridge, England)* **74**(4): 385–417.
- Tsukita, S., Tanaka, H. and Tamura, A. (2019): The Claudins: From Tight Junctions to Biological Systems. – *Trends in Biochemical Sciences* **44**(2): 141–152.

V

- Vala, M., Robelek, R., Bocková, M., Wegener, J. and Homola, J. (2013): Real-time label-free monitoring of the cellular response to osmotic stress using conventional and long-range surface plasmons. – *Biosensors & bioelectronics* **40**(1): 417–421.
- van Itallie, C. M., Holmes, J., Bridges, A. and Anderson, J. M. (2009): Claudin-2-dependent changes in noncharged solute flux are mediated by the extracellular domains and require attachment to the PDZ-scaffold. – *Ann. NY Acad. Sci.* **1165**: 82–87.
- van Itallie, C. M., Holmes, J., Bridges, A., Gookin, J. L., Coccaro, M. R., Proctor, W., Colegio, O. R. and Anderson, J. M. (2008): The density of small tight junction pores varies among cell types and is increased by expression of claudin-2. – *Journal of cell science* **121**(Pt 3): 298–305.
- van Winkle, L. J. (1999): *Biomembrane Transport*. Elsevier Science.
- Verkman, A. S. (1995): Optical methods to measure membrane transport processes. – *The Journal of membrane biology* **148**(2): 99–110.
- Verkman, A. S. (2003): Role of aquaporin water channels in eye function. – *Experimental eye research* **76**(2): 137–143.
- Verkman, A. S. (2005): More than just water channels: Unexpected cellular roles of aquaporins. – *Journal of cell science* **118**(Pt 15): 3225–3232.
- Verkman, A. S. (2006): Aquaporins in endothelia. – *Kidney international* **69**(7): 1120–1123.
- Verkman, A. S. (2011): Aquaporins at a glance. – *J Sell Sci* **124**(Pt 13): 2107–2112.
- Verkman, A. S. (2012): Aquaporins in clinical medicine. – *Annual review of medicine* **63**: 303–316.
- Verkman, A. S. and Mitra, A. K. (2000): Structure and function of aquaporin water channels. – *American journal of physiology. Renal physiology* **278**(1): F13-28.
- Verkman, A. S., van Hoek, A. N., Ma, T., Frigeri, A., Skach, W. R., Mitra, A., Tamarappoo, B. K. and Farinas, J. (1996): Water transport across mammalian cell membranes. – *The American journal of physiology* **270**(1 Pt 1): C12-30.
- Vogt, S., Su, Q., Gutiérrez-Sánchez, C. and Nöll, G. (2016): Critical View on Electrochemical Impedance Spectroscopy Using the Ferri/Ferrocyanide Redox Couple at Gold Electrodes. – *Analytical chemistry* **88**(8): 4383–4390.

W

- Wan, H., Winton, H. L., Soeller, C., Tovey, E. R., Gruenert, D. C., Thompson, P. J., Stewart, G. A., Taylor, G. W., Garrod, D. R., Cannell, M. B. and Robinson, C. (1999): Der p 1 facilitates transepithelial allergen delivery by disruption of tight junctions. – *The Journal of clinical investigation* **104**(1): 123–133.
- Watson, C. J., Rowland, M. and Warhurst, G. (2001): Functional modeling of tight junctions in intestinal cell monolayers using polyethylene glycol oligomers. – *American journal of physiology. Cell physiology* **281**(2): C388-97.
- Wegener, J. (2010): *Impedance Analysis of Cell Junctions*. – In: Fuchs, H., Grätze, M., Krug, H., Schmid, G., Vogel, V. and Waser, R. (eds): *Nanotechnology*: 9 volumes. Wiley Interscience, Hoboken, NJ, p. 660.
- Wegener, J., Abrams, D., Willenbrink, W., Galla, H.-J. and Janshoff, A. (2004): Automated multi-well device to measure transepithelial electrical resistances under physiological conditions. – *BioTechniques* **37**(4): 590 - 597.
- Wegener, J. and Seebach, J. (2014): Experimental tools to monitor the dynamics of endothelial barrier function: A survey of in vitro approaches. – *Cell Tissue Res.* **355**(3): 485–514.
- Wise, C. (2002): *Epithelial Cell Culture Protocols*. – *Methods In Molecular Medicine™*, No. 188. Humana Press, Totowa, NJ, 1 p.

References

Wolburg, H., Lippoldt, A. and Ebnet, K. (2006): *Tight Junctions and the Blood-Brain Barrier*. – In: Gonzalez-Mariscal, L. (ed.): *Tight Junctions*. Molecular biology intelligence unit. Landes Bioscience and Springer Science+Business Media LLC, Boston, MA, pp. 175–195.

Wu, B. and Beitz, E. (2007): Aquaporins with selectivity for unconventional permeants. – *Cellular and molecular life sciences* : *CMLS* **64**(18): 2413–2421.

X

Xia, Y. and Ouyang, J. (2009): Salt-Induced Charge Screening and Significant Conductivity Enhancement of Conducting Poly(3,4-ethylenedioxythiophene):Poly(styrenesulfonate). – *Macromolecules* **42**(12): 4141–4147.

Xia, Y. and Ouyang, J. (2010): Significant conductivity enhancement of conductive poly(3,4-ethylenedioxythiophene):poly(styrenesulfonate) films through a treatment with organic carboxylic acids and inorganic acids. – *ACS applied materials & interfaces* **2**(2): 474–483.

Xia, Y. and Ouyang, J. (2011): PEDOT: PSS films with significantly enhanced conductivities induced by preferential solvation with cosolvents and their application in polymer photovoltaic cells. – *J. Mater. Chem.* **21**(13): 4927.

Xia, Y., Zhang, H. and Ouyang, J. (2010): Highly conductive PEDOT:PSS films prepared through a treatment with zwitterions and their application in polymer photovoltaic cells. – *J. Mater. Chem.* **20**(43): 9740.

Y

Yang, B., Kim, J. K. and Verkman, A. S. (2006): Comparative efficacy of HgCl₂ with candidate aquaporin-1 inhibitors DMSO, gold, TEA⁺ and acetazolamide. – *FEBS Letters* **580**(28-29): 6679–6684.

Ye, R. and Verkman, A. S. (2002): Simultaneous optical measurement of osmotic and diffusional water permeability in cells and liposomes. – *Biochemistry* **28**(2): 824–829.

Yokoshima, T., Mukoyama, D., Nakazawa, K., Gima, Y., Isawa, H., Nara, H., Momma, T. and Osaka, T. (2015): Application of Electrochemical Impedance Spectroscopy to Ferri/Ferrocyanide Redox Couple and Lithium Ion Battery Systems Using a Square Wave as Signal Input. – *Electrochimica Acta* **180**: 922–928.

Youdim, K. A., Avdeef, A. and Abbott, N. J. (2003): In vitro trans-monolayer permeability calculations: Often forgotten assumptions. – *Drug Discov. Today* **8**(21): 997–1003.

Yukutake, Y., Hirano, Y., Suematsu, M. and Yasui, M. (2009): Rapid and reversible inhibition of aquaporin-4 by zinc. – *Biochemistry* **48**(51): 12059–12061.

Yukutake, Y., Tsuji, S., Hirano, Y., Adachi, T., Takahashi, T., Fujihara, K., Agre, P., Yasui, M. and Suematsu, M. (2008): Mercury chloride decreases the water permeability of aquaporin-4-reconstituted proteoliposomes. – *Biology of the cell* **100**(6): 355–363.

Z

Zaidel-Bar, R., Itzkovitz, S., Ma'ayan, A., Iyengar, R. and Geiger, B. (2007): Functional atlas of the integrin adhesome. – *Nature cell biology* **9**(8): 858–867.

Zelenina, M., Tritto, S., Bondar, A. A., Zelenin, S. and Aperia, A. (2004): Copper inhibits the water and glycerol permeability of aquaporin-3. – *The Journal of biological chemistry* **279**(50): 51939–51943.

11 Appendix

11.1 Supplementary information

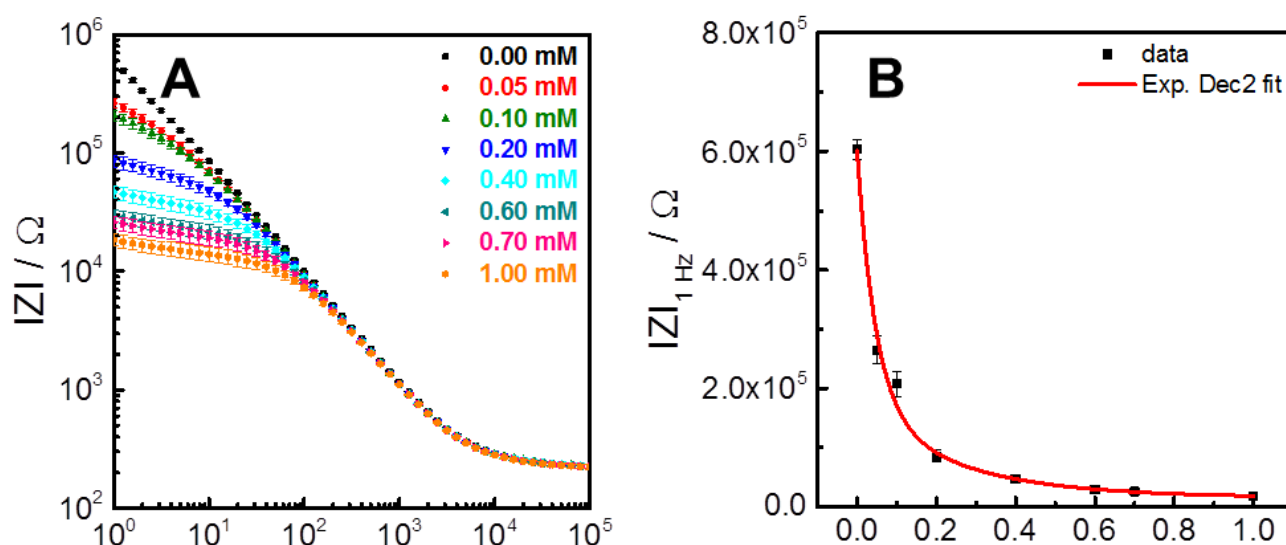


Fig. 11.1: (A) Frequency spectra of the impedance magnitude $|Z|$ in presence of different $[\text{Fe}(\text{CN})_6]^{3-/4-}$ solutions recorded with the spatially resolved $\text{P}_E\text{-TER}$ -device ($\text{P}_E\text{-mode}$) and averaged for all six working electrodes (chapter 4.2.1, Fig. 4.7, mean \pm SE, $n = 6$). (B) $|Z|_{1\text{Hz}}$ as a function of $[\text{Fe}(\text{CN})_6]^{3-/4-}$ concentration. The experimental raw data is fitted by an exponential decay function of 2nd order which makes the further data analysis less convenient compared to the final readout parameter $1/|Z|_{1\text{Hz}}$.

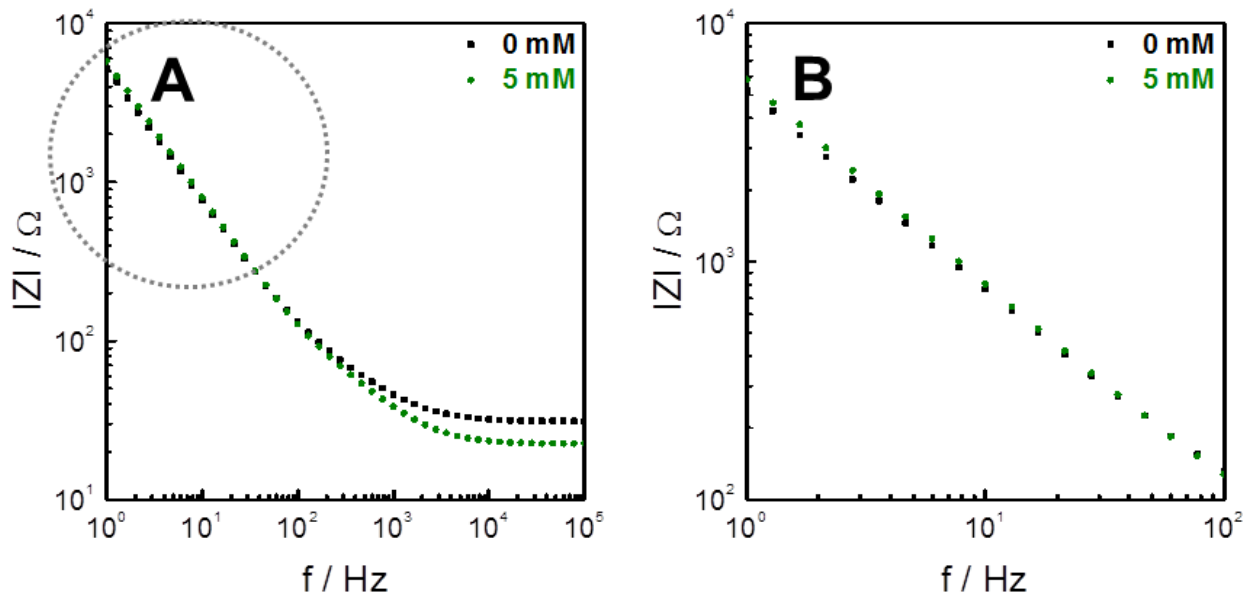


Fig. 11.2: (A) Frequency spectra of the impedance magnitude $|Z|$ recorded with a conventional TER-device composed of stainless steel and (B) a zoom into the low frequency end of the same spectrum. A cell-free filter insert is sandwiched between the apical and basolateral stainless steel electrodes. The impedance magnitudes in the lower frequency range are not influenced by the presence of a 5 mM $[\text{Fe}(\text{CN})_6]^{3-/4-}$ solution indicating that no electron transfer takes place between the redox pair and the surface of the stainless steel electrodes. Thus, the faradaic effects R_{CT} and Z_{W} which have a huge impact on the impedance spectra recorded with gold electrodes are negligible when using stainless steel electrodes. This is the justification for taking an experimental setup composed of two different electrode materials (apical: stainless steel / basolateral: gold) in the $\text{P}_{\text{E}}\text{TER}$ - and $\text{P}_{\text{OS}}\text{TER}$ -assays.

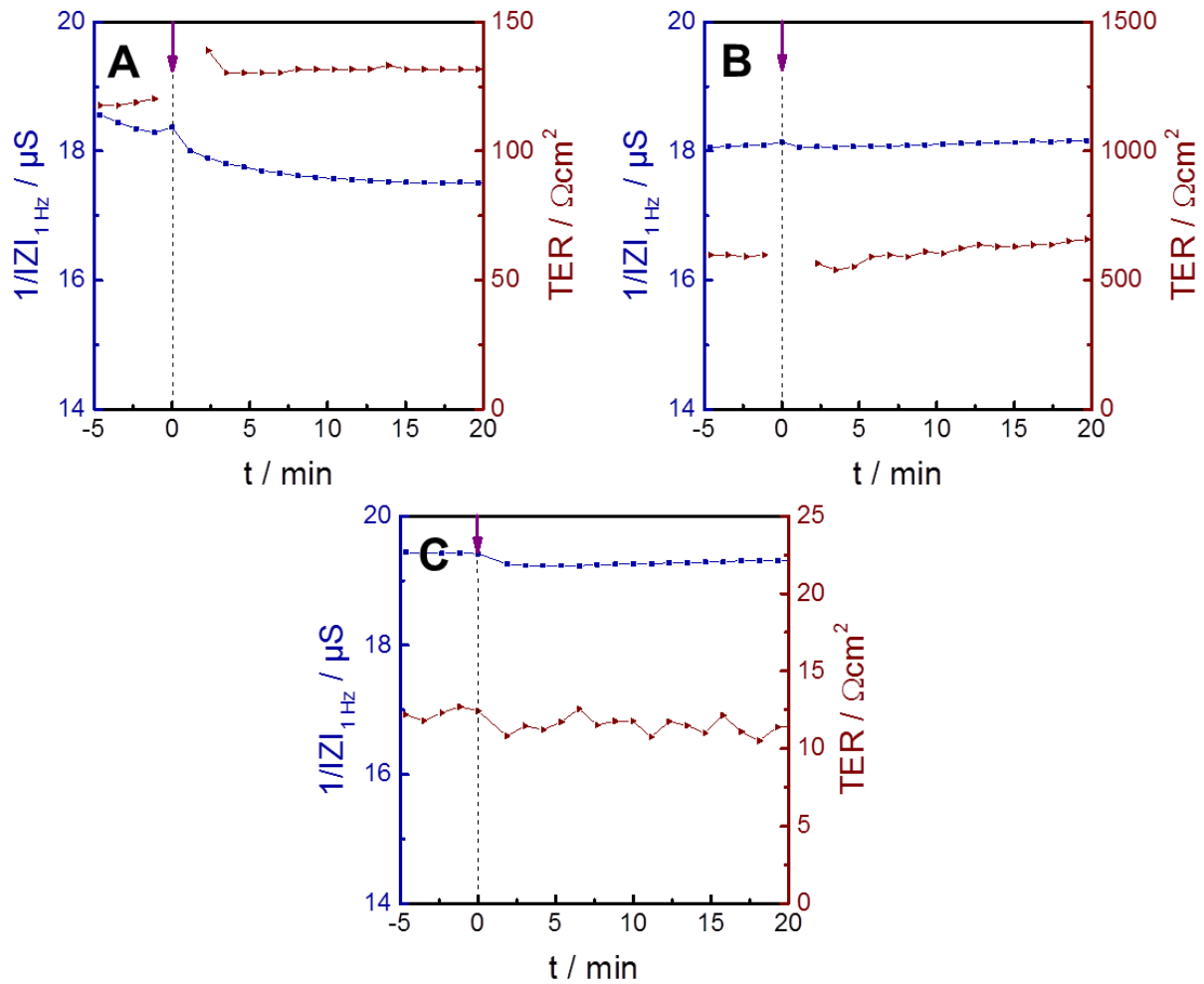


Fig. 11.3: Control experiments for the $P_E\text{TER}$ -assay recorded with IDE-200 for (A) MDCK-II, (B) MDCK-I and (C) NRK cell layers. The mere addition of PBS⁺/glucose (1 g/L) to the apical compartment does neither influence $1/|Z|_{1\text{Hz}}$ nor TER in a significant way. Therefore, signal changes of the actual $P_E\text{TER}$ -measurements are due to $[\text{Fe}(\text{CN})_6]^{3-/4-}$. Unspecific effects arising from the addition of the redox tracer are negligible.

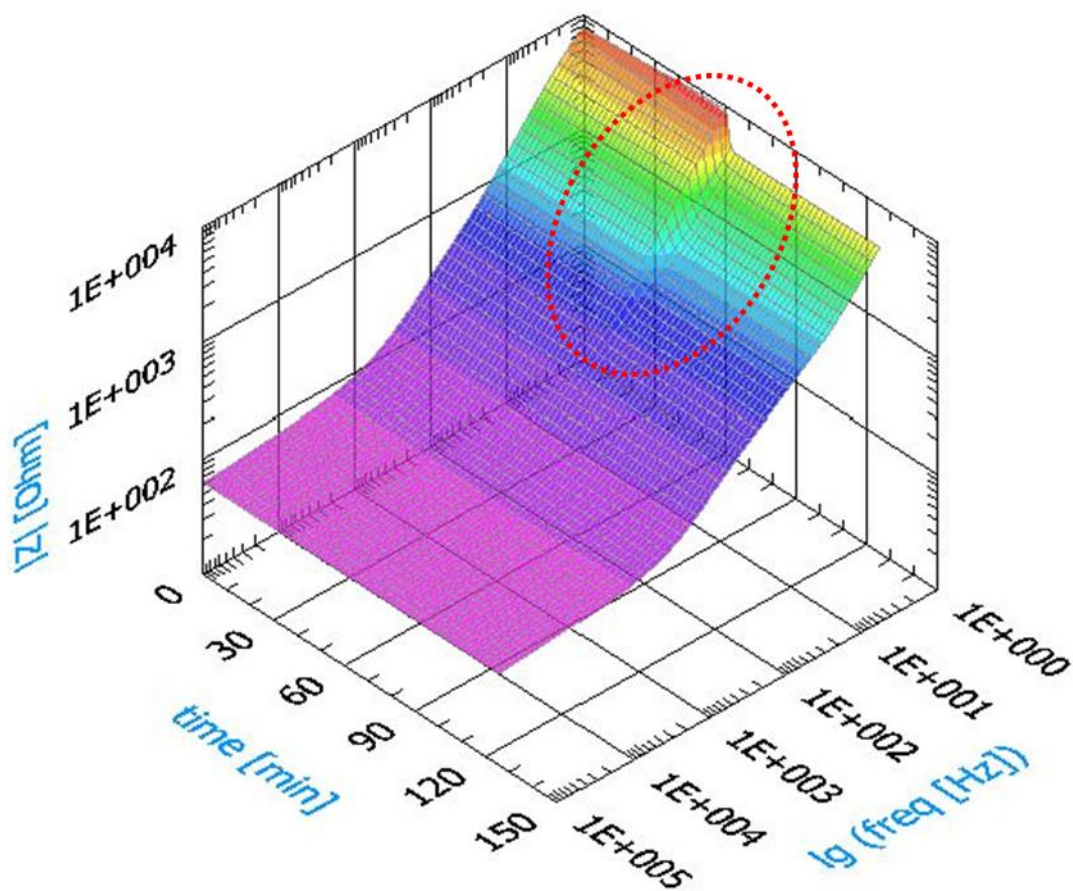


Fig. 11.4: Time- and frequency dependent changes of the impedance magnitude $|Z|$. The data is recorded with the spatially resolved P_E TER-device (chapter 4.2.1, Fig. 4.7) in **TER-mode**. A confluent monolayer of NRK cells is the cellular barrier. The leaky character of NRK cells and the associated increased $[\text{Fe}(\text{CN})_6]^{3-/4-}$ permeation into the receiver compartment evoke a serious impact on the impedance magnitudes in the frequency region from 1 Hz to 100 Hz. Consequently, the frequency range has to be narrowed for TER-analysis to apply the conventional equivalent circuit (chapter 3.1.2, Fig. 3.3 and Fig. 3.5) when investigating very leaky cell layers.

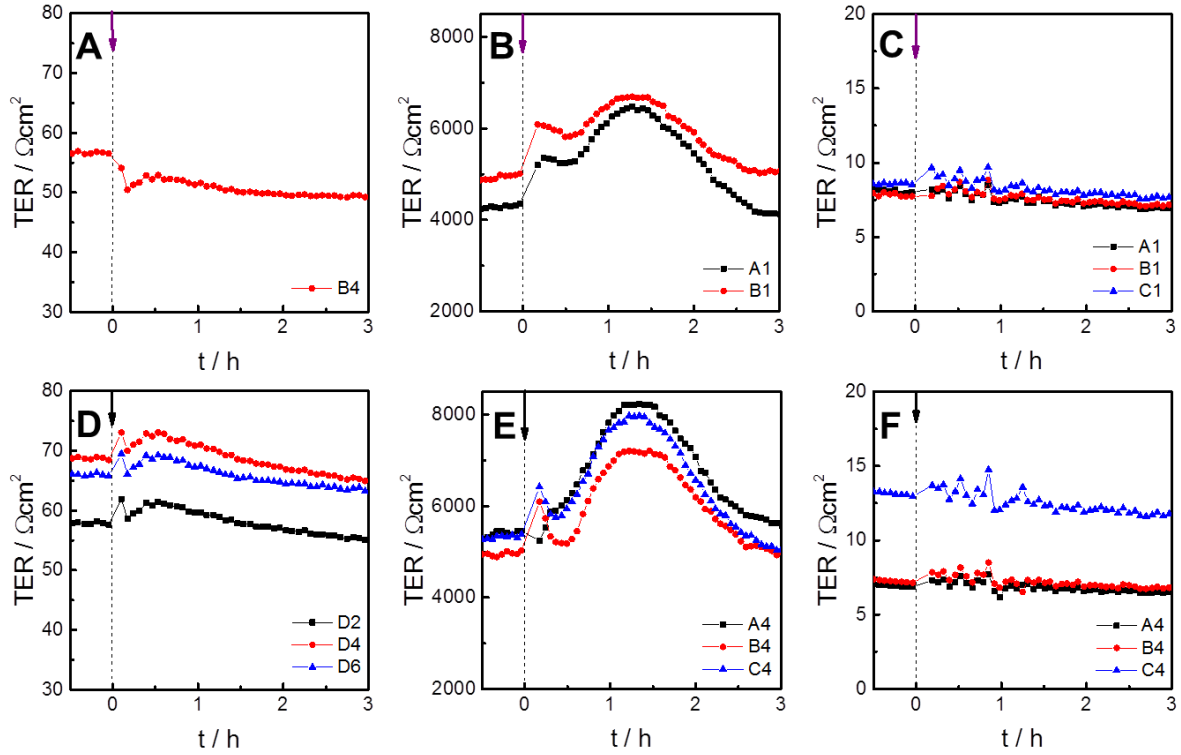


Fig. 11.5: Time-dependent changes of TER values after an exchange of **PBS⁺/glucose (1 g/L)** in the apical compartment or after the apical addition of **1 mM [Fe(CN)₆]^{3-/4-}**, respectively. **(A, D)** MDCK-II, **(B, E)** MDCK-I and **(C, F)** NRK monolayers serve as epithelial barriers. The data is recorded with a cellScope[®]-device kindly provided by nanoAnalytics GmbH (Münster, Germany).

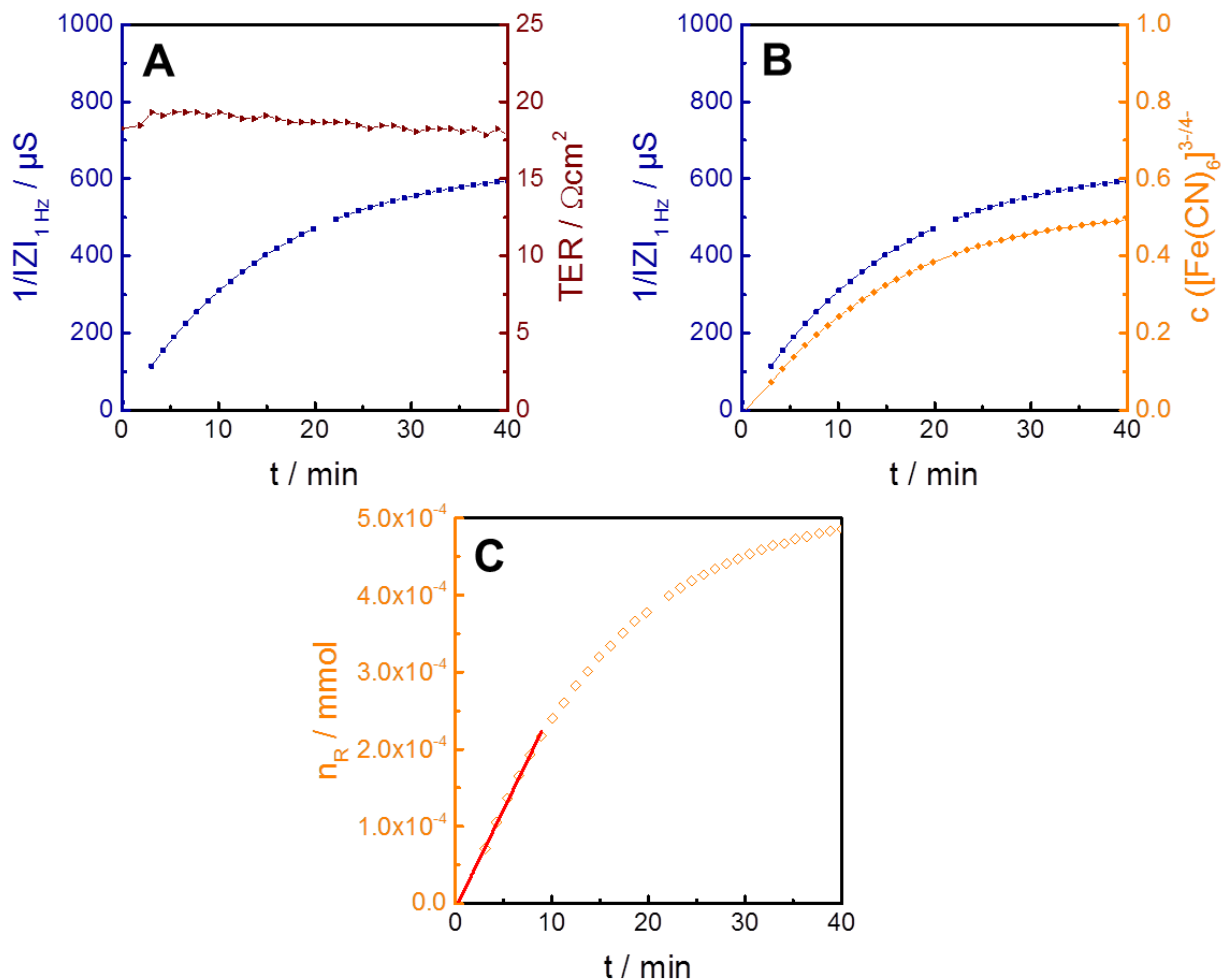


Fig. 11.6: Graphical illustration of the calculation procedure of P_E demonstrated for an examination of NRK cells. **(A)** The raw data of the P_E TER-assay contains the time-courses of $1/|Z|_{1\text{Hz}}$ and TER. **(B)** By using the linear calibration function, $1/|Z|_{1\text{Hz}}$ is transformed into the receiver concentration of $[\text{Fe}(\text{CN})_6]^{3-/4-}$. **(C)** By means of a defined receiver volume V_R ($9.85 \cdot 10^{-3} \text{ cm}^3$), the receiving amount of redox tracer is calculated time-dependently. The linear phase of this increase is analyzed via linear regression to provide the parameter $dn_R(t)/dt$, which is needed for the computation of P_E values (chapter 3.2.1, equation 3.32).

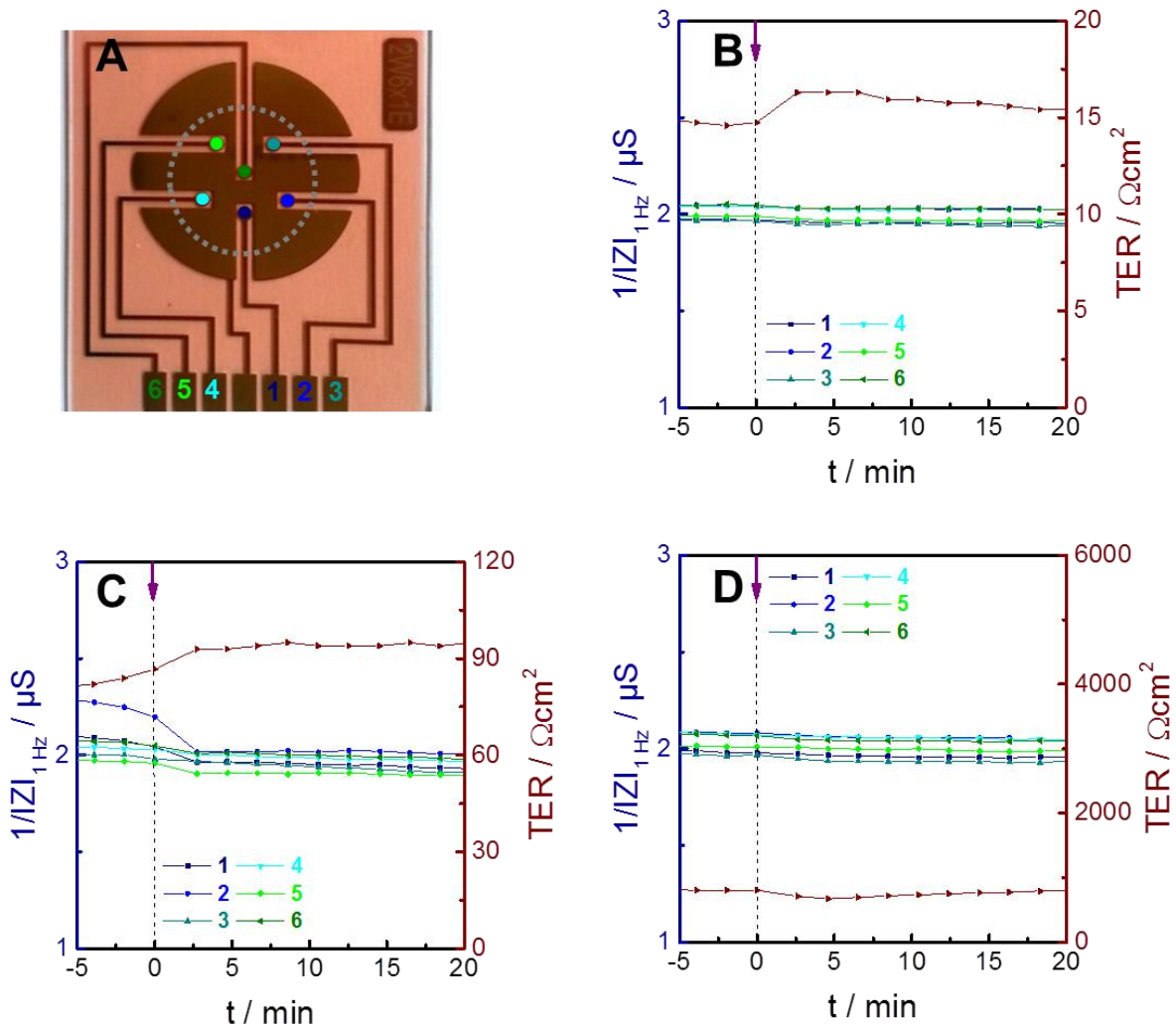


Fig. 11.7: Control experiments for the spatially resolved P_E -TER-device for **(B)** NRK, **(C)** MDCK-II and **(D)** MDCK-I monolayers. The mere addition of **PBS⁺⁺/glucose (1 g/L)** to the apical compartment does neither influence $1/|Z|_{1\text{Hz}}$ nor TER in a significant way. Thus, signal changes of the actual P_E -TER-studies are related to the basolateral tracer accumulation. Unspecific effects arising from tracer addition are negligible. **(A)** Image of a 2W6x1E array with color coded electrodes and a rough estimation of the filter position indicated by a grey, dashed circle.

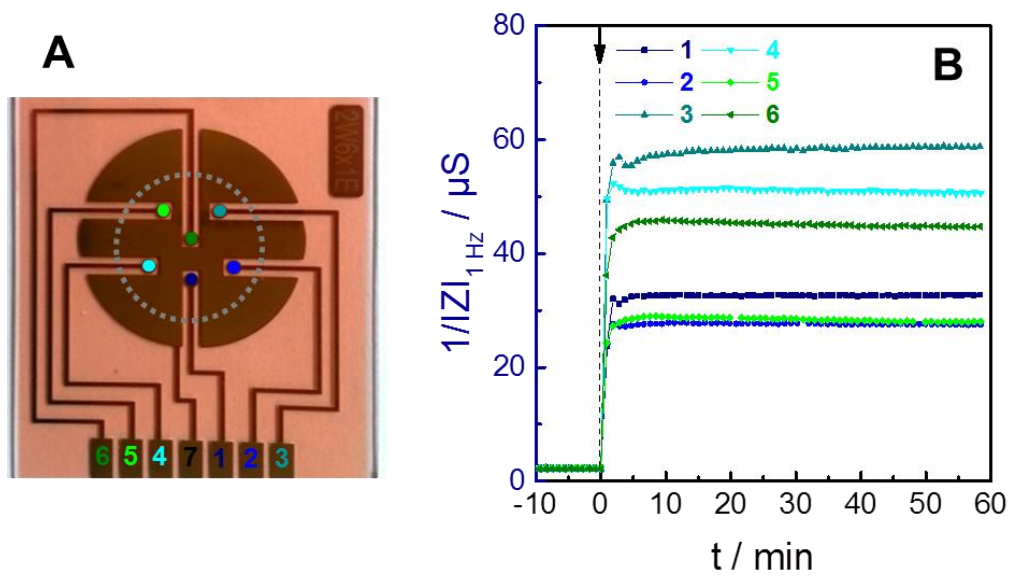


Fig. 11.8: Laterally resolved permeability monitoring using a cell-free filter insert. **(A)** Image of a 2W6x1E array with color coded working electrodes. The filter position is roughly estimated by a grey, dashed circle **(B)** Changes of $1/|Z|_{1\text{Hz}}$ for six laterally distributed gold electrodes beneath the filter membrane are followed over time to measure basolateral tracer accumulation at different positions. At time point zero, $1 \text{ mM } [\text{Fe}(\text{CN})_6]^{3-/4-}$ is added apically.

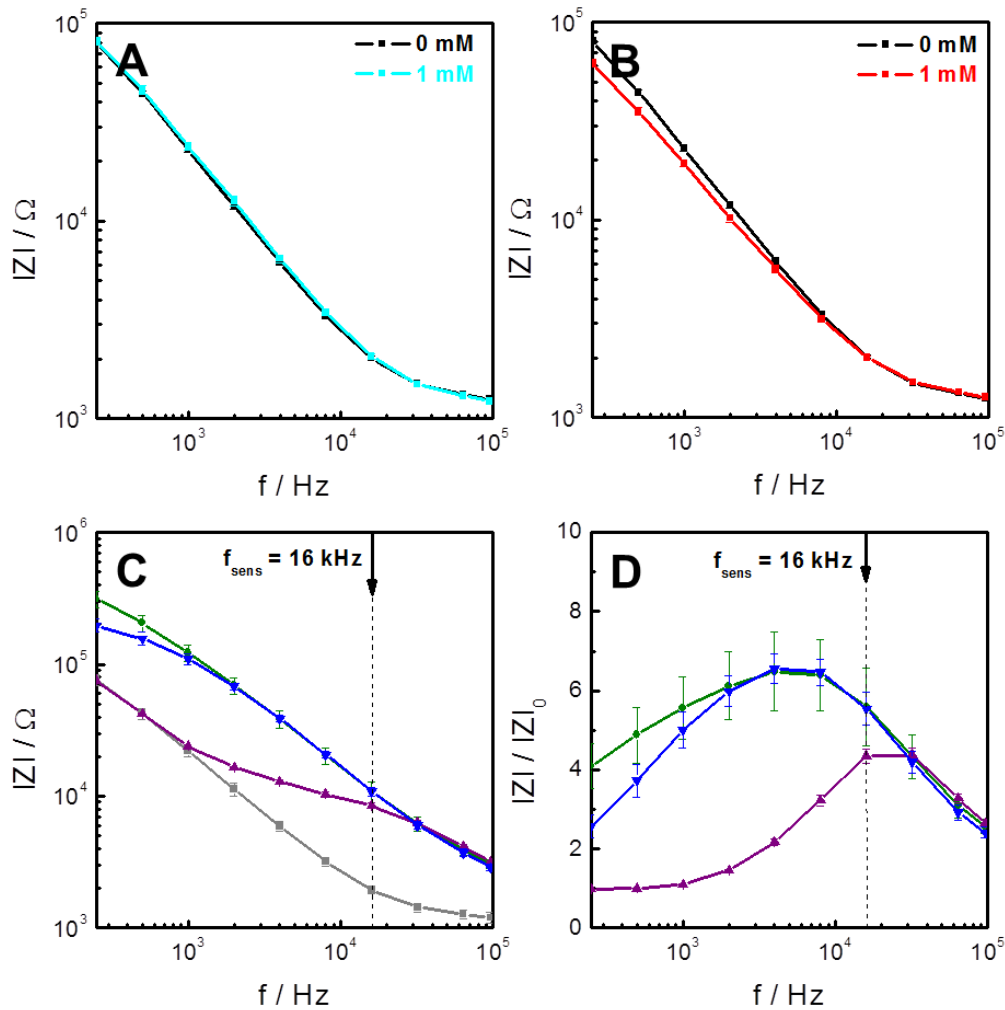


Fig. 11.9: Determination of a frequency that is appropriate for all cell lines under study using a 96W1E+ array. Impedance spectra (mean \pm SE, $n = 6$) in presence of **(A)** $\text{PBS}^{++}/\text{glucose}$ (1 g/L) and 1 mM $[\text{Fe}(\text{CN})_6]^{3-/4-}$ and **(B)** $\text{PBS}^{++}/\text{glucose}$ (1 g/L) and 1 mM FcMeOH show that a frequency of 16 kHz is not significantly influenced by R_{CT} and Z_{W} . **(C)** Impedance spectra monitored with the cell-free device, NRK, MDCK-I and MDCK-II monolayers (mean \pm SE, $n \geq 22$). **(D)** Normalized impedance spectra ($|Z|/|Z|_0$) for the three cell lines (mean \pm maximal error, $n \geq 22$). Taking all aspects into consideration, a frequency of 16 kHz in the ECIS-cytotoxicity measurements appears suitable for all three cell lines.

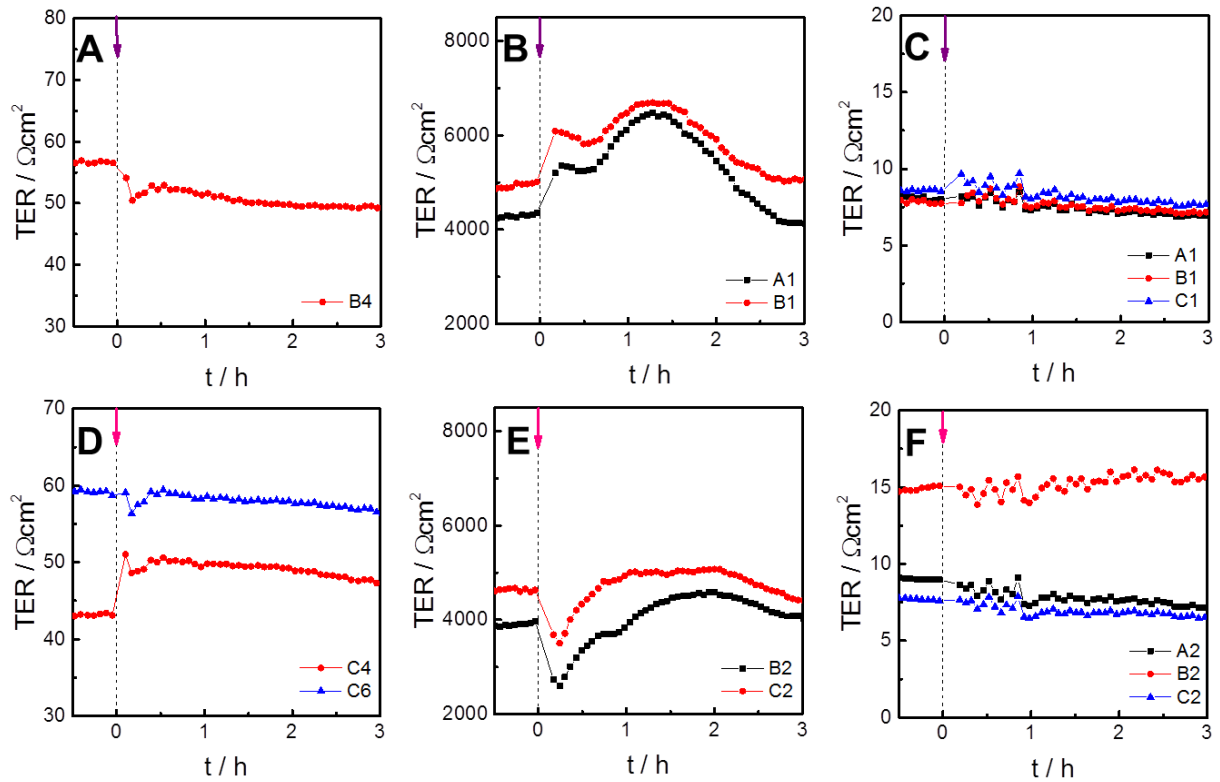


Fig. 11.10: Time-dependent changes of TER after an exchange of $\text{PBS}^{++}/\text{glucose}$ (1 g/L) in the apical compartment or after the apical addition of 1 mM FcMeOH , respectively. (A, D) MDCKII, (B, E) MDCK-I and (C, F) NRK monolayers serve as cellular barriers. The data is recorded with a cellZscope[®]-device kindly provided by nanoAnalytics GmbH (Münster, Germany).

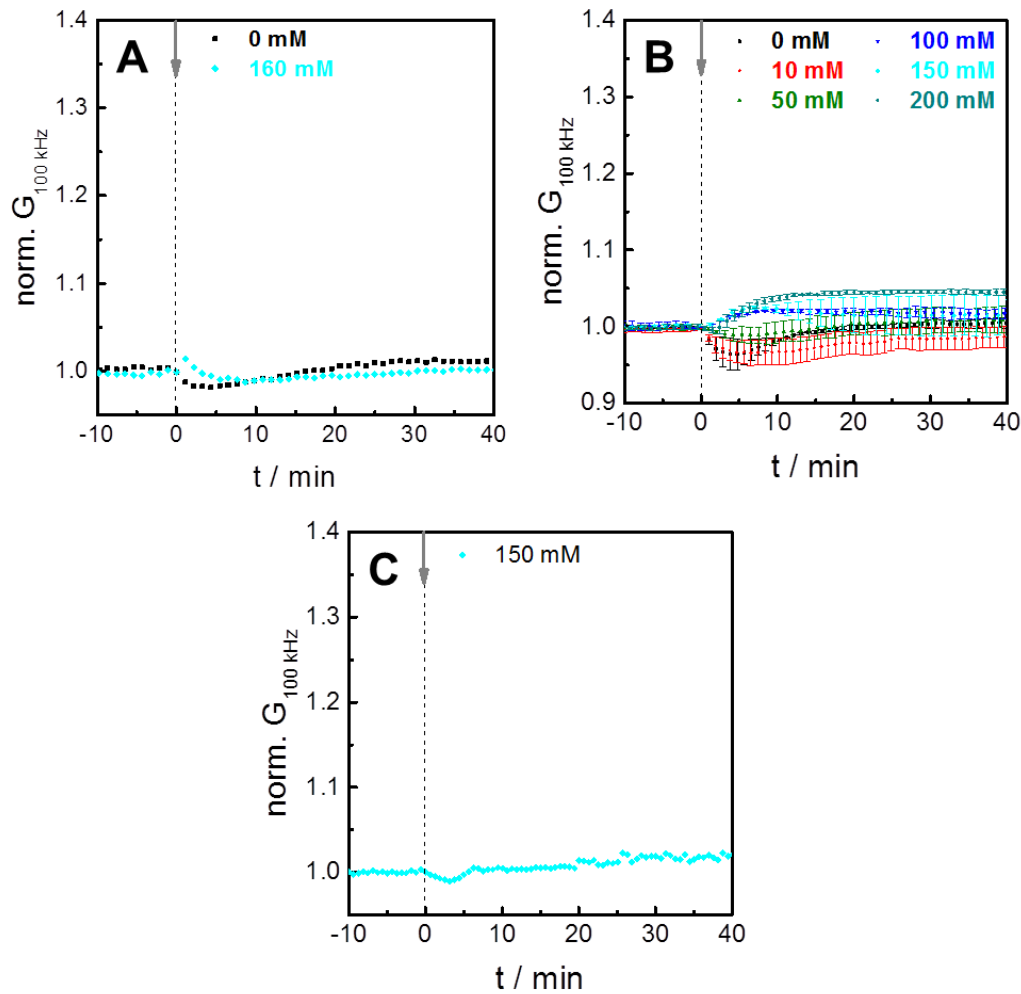


Fig. 11.11: Control measurements supporting the rationale of the impedance-based water flux detection. In all cases, water permeability is followed via time-dependent conductance changes of the basolateral buffer. **(A)** Hypertonic stimulation with **sucrose** of a cell-free filter device. In absence of an epithelial barrier, no transepithelial water transport occurs and thus, no conductance change is observed. **(B)** A NRK-covered filter insert was apically exposed to different sucrose solutions at $t = 0$ min (mean \pm SE, $n = 2$). Due to the leaky character of NRK monolayers, no osmotic pressure gradient across the barrier is induced. Therefore, the driving force of transepithelial water flux is not provided. This is reflected in the relatively constant basolateral conductance after the hypertonic stimulation. **(C)** A MDCK-II monolayer cultivated on a modified filter insert was hypertonically stimulated with sucrose. The modified filter membrane was covered with non-cytotoxic silicon glue at the backside to prevent water flux across the cellular barrier. Therefore, no conductance increase is visible after the hypertonic stimulation.

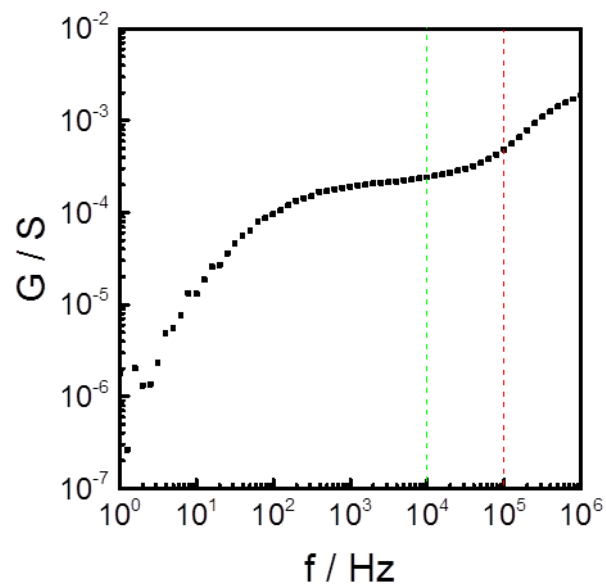


Fig. 11.12: Justification for changing the readout frequency in hypotonic water flux experiments compared to hypertonic stimulation experiments. The conductance spectrum recorded with the central electrode pair in presence of an isotonic buffer (chapter 4.1.5, Tab. 4.11) reveals a strong impact of the parasitic capacitance at the standard readout frequency of **100 kHz**. In contrast, no significant perturbances are visible at **10 kHz**.

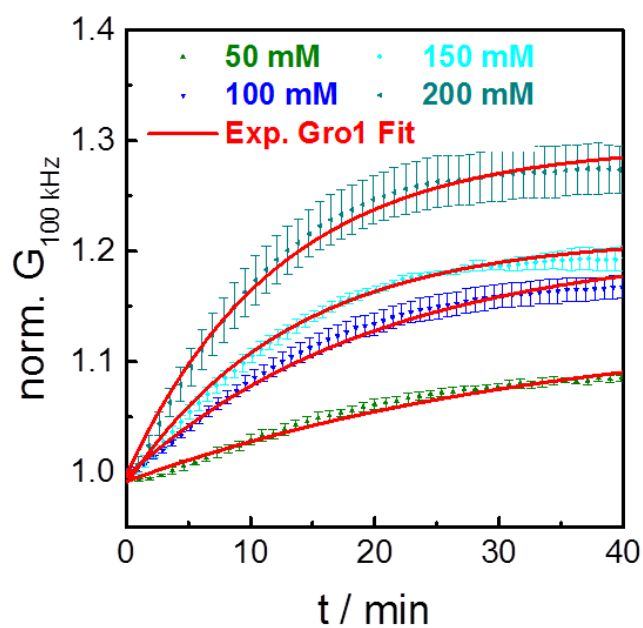


Fig. 11.13: Typical fitting procedure for impedimetric water flux analysis. The parameters of an exponential growth function of 1st order are fitted to the time-dependent changes of the basolateral conductance making the parameters τ (time-constant) and A (amplitude) accessible. This example refers to the hypertonic stimulations of MDCK-II cells (mean \pm SE, $n = 3$) recorded the central electrode pair.

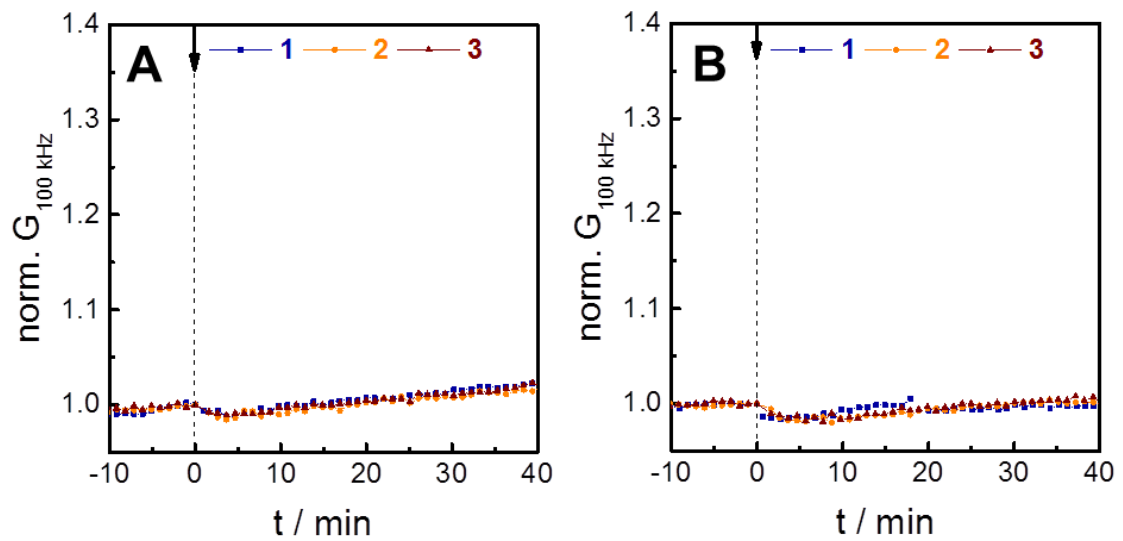


Fig. 11.14: Control experiment for the spatially resolved water flux assay. The addition of **PBS⁺⁺/glucose (1 g/L)** has no impact on the basolateral conductance in case of **(A)** MDCK-I and **(B)** MDCK-I-AQP1 monolayers indicating that water is not transported in absence of an osmotic pressure gradient.

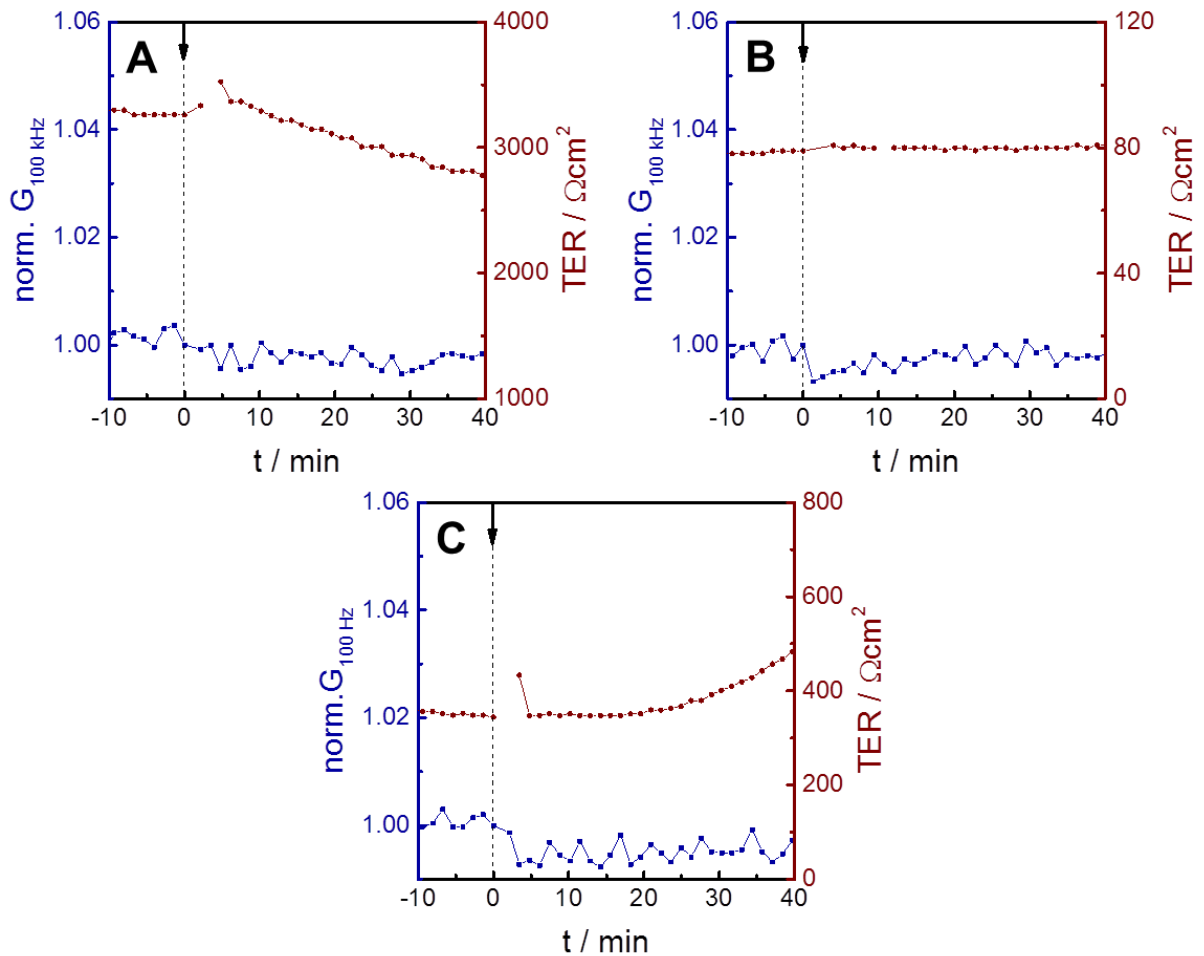


Fig. 11.15: Control experiments for the P_{OS} TER-assay recorded with IDE-400 for **(A)** MDCK-I, **(B)** MDCK-II and **(C)** MDCK-I-AQP1 monolayers. A mere addition of **PBS⁺/glucose (1 g/L)** to the apical side of the barrier does not affect the time-course of the (normalized) basolateral conductance at a frequency of 100 kHz. Consequently, conductance changes recorded with IDE-400 are due to transepithelial water flow. Unspecific effects arising from the addition are negligible.

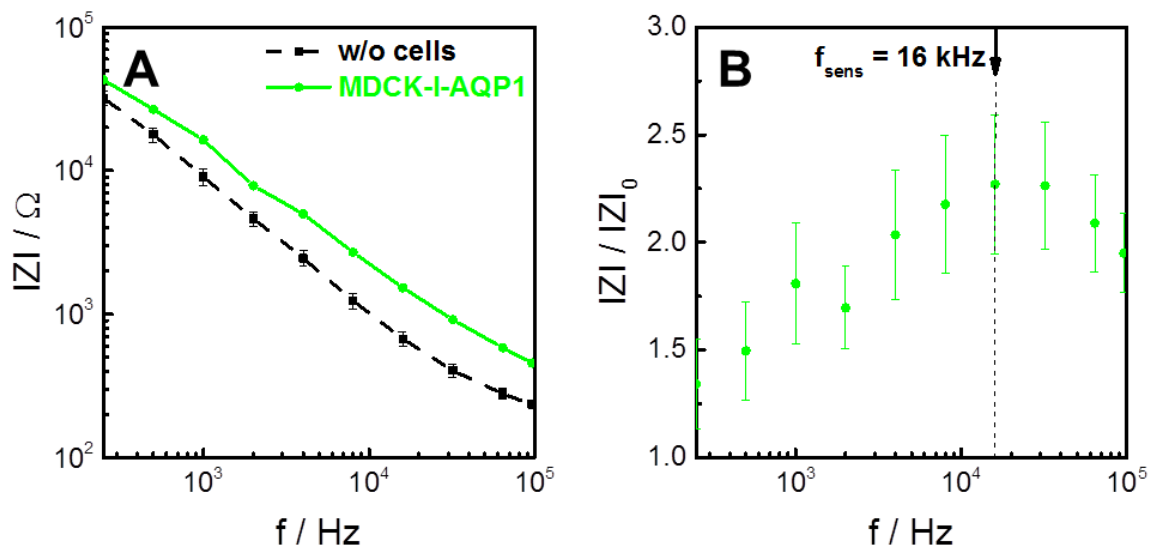


Fig. 11.16: Determination of an appropriate frequency for MDCK-I-AQP1 cells using an 8W10E+ array. **(A)** Impedance spectra recorded with the **cell-free device** and **MDCK-I-AQP1** (mean \pm SE, $n \geq 8$). **(B)** Normalized impedance spectra ($|Z|/|Z|_0$) for MDCK-I-AQP1 monolayers (mean \pm maximal error, $n \geq 8$). The spectra reveal an appropriate measurement frequency of 16 kHz for the ECIS-cytotoxicity studies.

11.2 Abbreviations and symbols

°	degree
°C	degree Celsius
%	percent
(v/v)	volume concentration
∅	diameter
A	electrode area, Ampere, amplitude
α	subcellular impedance (ECIS model), reaction order
Å	angstrom
AC	alternating current
A_{CPE}	parameter of CPE
AQP	aquaporin
B	susceptance
BBB	blood-brain-barrier
C	capacitor, capacitance
c	concentration
c^*	bulk concentration
γ	specific conductivity
ΔC	solute concentration gradient
Caco-2	heterogeneous human epithelial colorectal adenocarcinoma
cal	calorie
c_w	water concentration
C_{cl}	capacitance of the cell layer
cD	cytochalasin D
CI	cytotoxic index
C_{ins}	capacitance of the filter insert
cm	centimeter
C_m	membrane capacitance
CP	conductive polymer
CPE	constant phase element
D	diffusion coefficient, Dalton
d	distance
δ	membrane thickness
DC	direct current
Dig1	drosophila disc large tumor suppressor
DMSO	dimethyl sulfoxide
DSMZ	Deutsche Sammlung von Mikroorganismen und Zellkulturen
E_a	activation energy
EC_{50}	half maximal effective concentration
ECIS	electric cell-substrate impedance sensing
ECM	extracellular matrix
EDTA	ethylenediaminetetraacetic acid
EG	ethylene glycol

Appendix

f	frequency
F	Farad, Faraday constant, fluorescence intensity
FcMeOH	ferrocenemethanol
FCS	fetal calf serum
FITC	fluorescein isothiocyanate
Φ	phase shift
g	gram, gravity
G	conductivity, conductance
h	hour
HAuCl ₄	chloroauric acid
HBE	human bronchial epithelium
HYPO A	hypotonic buffer A
HYPO B	hypotonic buffer B
Hz	Hertz
I	current
I_0, I_1	modified Bessel functions of the first kind (order 0,1)
i_0	exchange current density
IDE	interdigitating electrode
IDE-200	interdigitating electrode (gap 200 μm / width 200 μm)
IDE-400	interdigitating electrode (gap 400 μm / width 400 μm)
IDE-combi	interdigitating electrode (width #1 1000 μm / gap 200 μm / width #2 200 μm)
Im	imaginary part
IS	impedance spectroscopy
ISO	isotonic buffer
J	tracer flow
JAM	junction adhesion molecule
J_v	volume flux
K	distribution coefficient
$\text{K}_4[\text{Fe}(\text{CN})_6]$	potassium ferrocyanide
$\text{K}_3[\text{Fe}(\text{CN})_6]$	potassium ferricyanide
k	kilo
k_{app}	apparent charge-transfer rate constant
KCl	potassium chloride
L	Liter, inductor
λ	wavelength
L_p	hydraulic permeability
LSG	laser-scribed graphene
m	milli, meter
M	molarity (mol/L), Mega
MAGI	membrane-associated guanyl kinase inverted
MAGUK	membrane-associated guanylate kinase
MDCK	Madin Darby canine kidney
min	minute
μ	micro, overpotential

Appendix

n	amount of substance, stoichiometric number of electrons, nano, number of experiments
n_R	amount of permeability probe in the receiver compartment
NAD ⁺ /NADH	nicotinamide adenine dinucleotide
n_{CPE}	parameter of CPE
NMR	nuclear magnetic resonance
NRK-52E	normal rat kidney (clone 52E)
OFET	organic field effect transistor
OLED	organic light emitting diode
Osmol	osmolality
ΔP	hydrostatic pressure gradient
PAni	polyaniline
P_{app}	apparent (molecular) permeability coefficient
P_D	diffusional water permeability coefficient
P_E	(molecular) permeability coefficient
PEDOT	poly-3,4-ethylenedioxythiophene
PEG	polyethylene glycol
PET	polyethylene
$P_{E,TER}$	Impedance-based assay for combined determination of P_E and TER
P_F	osmotic water permeability coefficient
PPy	polypyrrole
PSD95	post synaptic density protein
PSS	polystyrene sulfonic acid
PTh	polythiophene
$\Delta \Pi$	osmotic pressure gradient
R	resistor, resistance, gas constant
ρ	specific electrolyte resistance
R^2	coefficient of determination
R_{adh}	cell-substrate adhesion zone resistance
R_b	barrier resistance (ECIS model)
R_{bulk}	bulk resistance
r_c	cell radius
R_{cl}	resistance of the cell layer
R_{CT}	charge-transfer resistance
Re	real part
R_{ins}	resistance of the filter insert
rms	root mean square
R_{para}	paracellular resistance
rpm	rounds per minute
R_{trans}	transcellular resistance
[Ru(NH ₃) ₆]Cl ₃	ruthenium hexamine chloride
RVC	regulatory volume change

Appendix

RVD	regulatory volume decrease
RVI	regulatory volume increase
sec	second
S	Siemens, weighted sum of squares, membrane surface
σ	Warburg coefficient, conductivity
σ_s	solute reflection coefficient
SDS	sodium dodecyl sulfonate
SE	standard error
SECM	scanning electrochemical microscopy
SPR	surface plasmon resonance
$\Delta\Psi_{osm}$	osmotic driving force
t	time
T	absolute temperature
τ	time-constant
TER	transepithelial / -endothelial electrical resistance
U	voltage
V	volume
V_R	initial volume of the receiver compartment
V_W	partial molar volume of water
V_0	initial volume of dye-containing compartment, initial volume of basolateral compartment
Ω	Ohm
ω	angular frequency
X	reactance
Y	admittance
Z	complex impedance
Z_{adh}	cell-substrate adhesion zone impedance
Z_f	faradaic impedance element
Z_W	Warburg impedance
Z	impedance magnitude
ZO	zonula occludens

11.3 Eidesstaatliche Erklärung

Ich erkläre hiermit an Eides statt, dass ich die vorliegende Arbeit ohne unzulässige Hilfe Dritter und ohne Benutzung anderer als der angegebenen Hilfsmittel angefertigt habe; die aus anderen Quellen direkt oder indirekt übernommenen Daten und Konzepte sind unter Angabe des Literaturzitats gekennzeichnet.

Weitere Personen waren an der inhaltlich-materiellen Herstellung der vorliegenden Arbeit nicht beteiligt. Insbesondere habe ich hierfür nicht die entgeltliche Hilfe eines Promotionsberaters oder anderer Personen in Anspruch genommen. Niemand hat von mir weder unmittelbar noch mittelbar geldwerte Leistungen für Arbeiten erhalten, die im Zusammenhang mit dem Inhalt der vorgelegten Dissertation stehen.

Die Arbeit wurde bisher weder im In- noch im Ausland in gleicher oder ähnlicher Form einer anderen Prüfungsbehörde vorgelegt.

11.4 Curriculum vitae



Personal Information

Name	Florian Urban
Date of birth	05.04.1991
Place of birth	Oberviechtach
Nationality	German

University Studies and School Education

since 03/16	<p>Doctoral Student for a PhD in science (Dr. rer. nat.) University of Regensburg, Germany PhD thesis: „<i>Expanding the Scope of Impedance Analysis of Epithelial and Endothelial Barrier Function: Novel Assays and Devices</i>“ Lab: Prof. Dr. J. Wegener Institute of Analytical Chemistry, Chemo- and Biosensors</p>
10/13 – 09/15	<p>Master of Science in Chemistry University of Regensburg, Germany Master thesis: „<i>Entwicklung eines elektrochemischen Assays zur Untersuchung der Substratpermeabilität von 2D-Zellschichten</i>“ Lab: Prof. Dr. J. Wegener Institute of Analytical Chemistry, Chemo- and Biosensors</p>
04/11 – 09/13	<p>Bachelor of Science in Chemistry University of Regensburg, Germany Bachelor thesis: „<i>SPR gestützte Verfolgung der Adhäsion von MDCK-II Zellen unter diversen adhäsionsvermittelnden bzw. adhäsionsinhibierenden Bedingungen</i>“ Lab: Prof. Dr. J. Wegener Institute of Analytical Chemistry, Chemo- and Biosensors</p>
09/01 – 06/10	<p>University-entrance Diploma (Abitur) Joseph-von-Fraunhofer-Gymnasium ,Cham, Germany</p>

11.5 Danksagung

Zuallererst möchte ich mich aus tiefstem Herzen bei meinen grandiosen Eltern bedanken, ohne deren Hilfe ich weder mein Studium noch meine Promotion bewerkstelligen hätte können. Vielen Dank für all die mentale und finanzielle Unterstützung, das werde ich euch nie vergessen!

Größtmöglicher Dank gilt natürlich auch meinem Doktorvater Prof. Dr. Joachim Wegener, kurz Joe, für deine hervorragende Betreuung und deine stets zündenden Ideen. Dabei möchte ich neben deiner enormen fachlichen Kompetenz vor allem deine überragende menschliche Seite hervorheben! Auch für das spannende und interessante Promotionsthema möchte ich mich bei dir bedanken. Joe, dein einziges Manko ist die Wahl des falschen Fußballvereins! Ich habe allerdings die Hoffnung noch nicht aufgegeben, dass dir eines Tages doch noch ein Licht aufgeht; sagen wir in Form eines Stern des Südens ☺

Ebenfalls bedanken möchte ich mich bei PD Dr. Miriam Breunig für das freundliche und unkomplizierte Übernehmen des Zweitgutachtens.

Daneben möchte ich mich inständig bei meiner Freundin Carina dafür bedanken, dass du mir immer ein offenes Ohr für meine eigentlich so langweiligen laborspezifischen Probleme und Herausforderungen geliehen hast. Und natürlich auch dafür, dass du mich jedes Mal wieder aufgebaut hast, wenn mal eine Zeit lang wenig bis gar nichts im Labor funktioniert hat. Vielen Dank dafür mein Schatz!

Ich möchte mich natürlich auch bei dir bedanken, Maria! Jetzt haben wir tatsächlich das komplette Studium inklusive Promotion miteinander verbracht, oder anders ausgedrückt, fast ein ganzes Jahrzehnt! Vielen Dank für die tolle Zeit! Es war mir stets eine Freude, zusammen mit dir das Amt des „Bierdimpfls“ unserer Arbeitsgruppe auszuüben. Und natürlich auch tausend Dank für das gelegentliche „Passageiäern“! Und vergiss bitte nicht, zwischendurch mal den Inkubator zu „desinfizeiern“ ☺

Ich möchte mich zudem bei dir bedanken, Kathrin, dafür dass du mir die Zellkultur und Filtermessungen beigebracht hast! Dank deiner sensationellen Betreuung während der Masterarbeit habe ich wirklich viel gelernt, was mir definitiv zugute gekommen ist während der Promotion.

Natürlich gebührt auch der Arbeitsgruppe Wegener an sich Dank. Ich glaube nicht, dass es viele andere Arbeitsplätze mit einer solch positiven Arbeitsatmosphäre und gegenseitigen Hilfe gibt. Deswegen vielen Dank an alle! Besonderer Dank gilt natürlich unseren TAs Barbara und Nadja, die mich insbesondere am Ende meiner Arbeit in der Zellkultur unterstützt haben.

Außerdem danken möchte ich meinen beiden Praktikanten Tobias Naber und Ina-Maria Hierlmeier, die im Rahmen einer Bachelor-Arbeit bzw. eines Forschungspraktikums einige Vorarbeiten der in der Arbeit präsentierten Ergebnisse leisteten. Eure Betreuung hat mir großen Spaß gemacht!

Auch möchte ich mich recht herzlich bei der Firma nanoAnalyticsGmbH bedanken für die angenehme, zuverlässige und effektive Zusammenarbeit in den letzten drei Jahren. Unsere Zusammenarbeit hat mir von Anfang an großen Spaß bereitet und ich finde, dass man mit unseren Ergebnissen auch durchaus zufrieden sein kann!

Zu guter Letzt möchte ich mich noch bei allen „Quersties“ bedanken für einen wunderbaren Studiumseinstieg und die vielen gemeinsamen Erinnerungen, die wir miteinander teilen.